A Measurement of Electrons From Heavy Quarks in p+p Collisions at $\sqrt{s} = 200$ GeV

A Dissertation Presented

by

Harry William Joseph Themann

to

The Graduate School

in Partial Fulfillment of the Requirements

for the Degree of

Doctor of Philosophy

in

Physics

Stony Brook University

September 2011

Stony Brook University

The Graduate School

Harry William Joseph Themann

We, the dissertation committee for the above candidate for the Doctor of Philosophy degree, hereby recommend acceptance of this dissertation.

Axel Drees – Dissertation Advisor
Professor, Department of Physics and Astronomy

Jacobus Verbaarschot – Chairperson of Defense
Professor, Department of Physics and Astronomy

Alfred Goldhaber
Professor, Department of Physics and Astronomy

Helio Takai
Adjunct Professor and Brookhaven National Laboratory

Edouard Kistenev
Senior Scientist
Brookhaven National Laboratory

This dissertation is accepted by the Graduate School.

Lawrence Martin
Dean of the Graduate School

Abstract of the Dissertation

A Measurement of Electrons From Heavy Quarks in p+p Collisions at $\sqrt{s} = 200$ GeV

by

Harry William Joseph Themann

Doctor of Philosophy

in

Physics

Stony Brook University

2011

The Relativistic Heavy Ion Collider (RHIC) at BNL offers a unique opportunity in that it is capable of colliding protons and nuclei, including asymmetric collisions of different species. Open heavy quarks, that is charm or bottom not forming bound $c\bar{c}$ or $b\bar{b}$ pairs are important probes of the Quark Gluon Plasma at the Relativistic Heavy Ion Collider at BNL. They are formed at the initial collision of the nuclei and thus any effect to their transverse momentum spectra or azimuthal distribution can only come from their interaction with the matter created in the collision. One of the most powerful techniques of measuring these effects is to divide AuAu data by appropriately scaled pp data. This work focuses on providing the best possible pp reference both in scope and precision.

Transverse momentum (p_T) spectra of electrons from semileptonic weak decays of heavy flavor mesons in the range of $0.3 < p_T < 15.0 GeV/c$ have been measured at mid-rapidity ($|y| < 0.35$) beyond the previous published range of $p_T < 9.0 GeV/c$. This is done using a new technique exploiting the observed characteristics of energy deposition in the PHENIX electromagnetic calorimeters. We present this technique as well as the final measurement compared to FONLL theory predictions of open charm and bottom cross section

To Hannah, Kristian and, the love of my life, Jenny.

Contents

List of Figures viii

List of Tables xiii

Acknowledgements xiv

1 Introduction 1

2 PHENIX Experiment 4
- 2.1 Introduction . . . 4
- 2.2 Detector Coordinates . . . 5
- 2.3 BBC . . . 7
- 2.4 Drift Chamber . . . 9
- 2.5 Pad Chamber . . . 18
- 2.6 Ring Imaging CHerenkov . . . 21
- 2.7 ElectroMagnetic Calorimeters . . . 25

3 Initial Data Processing 30
- 3.1 Data Files . . . 31
- 3.2 Overview . . . 31
- 3.3 Selection Cuts . . . 32
- 3.4 Run QA . . . 34

4 Inclusive $e^{\pm}$ Cross Section 39
- 4.1 "Raw" Electron Yield . . . 40
- 4.2 BBC Correction Factors . . . 40
- 4.3 Acceptance and Efficiency . . . 41
  - 4.3.1 Matching of E & p: Data and PISA . . . 43
  - 4.3.2 Verifying Selection Cuts . . . 56
  - 4.3.3 Final Correction Curve . . . 60
- 4.4 Trigger Efficiency . . . 62

4.4.1 Systematic Error of Trigger Correction 65
4.5 Bin Width Correction 67
4.6 Inclusive Spectra 69

5 Background Subtraction at High p_T 71
5.1 Technique 71
5.2 Principle 73
5.3 FastMC 76
5.4 Constructing an Overall Fit Function 79
5.4.1 Electrons 80
5.4.2 γ Conversion Electrons 81
5.4.3 π's 83
5.4.4 Ke3 84
5.4.5 Final Fit to Data 86
5.5 Yield Fraction 89
5.6 Determination of R_π Using Reverse prob Cut 93
5.7 Comparison Subtraction Techniques 96
5.8 Systematic Error of R_π 98

6 Final Spectrum 100
6.1 Cocktail Calculation 100
6.1.1 Cocktail Input 102
6.1.2 Systematic Error on Cocktail 109
6.2 Systematic Errors 113
6.3 Heavy Flavor Spectrum 114

7 Implications for Heavy Flavor Production 117
7.1 Comparison to previously published PHENIX data 117
7.2 Final Invariant Cross Section 117
7.3 Heavy Flavor Cross Sections 121

8 Summary and Outlook 136

A Tables 138

B Supplementary Figures 145
B.1 eID Selection Cut Profiles 146
B.1.1 EMC Matching 146
B.1.2 Shower Shape 149
B.1.3 RICH Variable 152
B.2 Fits to electron E/p profiles 155
B.3 Fits to γ conversion electron E/p profiles 159

B.4 Fits to π E/p profiles 163
B.5 Fits to Ke3 E/p profiles 166
B.6 Fits to data E/p profiles 169

Bibliography **173**

List of Figures

1.1 Some semi-leptonic decays of D and B mesons. 2
1.2 LO and most important NLO heavy quark production diagrams. LO - a) "gluon fusion" b) "quark-antiquark annihilation" NLO - c) Pair creation with gluon emission in output channel d) " flavor excitation" e) "gluon splitting" f) "gluon splitting but of " flavor excitation" character 3

2.1 "Beam's eye" view of PHENIX showing the central arm detectors. 4
2.2 Side view of PHENIX showing the **B** field return iron and the muon arms. 5
2.3 PHENIX coordinate system 6
2.4 Pseudorapidity illustration 7
2.5 Schematic View of the BBC 8
2.6 Photograph of one BBC barrel before the installation. 9
2.7 The titanium frame that supports all of the DCH components. 10
2.8 The layout of wire position within one keystone. The beam direction is into(out of) the page. 11
2.9 The field lines that are seen by a signal electron. 12
2.10 A track superimposed on a keystone 13
2.11 Simple Hough transform example[1] 14
2.12 Hough space plot example[1] 15
2.13 This is how p_T is determined. 16
2.14 Bending-plane Hough space distribution for one sample track. Black points (tight cluster) correspond to X1 versus X2 hit combinations while red (upper right streak) and blue (lower right streak) points come from X1 only and X2 only combinations respectively. 17
2.15 Simulated hits in a portion of the drift chamber and the corresponding Hough transform for X1 and X2 wires. 17
2.16 Schematic of the PHENIX pad chambers. Some sectors of the PC2 and PC3 sections are removed for clarity. 19

2.17 Concept of a pad chamber. 19
2.18 Principles of the PC pad geometry. 20
2.19 Schematic of Cherenkov radiation. 21
2.20 A plot of Eq. 2.10 for π's and $e^{\pm}$'s in the RICH 22
2.21 The placement and internal layout of the RICH. 23
2.22 The RICH use of a spherical reflector. 24
2.23 Derivation of RICH Variables. 24
2.24 A cartoon of an electromagnetic shower in a homogeneous block of material. 25
2.25 EM showers in PbGl and PbSc calorimeters 26
2.26 PbGl and PbSc modules 27

3.1 Initial Run 6 Electron Candidate Yield/Event 34
3.2 Run 6 Electron Candidate Yield/Event 35
3.3 The ratio of MB::ERT trigger in the MB data set and the ERT data set for the Run 5 data set. One entry of the histogram is for one run 37
3.4 The ratio of MB::ERT trigger in the MB data set and the ERT data set for the Run 6 data set. One entry of the histogram is for one run 38

4.1 BBC trigger bias as a function of π^0 p_T with a zeroth order polynomial fit. 41
4.2 $\frac{dN}{d\phi}$ plot for Run 6 42
4.3 Some Examples of E/p Profiles with Gaussian Fits 44
4.4 μ of E/p profiles as a function of p_T 45
4.5 σ of E/p profiles as a function of p_T 46
4.6 Drift Chamber determination of p 48
4.7 Invariant mass spectrum of dielectrons [2] 50
4.8 Fit to J/Ψ peak, Run8 dAu dielectrons [2] 50
4.9 Fit to ϕ peak, Run8 dAu dielectrons [2] 52
4.10 Final Fit to E/p σ's 52
4.11 Overlay of E/p profiles from simulation. Three curves corresponding to the central, upper and lower values of the C_1 parameter. 54
4.12 Relative uncertainty of E/p as a function of p_T 55
4.13 Yield as a function of the EMC matching cut. 56
4.14 EMC matching cut efficiency. 57
4.15 Yield as a function of the prob cut. 58
4.16 EMC shower shape cut efficiency. 58
4.17 Yield as a function of the n_1 cut. 59

4.18 Ratio, in data, of $n_1 \geq 3$ to $n_1 \geq 5$. 59
4.19 n_1 efficiency at $n_1 \geq 3$ for both data and simulation. 60
4.20 The effect of finite resolution on steeply falling spectra 62
4.21 Acceptance and Efficiency Correction Curve for Run 6 63
4.22 Run 6 raw p_T spectra 64
4.23 Run 6 trigger efficiency 65
4.24 Run 6 corrected and normalized spectra 66
4.25 Ratio of MB to ERT 67
4.26 Inclusive invariant cross section for Run 6, re binned 69
4.27 Inclusive Yield ERT Data plotted with a heavy flavor theory prediction. 70

5.1 Typical E/p profile without hadron contamination 72
5.2 Significant hadron contamination 73
5.3 Cartoon of Longitudinal Development of a Hadronic Shower. The fraction of deposited energy can vary widely 74
5.4 Showers can start anywhere 74
5.5 EMC response to 1 GeV/c ps $\pi's$ and electrons. Notice the profile of the π energy distribution 75
5.6 RICH focal plane in FastMC 76
5.7 The number of Cherenkov γ's as a function of momentum for π's and $e^{\pm}$'s from Eq. 5.5 normalized to the mean value of n_1 for electrons. 78
5.8 n_1 plotted as a function of mean number of Cerenkov $\gamma's$ generated. 79
5.9 n_1 plots from data and FastMC, with Cherenkov mean set to 10 in FastMC. 80
5.10 Two gaussian fit to simulated electrons, these last few bins clearly show the tail in E/p 81
5.11 Six gaussian fit to simulated γ conversions. 83
5.12 Fit to π E/p profiles 84
5.13 Ke3 E/p profiles 86
5.14 R_π determined from simulation with no eID cuts 89
5.15 Fits $e^{+/-}$ published data. 91
5.16 Fits published non heavy flavor to heavy flavor ratio. 91
5.17 Fit functions for π's and inclusive $e^{\pm}$'s. 92
5.18 Division of fits, plotted in 0.01 GeV bins. 92
5.19 Final calculation of the yield fraction in simulation compared to data. 93
5.20 R_π from simulation and CuCu data calculated with RICH ignored and various prob cuts 94

5.21 R_π from simulation and CuCu data calculated with RICH $n_1 \geq 3$ and various prob cuts . . . 95
5.22 R_π from simulation with all eID cuts with a third degree polynomial fit . . . 95
5.23 Four different methods of determining the heavy flavor cross section . . . 97
5.24 π/e ratio of the four different methods of determining the heavy flavor cross section . . . 98
5.25 Ratio of R_π's, the solid line is at 1 and the dashed lines are at $\pm 25\%$ . . . 99

6.1 Hagedorn fit to combined neutral and charged π's . . . 103
6.2 Measured combined neutral and charged π's spectrum divided by Hagedorn fit. cf. 6.1 . . . 103
6.3 Hagedorn fit, with m_T scaling, to various meson species . . . 104
6.4 Cross sections divided by m_T scaled Hagedorn . . . 105
6.5 Corrected m_T scaled Hagedorn, compared to various meson species . . . 106
6.6 Ratio of π invariant spectrum to the invariant spectrum of all π decay γ's. . . . 109
6.7 Direct photon data, blue(lower) triangles. The red(lower) triangles are this same data scaled by π/γ ratio to represent the direct pions. The black line is the fit whose parameters are entered into EXODUS. . . . 110
6.8 Direct γ data from [3] plotted with the various γ spectra from EXODUS. . . . 110
6.9 Ratio of direct γ data from [3] to direct γ from EXODUS. . . . 111
6.10 The final cocktail . . . 111
6.11 Individual contributions to the cocktail systematic error. The total error is depicted by the data points which are shown together with a fit . . . 112
6.12 Same as Fig. 6.11, now showing fit parameters . . . 113
6.13 The inclusive spectrum with the cocktail and two different subtracted spectra (see text) . . . 115
6.14 Heavy flavor invariant cross section for Run 6 with systematic errors . . . 116

7.1 Heavy flavor invariant cross section for Run 6 and previous PHENIX data. . . . 118
7.2 Ratios showing agreement of current measurement to ppg077 . 119
7.3 Final spectrum with theory curves and systematic errors Run 6 120

7.4 Final spectrum with Drell-Yan and published PHENIX data. . 121
7.5 Fit to heavy flavor spectrum with a single parameter with the sum of the D & B curves from 1.4 GeV and above. 126
7.6 Fit to heavy flavor spectrum with both D and B from 1.4 GeV and above. 128
7.7 Fit to heavy flavor spectrum with B only from 6 GeV and above. 129
7.8 Our cross section calculations compared with other measurements and the FONLL prediction. 130
7.9 Our cross section calculations compared with other measurements and the FONLL prediction. 131
7.10 The variation of the crossing point of bottom quark dominance. 132
7.11 Our cross section calculations compared with other measurements and the FONLL prediction. The red and blue points are our measurements, Table 7.2. The red points are from the scaling method and the blue points are the integral method. All points are displaced slightly along the abscissa to make them visible, all measurements are at $\sqrt{s} = 200GeV$. 134
7.12 Our cross section calculations compared with other measurements and the FONLL prediction.The black arrow is the upper limit measurement and the red points are the other two measurements from Table 7.3. The red points are displaced slightly along the abscissa to make them visible, all measurements are at $\sqrt{s} = 200GeV$. 135

B.1 EMC matching cut profiles. 146
B.2 EMC matching cut profiles. 147
B.3 EMC matching cut profiles. 148
B.4 Shower shape cut profiles. 149
B.5 Shower shape cut profiles. 150
B.6 Shower shape cut profiles. 151
B.7 RICH cut profiles. 152
B.8 RICH cut profiles. 153
B.9 RICH cut profiles. 154

List of Tables

4.1 $\frac{dN}{d\phi}$ systematic error numbers. 43

5.1 Conversion Material Parameters 82

6.1 Decays channels in EXODUS 101
6.2 meson rapidity densities used in our meson decay generator. . 105

7.1 Scale factors from fitting FONLL shapes to data. 125
7.2 Total charm cross sections 125
7.3 Total bottom cross sections 125

A.1 raw numbers Run6 $n_1 \geq 5$ 139
A.2 Heavy flavor raw yield, yield fraction. 139
A.3 Heavy flavor raw yield, $\pi's$ from fit. 140
A.4 Heavy flavor raw yield, $\pi's$ from absolute normalization. . . . 140
A.5 Raw Non-Photonic $\pi's$ subtracted using R_π Run6 $n_1 \geq 5$ . . . 141
A.6 Raw Non-Photonic $\pi's$ subtracted using R_π Run6 $n_1 \geq 5$ . . . 142
A.7 Differential invariant cross section of electrons $((N_{e^+} + N_{e^-})/2)$ from heavy-flavor decays for 200 GeV $p + p$ collisions at mid-rapidity. The cross section and corresponding errors are in units of millibarns. This table is in reference to Fig. 7.3 143
A.8 Individual Systematic Errors 144

Acknowledgements

A journey such as mine could not have taken place without the help of many people and I thank all of them. But there are some that I would name so that some small recognition of the good deeds they have done in my cause exists in the world.

The first person I ever met at Stony Brook, Harold Metcalf, taught me to believe in myself.

Two people, Professor Lee Wilcox and David Rahm of Brookhaven National Lab, with no amount of patience at all, taught me to think as a scientist.

Michael Marx, my adviser as a Master's student got me started.

And of course my doctoral adviser, Axel Drees, who brought me to the end my journey with infinite patience and a large hammer to beat things into my thick skull.

Chapter 1

Introduction

The Relativistic Heavy Ion Collider (RHIC) was built to produce and study the so called quark gluon plasma (QGP). The QGP is a state of matter in which the degrees of freedom are colored partons, quarks and gluons as opposed to the color free hadrons that we actually see in our detectors. RHIC is able to create the matter/energy density thought to be necessary to create the QGP. We now believe that this creation is indeed happening, there are a series of "white papers" from the four experiments at RHIC that present an overview of this evidence [4–7].

Whether or not a QGP is formed does not preclude the study of the properties of the hot dense matter that is certainly created in a RHIC Au-Au collision. The medium that is created is exceedingly small, on the order of $1000fm^3$ and its lifetime exceedingly short, $\approx 100fm/c$. This means that the medium can only be probed with particles created in the collision. The white papers outline many observables that can be used to measure the properties of the medium.

In this thesis we will focus on so called hard probes, a particle created from a QCD hard scattering event which occurs at the very earliest stage of a collision. A hard probe has well measured creation properties that can also be well described by theory. Since it is only created in the initial collision, any alteration of measured properties can only come from interacting with the matter created in the collision of the nuclei.

The charm quark was discovered in 1974, the bottom quark three years later in 1977, with masses, $m_c \approx 1.2 - 1.5GeV, m_b \approx 4.19 - 4.67GeV$. There are two types of charm and bottom carrying mesons, so called "open" where we have a charm(bottom) quark paired with another quark and a so called "closed" where

one has charm(bottom) anti charm(anti bottom) pairs. The energy needed to create charm and bottom quarks is much larger than Λ_{QCD} thus allowing the use of perturbative Quantum Chromodynamics (pQCD), a theoretical model of the strong color field interaction, to describe the production mechanisms and rates of Open Charm and Bottom.

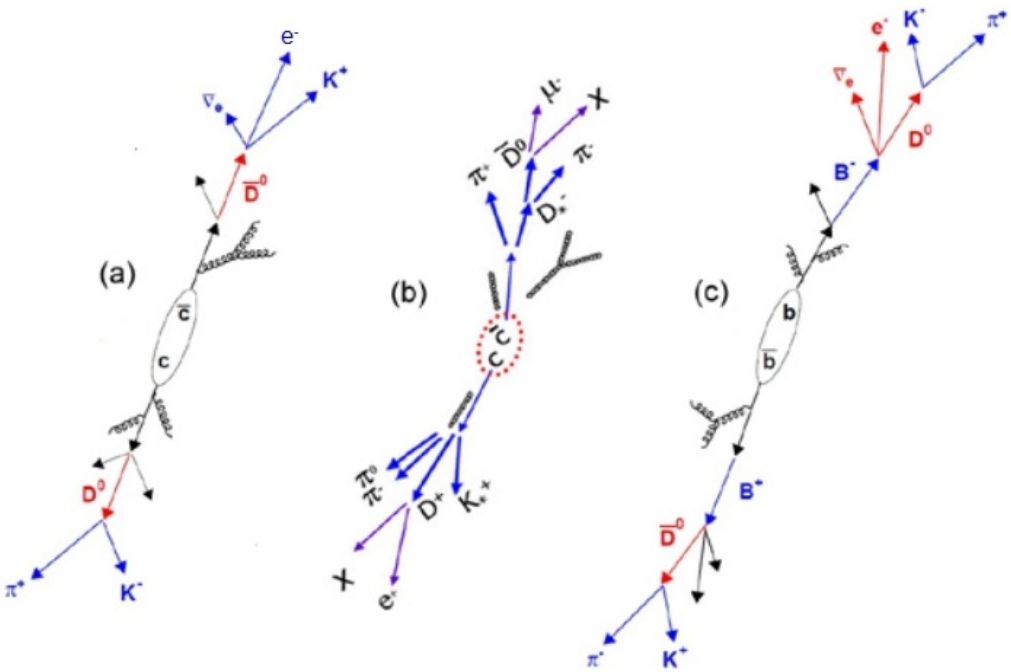

Figure 1.1: Some semi-leptonic decays of D and B mesons.

Open charm particles are produced by the fragmentation of $c\bar{c}$ pairs, Fig 1.1. The dominant mechanism is the leading order (LO) gluon fusion Fig 1.2a. Consequently they should provide us information as to the gluon densities of the incoming particles. With RHIC we now have the possibility of studying this gluon density as a function of system size by measuring open charm.

Of particular interest are effects which modify the transverse momentum spectra of heavy flavor hadrons and their decay products, including energy loss, transverse momentum broadening in both cold nuclear matter and in passage through a hadronizing QGP as well as collective effects such as transverse flow. In addition, J/Ψ regeneration in a QGP from the initial open charm yield has been suggested. Thus up-to-date benchmark calculations of both the total charm yield and the transverse momentum spectra are imperative.

We will present a measurement of the electrons from the decay of D and B

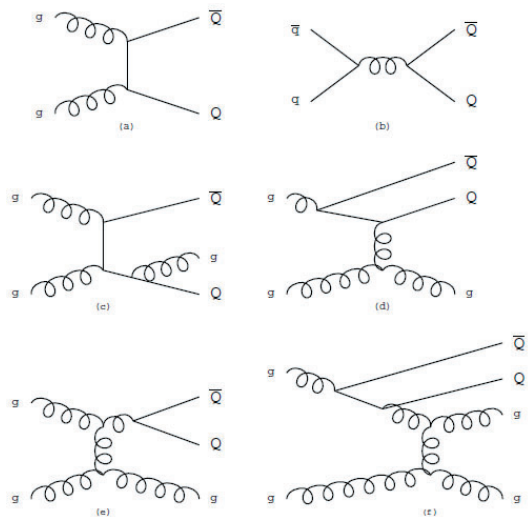

Figure 1.2: LO and most important NLO heavy quark production diagrams. LO - a) "gluon fusion" b) "quark-antiquark annihilation" NLO - c) Pair creation with gluon emission in output channel d) " flavor excitation" e) "gluon splitting" f) "gluon splitting but of " flavor excitation" character

mesons in pp collisions at 200GeV center of mass energy using the PHENIX detector at RHIC, Fig 1.1. The current state of the art in theory predictions are so called Leading Order (LO), Next to Leading Order (NLO) and First Order Next Leading Logarithm (FONLL). These are "lattice" type calculations using various levels of the diagrams of Fig 1.2 which represent various orders of the strong coupling constant α_s. For a comprehensive overview of these calculations please see Creutz[8], Vogt[9] and Sterman[10].

Chapter 2

PHENIX Experiment

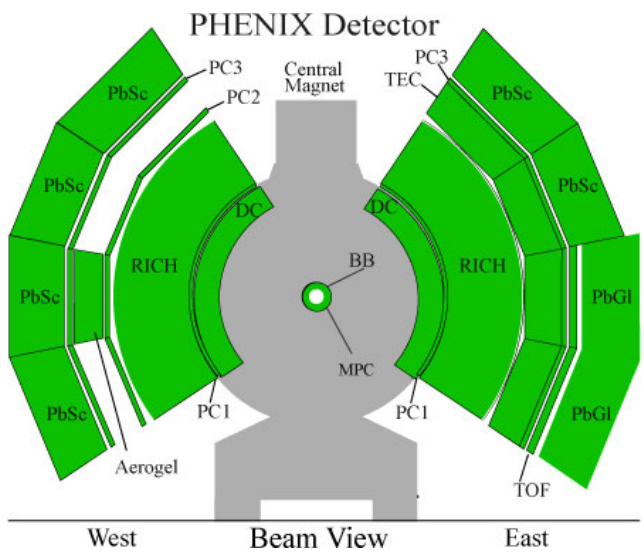

Figure 2.1: "Beam's eye" view of PHENIX showing the central arm detectors.

2.1 Introduction

The PHENIX experiment has been taking physics data at RHIC since 1999. It is a high rate high multiplicity spectrometer designed to make precision measurements of rare processes even in the environment of the dense particle production in AuAu collisions. It is well described elsewhere [11], Fig. 2.1 shows schematic representation of PHENIX from the point of view of the beam axis. Fig. 2.2 is a side view. In this analysis we use a sub set

of PHENIX, the BeamBeamCounter [BBC], the DriftCHamber [DCH], PadChamber1 [PC1], the RingImagingCHerenkov(counter) [RICH] and the ElectroMagneticCalorimeter [EMC]. We will go through each subsystem separately explaining what it is and how it is used.

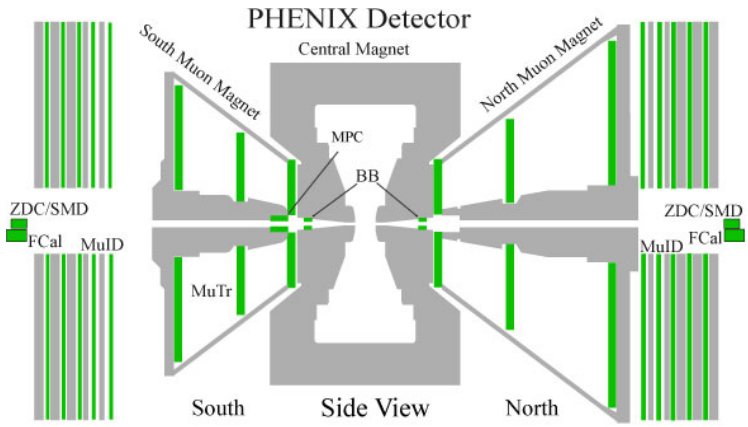

Figure 2.2: Side view of PHENIX showing the **B** field return iron and the muon arms.

2.2 Detector Coordinates

The cartesian coordinates of any collider experiment have the z axis along the beam line, the y axis straight up and the x axis horizontal. In PHENIX, Fig. 2.3, positive x points West, and positive z points North. The Central arms are at right angles to the beam axis and are designated the East and West arms. The Muon Arms are arrayed parallel to the beam axis and are designated North and South.

Most of the time we speak in terms of cylindrical coordinates, the z axis and ϕ, the azimuthal angle, with $\phi = 0$ in the West direction.

Another important coordinate is called pseudorapidity, it is a description of the angle, θ, relative to z, the beam axis,

$$\eta = -\ln\left[\tan\frac{\theta}{2}\right]. \tag{2.1}$$

It can be written in terms of the momentum,

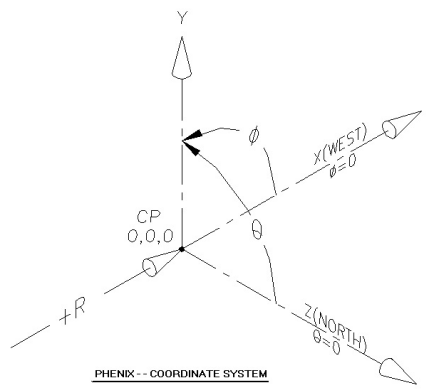

Figure 2.3: PHENIX coordinate system

$$y = \frac{1}{2}\left[\frac{|\mathbf{p}| + \mathbf{p_L}}{|\mathbf{p}| - \mathbf{p_L}}\right], \tag{2.2}$$

the L standing for longitudinal.

Pseudorapidity only requires knowledge of the polar angle. It is related to the rapidity which requires knowledge of a particular particle,

$$y = \frac{1}{2}\left[\frac{E + p_L}{E - p_L}\right]. \tag{2.3}$$

For highly relativistic particles the mass can be ignored and then $y = \eta$.

As can be seen in Fig. 2.4, as $\theta \to 0(\pi)$ or as p_L increases the magnitude of the pseudorapidity and rapidity increase respectively, we say that we are going in a more forward direction. Units of pseudorapidity represent smaller and smaller $\Delta\theta$, the unit is preferred because, loosely speaking, particle production is constant as a function of rapidity.

The PHENIX central arms cover a pseudorapidity range $-0.35 \leq \eta \leq 0.35$, we correct our measurements up to $-0.5 \leq \eta \leq 0.5$ or 1 unit of rapidity when we quote results. Implicit in this is our assumption that $dN/d\eta$ is constant in the range $-0.5 \leq \eta \leq 0.5$

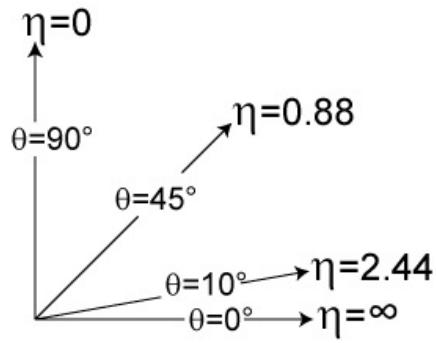

Figure 2.4: Pseudorapidity illustration

2.3 BBC

The BBC consists of two arrays of hexagonal Cerenkov radiators each arranged as an annuli about the beam pipe. The face of each array is 1.44m from the center in z of PHENIX and cover a pseudo rapidity of 3.1-4.0 and 2π azimuth. In a proton proton collision the BBC has three purposes;

1. Provide a minimum bias trigger.
2. Determine the collision vertex in z.
3. Set time zero, t_0. This aids in assembling events and provides the start time for timing detectors e.g. the Drift Chamber.

A high energy particle detector is essentially a camera taking snapshots of events. In the case of this analysis the event is the impact of protons in counter rotating bunches in the RHIC rings. The proton bunches are steered such that they intersect in the center of PHENIX, the interaction point or IP. When the bunches propagate through each other one proton from each bunch may collide, either "head on", a so called hard scatter or grazingly where only the fringe of the color fields interact, a so called diffractive event.

We only want the camera to snap when there is actually an event happening. The assumption is that in any collision at least one secondary will go forward and one backward. When the BBC sees these two in coincidence a minimum bias trigger is issued and PHENIX makes a measurement and writes out the information.

Each of the phototubes of the BBC has an intrinsic timing resolution of $\sigma_t = 50ps$. RHIC supplies a reference clock signal, the time of impact into

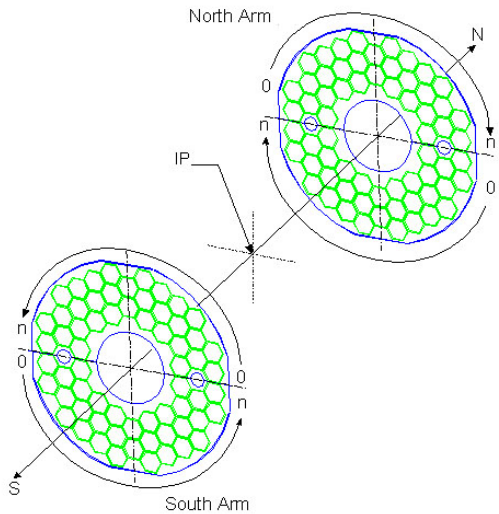

Figure 2.5: Schematic View of the BBC

each BBC module is measured relative to this clock and is used to calculate the BBC t_0. This is determined by taking the average time measured by each PMT of a module and then taking the half sum of these averages,

$$t_0^{BBC} = \frac{(t_N^{BBC} + t_S^{BBC})}{2}. \tag{2.4}$$

Then the vertex position will be the half difference,

$$Z_{vtx}^{BBC} = (t_N^{BBC} - t_S^{BBC})/2c. \tag{2.5}$$

The majority of pp events will have only one particle in each BBC module so the estimated vertex resolution from Eq. 2.4 as $\sigma_z = \sigma_t/\sqrt{2} \approx 1.2cm$ For a central AuAu event this becomes much better ($\sigma_z \leq 0.3cm$) since many more secondaries are hitting the BBC modules, when the times are averaged a much more precise measurement is possible.

This position determination is used to restrict our triggering to a z range about the center of PHENIX so that grazing interactions of the secondaries with the magnet pole tip are minimized. The magnet pole tips can be seen in the lower half of Fig 2.2, the collision occurs in the very center

Since the BBC trigger only requires one hit per side, it is efficient for a wide variety of interaction processes, this is why it is referred to as a "Minimum

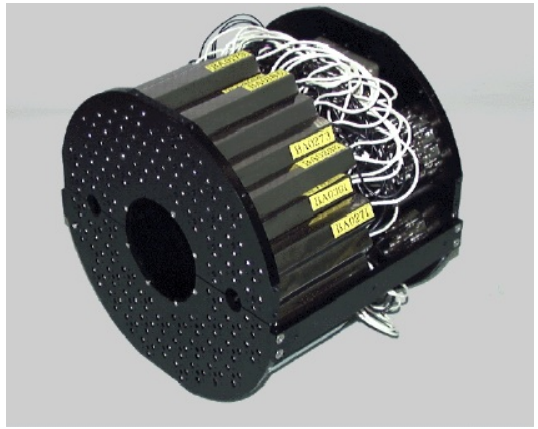

Figure 2.6: Photograph of one BBC barrel before the installation.

Bias" trigger.

2.4 Drift Chamber

The Drift Chamber is the first of the central arm detectors of PHENIX that is used in this analysis, Fig 2.1, and is the main tracking device in PHENIX. All of the central arm detectors occupy two 90° patches in azimuth and cover a polar angle, θ, range corresponding to a pseudorapidity, $|\eta| < 0.35$, centered about $\theta = 90°$. It is placed at a radius $202cm < r < 246cm$ with a module in both central arms. This spatial region is well visualized in Fig. 2.7 which is a drawing of the frame which is the backbone of the DCH.

The DCH performs the following tasks:

- Accurate determination of charged track transverse momentum p_T .
- Measure, in concert together with PC1 and BBC, z at the DCH and, consequently, the angle of a particle track w.r.t. beam axis, θ.
- Determine the tracks of charged particles though PHENIX.

The DCH is a multi wire detector and uses drift time to measure distance. A particle traverses the chamber leaving a trail of ionization in its wake. The ionization electrons drift towards anode wires with a known velocity so that drift time equals distance. With known locations of the wires spatial points along the particle trajectories can be plotted. The DCH is a jet type detector

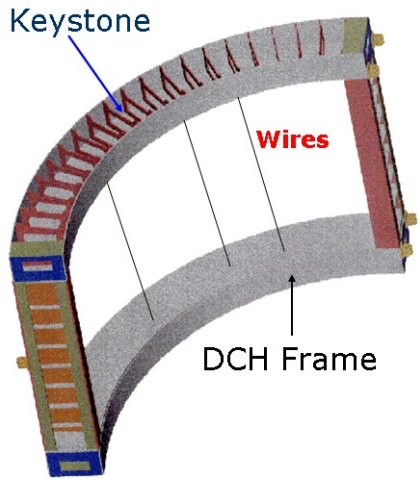

Figure 2.7: The titanium frame that supports all of the DCH components.

[12, 13] in that the drift direction of the signal electrons is transverse to the wire direction and the wires are arranged in cells.

There are six layers of wires in a cell, in PHENIX parlance, a keystone Fig. 2.8. The X1 and X2 wires are the main tracking wires, they project at right angles to the keystone to the opposite keystone on the other side of the DCH. The wires are electrically broken at the mid point, there is a circuit board strip along the mid point to which the wires are attached. The wires are instrumented with Front End Modules that contain all of the front end electronics as well as digitizing and fiber optic circuitry.

The other four layers are so called "stereo" wires and they are used to determine the z coordinate. They are at angles to the left and right of the keystone in the figure and are attached to the adjacent opposite keystones. Since these wires cross the X1 and X2 wires simultaneous hits in particular groupings of these layers shows the possibility of determining the z coordinate. In practice this has not worked out with sufficient accuracy and the use of PC1 (section 2.5) for z determination is preferred.

Each plane of wires has particular specialized wires as whose functions are as follows;

- Cathode Wires Create uniform drift field between anode and cathode.
- Field/Potential Wires Separate adjacent anode wires and help to control gas gain.

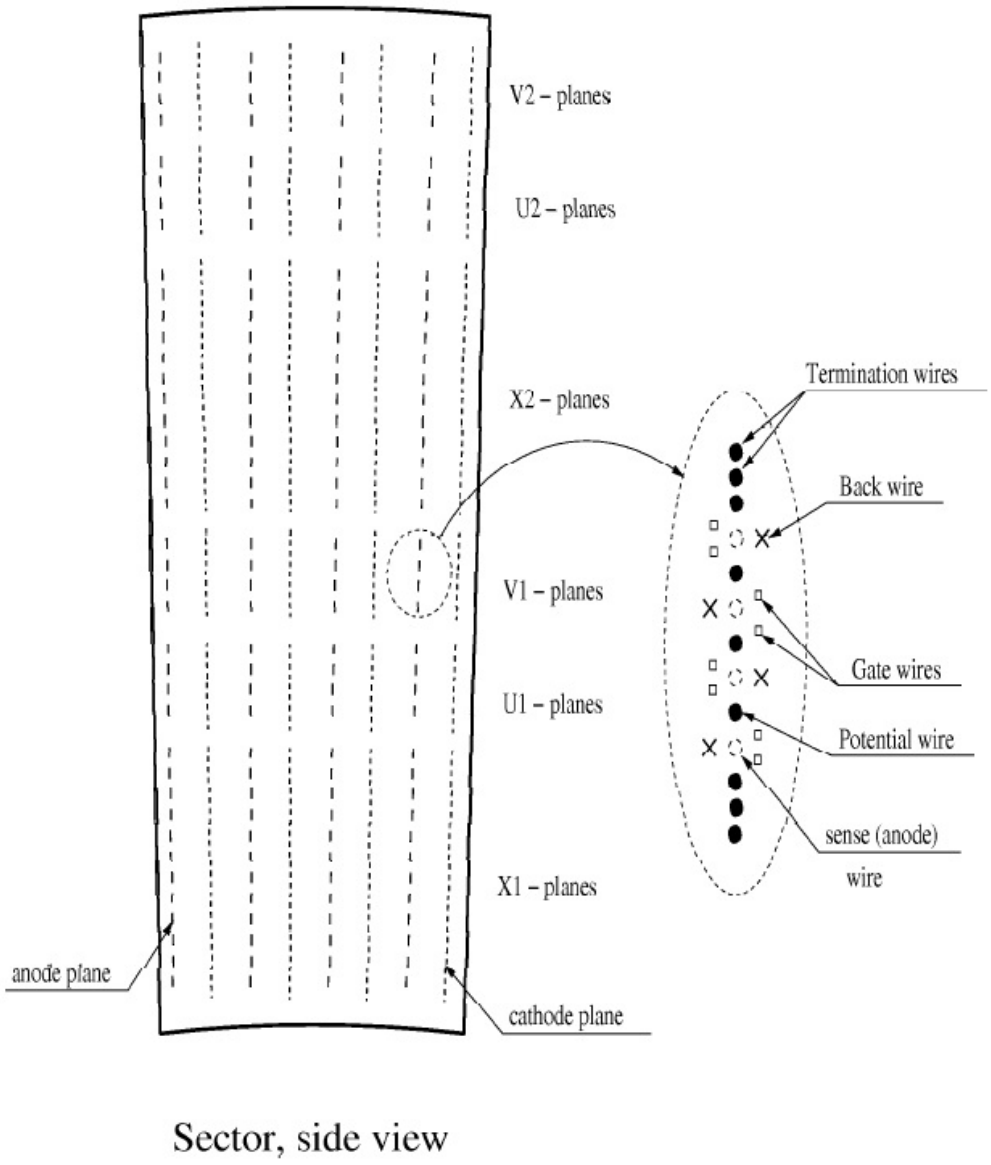

Figure 2.8: The layout of wire position within one keystone. The beam direction is into(out of) the page.

- Back Wires Stop drift from one side of the anode wire.
- Gate Wires Localize the drift region width.
- Termination Wires Help to reduce boundary affects, make gas gain uniform along the plane.

The most obvious advantage of this arrangement of wires is that the back wires remove the left/right ambiguity. If one imagines that the sense wires are numbered consecutively then only even(odd) numbered wires will fire depending on which side the track is on.

The other important design strength are the gate wires. These wires restrict the path length that is sampled by a sense wire. Referring to Fig. 2.9, the blue field lines lead to the sense wires, signal electrons from points along the path that are intersected by blue field lines will be collected. The length of a field line is proportional to the time needed for a signal electron to travel from the point of generation to the sense wire. If one focuses on the orange field lines the point is more easily illustrated. The path lengths are significantly longer at the outer edges of the region, the electrons traveling along these lines will take longer to arrive than the electrons traveling along the central lines.

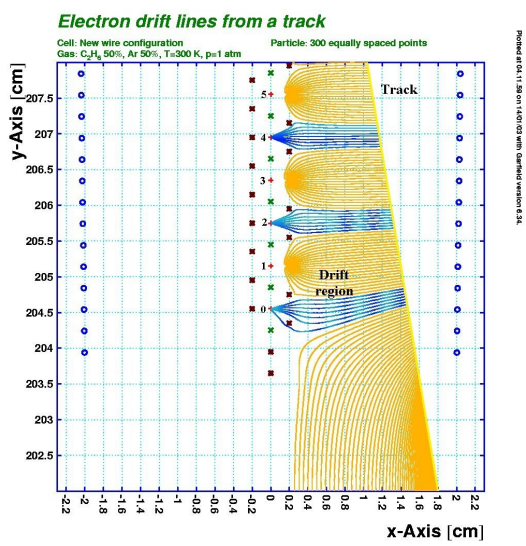

Figure 2.9: The field lines that are seen by a signal electron.

This spread of path lengths represents a spread in time during which one could not distinguish between separate tracks. By limiting the path length

sampled, the blue field lines, we also limit the spread in time of a particular signal thus allowing separation of adjacent tracks that are closer together than if we sampled complete tracks.

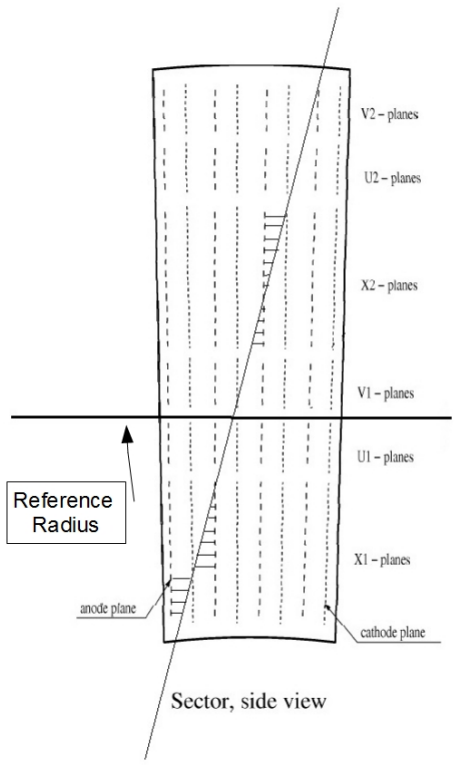

Figure 2.10: A track superimposed on a keystone

In Fig. 2.10 we see a hypothetical track traversing a typical keystone. There is no requirement that a track be constrained to one keystone, this is drawn for convenience. The short horizontal lines are the paths of the ionization electrons from the track to the anode wires. Recall that the anode plane "knows" which side the track is on because of the guard wires. The result is an unambiguous set of points.

There are, of course, mitigating factors to this. The simplest factor are dead anode wires, either broken or with dead electronics, even if a particular

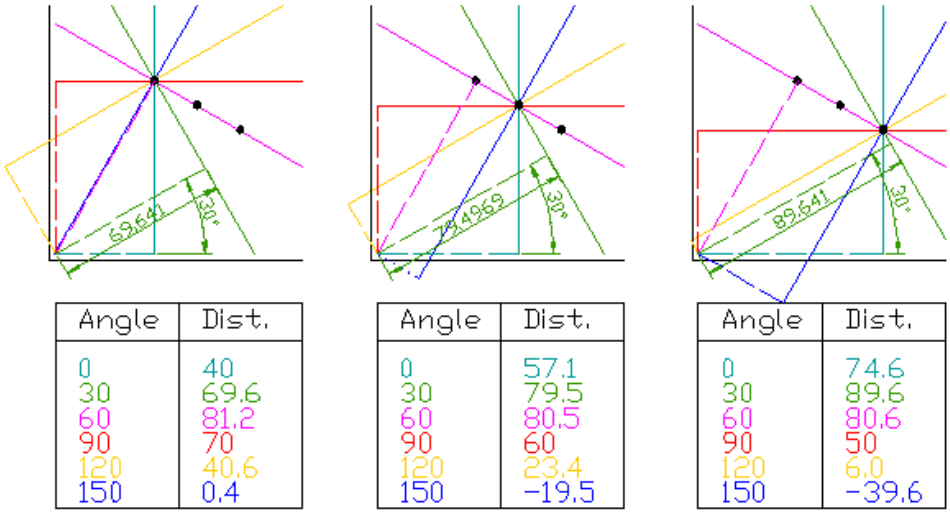

Figure 2.11: Simple Hough transform example[1]

wire is unbroken it could be shorted by a neighboring broken wire. Another issue could be a coincident track very close and at a similar angle, not usually an issue in pp collisions where the average number of secondaries is ≈ 30.

Another source of ambiguity is if a track passes within the guard wires, the left right ambiguity returns.

The hits in the X1 and X2 planes are combined into tracks using a pattern recognition algorithm called a Hough transform. The bend plane of the magnetic field is the xy plane in PHENIX coordinates. The DCH is outside of the magnetic field so all potential tacks are straight lines in the xy plane and can be thought of as having a slope, m, and and a y-intercept, b. If one were to imagine several lines drawn through each point it can be easily seem that a slope and intercept can be calculated for each line. If one were to create a two dimensional histogram of these parameters there would be clustering near to the slope and y-intercept represent a line through the points.

Since m and b are not bounded one usually transforms into a more appropriate space as in the following example from Wikipedia[1].

Consider three data points, shown here as black dots in Fig. 2.11

- For each data point, a number of lines are plotted going through it, all at different angles. These are shown here as solid lines.
- For each solid line a line is plotted which is perpendicular to it and which intersects the origin. These are shown as dashed lines.

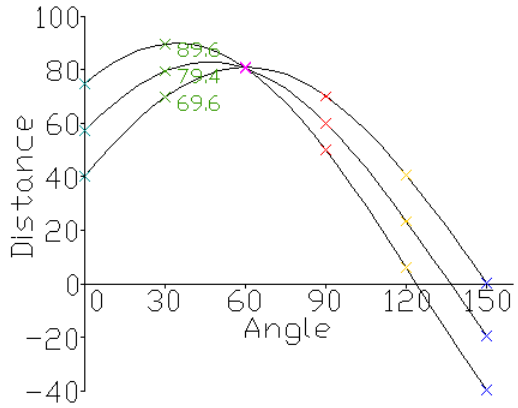

Figure 2.12: Hough space plot example[1]

- The length (ie perpendicular distance to the origin) and angle of each dashed line is measured. In the diagram above, the results are shown in tables.
- This is repeated for each data point.
- A graph of the line lengths for each angle, known as a Hough space graph, is then created, Fig. 2.12.

The point where the curves intersect gives a distance and angle. This distance and angle indicate the line which intersects the points being tested. In the graph shown the lines intersect at the purple point; this corresponds to the solid purple line in the diagrams above, which passes through all three points. (end example)

This could be plotted as a two dimensional histogram as well and would tend to peak about the purple point. There are two issues with the technique for the DCH, the density of hits in a central Au-Au collision would require a prohibitive number of test lines and the peaks are not sharp enough to separate the tracks in any event. A technique was developed at Stony Brook to overcome this called the combinatorial Hough transform [14].

What the DCH measures is ϕ, the azimuthal angle at the intersection of the track with a reference radius near the mid-point of the DCH, and α, the inclination of the track at that point, Fig. 2.13. Incidentally, the relationship to momentum, determined empirically,

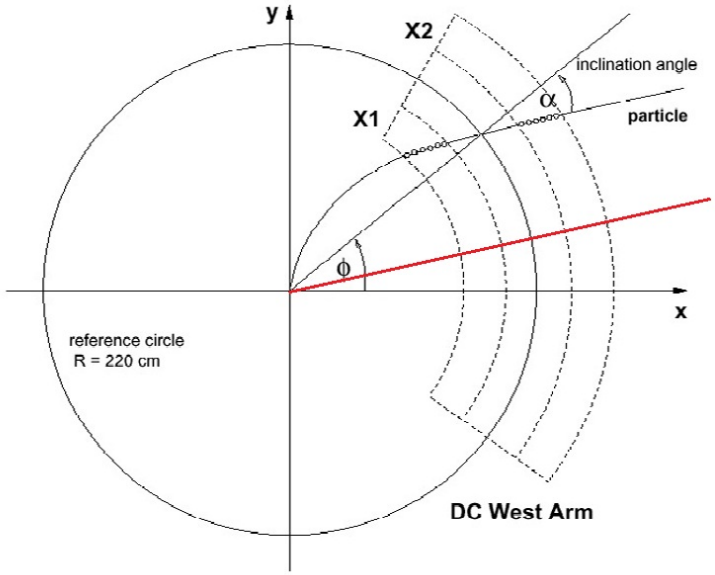

Figure 2.13: This is how p_T is determined.

$$p = \frac{const}{\alpha}, \tag{2.6}$$

which we present without proof.

As one can infer from Fig 2.13, α and ϕ are natural coordinates for a new Hough space. All possible pairs of X1 and X2 points are made and then α and ϕ are determined for the pair. An example of this is shown for a single track in Fig. 2.14. The tightly clustered space points are from X1,X2 pairs, the displaced colored points are from either X1 or X2 only pairs. The presence of residual magnetic field causes the displacement, X1 and X2 hits are not collinear in this fringe field. The smearing is because of the greater variation in angular determination as the points get closer together. Because of these two points, only X1,X2 pairs are used and as a result the image has dimension 2.75 mrad in ϕ and 50 mrad in α

Fig 2.15 shows an example of a portion of the DCH on the left and the Hough space on the right as a lego plot. This is the sort of hit density expected for AuAu collisions, the tracks are clearly visible. At this point in the tracking algorithm each of the peaks corresponds to an actual track in the drift chamber. At the expected multiplicity of a Au+Au collision at RHIC, over 98% of the tracks from the origin and passing completely through the drift chamber are

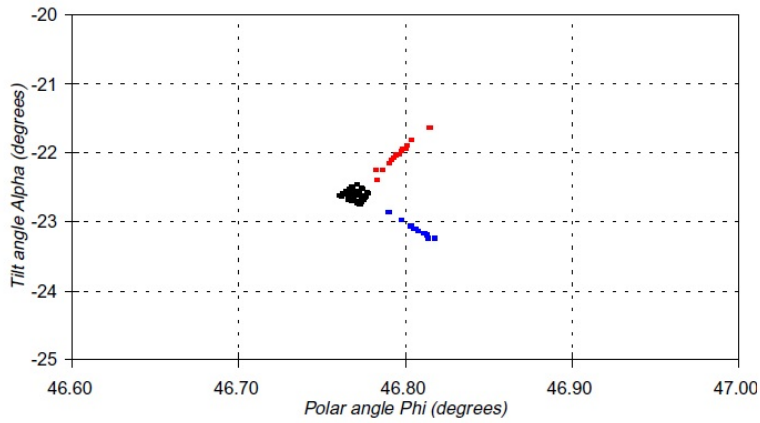

Figure 2.14: Bending-plane Hough space distribution for one sample track. Black points (tight cluster) correspond to X1 versus X2 hit combinations while red (upper right streak) and blue (lower right streak) points come from X1 only and X2 only combinations respectively.

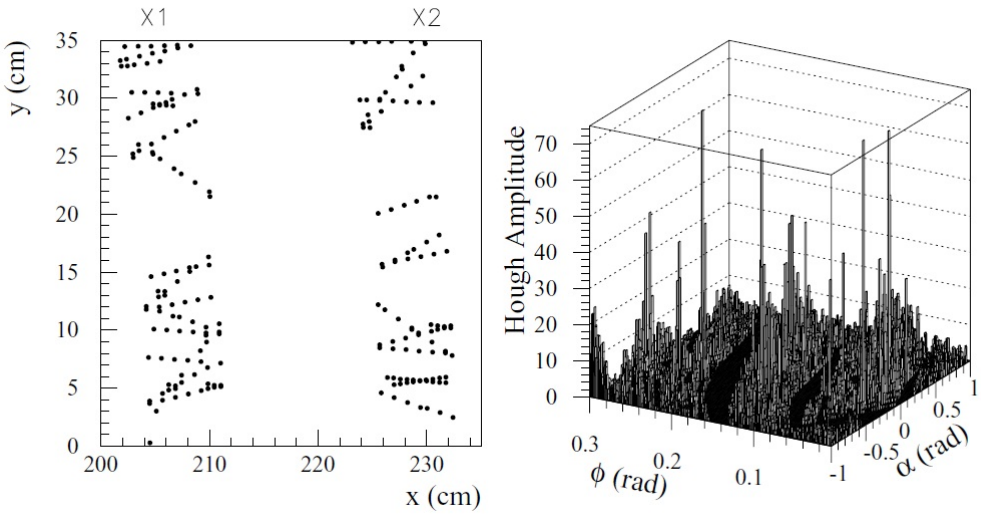

Figure 2.15: Simulated hits in a portion of the drift chamber and the corresponding Hough transform for X1 and X2 wires.

found from the combinatorial Hough transform with no further tracking. The ghost track rate is less than 1%[15].

The drift chamber tracking algorithm described above has been implemented in the PHENIX tracking package. Track finding efficiency for the complete three dimensional algorithm was determined with the help of Monte Carlo simulations that included realistic detector response and position resolution. More than 92% of all tracks which pass fully through the drift chamber are reconstructed with fewer than 1% spurious (ghost) tracks[15].

The CPU time to process one central Au+Au event is currently ≈120 SPECINT95[16] seconds, which is about 10% of the total central arm reconstruction time. Recent studies of the robustness of the algorithm at double the expected central Au+Au track density show that the tracking efficiency is still $> 80\%$ for this extreme situation[15].

The DCH has one key drawback that is a product of the design trade offs of PHENIX. The tracking algorithm assumes that all tracks originate from the origin. The DCH measures α the angle between an infinitely straight track and a charged particle's actual track after having passed through the magnetic field. The DCH has no way of determining a particle's actual origin, so the origin is assumed to be the interaction point and the path length in the magnetic field to be commensurate with this and the measured α. What this means is that charged particles that originate from a point closer to the DCH will have less bend per p_T and will be assigned a measured P_T that is too high. Anything that decays, K's or converts, γ's, into electrons is a potential source of background.

2.5 Pad Chamber

The PHENIX central arms contain three layers of two dimensional readout wire chambers called the Pad Chambers Fig. 2.16. The first layer, PC1, is located just behind the DCH in both central arms. PC3 is installed just in front of the EMC in both arms. PC2 is located behind the RICH in the west arm only. The combination of the three PC's reinforces the tracking information of charged charged tracks in the $r - \theta$ plane. In particular, PC1 is used to determine the z coordinate of charged tracks at the DCH.

Each chamber contains a single plane of wires inside a gas volume between two cathode planes, one of which is finely segmented into with a novel pad design to maximize segmentation while reducing the cost at the same time.

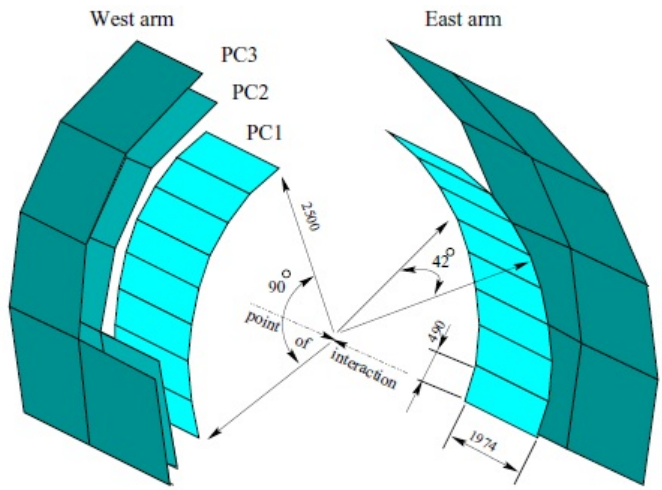

Figure 2.16: Schematic of the PHENIX pad chambers. Some sectors of the PC2 and PC3 sections are removed for clarity.

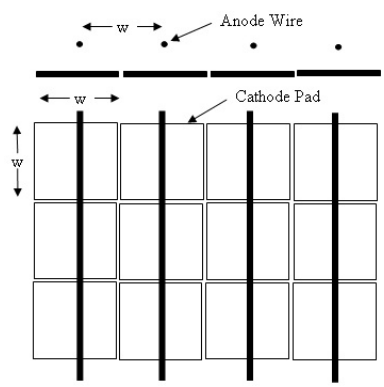

Figure 2.17: Concept of a pad chamber.

For complete details of the PC's please see Ref.[17], we present the basic principle here.

In Fig. 2.17 we see the basic principle of a pad chamber. A set of wires held at positive HV are suspended above a grid of conductive pads usually held at ground. The volume about the wires is filled with a suitable gas as in a conventional wire chamber. Each pad has a preamp and other associated electronics. A particle traverses the gap between the wires and the pad plane. The ionization electrons will drift towards the wires and avalanche as they approach. The pads see the multiplied image charge and the position of the hit is simply determined by the pad position, with a resolution governed by the size of the pads.

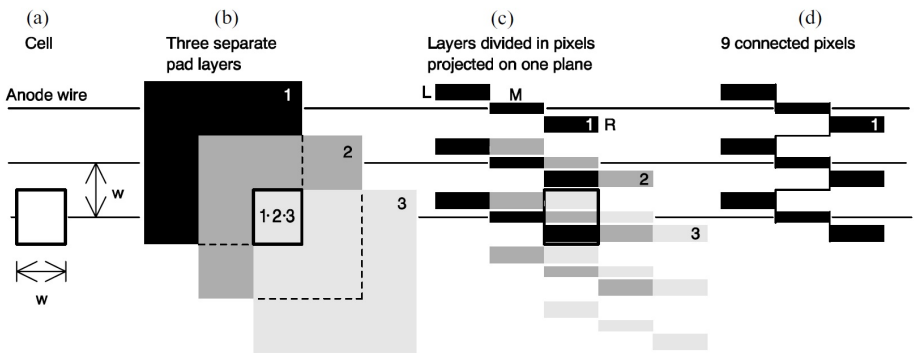

Figure 2.18: Principles of the PC pad geometry.

One can increase the distance from the wires to the pads or shrink the pad size below the wire pitch to get charge sharing among the pads to allow a center of gravity calculation. In the case of the PHENIX PC's the idea of pad size being the position resolution is sufficient.

In Fig. 2.18 we can see the evolution of the PC pad scheme. Fig. 2.18(a) is essentially a duplicate of Fig. 2.17 defining the concept of resolution as a function of pad size and wire pitch. In Fig. 2.18(b) we see three pads of dimension 3w x 3w, they are displaced as shown and placed on electrically isolated layers. The area of mutual overlap has dimension w x w just as in Fig. 2.18(a), a particle that produces an image charge on all three large pads than can be isolated to the w x w sized area. Each of these large pads has a preamp and electronics but there are now required 1/3 the number of preamps as in Fig. 2.18(a) saving cost.

However, realizing this geometry would be costly in and of itself so there would be no net saving. The cleverness is to design a pad structure that mimics Fig. 2.18(b) on one plane as seen in Fig. 2.18(c). In PC parlance the new pads are called pixels, the pixels of the same shade are electrically connected to each other and to readout electronics. A "cell" is a group of 3 pixels as seen in the center of Fig. 2.18(c) inside a superimposed box. The avalanches always occur on the wires so charge collection is dictated only by pixel geometry. One sees that the pixel in the center of a cell is smaller than the other two, the sizes are driven by the goal of equal charge deposition. This ensures uniform performance of each cell. Furthermore, a particle will always be sensed by three pixels so the coincidence that can be formed will drastically lower the number of false hits from noise.

The new "pad" is now seen in Fig. 2.18(d) and is made of 9 pixels. The

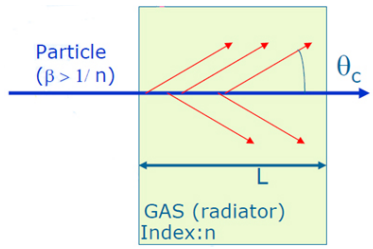

Figure 2.19: Schematic of Cherenkov radiation.

final z resolution of PC1 at the chamber is 1.7mm. PC1 measures a point just behind the DCH, providing the z-coordinate of a track thus being essential for the reconstruction of the three-dimensional momentum of a particle.

The combination of the DCH and PC1 is used to produce the Quality selection cut used in this analysis. We require hits in X1 and X2 layers of the DCH and hits in PC1 or at least the stereo, U and V wires. This variable is presented to the user as a binary word that when converted to decimal corresponds to these conditions.

2.6 Ring Imaging CHerenkov

The principle electron ID subsystem of PHENIX is the Ring Imaging CHerenkov (RICH) detector, the complete details of which can be found elsewhere [18]. The RICH takes advantage of the fact that it is possible for a massive particle to exceed the speed of light in a medium that it is traversing. If this particle is charged it will emit Cherenkov light. If the particle's $\beta = v/c$ exceeds the inverse of the index of refraction,

$$\beta > \frac{1}{n} = \frac{c_{medium}}{c}, \tag{2.7}$$

Cherenkov light is emitted.

The angle of this plane wave with respect to the axis of propagation can be calculated using,

$$\cos\theta_C = \frac{1}{\beta n}. \tag{2.8}$$

This angle is illustrated in Fig. 2.19

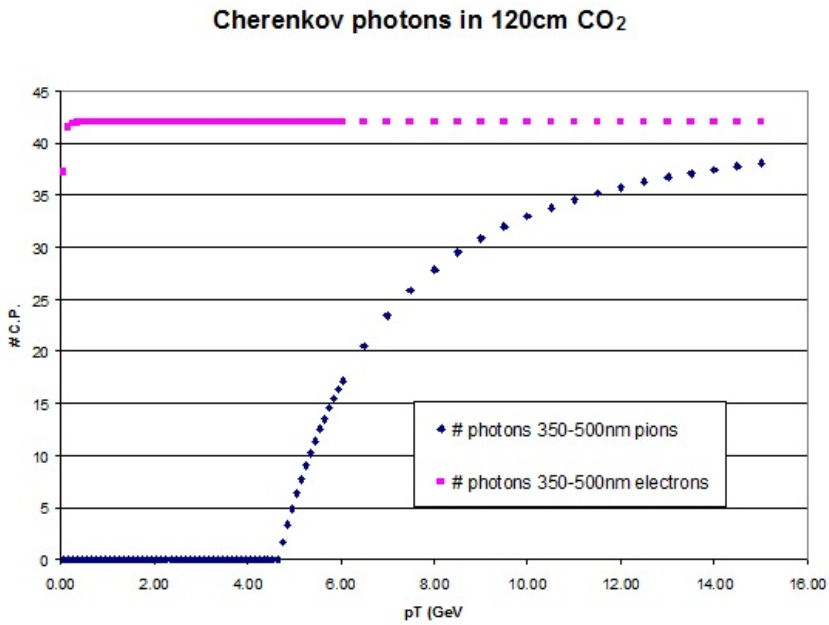

Figure 2.20: A plot of Eq. 2.10 for π's and $e^{\pm}$'s in the RICH

The RICH is located behind the DCH, Fig 2.21 the cross sectional area is twice that of its acceptance to provide room for phototube arrays. The radial extent of the RICH is dictated by providing sufficient path length in the radiator to produce enough Cherenkov photons for a relativistic electron. The radiator is 1 atmosphere CO_2 gas, it has an index of refraction of 1.00045 and the path length is 120cm.

To calculate the number of Cherenkov photons produced by a particle we use the Frank-Tamm formula [19],

$$dE = \frac{\mu(\omega)q^2}{4\pi}\omega\left(1 - \frac{c^2}{v^2 n^2(\omega)}\right) dx d\omega, \tag{2.9}$$

this can be rearranged,

$$N_{\gamma}^{350-500nm} = 390 * sin^2\theta_C * n_{CO_2} * l. \tag{2.10}$$

Plugging these parameters into Eq. 2.10, a 0.25 GeV electron has all but reached the plateau of 42 Cherenkov electrons, Fig. 2.20. Since only electrons with $p_T > 0.2GeV$ will escape the central solenoidal field the conditions are well satisfied.

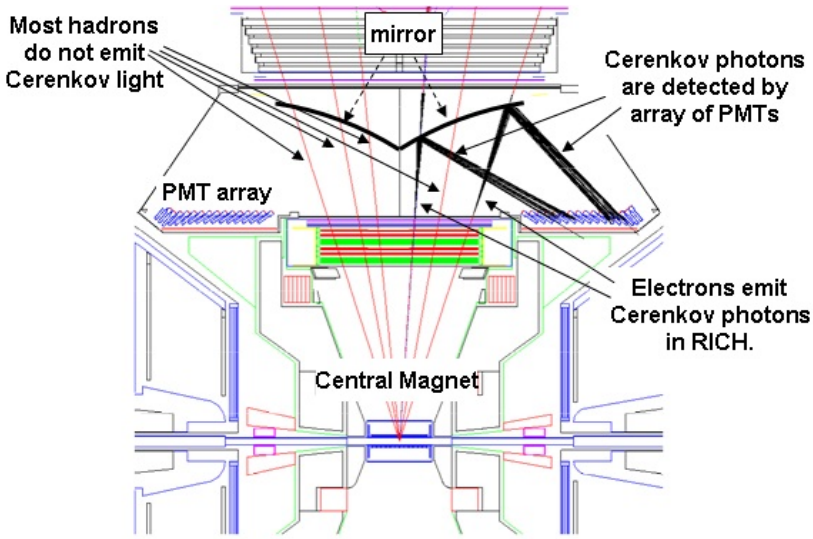

Figure 2.21: The placement and internal layout of the RICH.

The mirrors that reflect the Cherenkov light are spherical, parallel rays will always reflect to the same point, Fig 2.22a, if we rotate the figure about the bold line we get a ring. This configuration puts the focal plane in the acceptance so the actual mirrors are tilted as shown in Fig 2.21.

So we now see how circular rings are projected on to the plane of the phototube array, Fig 2.22b. The mean value of the radii of these rings is 5.9 cm at the array. Of the several variables associated with the RICH there are two that are important to this thesis, n_0 and n_1, Fig. 2.23.

To produce the n_0 variable the software looks for clusters of fired phototubes. (Whenever discussing n_0 or n_1 one must think in terms of number of photo*tubes* not Cherenkov photons.) An annulus is superimposed centered about the projected track (provided by the DCH and the DCH's) of an electron candidate, n_0 is the number of phototubes that have fired that fall into this mask. The inner radius of the annulus is 3.4cm and the outer is 8.4cm, this is symmetric about the 5.9cm Cherenkov radius of an electron. In Fig. 2.23 one gets the sense of the dimensional choices. The radii of the phototubes is 2.5cm and they are arrayed as shown, this size corresponds nicely with the 5.9cm. Of course, not all tracks fall in the middle of a phototube as shown, the dimensions of the ring accommodate this as well as the distortions of the ring caused by the reflection and the random fluctuations of the angle of emission of the Cherenkov radiation.

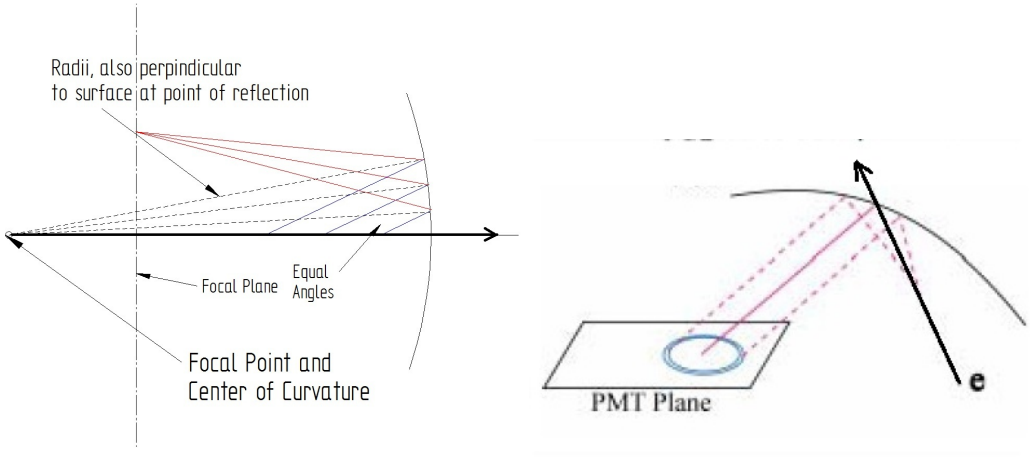

(a) (b)

Figure 2.22: The RICH use of a spherical reflector.

With all of these choices one gets an average value of 2-3 for n_0 no matter where the track goes. There are other variables that do incorporate pulse heights of the phototubes, and thus indicate number of Cherenkov photons. This becomes important in the higher multiplicity environment of Au-Au collisions and are unnecessary in this analysis.

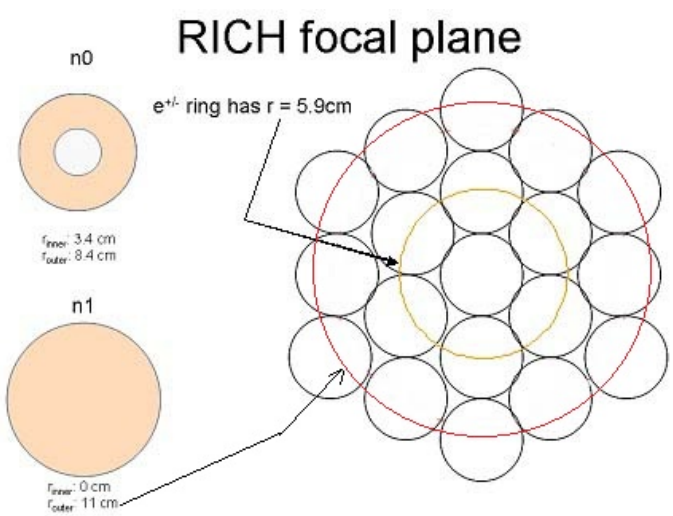

Figure 2.23: Derivation of RICH Variables.

The other variable in the figure is n_1 in which the number of fired phototubes that are contained within a disk is used instead of an annulus. This disk has the larger radius of 11cm. This is the variable used in this analysis.

The reason being that there was an error in the code that processed the raw output of the detector causing a misalignment of the tracks with the actual rings in the RICH. This misalignment was not so large as to adversely affect n_1. The other reason to choose n_1 is that it is easier to model and study the "turn on" of Cherenkov light from charged $\pi's$ with the absence of the hole of the annulus. This will be discussed further in Chapter 5.

2.7 ElectroMagnetic Calorimeters

The PHENIX ElectroMagnetic Calorimeters (EMC) are the outermost detectors of the central arms. Their job is to measure the energy of the electrons and photons that are incident upon them. As before, we present some basic ideas, for complete details please see [20, 21].

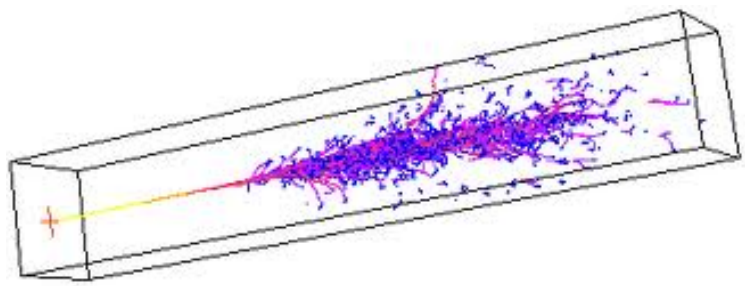

Figure 2.24: A cartoon of an electromagnetic shower in a homogeneous block of material.

A calorimeter measures energy, the term calorimeter is used because a calorimeter absorbs all of the measured particles energy. A calorimeter has increasingly better relative resolution as a function of particle energy. This is true because a calorimeter exploits the particle multiplication process known as showering. There are two types of such showers, electromagnetic and hadronic. Electromagnetic showering occurs because of bremsstrahlung, electrons shower, much more massive muons generally do not due to their greater mass. Photons don't shower but after pair conversion the electon/positron pair do shower.

Electrons also lose energy by ionization, also called dE/dx loss which is described by the Bethe-Bloch formula. The so called critical energy, E_c, is the energy at which the loss due to ionization equals that of bremsstrahlung. This is material dependent, high Z materials will have a low E_c so that bremsstrahlung

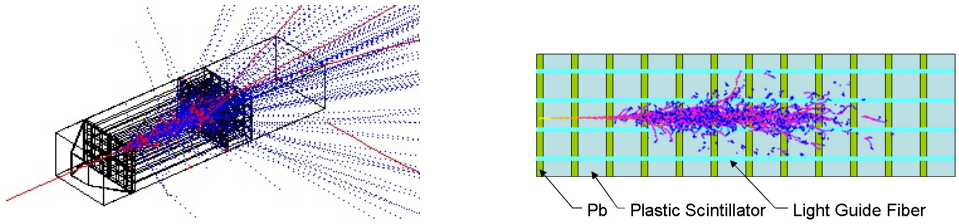

(a) PbGl (b) PbSc

Figure 2.25: EM showers in PbGl and PbSc calorimeters

is the dominant loss mechanism, a low Z material will be dominated by ionization loss. This is exploited in a sampling calorimeter as we shall see shortly.

An impinging electron will bremsstrahl numerous photons until the critical energy is reached and then ionization loss brings it to rest. These photons then convert, the pairs then repeat the process until all of the energy is absorbed. The only difference for an impinging photon is that a conversion happens first. Because of the multiplication process there are two benefits derived. The first is that the penetration depth of the shower increases only logarithmically with the incident energy. The second is that with greater numbers of particles with greater incident energy the resolution improves. For a complete description of the operating principles of calorimeters please see these to compilations edited by Ferbel and Sauli [22, 23].

Fig 2.24 is a cartoon of an electromagnetic shower within a homogeneous block of material. The shower is completely contained, this can be accomplished for example in a block of lead 10cm x 10cm x 9cm deep. This would not be very practical as it would be difficult to measure any signal. Additionally transverse segmentation is desirable to be able to separate adjacent showers. Typical designs have the transverse dimensions of a shower contained in a matrix of 2x2 or 3x3 cells. One can then do weighted averages of the energy deposition in the cells to determine shower centers and distinguish showers from particle incident near each other. This is of particular importance in π^0 identification as the EMC is the only PHENIX detector sensitive to them.

There are two different geometries used in PHENIX to make shower containment possible while also being able to read out the signal. The first is the use of lead glass (PbGl) which is a variety of glass in which lead replaces the calcium content of a typical glass. This raises the density of the glass so that the electrons will bremsstrahlung and it also raises the index of refraction. The signal that is read out from a PbGl calorimeter is Cherenkov light,

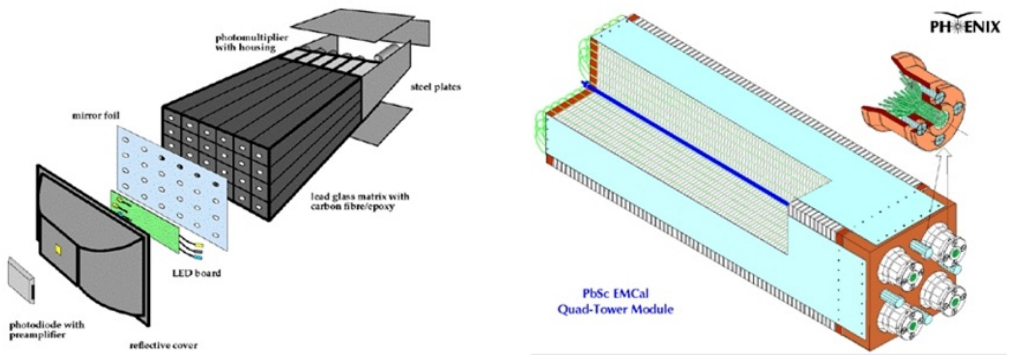

(a) PbGl (b) PbSc

Figure 2.26: PbGl and PbSc modules

electrons traversing the PbGl emit both Cherenkov and bremsstrahlung photons. A typical cell resembles Fig 2.25a, these are wrapped in a light isolating cover and stacked together. The Cherenkov photons propagate in the general direction of the incident particle, a phototube of photodiode is glued to the end the the PbGl to read out a signal.

Fig 2.26a shows a PHENIX PbGl module, the PbGl blocks are approx 4cm x 4cm x 40cm. The parts that attach to the face allow for pulsing with measured amounts of light to calibrate the system.

The second type of EMC used in PHENIX is a lead scintillator (PbSc) sampling calorimeter. The concept is seen in Fig 2.25b, layers of lead are alternated with layers of plastic scintillator. Pair production and bremsstrahlung occur in the lead, which is sometimes referred to as the absorber. The signal is produced by the shower electrons in the scintillator, sometimes referred to as the active medium. Energy loss occurs in both media, in fact most of the energy loss occurs in the lead. This type of calorimeter is called sampling because only $\approx 20\%$ of the energy is deposited in the scintillator. There is only a small loss in resolution since relative variation of energy deposition remains low due to the large numbers of particles in a shower.

The principle advantages of a sampling calorimeter using scintillator as an active medium is fast response, good for timing information and cost, PbGl is much more expensive than lead and plastic. Another advantage of sampling calorimeters is the ease of longitudinal segmentation, which is not practical in a PbGl calorimeter. Having phototubes at the face would place too much material in front of the calorimeter and since the Cherenkov light is projected towards the back of the module, the signal would be very slow with a long

dwell. Longitudinal segmentation was not used in PHENIX.

The challenge with a sampling calorimeter is to bring the signal out from the active medium to the transducer, in this case a photodiode. Putting light guide "buss bars" along the sides of a cell creates dead areas, "cracks" in the detector that are unacceptable. The solution developed for PHENIX was to interpenetrate optical fibers into the lead and scintillator layers, these can be seen schematically in Fig 2.25b. A PHENIX PbSc module of four cells can be seen in Fig 2.26b, in this case a cell is $\approx$ 5cm x 5cm. The green optical fibers loop out and back in at the front face of the module. At the back of the module the fibers from each cell are gathered into a coupling into which a photo diode is mounted. The stacked squares of lead and scintillator are as large as four cells, there is no need for optical isolation as the fibers define the cells. The blue line in the center is a light guide that delivers laser pulses for calibration.

As previously mentioned the EMC measures energy. The size of the cells is chosen such that, for an electromagnetic shower, 90% of the energy is contained in an array of 3x3 cells. This is a compromise between being able to separate neighboring clusters and the increased cost of smaller cells. In fact, the variable produced by the EMC that is used in this analysis, called ecore, is the energy deposited in a 3x3 array centered at the "center of gravity" of an energy cluster. The center of gravity is an energy weighted average of the position of the deposited energy.

The other relevant variable produced by the EMC is called "prob", the probability of a shower being electromagnetic. It is based on the radius of the total energy deposition around the center of gravity. Because the processes involved in a hadronic shower are lower cross section, the radius of a typical hadronic shower is a factor four greater than that of an electromagnetic shower. The prob variable ranges from 0-1, with one being the most probable, prob profiles can be seen in Appendix B.1.2.

Most hadronic showers have a $prob < 0.1$ however whenever a strong force interaction occurs in matter there is the possibility of a π^0 being produced. A π^0 decays electromagnetically essentially instantaneously, $10^{-27}s$, into two photons which then shower electromagnetically.

These now electromagnetically showering hadrons's will have a greater prob value and be difficult to discriminate with a cut on the prob variable. Indeed, if the hadron has a β above the Cherenkov threshold the RICH no longer has the ability to veto it as well. A new technique of removing these hadrons is then necessary. This thesis is motivated by the development of such a technique to

discriminate these unwanted hadrons as will be discussed in Chapter 5.

The EMC also serves as the primary "enrichment" trigger in this analysis. The BBC already provides a minimum bias trigger, if we had infinite amounts of time to collect data we would be able to find all events of interest using only an MB trigger. Since we have only available a finite amount of time we need a method to focus the attention of the detector towards events of interest.

The crossing rate at RHIC is $\approx 10MHz$ not every crossing yields a collision but in pp PHENIX sees MB triggers at a rate of $50kHz$ at the beginning of a fill. Since we can only write to tape at 6kHz we cannot accept every MB trigger and consequently this trigger is down scaled, the official term is prescale. The prescale is a limit for a counter, if the prescale is zero then all events are taken, prescale equal to one means every other event is taken and so on. The collision rate drops during a fill of the collider so the prescale is adjusted during the run.

The trigger we use is the simplest case of an enrichment trigger. We are interested in counting electrons to the highest p_T possible. A typical spectrum of invariant cross section as a function of transverse momentum covers 10 orders of magnitude, electrons at the highest p_T's are extremely rare.

The trigger we use is called "ERT4x4c", the "E" is for EMC, the "R" is for RICH and the "T" for trigger. The 4x4 means that a trigger "tile" is made up of 16 EMC cells in a 4x4 array and the "c" is a threshold level indicator, in this case 1.4GeV. A tile is created by sending all of the cell outputs to a separate set electronic circuit boards that make any grouping that the user desires.

In fact, this particular trigger does not use the RICH, it only looks for an energy deposition of > 1.4GeV in an EMC trigger "tile". It is commonly referred to as a photon trigger since it does not require a RICH response and hence insensitive to charge. The size of the trigger tile is also a clue, a typical charged particle trigger uses 2x2 tiles, there is no track information for a photon.

Chapter 3

Initial Data Processing

Two analysis methods, a converter subtraction method and a cocktail subtraction method are the generally accepted techniques to extract the heavy-flavor electron signal. These are well established methods used in RUN1-RUN3, RUN4 Au+Au and RUN5 p+p single electron analysis. The converter method was not used in this analysis as it is primarily used at low p_T, where the measurements are well established. This analysis focuses on the p_T range where the converter technique does not apply. We build on the RUN5 analysis [24] significantly extending the p_T range of the PHENIX single electron measurement.

Two data sets are used for the analysis: Minimum (MB) data set and ERT4x4c (ERT) data set. ERT is Electromagnetic calorimeter RICH Trigger, a certain minimum energy in the calorimeter is required to fire this trigger, in this way we enhance the collection of high p_T events. The format of the data files is labeled CNT in PHENIX, these are data files that only contain information from the central arm detectors that are described in chapter 2. In this chapter we will describe the steps to produce a spectrum of all electron candidates, the inclusive spectrum. Subsequent chapters will describe the process to arrive at a final invariant cross section spectrum.

Throughout the text, we document the location and names of analysis codes, analysis macros, and intermediate ROOT files and other files related to the analysis. The final analysis are done in directory

/phenix/hhj/themann/analysis

3.1 Data Files

PHENIX has one of the most efficient Data AQuisition (DAQ) systems in the world, we have been able to write out 6,000 events per second for the last 5+ years. We have been able to maintain this rate in Run 11 (2011) even with the introduction of our central Silicon Vertex Tracker with 4,000,000 channels in the first two (of four) layers. Because of this success, it is not possible to keep our data instantly accessible. The data are all stored on tape and we have developed a queuing system to access it.

As with many things in physics we have given it the whimsical name of Analysis Train as users booked jobs that were added as "cars" to the train. The train would start when a set number of "cars" were assembled. At the time data were still available on disk but as this went away and as the efficacy of the train concept was proven, so many users wanted access that the system needed a re invention. We now have the Analysis Taxi with the implication of easier, shorter term access, taxi run every week instead of opportunistically as with the train. Users now develop and test their code, PHENIX has a standardized procedure for this. The code is then placed it a designated area in CVS. The user fills out a form at a web page giving paths to their code, to an output area and to the log files from the testing process. Output from the train arrives in no more than two weeks in the users area.

We use Analysis Taxi output of Taxi's 258 and 259 all analysis code used on data can be found in CVS

https://www.phenix.bnl.gov/viewcvs/offline/AnalysisTrain/se_ana_lite/

https://www.phenix.bnl.gov/viewcvs/offline/AnalysisTrain/se_ana/

We use MB and ERT CNT files, the outputs are here;

/direct/phenix+hhj/themann/Run6pp200MinBias
/direct/phenix+hhj/themann/Run6pp200ERT

3.2 Overview

In the first step, the CNT files are processed by a program, *se_ana*. The program applies event selection, fiducial volume cuts and electron identification cuts, and produces histograms of p_T distributions of electron candidates for

the MB trigger events and for the ERT trigger events. For the ERT trigger p_T distribution, the electron track is required to hit a trigger tile that causes the ERT trigger. This is to avoid so-called "random benefit" in the analysis. The histogramming program also produces many other histograms that are used to check the quality of the data. One histogram file is produced for each run.

The use of the word "run" in our field is, unfortunately, somewhat ambiguous. In general Run with a capital "R" means the overall contiguous data collection period. At RHIC this is a yearly process as the shutdown period is always during the summer months due to the large increase in the cost of electricity. Data is collected in one hour "runs" with a lower case "r". Every "run" has a unique number and there is no requirement to reference the "Run" during which it occurred, however, it is customary to refer to data by its "Run" number as this offers a more natural association to the species and collision energy as well as the state of the detector.

Once the analysis code has processed all of the raw data the results then processed by a series of ROOT macros. The macros manipulate the histograms in the data set files and derive the cross section of electrons from heavy flavor decays. These macros are located here;

/phenix/hhj/themann/analysis/1_run_QA
/phenix/hhj/themann/analysis/2_trig_eff
/phenix/hhj/themann/analysis/3_a_dN_dphi (acceptance and efficiency)
/phenix/hhj/themann/analysis/3_b_selection_cuts (acceptance and efficiency)
/phenix/hhj/themann/analysis/3_c_ratio (background subtraction)
/phenix/hhj/themann/analysis/4_final_spectra

A section follows for each set of macros describing what is done at each step

The output of these directories are here

/phenix/hhj/themann/analysis/background
/phenix/hhj/themann/analysis/Run6pp200

3.3 Selection Cuts

In se_ana, the following cuts are applied to select good electron candidates.

z-vertex cut

This is to avoid tracks that might graze the magnet pole tips.

$$-20cm < z_{vertex} < 20cm$$

Quality

X1 and X2 found and PC1 found/unique.

EMC matching

The difference between a track's projection to the EMC face and the center of an energy deposition in same. PHENIX provides sigmalized variables in ϕ and z, we add them in quadrature to produce a circular cut.

$$\sqrt{(emcsdphi_e^2 + emcsdz_e^2)} < 3\sigma$$

EMC shower shape

Probability that a shower is electromagnetic

$$prob > 0.01$$

RICH

The number of phototubes fired in disk shaped mask

$$n_1 \geq 5$$

E/p

A particle's energy divided by its momentum, for a highly relativistic electron this is centered at one.

$$0.80 \leq E/p < 1.2$$

Fiducial Cuts

In Run 6 fiducial cuts are applied in simulation using detector dead maps.(see sec 4.3), any cut applied in simulation is also applied to data.

DCH structure

The DCH has an insulator at the mid point of each wire to separate Noth and South halves. This creates a p_T dependent dead spot within this 4cm region.

$$|z_{DCH}| < 2cm$$

After these cuts, hadron contamination in the electron sample is negligible in the p_T region below π Cherenkov threshold in RICH. At $p_T > 5GeV/c$, charged π's start emitting Cerenkov light, and this becomes the main background source. To reject π background, we have developed a new subtraction technique that will be discussed in Chapter 5.

3.4 Run QA

The histogram files produced by se_ana are first processed by macros that perform quality checks of the data. The first Q/A macro is run_QA.C. The objective is to look for variations in the detector response. This is done by plotting the electron candidate yield per minimum bias event as a function of run number. At this point there is separate MB and ERT file for each run number. For this plot an electron candidate is a track that has passed all eID cuts and is within the p_T range $0.6 < p_T < 4.0$ GeV/c. The lower limit insures tracks that are easily reconstructed and the higher limit is firmly in the range where the RICH has maximum discriminatory power.

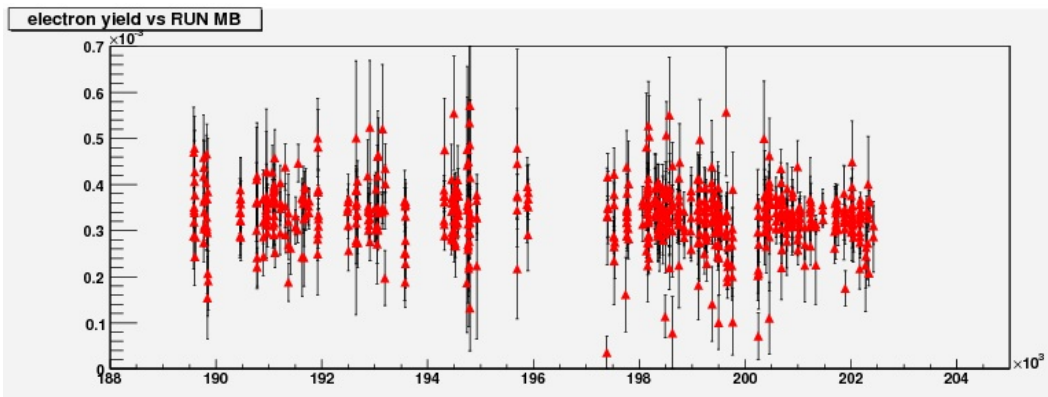

Figure 3.1: Initial Run 6 Electron Candidate Yield/Event

This plot appears in Fig. 3.1, all available runs are in this plot. Next come the QA procedures.

First runs with less than 50K Minimum Bias events in are rejected. This number was 200K in previously published PHENIX Run 5 data [24]. Since the MB scaledowns are, on average, an order of magnitude higher in Run 6 we chose the conservative 50K. A scaledown is used to adjust the relative numbers of event types that are written to tape. In Run 6 one of the objectives was to sample the p_T spectra of electrons at the high end. This means that there are less MB events per file, it doesn't mean that there are lesser numbers of interesting events so we take care not to discard them.

If electron candidate yield per event is less than $2x10^{-4}$, the run is rejected as a bad run as this is an indication of a sub-system failure during the run. After these bad runs are rejected the plot is examined for systematic variations in yield, this would indicate a section of a sub-system becoming inoperative

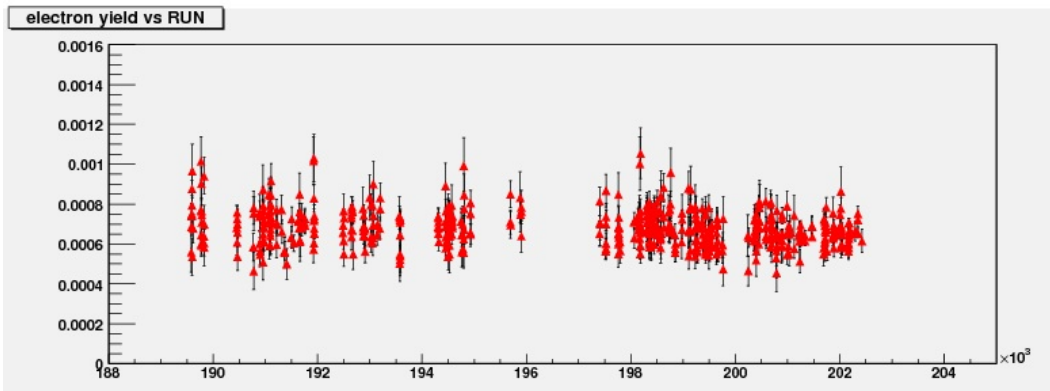

Figure 3.2: Run 6 Electron Candidate Yield/Event

(or restored). If none are seen, the average electron yield for the entire data set, $< N_e >$, is calculated. Any run in which the electron yield is more than 3σ from $< N_e >$ are rejected as a bad run. Once again the yield plot is checked for systematic variations.

The average of the remaining set of runs is calculated and the 3σ cut is then applied once again, and once again the yield is checked for consistency. This is repeated for a total of five times. The end result is that in Run 6 804 runs and 555 runs, respectively.

The purpose of this process is to prepare for correction of the measurement for acceptance and efficiency (sec 4.3). It is not possible to correct for acceptance and efficiency on a run by run basis. A reference run is chosen by common assent of the various sub-system experts as representing the average behavior of PHENIX over the course of a Run. This is used as the model for the simulation that is used in the acceptance efficiency correction process.

If a systematically low or high yield group of runs were to be found then separate list of runs would be produced and Run Q/A process would applied to the groups individually. The average yields of these groups would be normalized to the group containing the reference run and there would be a slight increase of the systematic error on the corrected groups.

The electron yield per MB event per run for Run 6 in Fig. 3.2. The electron yield per event is quite stable over the course of the Run. The stable electron yield is a result of the stringent fiducial cuts applied. The parts of the central arm detectors that are intermittently working are removed by the fiducial cuts. In the event that the detector response was not stable

Once a list of each of the runs that passed the MB run Q/A check is

obtained, the electron yield per MB sampled event is measured. This is done by a macro c_comp_mb_ph.C.

To determine the electron yield per sampled event, one needs to know the number of sampled events in the data set. We determined the sampled events as follows. For each run, we have a MB trigger histogram file and a ERT trigger histogram file. Each of them has a histogram of the BBC z vertex distribution (hbbcz). From this histogram, number of events in MB and ERT triggered events after the z vertex cut $-20cm < z\ vertex < 20cm$ is counted. The number of events in the MB file is then scaled up by the scaledown factor (+1),

$$N_{MB}^{sampled} = N_{recorded}^{MB} * scaledownfactor + 1. \tag{3.1}$$

This $N_{MB}^{sampled}$ should be the number of sampled MB events in the ERT trigger file, if both of the MB and the ERT trigger file come from the same set of CNT's. Unfortunately, in Run 5[24] this was discovered not to be the case. Some of the segments were lost or crashed or not processed for some reason during production, so these two data sets could have different statistics.

To check and correct for this potential problem, we compared the number of MB triggered events in the ERT data set (N_{MB}^{ERT}) and the number of ERT triggered events in the MB data set (N_{ERT}^{MB}). Since both of them are the number of $ERT\&MB_{scaled}$ trigger events in the run, these two numbers should be identical if the original data set is identical, and their ratio should equal one. However, if some of the run file segments are lost for any reason during the data processing, this ratio deviates from unity. The ratio then can be used to determine the true sampled MB triggers in the ERT data set.

The distribution of the ratio,

$$ERT :: MB = \frac{N_{ERT}^{MB_{scaled}}}{N_{MB}^{ERT}}, \tag{3.2}$$

is shown in Fig. 3.3. In the 605 good Run 5 MB runs we processed, 392 runs (60%) have the ratio exactly 1.0. This means that for these 392 runs, the ERT data set and the MB data set has the identical original CNT segments. In most cases this means that no file segment is crashed in production of CNT's or their transfer from CCJ (Japanese computing center) to RCF (RHIC Computing Facility) or during the processing of CNT files (which are the output of CCJ and RCF) to produce the histogram files. We accepted 569

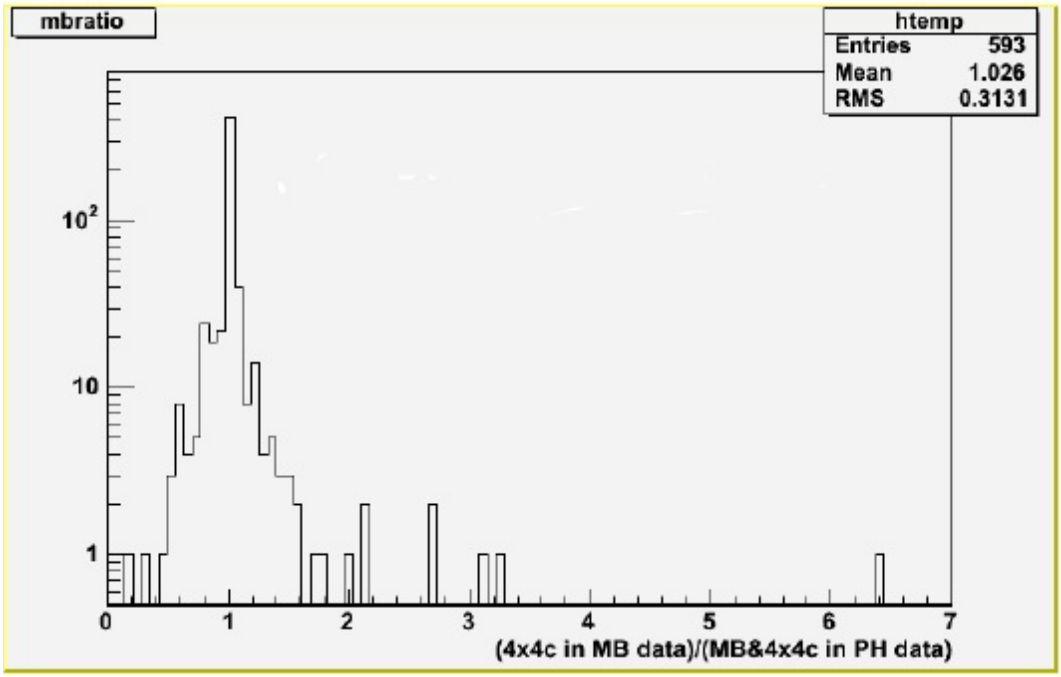

Figure 3.3: The ratio of MB::ERT trigger in the MB data set and the ERT data set for the Run 5 data set. One entry of the histogram is for one run

runs within $0.5 < ratio < 2.0$. In Run 6 the ratio is 1.0 for all runs Fig. 3.4.

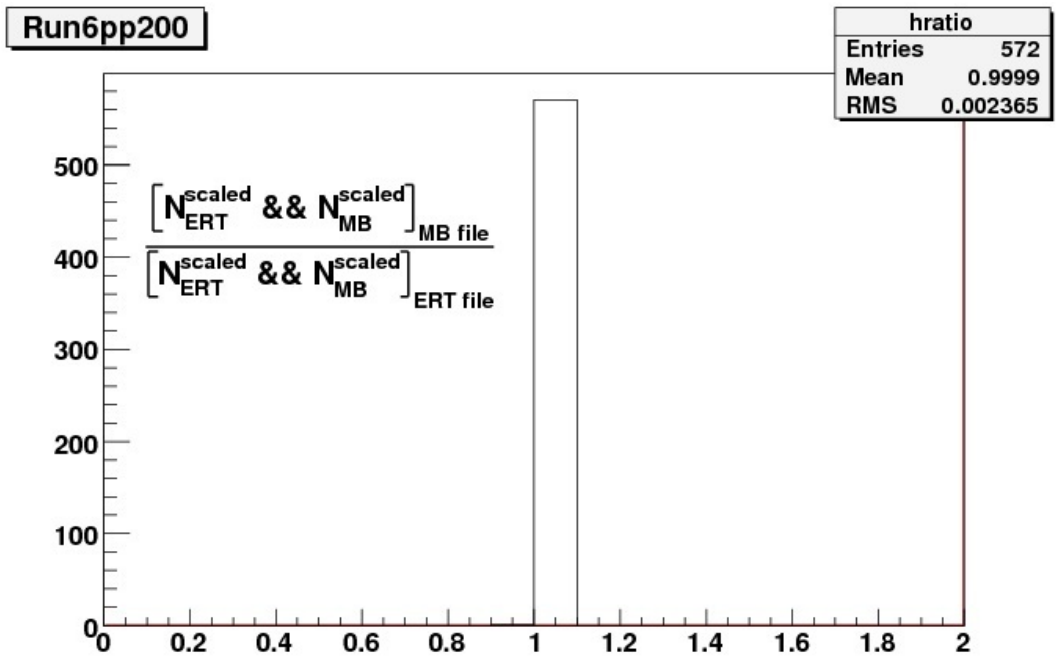

Figure 3.4: The ratio of MB::ERT trigger in the MB data set and the ERT data set for the Run 6 data set. One entry of the histogram is for one run

Chapter 4

Inclusive $e^{\pm}$ Cross Section

$$
\begin{aligned}
E\frac{d\sigma}{dp^3_{T\,MB}} &= \frac{1}{N_{MB}\text{ recorded}} \cdot \frac{1}{2\pi} \cdot \frac{1}{2} \cdot \frac{1}{p_T} \cdot \frac{N_e\text{ MB}}{\Delta p_T} \cdot \frac{1}{\Delta y} \cdot \frac{\sigma_{pp}\text{ tot} \cdot \epsilon_{BBC}}{\epsilon_{reco}(p_T) \cdot \epsilon_{bias}(p_T)}. \\
E\frac{d\sigma}{dp^3_{T\,ERT}} &= \frac{1}{N_{MB}\text{ live}} \cdot \frac{1}{2\pi} \cdot \frac{1}{2} \cdot \frac{1}{p_T} \cdot \frac{N_e\text{ ERT}}{\Delta p_T} \cdot \frac{1}{\Delta y} \cdot \frac{\sigma_{pp}\text{ tot} \cdot \epsilon_{BBC}}{\epsilon_{reco}(p_T) \cdot \epsilon_{bias}(p_T) \cdot \epsilon_{ERT}(p_T)}.
\end{aligned}
\tag{4.1}
$$

The various factors are;

- $N_{MB_{recorded}}$ number of Minimum Bias events recorded in MB data.
- $N_{MB_{live}}$ number of live MB events in ERT files, Eq. 4.34.
- $\frac{N_e}{\delta p_T}$ "raw" electron count in p_T bin, $\delta p_T = 0.1 GeV$.
- $\frac{1}{2} \rightarrow \frac{e^+ + e^-}{2}$ our measurement counts all electrons.
- $\epsilon_{BBC} = 0.516 \pm 0.051$ BBC efficiency for Minimum Bias [25].
- $\frac{1}{\epsilon_{bias}(p_T)} = \frac{1}{0.750 \pm 0.02}$ BBC trigger bias towards "hard" scatterings [26].
- $\sigma_{pp} = 42.2 mb \pm 1.9$ pp total inelastic cross section [25].

4.1 "Raw" Electron Yield

The first thing to do in any spectroscopic measurement is to tally up the "raw" count over the spectrum we are measuring. We use a standard set of 20 p_T bins, "1.2-1.4", "1.4-1.6", "1.6-1.8", "1.8-2.0", "2.0-2.5", "2.5-3.0", "3.0-3.5", "3.5-4.0", "4.0-4.5", "4.5-5.0", "5.0-6.0", "6.0-7.0", "7.0-8.0", "8.0-9.0", "9.0-10.0", "10.0-11.00", "11.00-12.00", "12.00-13.00", "13.00-14.00", "14.00-15.00", all GeV. The counts in each of these bins are listed in Table A.1, here the two columns labeled $0.8 \leq E/p < 1.2$, the other two columns refer to the background subtraction described in Chapter 5.

4.2 BBC Correction Factors

The BBC efficiency is the fraction of the total pp cross section that he BBC actually triggers on, this factor was measured to be 0.516 [25]. The total inelastic cross section for pp collisions at 200GeV is 42.2mB, 51.6%, $21.8 \pm 2.1mb$, registers in the BBC. This contributes a systematic error to the normalization of the final measurement of $2.1/21.8 = 9.6\%$.

The BBC depends upon particle multiplicity produced by the collision, obviously direct parton parton scattering will produce higher multiplicity than soft scattering, diffractive and double diffractive will have even less. This means that the BBC will tend to trigger on a higher fraction of hard scattering events than non hard scattering events, the BBC is biased.

This bias, $\epsilon_{bias}(p_T)$, was measured in [26] in π production in pp collisions at $\sqrt(s) = 200GeV$ with the following technique

- An unbiased sample of events was created using the ERT trigger without the BBC.
- The BBC trigger bias was calculated as the fraction of ERT events that also have the MB trigger fired function of p_T.

The result is seen in Fig.4.1, the fit sets the value $\epsilon_{bias} = 0.75 \pm 0.02$ independent of p_T. The uncertainty in ϵ_{bias} contributes a systematic error to the measurement as it affects the number of Minimum Bias events recorded, we quote this error as $0.02/0.75 = 2.7\%$.

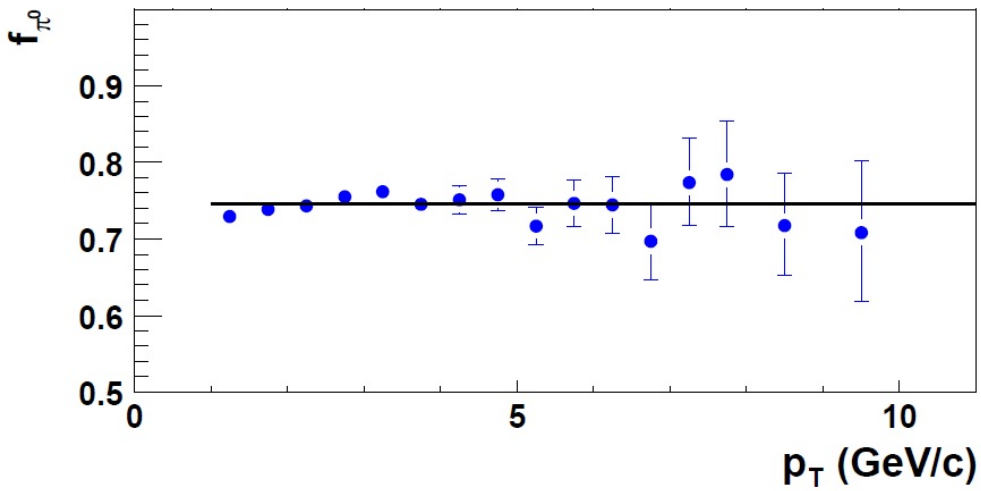

Figure 4.1: BBC trigger bias as a function of π^0 p_T with a zeroth order polynomial fit.

4.3 Acceptance and Efficiency

A measurement with any detector needs to be corrected up to the total phase space of mother nature. This is for two important reasons. The first is that no detector can cover the full 4π steradian, any measurement has to be augmented by a calculation of what would hit the missing pieces. The second effect is that we use selection cuts to enhance the purity of the sample we measure. In the ideal case, these cuts eliminate non-electrons while accepting only electrons. In reality, the cuts eliminate electrons as well, the best we can hope for is to preferentially eliminate non-electrons. Consequently our measurement has to be augmented by our calculation of how many electrons our cuts eliminate.

Acceptance and electron reconstruction efficiency is calculated by using a detector simulation, PHENIX Integrated Simulation Application (PISA). Each of the central arm detectors used in this analysis is represented in this simulation and behaves as the real detector. Electron tracks are generated and propagated through the detector, the simulation also contains the performance of the readout electronics. These electrons are generated homogeneously in;

- p_T, $0 < p_T < 20GeV$
- pseudorapidity, $-0.5 \leq \eta \leq 0.5$

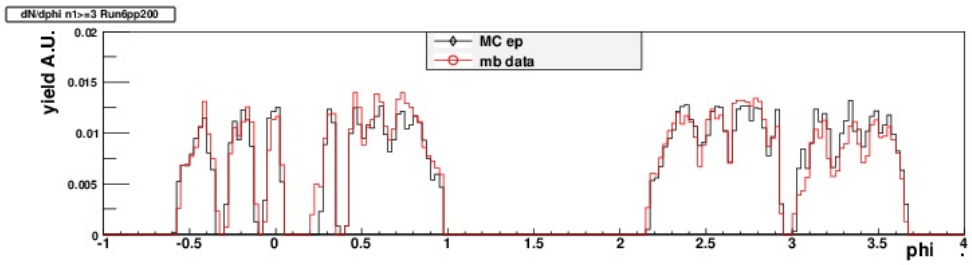

Figure 4.2: $\frac{dN}{d\phi}$ plot for Run 6

- azimuth $0 \leq \phi < 2\pi$
- z vertex, $-30 \leq z \leq 30cm$

They are then run through PISA to produce CNT files (simCNT) that are exactly the same as real data CNT's. The simulation analysis code is virtually identical to se_ana, all of the same electron ID cuts are applied and the same histograms are filled. To ensure that we will perform a proper correction we first check that PISA has a correct physical description. This is seen in Fig. 4.2 where the yield of electron candidates is plotted differentially in ϕ. There is a further restriction in addition to our standard electron identification cuts in that the p_T of candidates in the plots is restricted to be from 0.6 GeV to 4.0 GeV. In this way we get very straight tracks at the low end and at the high end we are below the Cerenkov threshold of the RICH. What this does is assure that we are looking only at electrons with a high degree of confidence.

An electron candidate will only be placed in this plot if all detector elements are functioning properly, this plot is handy as a quick snapshot of the PHENIX health. The dead areas in PHENIX are entered into the PISA simulation, we then produce this same plot and overlay it with real data. As one can see from the figures we have good agreement in Run 6.

To calculate the systematic error introduced by the physical match of detector and simulation we divided Fig. 4.2 into eight ϕ sections. These roughly correspond to the eight EMC sectors but there is not a direct correlation to this in the number of slices chosen, a greater or lesser number would also suffice. For each slice the ratio of the integrals was made, then the RMS was computed,

$$x_{RMS} = \sqrt{\frac{x_1^2 + x_2^2 + ... + x_8^2}{8}}, \tag{4.2}$$

Ratio 1	1.0057
Ratio 2	1.0107
Ratio 3	0.8796
Ratio 4	0.9069
Ratio 5	1.0063
Ratio 6	0.9521
Ratio 7	1.1994
Ratio 8	1.1309
RMS	1.0048
$average^2$	1
σ	0.0986
rel. er.	9.86%

Table 4.1: $\frac{dN}{d\phi}$ systematic error numbers.

this was used to compute the standard deviation or σ of the ratios,

$$\sigma_x = sqrtx^2_{RMS} - \bar{x}^2. \tag{4.3}$$

The results are in Table 4.1, so we quote this error as 10.2%.

We now can feel confident that the physical description of PHENIX in PISA is correct, we now move on to insuring that the response of the detector in PISA matches the response in the "real" world.

4.3.1 Matching of E & p: Data and PISA

It is well known in PHENIX that PISA does not exactly model the detector. For example, as will be shown, the n_1 curves of PISA do not match data. The background subtraction technique, that will be described in subsequent sections, for single electrons at high p_T requires a detailed understanding how each source of background contributes. Our principle figure of merit is the E/p profile and our modeling tool is PISA. In the past we have come up with an adjustment of the E/p variable to match PISA output to data for calculating electron ID efficiencies. This is easily justified since, for electrons, E/p is centered about 1.

As we have progressed into background subtraction it became increasingly obvious that a separate smearing of E and p was necessary both because

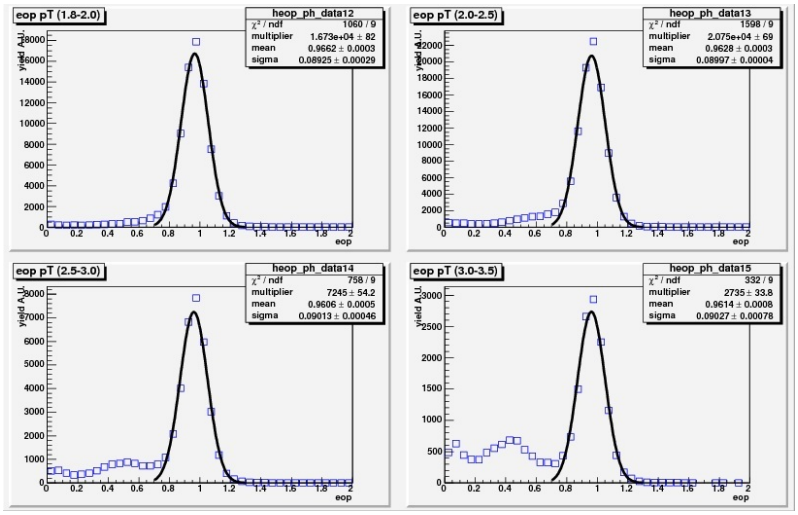

Figure 4.3: Some Examples of E/p Profiles with Gaussian Fits

the variable of interest is obtained by division, the effect of σ_{p_T} is obviously non-linear. Therefore it is critical to insure that σ_{p_T} be well understood and that the response of PISA matches this behavior. The further benefit is an improvement of the systematic error introduced by using the PISA simulation to correct up the data.

First we will show how the resolution is determined in both data and PISA. How we smeared originally. How we smeared at the end of the day

Determining μ and σ of E/p

We use a standard set of 20 p_T bins, for each of these p_T bins the E/p profile is plotted with all other eID cuts applied, four examples are shown in Fig. 4.3.

A Gaussian fit is then made to the electron peak in each distribution, the μ and σ of each fit is extracted and plotted as a function of p_T. This procedure was repeated for $e^{\pm}$ generated in PISA and for the E/p peak about one in data. The results are plotted in Figures 4.4 and 4.5.

Each of the plots has a fit to the points. In the case of the μ's a simple plateau function was used,

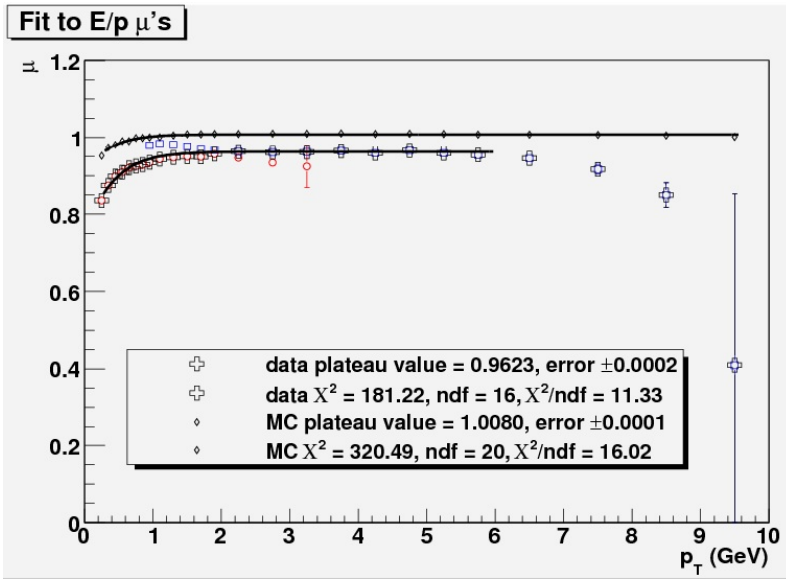

Figure 4.4: μ of E/p profiles as a function of p_T

$$f(\mu) = \left[\frac{par_0}{exp\left(-\frac{p_T - par_1}{par_2}\right)} \right]. \tag{4.4}$$

Derivation of σ Fit Function

The function to fit the $\sigma's$ is not simply one of convenience. E/p is determined by combining the measurements of two different subsystems with very well understood resolution characteristics. The measurement of the energy is done by the Electromagnetic Calorimeter (EMC). The resolution of a calorimeter is,

$$\sigma_{EMC} = \frac{C_0^{EMC}}{\sqrt{E}} \oplus C_1^{EMC}, \tag{4.5}$$

the resolution improves with increasing incidence energy.

The measurement of the momentum is made with the Drift CHamber (DCH). The resolution of the DCH is,

$$\sigma_{DCH} = C_0^{DCH} p \oplus C_1^{DCH}, \tag{4.6}$$

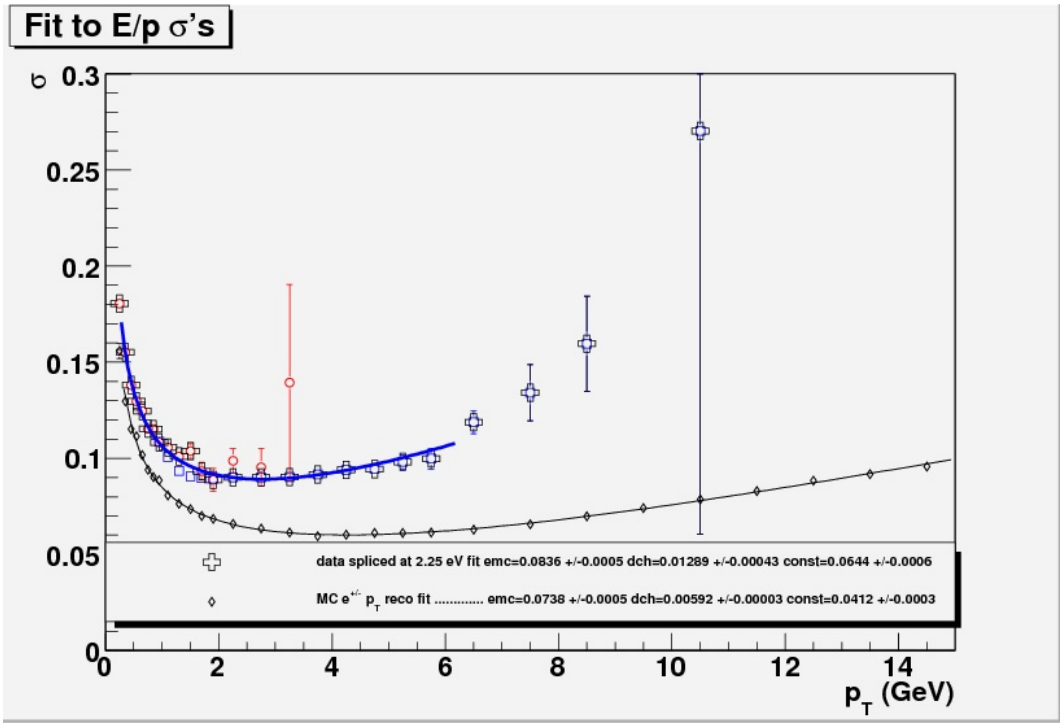

Figure 4.5: σ of E/p profiles as a function of p_T

the resolution degrades with increasing momentum. This leads us to a $f(\sigma)$ overall for E/p,

$$\sigma_{E/p} = \frac{C_{EMC}}{\sqrt{E}} \oplus C_{DCH}p \oplus C_{combined}. \tag{4.7}$$

Since we fit this function to E/p there is no way to disentangle the constant terms for the DCH and EMC consequently our equation has a combined constant. We now fit this equation to data and MC $e^{\pm}$ as seen in Fig.4.5. The fit is quite good as would be expected since the resolution equations for calorimeters and drift chambers are well understood.

The salient feature of Fig 4.5 is that PISA is not a good replication of the data as we need and expect if we are to use PISA with confidence. In the past we (among others) added a smearing factor to the calculated value of E/p within our simulation analysis code so the the μ's and σ's of data and MC matched. This is fine for acceptance and efficiency calculations for electrons, where E/p is centered about one.

We are interested in a precise modeling of backgrounds, principally π's

and this technique breaks down since the values of E/p for π's cover a broader spectrum where we can't depend on the relationship between the resolutions to track as they would for electrons. Consequently we decided to smear E and p separately.

Smearing Technique

Our method of smearing was to determine a "goal" number for a factor in the resolution function, Eq. 4.7. In the first approximation this would simply be factors extracted in the fit to the data. We then subtracted in quadrature,

$$\sqrt{\left(E * \sqrt{\left(\frac{C_1^{goal}}{\sqrt{E}}\right)^2 + \left(C_2^{goal}\right)^2}\right)^2 - \left(E * \sqrt{\left(\frac{C_1^{MC}}{\sqrt{E}}\right)^2 + (C_2^{MC})^2}\right)^2}. \tag{4.8}$$

This quantity we call σ_{smear} and we use it to generate a random number from a Gaussian distribution centered about zero with $\sigma = \sigma_{smear}$. We call this number E_{smear} and we add it to the PISA reconstructed E. Recall that the σ we use is a relative error, we multiply this to the PISA energy to get the absolute amount that is to be added(subtracted) from the PISA energy such that its ultimate σ is the one we desire,

$$E = (0.96 * E) + E_{smear}. \tag{4.9}$$

The 0.96 in Eq. 4.9 is from the fit to the μ's, Eq. 4.4 and Fig. 4.4, this brings the μ of E/p in MC to the same value of data.

Before we begin the discussion of the momentum smearing we digress momentarily to go over how the DCH determines a particle's momentum. Fig 4.6 is a schematic of this measurement. What the DCH actually measures is the angle, α between the particle's track and a radius vector at the reference radius. The momentum is then,

$$p = \frac{constant}{\alpha}. \tag{4.10}$$

The constant in Eq. 4.10 was determined by a fit to reconstructed $1/\alpha$ vs. momentum

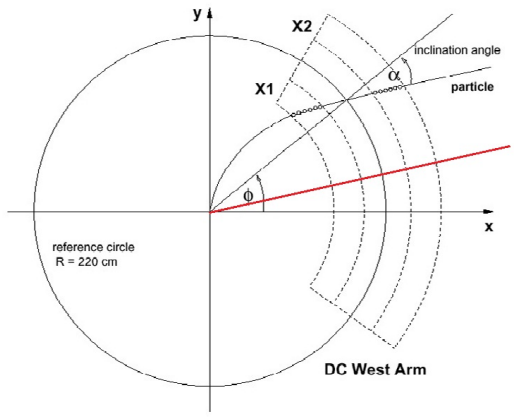

Figure 4.6: Drift Chamber determination of p

and is equal to 92.

Since it is the variation in α that determines the momentum resolution we smeared α in MC. Pisa does not write out $\alpha_{generated}$ only $p_{generated}$. So we rearranged Eq 4.10 to get,

$$\alpha_{generated} = \frac{92}{p_{generated}}, \tag{4.11}$$

and

$$\alpha_{reconstructed} = \frac{92}{p_{reconstructed}}. \tag{4.12}$$

So once again we do a subtraction in quadrature,

$$\alpha_\sigma = \sqrt{\left(\alpha_{gen} * \sqrt{(p_{gen} * C_1^{goal})^2 + (C_2^{goal})^2}\right)^2 - \left(\alpha_{gen} * \sqrt{(p_{gen} * C_1^{MC})^2 + (C_2^{MC})^2}\right)^2}. \tag{4.13}$$

α_σ is then used to generate a random number from a Gaussian distribution centered about zero with $\sigma = \alpha_\sigma$. This random number is than added to $\alpha_{reconstructed}$ to smear it and we then get;

$$p_{reconstructed(smeared)} = \frac{92}{\alpha_{reconstructed(smeared)}} \tag{4.14}$$

So at the end of the smearing day,

$$\frac{E}{p} = \frac{E_{reconstructed(smeared)}}{p_{reonstructed(smeared)}}. \tag{4.15}$$

What Goal, Smearing?

In our initial smearing efforts we set the goal value as those that we extracted from a fit to data. The limits of the fit were set to stay below the π threshold in the RICH. However this does not properly sample the region where DCH resolution dominates so we decided to search for independent ways to determine the goal values.

The resolution of the EMC was determined by others in the PHENIX collaboration [27] to be,

$$\left(\frac{\delta E}{E}\right) = \left(\frac{8.0}{\sqrt{E}}\right) \bigoplus (5.0). \tag{4.16}$$

A dilepton invariant mass spectrum contains, among other things, two peaks from the decay of the J/ψ and the ϕ mesons, Fig. 4.7.

To determine the resolution of the DCH we used the width of the J/Ψ and ϕ peaks from the dielectron invariant mass in Run8 dAu. We start with the relationship between mass width and momentum width,

$$\sqrt{2}\frac{\delta m}{m} = \frac{\delta p}{p}. \tag{4.17}$$

For the J/Ψ this is,

$$\frac{\delta m}{m} = \frac{51.1}{3082} = 1.66\% \text{ (From Fig. 4.8)}, \tag{4.18}$$

This implies,

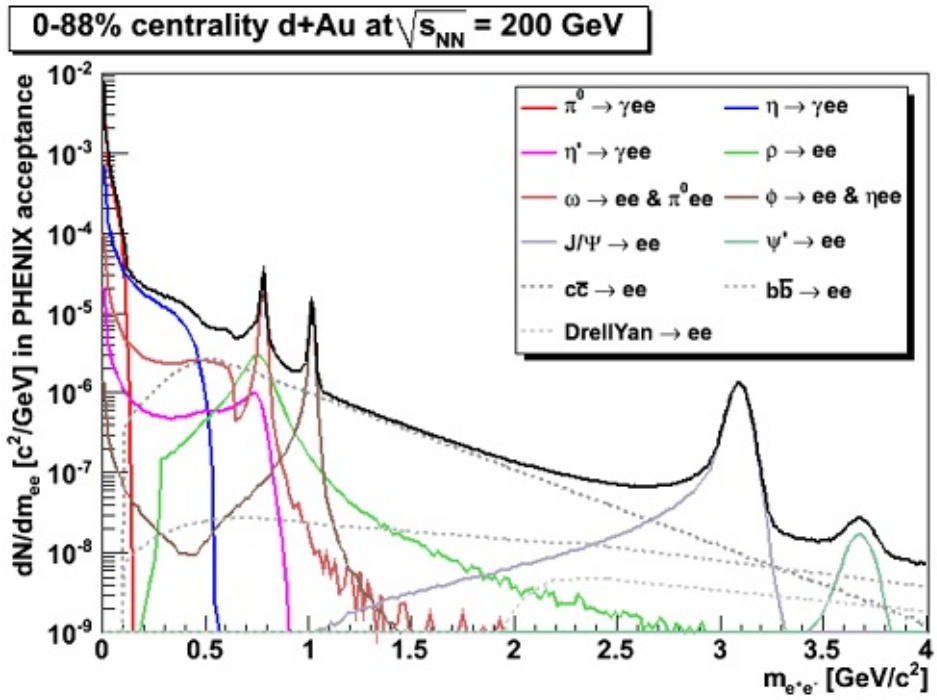

Figure 4.7: Invariant mass spectrum of dielectrons [2]

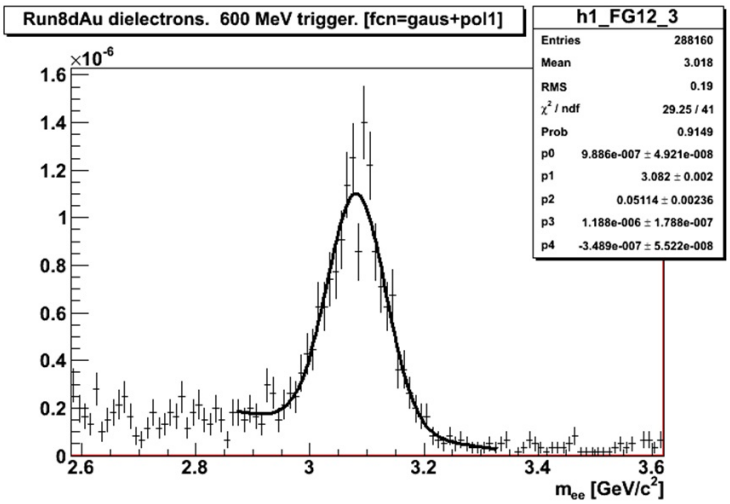

Figure 4.8: Fit to J/Ψ peak, Run8 dAu dielectrons [2]

$$\left(\frac{\delta p}{p}\right)_{J/\Psi} = 2.34\%. \tag{4.19}$$

Then for the ϕ,

$$\frac{\delta m}{m} = \frac{9.59}{1012} = 0.95\% \text{ (From Fig. 4.9)}. \tag{4.20}$$

Once again for the momentum width,

$$\left(\frac{\delta p}{p}\right)_{\phi} = 1.34\%. \tag{4.21}$$

We square the terms of Eq.4.6

$$\left(\frac{\delta p}{p}\right)^2 = C_1^2 p^2 + C_2^2. \tag{4.22}$$

We have two values of $\left(\frac{\delta p}{p}\right)^2$,

$$J/\Psi \rightarrow 2.34^2 = C_1^2(1.774)^2 + C_2^2 \tag{4.23}$$

and

$$\phi \rightarrow 1.34^2 = C_1^2(0.650)^2 + C_2^2. \tag{4.24}$$

We then have two equations and two unknowns. If we subtract Eq. 4.24 from Eq. 4.23 and re arrange we get

$$C_1^2 = \frac{(2.34^2 - 1.34^2)}{(1.774^2 - 0.650^2)} \tag{4.25}$$

$$C_1 = 1.16\% \ \Rightarrow C_2 = 1.1\%. \tag{4.26}$$

We then plug in the parameters from Eq. 4.26 into 4.13 and Eq. 4.16 into Eq. 4.8, re run our MC analysis code. The results are in Fig. 4.10.

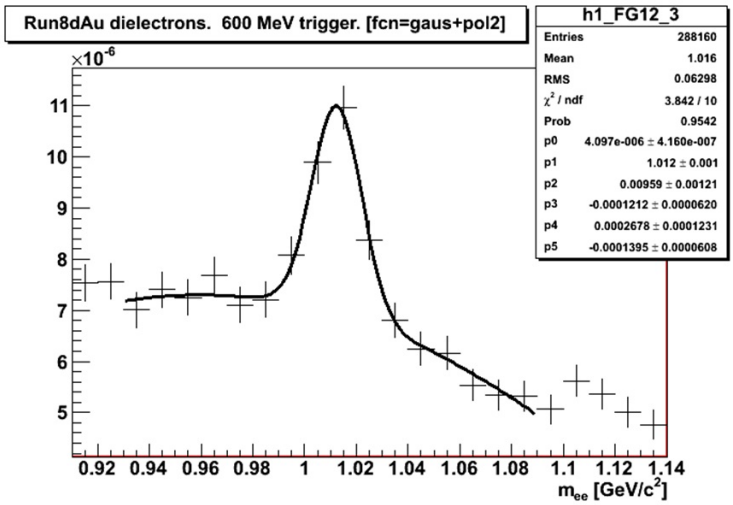

Figure 4.9: Fit to ϕ peak, Run8 dAu dielectrons [2]

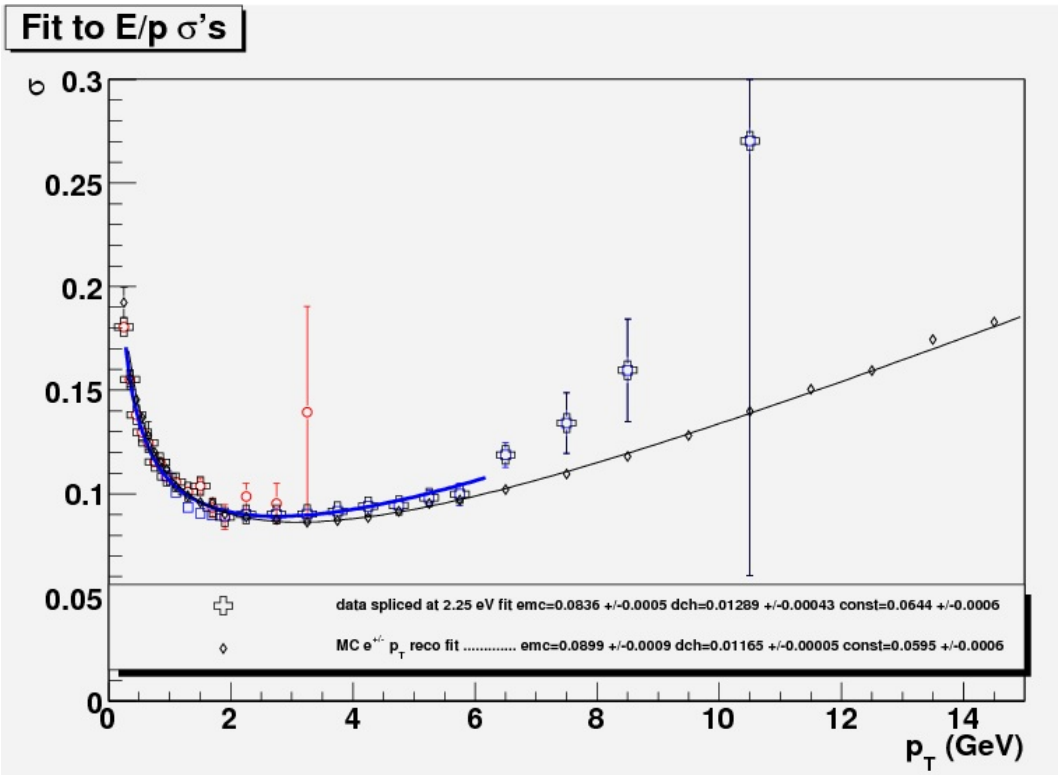

Figure 4.10: Final Fit to E/p σ's

Recalibrator Contribution to Systematic Error

The mass of the J/Ψ is known to 0.00035%, $3096.916 \pm 0.011 MeV$ [28], the width in di electron decays is $5.55 \pm 0.14 keV$ so we assign zero error to the mass measurement and the width of the invariant mass peaks is solely from the detector resolution.

For the J/Ψ,

$$\frac{\delta p}{p}_{J/\Psi} = \sqrt{2}\frac{\delta m}{m} = \sqrt{2}\frac{51.1 \pm 2.36}{3082 \pm 0}. \tag{4.27a}$$

The error propagation is,

$$\left(\frac{\sigma_{\frac{\delta p}{p}}}{\frac{\delta p}{p}}\right)^2 = \left(\frac{\sigma_{\delta m}}{\delta m}\right)^2 + \left(\frac{\sigma_m}{m}\right)^2, \tag{4.27b}$$

plugging in numbers,

$$\left(\frac{\sigma_{\frac{\delta p}{p}}}{2.34}\right)^2_{J/\Psi} = \left(\frac{2.36}{51.1}\right)^2 + \left(\frac{0}{3082}\right)^2, \tag{4.27c}$$

So the contribution to the systematic error from J/Ψ is,

$$\sigma^{J/\Psi}_{\frac{\delta p}{p}} = \frac{2.36}{51.1} * 2.34 = 0.11. \tag{4.27d}$$

Recall the equation for the relative uncertainty of the DCH resolution,

$$\left(\frac{\delta p}{p}\right)^2 = C_1^2 p^2 + C_2^2. \tag{4.28}$$

Equation 4.28 tells us that the maximum combined uncertainty of C_1 and C_2 is $\frac{0.11}{2.34}$. To begin we assign zero error to C_2 and assign all of the error to C_1,

$$\left(\frac{\sigma_{(\frac{\delta p}{p})^2}}{(\frac{\delta p}{p})^2}\right)^2 = \left(\frac{\sigma_{C_1^2}}{C_1^2}\right)^2 + \left(\frac{\sigma_{C_2^2}}{C_2^2}\right)^2, \tag{4.29a}$$

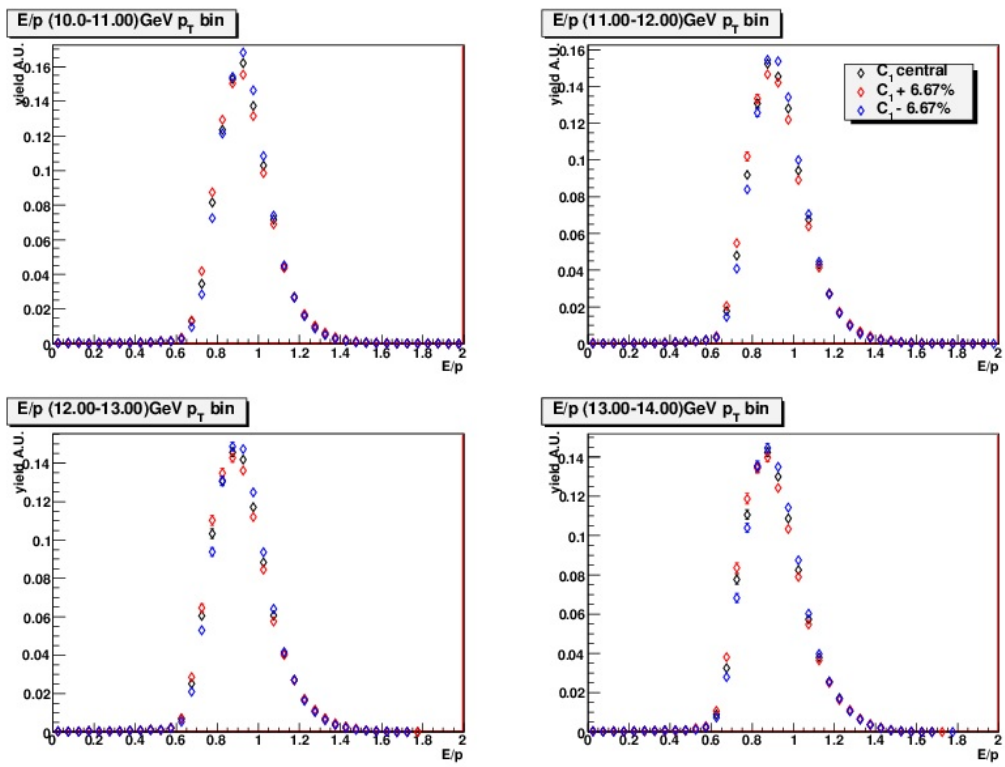

Figure 4.11: Overlay of E/p profiles from simulation. Three curves corresponding to the central, upper and lower values of the C_1 parameter.

with σ_{C_2} set to zero we get,

$$\left(\frac{\sigma_{(\frac{\delta p}{p})^2}}{(\frac{\delta p}{p})^2}\right) = \left(\frac{\sigma_{C_1^2}}{C_1^2}\right), \tag{4.29b}$$

once again plugging in numbers,

$$\left(\frac{0.37}{5.50}\right) = \left(\frac{\sigma_{C_1^2}}{C_1^2}\right) = 6.66\% \text{ rel. error.} \tag{4.29c}$$

Because C_1 is implemented as C_1^2 in code it was decided to choose the relative error on C_1 as 6.66%. In PISA, C_1^{goal} was raised(lowered) by 6.67% and the E/p profiles were compared to the E/p profiles when C_1 has it's central value of 1.16%. The profiles are plotted in Fig. 4.11, they are normalized to number of events generated.

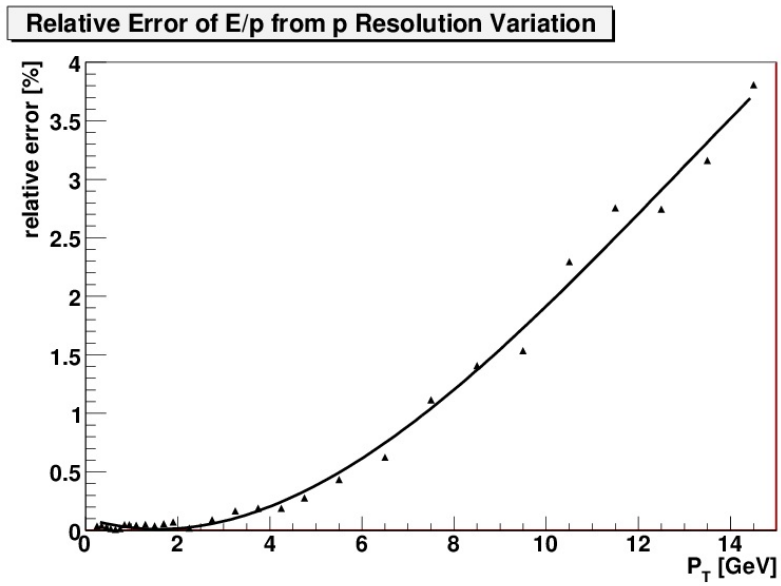

Figure 4.12: Relative uncertainty of E/p as a function of p_T

The relative uncertainty of E/p was calculated as follows,

$$Yield = \int_{0.8}^{1.2} E/p. \tag{4.30a}$$

This yield was calculated using the central, upper and lower values of C_1,

$$Relative\ Uncertainty = \frac{|Yield_{central} - Yield_{upper(lower)}|}{Yield_{central}} * 100\%. \tag{4.30b}$$

The upper and lower values were averaged and then fit with a third degree polynomial, Fig. 4.12, the fit will be used to combine systematic errors. A similar variation of the C_2 parameter was made as well, C_2 for the DCH was chosen to be 1.1%, this was varied by $\pm 0.11\%$, the resulting variation in the E/p yield was from 0.01% to 0.08%, it was decided to ignore this contribution to the systematic error.

4.3.2 Verifying Selection Cuts

In the previous section we demonstrated that we have successfully matched the energy and momentum performance of PISA to the PHENIX detector, and, consequently, that the behavior of E/p in PISA is reliable. Now we need to verify that remaining selection cuts in PISA behave in the same manner as the selection cuts in the real detector.

The first cut is the EMC matching cut, this is the distance between the projection of a charged track to the face of the EMC and the center of gravity of an energy deposition in a 3x3 array of EMC cells. The user is presented with this distance in ϕ and z at the EMC expressed as σ's. We add these in quadrature to produce a circular cut that we call dtrk,

$$dtrk = \sqrt{(emcsdphi_e^2 + emcsdz_e^2)}.$$

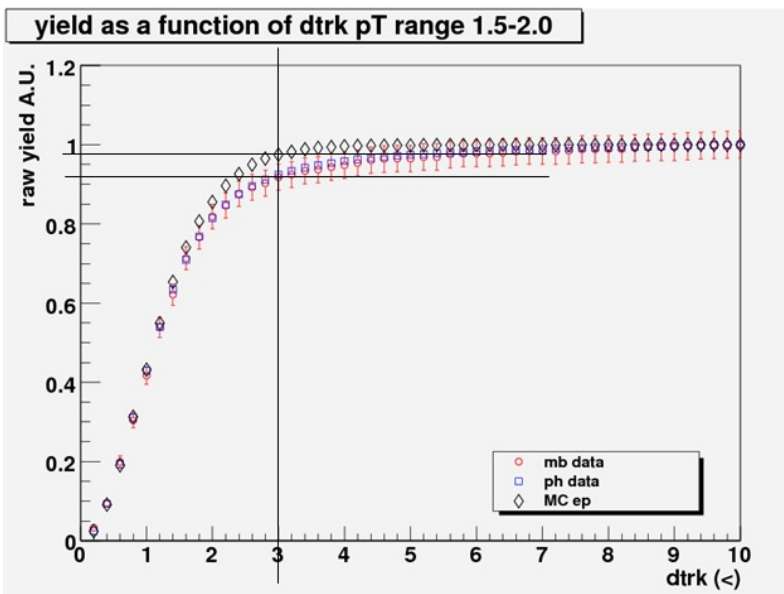

Figure 4.13: Yield as a function of the EMC matching cut.

In Fig. 4.13 we plot the fractional yield as a function of the dtrk variable. All other eID cuts are applied and, as before, $p_T \leq 4.0 GeV/c$ well below the π threshold in the RICH. We see that at the cut value of $dtrk < 3\sigma$ there is a small discrepancy between data and simulation. A plot was made of the efficiency of the dtrk variable, defined as the yield @ $dtrk < 3\sigma$ divided by the yield @ $dtrk < 10\sigma$. This was done for data and simulation as well as a ratio of data to simulation.

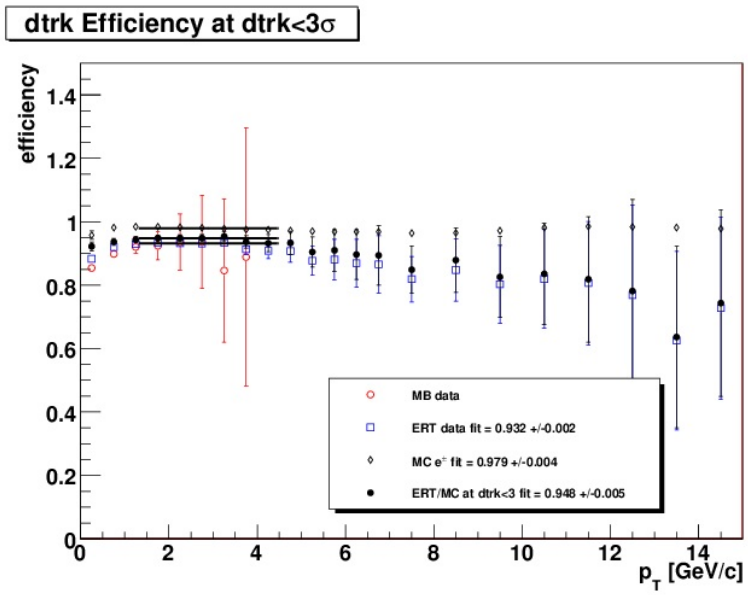

Figure 4.14: EMC matching cut efficiency.

The dtrk profiles in the p_T range of the fit are seen in Appendix B.1.1, they are well matched and justify a simple multiplicative correction. The result is a small 0.948 additional factor in the acceptance/efficiency correction. The relative error in this factor is $0.005/0.948 = 0.0053$, we quote a systematic error of 0.53%.

The prob variable is plotted in Fig. 4.15, we that there is little or no departure between data and simulation over the entire range of prob. Once again an efficiency plot was made as well as a ratio of data simulation, Fig 4.16. The prob profiles in the p_T range of the fit are seen in Appendix B.1.2, they are also well matched and justify a simple multiplicative correction. The result is a small 0.985 additional factor in the acceptance/efficiency correction. The relative error in this factor is $0.005/0.985 = 0.0051$, we quote a systematic error of 0.51%.

The fractional yield plot for n_1, Fig 4.17 reveals a discrepancy that is too large to ignore. The difference in fractional yield at $n_1 \geq 5$ is just short of 20%. The solution to this issue is to set n_1 cut to $n_1 \geq 3$ in simulation and then, in data, make a ratio of the yield at $n_1 \geq 3$ to $n_1 \geq 5$ as seen in Fig 4.18. The ratio is fit with a zeroth order polynomial below the π threshold, this value is used as an additional scale factor to create the inclusive yield, Sec. 4.6.

The efficiency of the n_1 cut for both simulation and data is plotted in

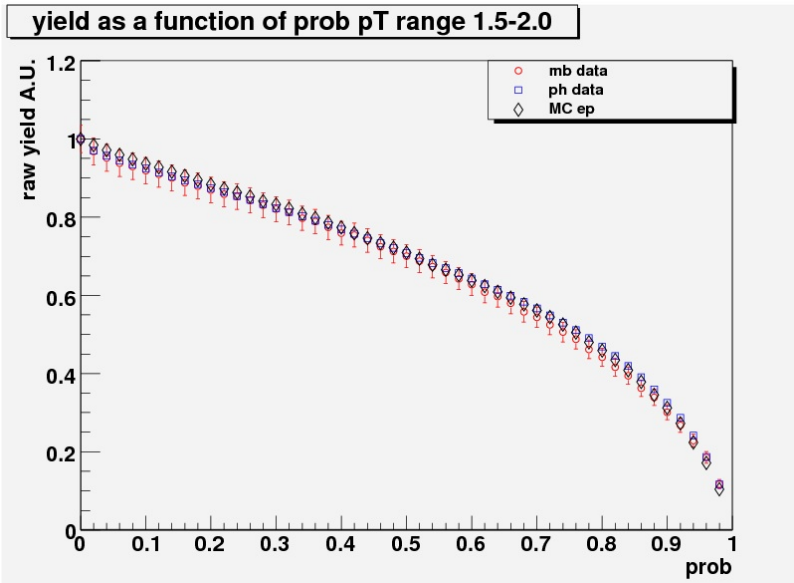

Figure 4.15: Yield as a function of the prob cut.

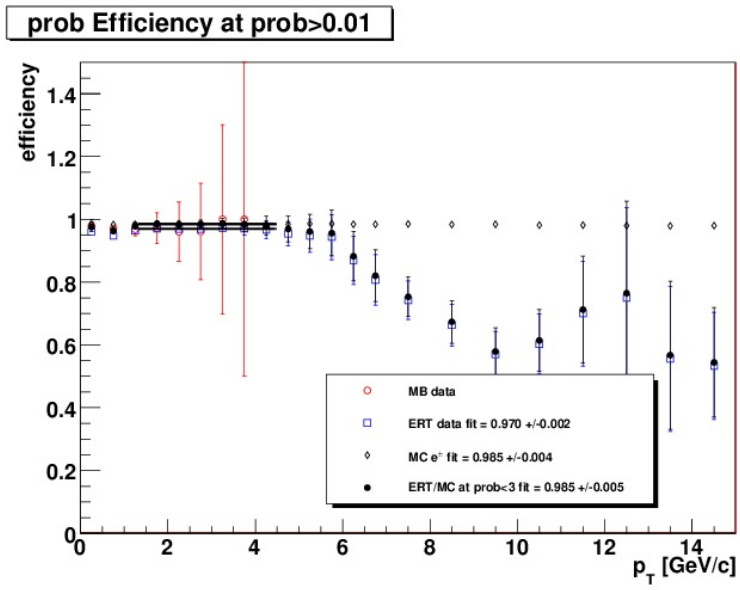

Figure 4.16: EMC shower shape cut efficiency.

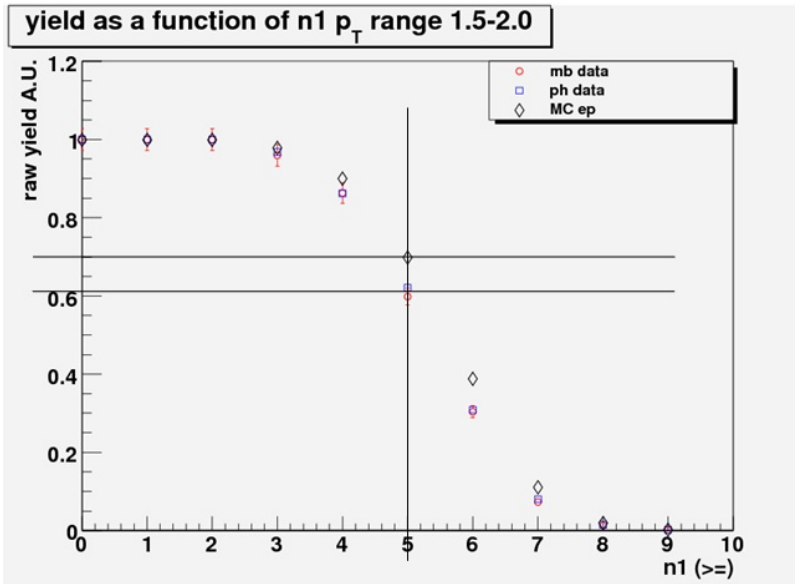

Figure 4.17: Yield as a function of the n_1 cut.

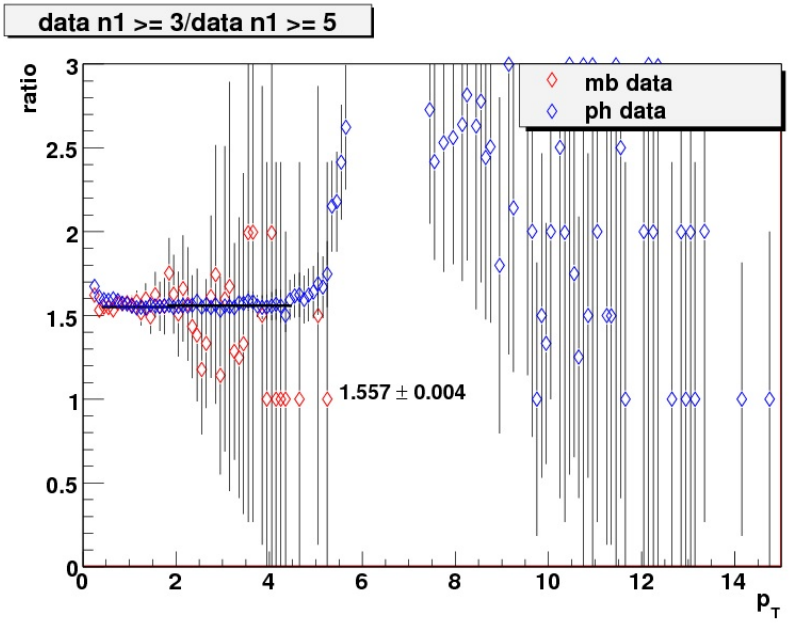

Figure 4.18: Ratio, in data, of $n_1 \geq 3$ to $n_1 \geq 5$.

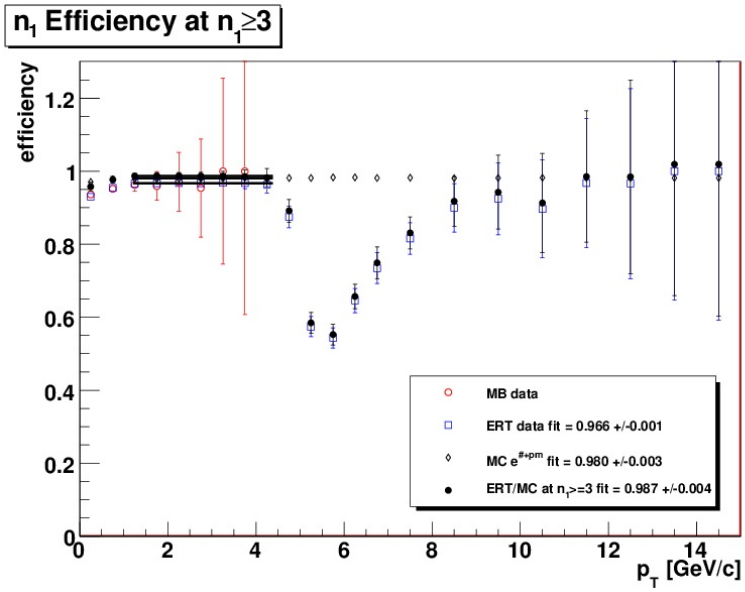

Figure 4.19: n_1 efficiency at $n_1 \geq 3$ for both data and simulation.

Fig 4.19 with straight line fits. The peak of the n_1 distribution is slightly higher in simulation, 5.1, than data, 4.9, (see profiles App. B.1.3) so we expect the $n_1 \geq 3$ cut to be less efficient in data than simulation and that is exactly what we see in the figure. Also plotted is the data efficiency divided by the simulation efficiency which shows us that the acceptance/efficiency correction needs an overall correction factor of 0.987. The relative error on this fit is $0.004/0.987 = 0.004$ so we quote a systematic error of 0.40%. An additional systematic error is introduced by the fit of Fig 4.18, but since the relative error is $0.004/1.557 = 0.26\%$ to give a total systematic of 0.47%.

The final result is a correction factor of 0.922 to the final correction curve of the next section with a fixed systematic error of 0.877% to go with the p_T dependent systematic of the E/p cut.

4.3.3 Final Correction Curve

Once that we are assured that the PISA simulation physically matches the real detector and that the selection cuts are equivalent, we have to deal with another aspect of taking measurements, the bias introduced by a detector with finite resolution. We do this by weighting the flat input spectrum of simulated electron tracks with a power law,

$$w = p_T * 0.786 * (0.547 + p_T)^{-6.87}. \tag{4.31}$$

The weighting function used, Eq. 4.31 approximates the expected spectrum of decay electrons from heavy quarks. In the final analysis, we use a fit to previously published data to further fine tune our simulation, this will be discussed in subsequent sections.

The reason for doing this is explained in detail by Mike Tannenbaum [29]. The summary for the case in point refers to Fig. 4.20. The numbered boxes are p_T bins, the solid diamonds the "true" spectrum. As already discussed, the momentum measurement is made by the DCH whose resolution goes as **p**. Consequently the resolution worsens as we go higher in momentum.

In Fig. 4.20 this is represented by the gaussian centered in each p_T bin. The mean represents the true momentum, the distribution the range of measured values for this true momentum. Particles in a particular gaussian that fall into another bin will be plotted in that bin and so will be incorrectly measured. If the parent spectrum was flat, there would be equal numbers of particles from either side of the gaussian contributing to neighboring bins. Since the parent distribution is steeply falling there are more particles in the lower edge of the gaussian so the neighboring bin on the low side gets preferentially filled and the resulting spectrum is flatter as represented by the crosses.

So, a p_T spectrum is produced by histogramming the reconstructed p_T, weighting each fill by the weight function. To produce the correction curve this histogram is then

- Scaled by $\frac{p_T \text{ range generated}}{\text{bin width}} * \frac{1}{N_{generated}} = \frac{20GeV}{0.10GeV} * \frac{1}{N_{generated}} = \frac{200}{N_{generated}}$.
- Scaled by $\frac{\text{vertex range generated}}{\text{vertex range used}} = \frac{30cm}{20cm} = \frac{3}{2}$.
- Scaled by $\frac{1}{\text{weight function}}$.

In the end we have the result of what we got out divided by what we put in, Fig. 4.21, the curve is fit with this function,

$$\frac{p_0 + p_1 * p_T + p_2 * p_T^2}{1 + exp\left[-\frac{p_T - p_3}{p_4}\right]}. \tag{4.32}$$

The raw p_T spectra of both MB and ERT data are then divided by this fit, $\epsilon_{reco}(p_T)$ and multiplied by the fit of Fig. 4.18.

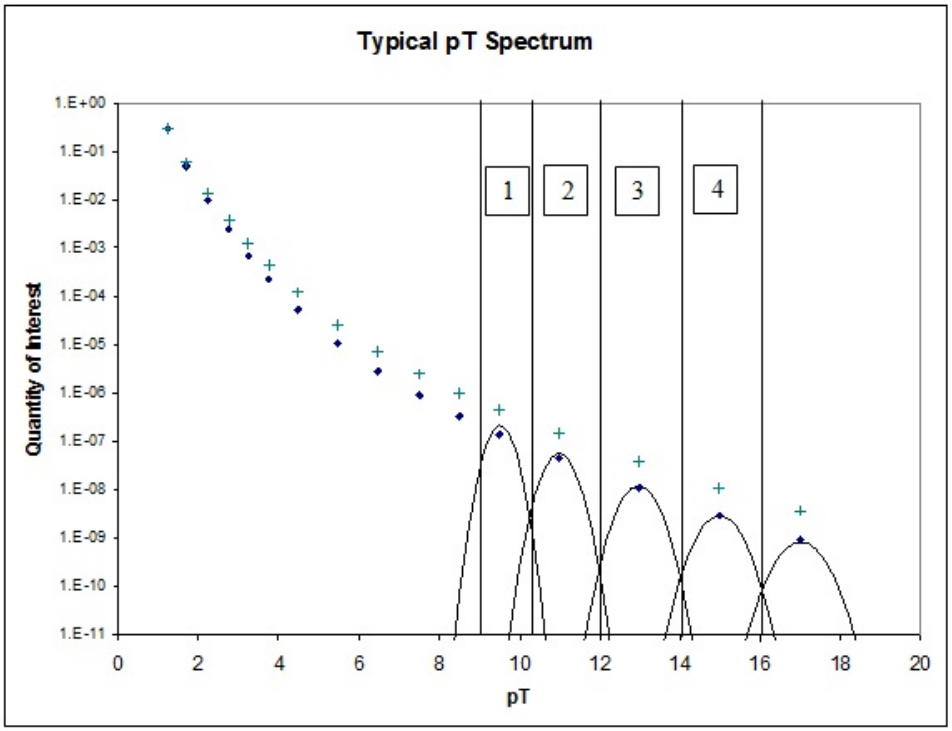

Figure 4.20: The effect of finite resolution on steeply falling spectra

4.4 Trigger Efficiency

For the ERT trigger data analysis, the trigger efficiency, ϵ_{trig} needs to be corrected for. The trigger efficiency is determined from the MB data set as a fraction of electrons that satisfies the 4x4c photon trigger. This is a simple trigger in that it is fired when an energy deposit of $> 1.4GeV$ is detected in a 4x4 array of EMC towers It is required that the trigger tile that sets the trigger be hit by the electron candidate to avoid the "random benefit" in the trigger efficiency.

In Fig. 4.22 we see plotted the raw p_T spectra from both MB & ERT files. Since the purpose of the ERT trigger is to enrich the yield of High p_T electrons the curve of triggered data from the ERT files lies above the MB data as one would expect.

As has been previously mentioned, a part of this enrichment process is that not all MB events are written to tape, a certain fraction are arbitrarily rejected. This is done with a scale down factor, if the scale down factor is equal to n, every n+1 event is written. Conversely, if we have m scaled events

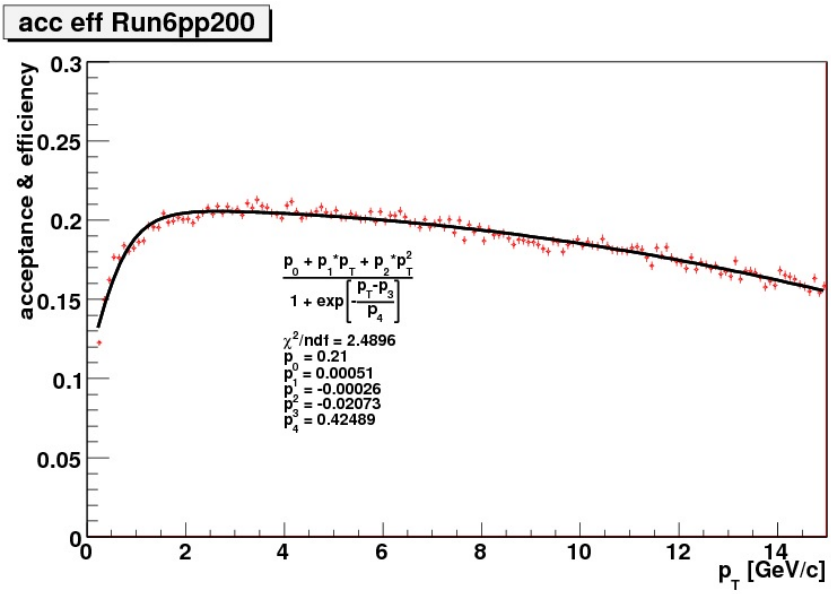

Figure 4.21: Acceptance and Efficiency Correction Curve for Run 6

recorded and a scale down factor of n, then the total number of events sampled is; $N_{sampled} = m * (n + 1)$ or,

$$N_{MB}^{sampled} = N_{MB_{recorded}} * (scaledownfactor + 1). \tag{4.33}$$

There is a limited number of events per second that can be written to tape, this is referred to as the bandwidth. The use of scale downs adjusts the fraction of this bandwidth that is allocated to each trigger type. Since the specialized triggers are usually of rarer events the MB receives the greatest scale down, the others low or none at all. This is a contributing factor in the relative magnitude of the curves in Fig. 4.22.

The two MB file curves in the plot are of minimum bias & triggered data. This plot shows the three things that need to be corrected.

The first is that by requiring a trigger tile to fire the acceptance of the detector is somewhat lower than without this requirement. Unfortunately there will be malfunctioning trigger tiles either dead or hot, which are then turned off. The evidence of this is seen in the two MB file curves, the triggered data, above the trigger threshold, is always somewhat lower than the minimum bias curve.

The second factor is the normalization factor, the triggered data is to

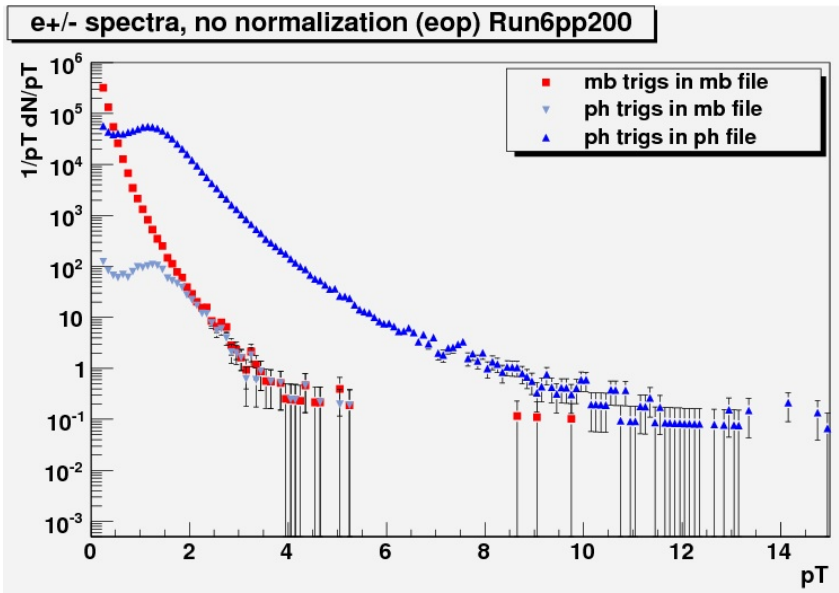

Figure 4.22: Run 6 raw p_T spectra

extend the minimum bias data and, at the end of the day, the measurement is quoted as per event. In the case of the MB data the normalization factor is the number of minimum bias events recorded, $N_{MB_{recorded}}$, in the case of the triggered data this factor is the number of minimum bias live events, $N_{MB_{live}}$, the number of minimum bias triggers that would have occurred if there were no scale downs,

$$N_{MB_{live}} = \frac{N_{MB_{recorded}} * (scaledownfactor + 1)_{MB}}{(scaledownfactor + 1)_{ERT}}. \tag{4.34}$$

So the minimum bias spectrum is scaled by $1/N_{MB_{recorded}}$ and the triggered spectrum is scaled by $1/N_{MB_{live}}$.

The third and final factor is the turn on curve of the triggered data. The nominal threshold value of the trigger is 1.4 GeV but due to noise in the electronics some lower energy electrons will fire the trigger and some higher energy electrons won't. It's only when the energy of the electrons is above 2 GeV that all of them fire the trigger all of the time.

The triggered spectrum from the MB file is divided by the minimum bias spectrum also from the MB file. The resulting ratio is then fit to produce a correction function. Fig. 4.23 shows the trigger efficiency of the 4x4c trigger thus determined. The effective trigger threshold is about 1.4 GeV, and the

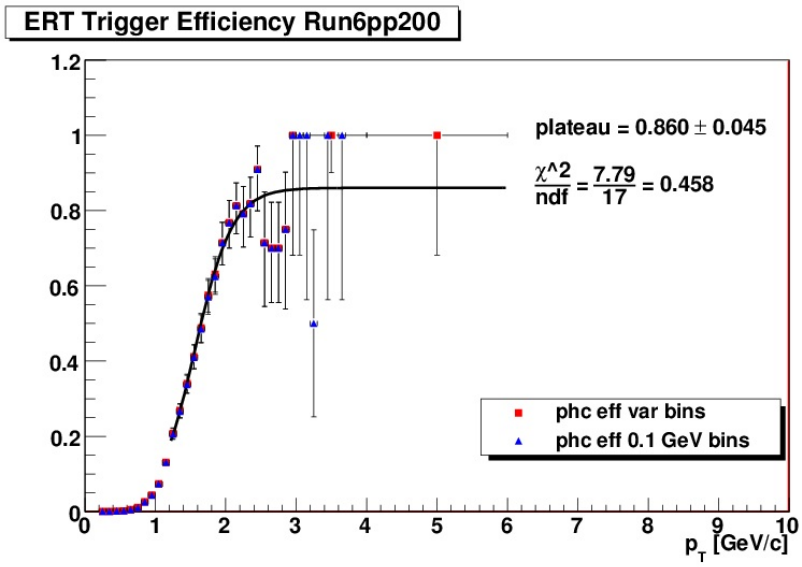

Figure 4.23: Run 6 trigger efficiency

efficiency saturates above 2 GeV. The trigger efficiency at the plateau is $\approx 86\%$. The curve in the figure is a Fermi function,

$$\epsilon_{trigger} = \frac{constant}{exp[-\frac{p_T - numerator}{denominator}]}, \tag{4.35}$$

that is fit to the data. This fit function is used as the trigger efficiency in the analysis.

The triggered spectrum, from the ERT file, is then divided by the fit function and the result is seen in Fig. 4.24. The most important feature of this plot is the overlap region of the two curves, the triggered and minimum bias lie directly on top of each other. This demonstrates that both the fit and the normalization are correct. One can notice that the correction to the low end of the triggered spectrum is not correct, this is not of concern since we only use the minimum bias data in this p_T range.

4.4.1 Systematic Error of Trigger Correction

Since the ERT triggered data set is used only at the high p_T region where the trigger efficiency is at its plateau value, only the error on this value is significant. In Fig. 4.25 is plotted the MB spectrum of Fig. 4.24 divided by

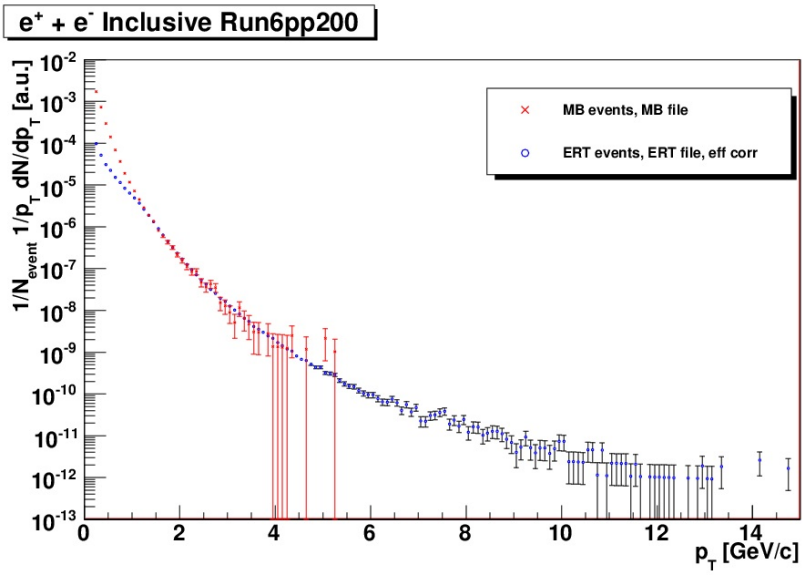

Figure 4.24: Run 6 corrected and normalized spectra

the ERT spectrum. This is "zoomed in" to the overlap region where there are still a sufficient statistics in the MB spectrum to allow a comparison. There are three factors involved in this comparison, $N_{MB\ \mathrm{recorded}}$, $N_{MB\ \mathrm{live}}$ and the trigger plateau.

The two normalization constants have a systematic error from the BBC, in this case only the error would be in a mismatch of the recorded counts in MB and ERT files. We know that this is not an issue from Fig 3.4 in Sec. 3.4, there are no mismatch in the book keeping of the numbers of MB and ERT Triggers. Consequently the only error is due to the trigger plateaus determination. We see from the fit in Fig. 4.25 that the matching of MB and ERT spectra are indeed quite good, the ratio is 0.982 ± 0.31 so we take the systematic error of the trigger correction to be 3.2%.

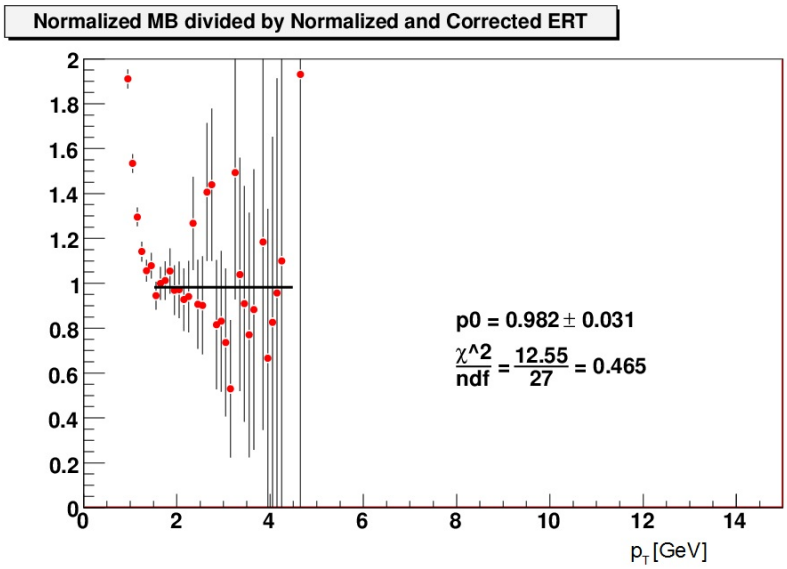

Figure 4.25: Ratio of MB to ERT

4.5 Bin Width Correction

We are trying to measure a differential distribution in p_T, specifically an invariant cross section. Due to limited statistics we cannot measure the yield for each p_T, what is done is that we make a measurement over a range of p_T's, that we call the bin width, and then take the average value of the bin as our measured yield. The average value is the yield in the bin divided by the bin width.

For a steeply falling spectrum, with increasing p_T, the actual p_T corresponding to the average value of the bin is to the left of the center. All initial histograms use bins that are 0.1GeV wide and the error introduced by assuming that the yield of the bin corresponds to the p_T of the center of the bin is negligible. As has been mentioned, we have a standard set of 20 bins, the last several bins are 1 GeV wide as they are the sum of 10 0.1 GeV bins. The statistics are limited at the highest p_T's, summing bins allows a smaller relative error at the price of less resolution of the shape of the spectrum. The error is now too large to neglect and must now be corrected for.

Since the actual value is to the left of the bin center the realized measurement tends to be too high as it is assumed that the center of the bin is the correct p_T. The standard PHENIX technique when re binning is to adjust the

height of the bin such that the center of the bin represents the value of the measurement at the p_T that is the bin center. The technique is as follows.

First, the spectrum is fit with a modified power law with the bin centers as the initial p_T values,

$$f(p_T) = \frac{A}{(p_0 + p_T)^2}. \tag{4.36}$$

This is a commonly used and accepted function that replicates the p_T spectra of interest. Next find the values of p_T at which the above function takes on its average value in each bin by solving for p_T in the equation

$$\langle f \rangle_{[a,b]} \equiv \frac{1}{b-a} \int_a^b f(x)dx = f(p_T^{mean}). \tag{4.37}$$

Where a and b are the lower and upper edges of the bin respectively. Plugging Eq. into Eq. 4.37 we can solve for p_T^{mean},

$$p_T^{mean} = \left(\frac{A}{\langle f \rangle}\right)^{-n} - p_0. \tag{4.38}$$

Each of the calculated p_T^{mean}'s are substituted for the bin centers of the (x,y) pairs. This is iterated until the p_T^{mean}'s converge.

The last step is to re scale the value of the bin such that the center of the bin does indeed correspond to the bin value,

$$y' = y * \frac{f\left(\frac{b-a}{2}\right)}{f(p_T^{mean})}. \tag{4.39}$$

This gives us the value of the invariant yield at the value of p_T at which the final plotted data point rests, so we can compare to other data and theories in a way which is independent of any particular momentum binning. The assumption which this procedure relies on is that the invariant differential yield as a function of p_T does not wildly oscillate, which is quite reasonable.

4.6 Inclusive Spectra

All of the factors are now plugged into Eq. 4.1 for the MB and ERT data, to produce an invariant cross section for all electron candidates, Fig. 4.26. The original 0.1GeV bins have been combined or rebinned in to the bins of Sec. 4.1 and then corrected as in Sec. 4.5. There are three data curves in this plot, minimum bias, triggered and "spliced". Since the ERT and MB data match in the overlap p_T region a single curve is created by splicing the MB curve and the ERT curve at $p_T = 2.2GeV$, well above the trigger threshold. At this point the errors are only statistical.

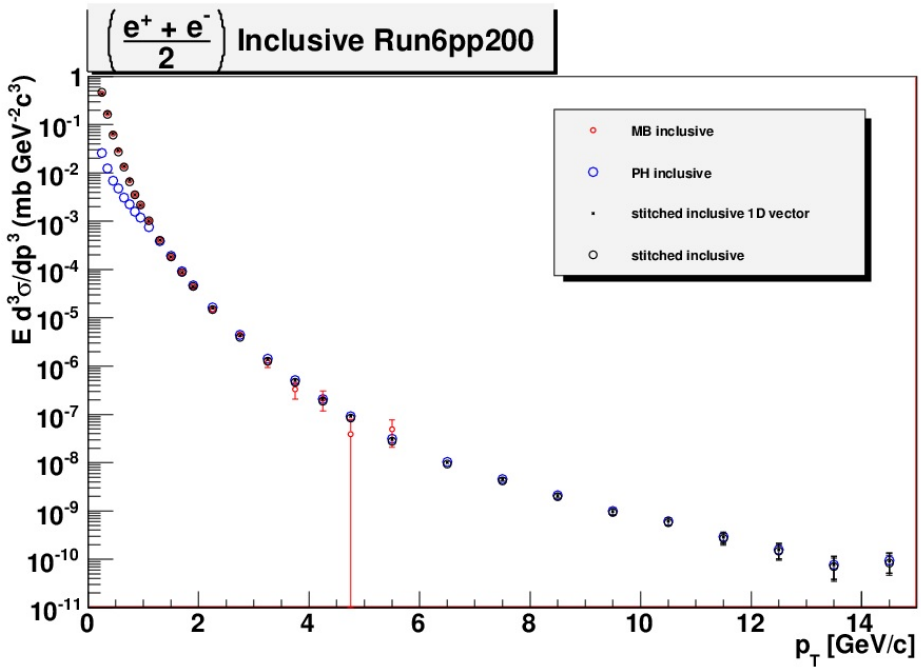

Figure 4.26: Inclusive invariant cross section for Run 6, re binned

The salient feature here is the kink in the curve at $p_T \approx 6.5GeV$. This is point where a significant fraction of the $\pi's$ are defeating the RICH cut. This can be seen more readily in Fig. 4.27. What's plotted here is the raw yield, $\frac{dN}{dp_T}$ from ERT data, all eID cuts are applied. There are no other factors other than a re binning to delineate the kink in the curve. The line is a FONLL curve fit to Run 5[24] heavy flavor invariant cross section data that is reverse engineered to be an inclusive yield.

Our assertion is that this background is dominated by $\pi's$ and that we can

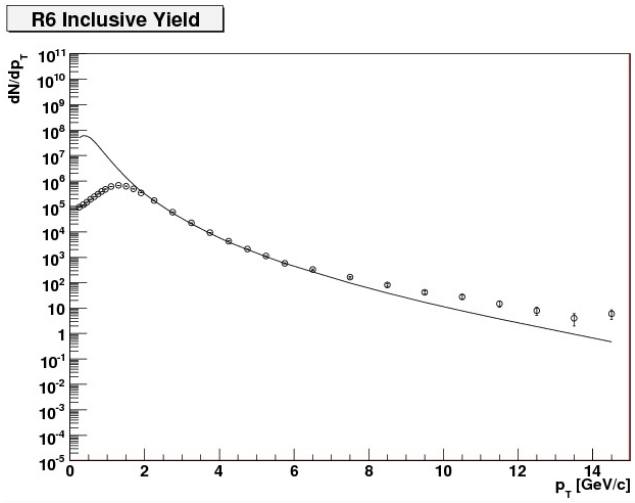

Figure 4.27: Inclusive Yield ERT Data plotted with a heavy flavor theory prediction.

subtract the background using a technique that takes advantage of the energy deposition characteristics of $\pi's$.

Chapter 5

Background Subtraction at High p_T

5.1 Technique

The Cherenkov threshold momentum for $\pi's$ in CO_2 gas at Standard Temperature and Pressure is 4.625GeV. As π's pass this momentum the $\pi's$ begin to emit Cerenkov light and they begin to be indistinguishable from electrons in the RICH. We exploit the characteristics of the energy deposition in the EMC to formulate a background subtraction technique using the E/p distribution.

In Fig. 5.1 we see a typical E/p profile in a p_T range below which the $\pi's$ are a significant contributor. In other word, even though we are above the Cherenkov threshold, the $n_1 \geq 5$ cut still removes most $\pi's$. We can see a clear distribution about the value of one.

Fig. 5.2 is now an E/p plot in a p_T bin well above the π threshold. Electrons are still centered about one but now we have a decaying continuum of hadrons that extends into the region of the electrons.

There is also a rising curve to the left of the E/p profile, this is from a few sources. The π's that don't shower in the EMC leave their energy as minimum ionizing particles. This referred to as a MIP peak, this peak moves to the left as one goes up in p_T since the energy deposit of a MIP in our EMC is 250 MeV, independent of momentum. We then have the situation where the E in E/p is constant and with increasing p, the MIP peak moves toward zero and is not a factor. In addition there will be the decay electrons from the so called ke3 decays of $K^{\pm}$ and K_L^0, since they decay away from the interaction

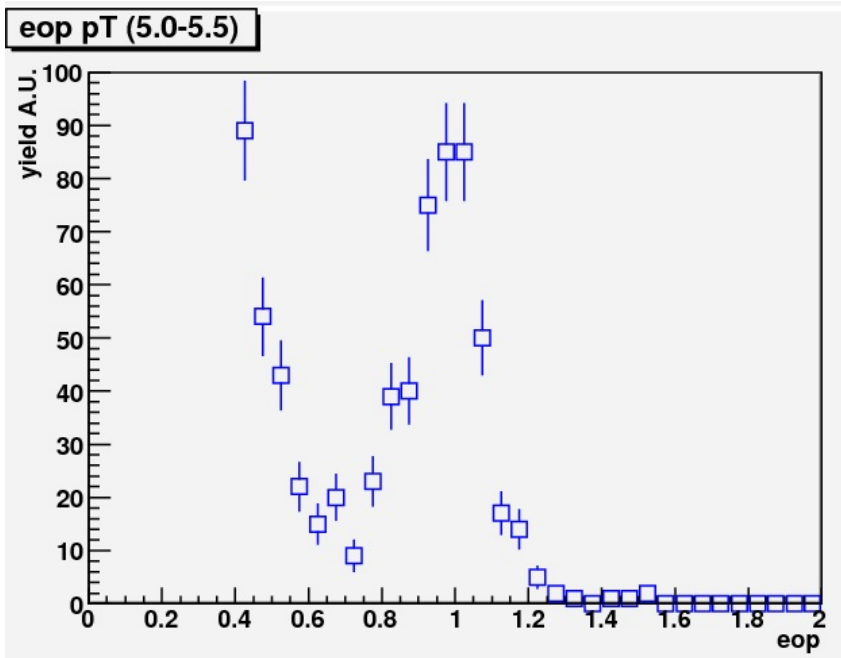

Figure 5.1: Typical E/p profile without hadron contamination

point they have a reconstructed p_T that is higher than their real p_T so E/p is lower than one. There will also be electrons from photon conversions, these will also have a high reconstructed p_T, however many come from beam pipe conversions, these will generally fall into the accepted E/p window. That is why conversion γ's are part of the cocktail of electron sources that will be subtracted from the inclusive spectrum.

We can also see in Fig. 5.2 a graphic of the technique that we will employ to remove the hadron background. We assume that the shape of the hadron continuum, aside from the MIP peak, is independent of p_T. The spectrum is divided into two regions as shown in the figure and a ratio is formed of the integral of Region II divided by Region I,

$$R = \frac{\int_{0.8}^{1.2} \left[\frac{E}{p}\right]_\pi}{\int_{0.6}^{0.8} \left[\frac{E}{p}\right]_\pi}. \tag{5.1}$$

Once R_π is known the following equation can be used to subtract the π background from the electron candidates,

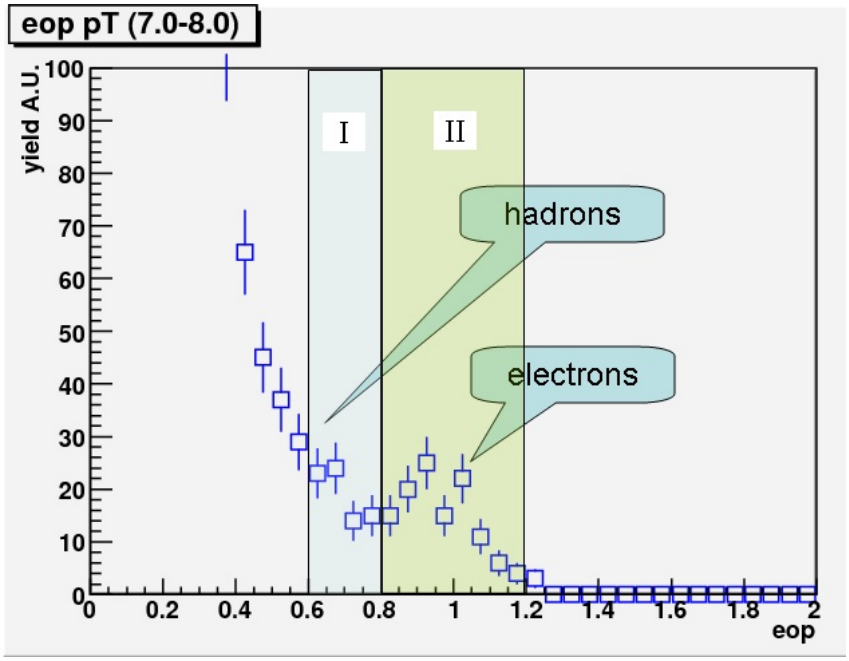

Figure 5.2: Significant hadron contamination

$$N_e = \int_{0.8}^{1.2} \left[\frac{E}{p}\right]_{all} - R_\pi \int_{0.6}^{0.8} \left[\frac{E}{p}\right]_{all}. \tag{5.2}$$

There are now three tasks set before us, demonstrating that R_π is indeed a viable concept and that we can accurately calculate it. Secondly, if this is so then we must demonstrate that the only background in region I is indeed $\pi's$, and last, we must be able to prove that we can accurately model the backgrounds.

5.2 Principle

An electromagnetic calorimeter is essentially a block of dense matter that induces a particle to shower, to produce multiple secondary and tertiary particles, many of which are charged and can therefore create a signal that we can read out. In the case of the lead glass (PbGl) calorimeter, the block of material is also the sensitive medium. The lead induces the shower, the charged particles emit Cherenkov light that passes through the clear glass to a photomultiplier tube. In this case all of the available signal is accumulated.

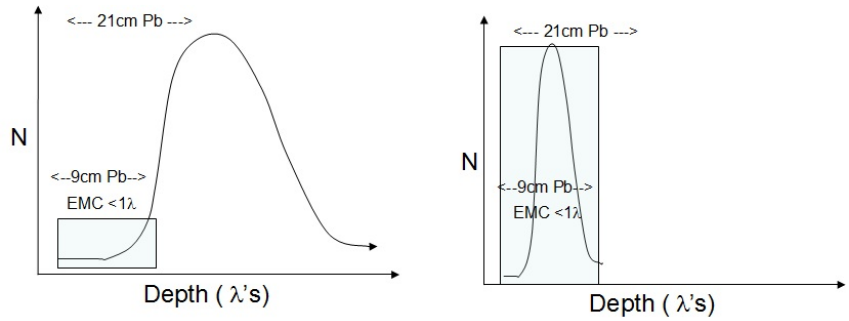

Figure 5.3: Cartoon of Longitudinal Development of a Hadronic Shower. The fraction of deposited energy can vary widely

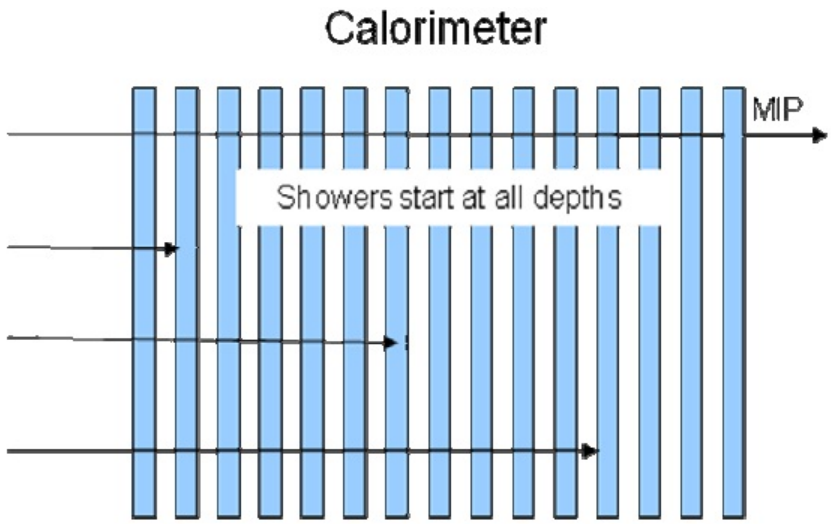

Figure 5.4: Showers can start anywhere

In the case of the lead scintillator (PbSc) calorimeter, a compromise is implemented whereby plastic scintillator is interleaved with sheets of lead. The amount of lead is equivalent to the PbGl, the finesse is to place enough scintillator into the mix to sample enough of the energy as to not adversely affect the resolution while at the same time keeping the longitudinal dimension of the calorimeter manageable.

An electromagnetic shower is basically an impinging electron, or pair of electrons from a converted impinging photon, "bremsstrahlung'ing" thousands of photons which then convert to $e^{\pm}$ pairs that either further bremsstrahlung or are absorbed in the lead or simply fluoresce in the scintillator. Of course, in the PbGl, the electrons also emit Cherenkov light while above the threshold.

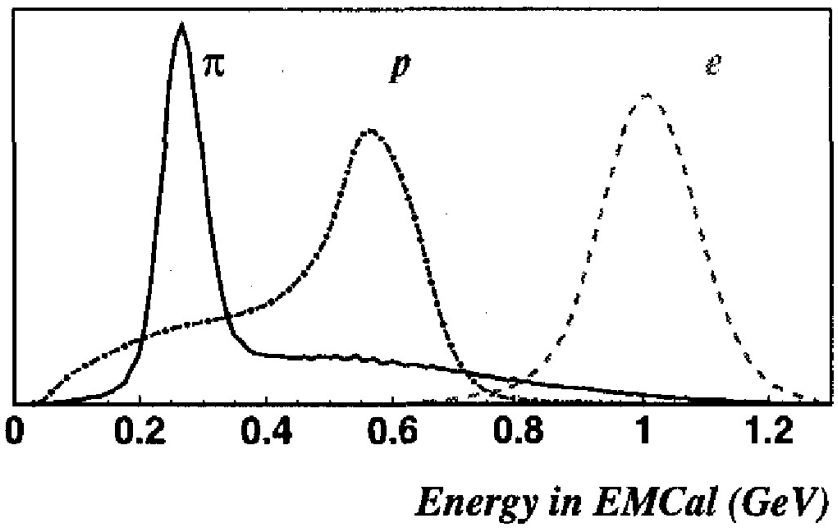

Figure 5.5: EMC response to 1 GeV/c ps $\pi's$ and electrons. Notice the profile of the π energy distribution

One important concept is that particle multiplication peaks, by design, at a longitudinal distance, weakly dependent on energy, about 1/3 the length of any electromagnetic calorimeter. This called the shower max, at this point $\approx 80\%$ of the shower energy has been deposited. Consequently the measured energy is not particulary sensitive to the position that the shower starts. This is a minor point for electromagnetic particles in an electromagnetic calorimeter but becomes important in our discussion of $\pi's$ in the calorimeter.

A purely hadronic shower depends on processes with a much smaller cross sections than of as electromagnetic shower. As such hadronic calorimeters are much larger that electromagnetic calorimeters, both longitudinally and radially. To get a sense of this we see that in Fig. 5.3 that, on average, the shower max of a purely hadronic shower occurs after passage though 21 cm of lead! The electromagnetic calorimeters of PHENIX represent 9cm of lead in total, seemingly not nearly enough to sample a sufficient amount of the $\pi's$ energy. Recall that we are studying E/p ≈ 1, so the particle in question needs to deposit all of its energy to approach this value

The interactions of a hadronic shower are also considerably more varied than in an electromagnetic shower, indeed there is such a widely varying electromagnetic component that there is a significant probability that all of a showering hadron's energy can be deposited in an EMC, as represented on the right side of Fig. 5.3. At any given interaction of a $\pi^{\pm}$ and a nucleon a π^0 can be produced which will then shower electromagnetically

Therefore, even though the longitudinal dimension of the EMC is considerably smaller than the average hadronic shower max, the widely varying electromagnetic character of the hadronic showers coupled with the short distance, that is logarithmically dependent on momentum, for the development of shower max, the distribution profile of the energy deposition scaled by momentum should be a constant.

This can be seen in Fig. 5.5 where we test beam data for 1 GeV momentum particle of three species. Even though this is an energy spectrum all of the particles are of the same momentum, which is conveniently 1 GeV. As expected, the electrons inhabit a gaussian about E/p = 1. The protons how a low energy tail and a peak at E/p $\approx$ 0.6, this is because the protons don't shower at such a low momentum, the massive protons give their energy as ionization, these are in the continuum as they are not behaving strictly as MIP's. Many of them make the transition to heavily ionizing particles, coming to a rest in the absorber where they give up all all of their remaining energy in a very short distance.

The most interesting curve in the plot is that of the $\pi's$. We see a clear MIP peak at $\frac{E}{p} = \frac{0.250Gev}{1GeV} = 0.250$, we then see a smooth continuum from the MIP peak to E/p $\approx$ 1.2. We have to demonstrate that the slope of the continuum is constant as a function of p_T. We will do this by demonstrating that we can accurately model the PHENIX detector with our simulation and that we can demonstrate an understanding of all background sources.

5.3 FastMC

As has already been demonstrated in sec. 3.3, PISA does not duplicate the PHENIX response at $n_1 \geq 5$. So we decided on alternative means to simulate the turn on curve for π's in the RICH. Since all other factors were in otherwise in hand it was decided to write a simple simulation of the RICH and the turn on of the n_1 variable, we will refer to it as the FastMC.

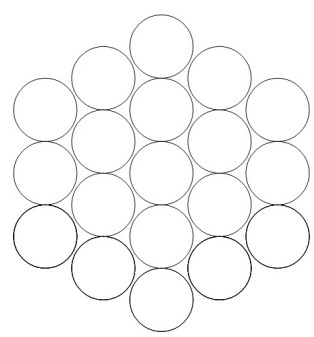

Figure 5.6: RICH focal plane in FastMC

The first part of the FastMC was to recreate the RICH focal plane that essentially consists of 50mm diameter rings grouped as seen in Fig. 5.6, this includes a dead area about the circumference corre-

sponding to a 2mm wall thickness. The next part is to propagate tracks to this array in a realistic manner. As in previous simulations a list of generated π's is created, this list contains only momentum from 0.2-20.0GeV. To quasi-simulate the variation of ϕ and η each generated π is given an impact point on the array of Fig. 5.6. This impact is randomly varied about the central circle, realistically a hexagonal shape would have proper but this added tremendous additional work for limited gain. Any effect from varying rapidities and track angle bend from the magnetic field will be absorbed in an added error factor later.

Since this FastMC is completely independent of PISA at this point the momentum resolution is infinitely precise. The smearing of the momentum is done adhering to the results of Sec. 4.3.1, and smearing is done in α, the angle between straight track and the particles actual track at the reference radius. The difference here is that there no inherent resolution to add to. One first determines $\alpha_{generated}$ from $p_{generated} = 92/alpha_{generated}$, this is then used as a mean of a gaussian distribution centered at $\alpha_{generated}$ with width

$$\sigma_{smear_dist} = \alpha_{generated} * \sqrt{(0.116 * p)^2 + 0.11^2}. \tag{5.3}$$

We now have an "$\alpha_{reconstructed}$" an α that would be produced by the real detector. We then use $\alpha_{reconstructed}$ to calculate $p_{reconstructed}$, this value is then saved to make any histograms later. When a measured value is plotted vs. p_T in data it is, of course, always reconstructed p_T. When calculating physical effects such as the Cherenkov angle, Mother Nature only cares about the "real" momentum, here $p_{generated}$.

Using $p_{generated}$, β_π is calculated and then the Cherenkov angle. To determine the number of Cherenkov γ's produced by any given π we generate a random number from a Poissonian with a mean given by a rearrangement of the Frank-Tamm formula Eq. 2.9,

$$\frac{dE}{dx} = \frac{q^2}{4\pi} \int_{v>c/n(\omega)} \mu(\omega)\omega \left(1 - \frac{c^2}{v^2 n^2(\omega)}\right) d\omega. \tag{5.4}$$

Which can be re arranged to the more practical form of the number of photons generated of a particular frequency range in a particular medium along a definite path length,

$$N_\gamma^{350-500nm} = 390 * sin^2\theta_C * n_{CO_2} * l. \tag{5.5}$$

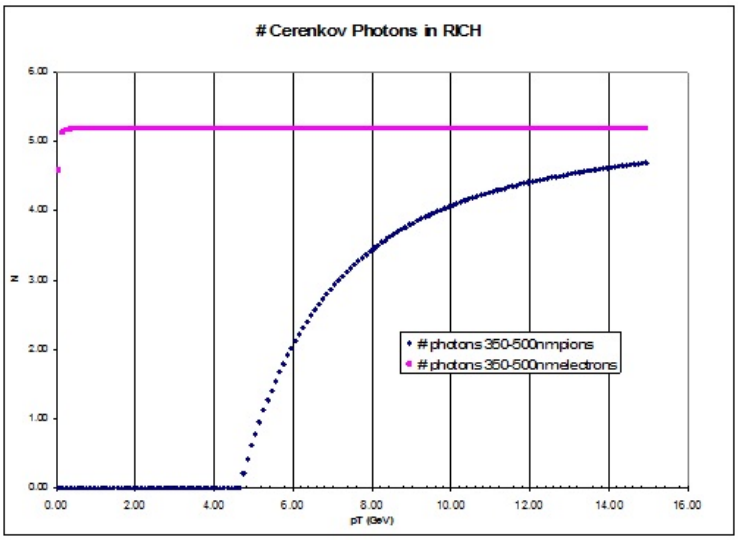

Figure 5.7: The number of Cherenkov γ's as a function of momentum for π's and $e^{\pm}$'s from Eq. 5.5 normalized to the mean value of n_1 for electrons.

So now we have an "impact point", an angle and a path length [18] over which the light propagates from the mirror to the focal plane. We can now calculate the radius of the ring formed by the emitted γ's with an added term for the imperfection of the mirrors. This is quoted as 2.5mm so a random number is generated from a gaussian distribution centered at 0.0 and a σ of 2.5mm.

The generated Cherenkov photons are then randomly distributed about the ring and propagated to the focal plane. A circular mask of radius 11cm is placed at the focal plane centered at the impact point just as in the real RICH, this is how the n_1 variable is determined. Any γ that impacts an active area of a phototube is added to a tally for that tube. The number of tubes that have at least one hit and are within the mask are counted, this is n_1.

All of these steps are repeated for a set of generated electrons as well. To overcome the intricacies of folding in the quantum efficiency of the phototubes as well as other factors a simple but well motivated normalization technique was used. First, the plateau, for electrons, of the Frank-Tamm plot, Fig 5.7 is normalized to one. The equation in code that determines the number of Cherenkov γ's as described above has an extra multiplicative factor applied to it. This factor was varied from 7 to 14 for a series of runs of the FastMC.

Since the Frank-Tamm plot plateaus at 0.250GeV and our lowest p_T bin is 0.200GeV an n_1 distribution covering all p_T's was made for each value of

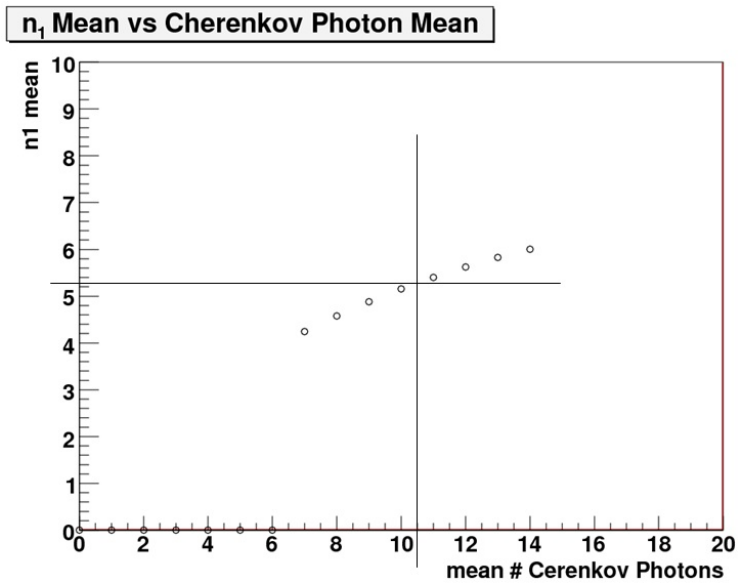

Figure 5.8: n_1 plotted as a function of mean number of Cerenkov $\gamma's$ generated.

Cherenkov mean. The mean of each distribution was determined and plotted as a function of Cherenkov mean, Fig. 5.8.

In data n_1 distributions were made for MB and ERT data in 0.20GeV p_T bins, the means of the distributions below the π threshold were examined and a value of 5.30 was chosen as the mean n_1 of electrons in data. A horizontal line is drawn through this value in Fig. 5.8, a vertical line is dropped from the point where the horizontal line crosses the plotted points. From this we chose the value of 10 for the mean number of Cherenkov photons generated by an electron in the RICH. This was then used the normalize the Frank-Tamm plot plateau to 10, scaling the π curve by the same amount.

We can see the results of this in Fig. 5.9 where the n_1 distributions of data and FastMC are plotted, each distribution is normalized to integrate to a value of 1.

5.4 Constructing an Overall Fit Function

We constructed a fit function with four elements; electrons, electrons from γ conversions, π's and electrons from so called Ke3 Kaon decays. The species were generated in simulation and functional form to fit the E/p profile was determined for each, these functions are combined and fit to the E/p profiles of

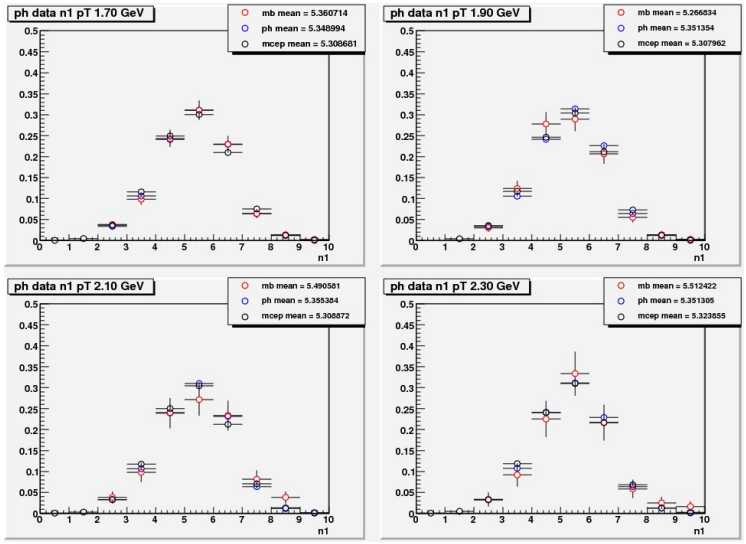

Figure 5.9: n_1 plots from data and FastMC, with Cherenkov mean set to 10 in FastMC.

data. In this fit the parameters from the individual element fits are held fixed, each element is weighted with a normalization constant as the free parameters. Following is a description of the determination of the function for each element.

5.4.1 Electrons

Just as was done in Sec. 4.3.1 an E/p profile is created for each of our standard 20 p_T bins from simulation. We had to take into account an effect of the recalibrators for energy and momentum in that a somewhat non-gaussian shape is created for the electron E/p distribution. Even though the momentum is smeared symmetrically, the momentum is in the denominator of E/p and this will have a "hyperbolic" effect on E/p. Because of this a fit function composed of two gaussians was used. Fig. 5.10 is an example of these fits, these are the last few bins and clearly show the non-gaussian tail caused by the finite momentum resolution. All 20 E/p profile fits can be seen in Appendix B.2

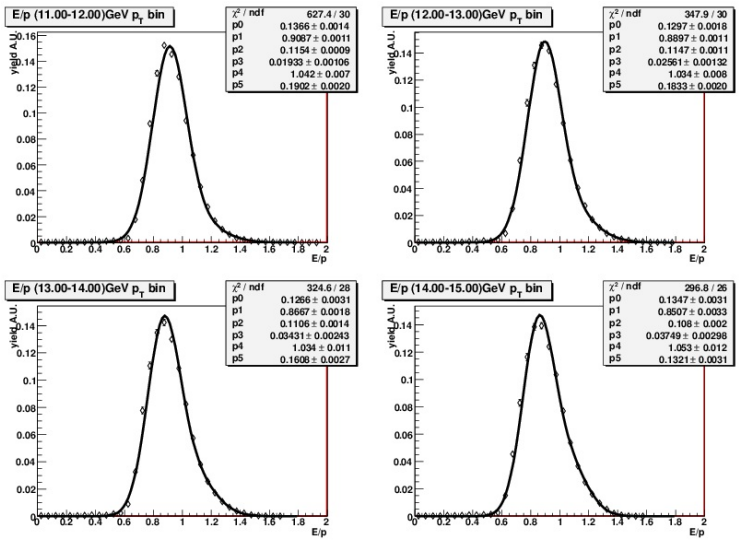

Figure 5.10: Two gaussian fit to simulated electrons, these last few bins clearly show the tail in E/p

5.4.2 γ Conversion Electrons

To simulate conversions one can certainly generate a sample of γ's and propagate them through PISA. However, since PHENIX is designed with the minimization of conversion material in mind, and of course, PISA reflects this, one would need to generate orders of magnitude larger amounts of γ's as the other species. The cost in cpu time becomes prohibitive so we developed an alternative technique. A sample of electrons was generated as in the past, this time with an added dimension, radial distance from the beam axis. A random number is generated with a flat probability distribution from 0-200cm (the face of the DCH) this is combined with the generated z coordinate as well as polar and azimuthal angles to generate a "conversion" vertex for the electron. The momentum vector is the same as if the electron had originated along the z axis.

There are then three material regions that the conversion vertex may be, the vacuum of the beam pipe, the beam pipe itself or the air between the beam pipe and the face of the DCH. For each of these regions a conversion weight is calculated based ont he radiation length of the material in question taken from the PDG booklet.[28]

material	X_0 radiation length	ρ density	λ attenuation length
vacuum	∞	0	∞
Be	36.62 $\frac{gm}{cm^2}$	1.2×10^{-5} $\frac{g}{cm^3}$	3.05×10^6 cm
air	65.16 $\frac{gm}{cm^2}$	1.85 $\frac{g}{cm^3}$	35.22 cm

Table 5.1: Conversion Material Parameters

Where,

$$\lambda = \frac{X_0}{\rho},$$

is the attenuation length.

The fraction of γ's converting after traversing a distance x of any material is

$$\text{fraction converting} = \frac{7}{9}\frac{x}{\lambda}.$$

We divide the path within a material into steps, 0.1mm steps in the Be beam pipe and 1mm steps in the air. We can then borrow the compound interest formula of economics to calculate the number of conversions

$$\text{fraction converting} = (1 - \frac{7}{9}\frac{step_size}{\lambda})^{\#\text{ steps}}.$$

This formula is then used to weight the electrons according to where they convert. Four typical E/p profiles are plotted in Fig 5.11, in this case the fit function is six gaussians. Since we extract no information using this fit other than the shape of the profile the six gaussian function presents no issues. All of the E/p profiles can be seen in Appendix B.3.

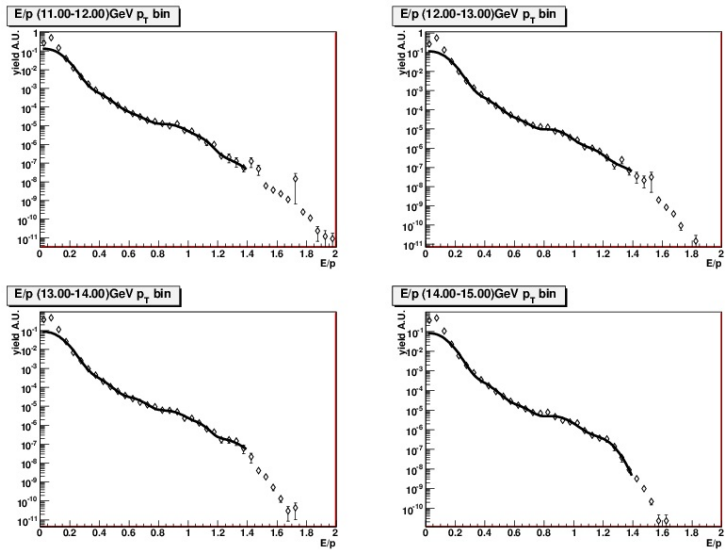

Figure 5.11: Six gaussian fit to simulated γ conversions.

5.4.3 π's

A sample of $\pi^{\pm}$ was generated for PISA with $0 < p_T <= 20$ flat in p_T, $0 < \phi <= 2\pi$, $|\eta| < 0.50$ and $|z| < 30cm$. To create a "real world" sample of π's to work with, the Hagedorn function used to fit published π data was used as a weighting function when filling all histograms.

Once again an E/p profile is created for each p_T bin as seen in Figure 5.12. In this case a simple Gaussian fit to a peak was not possible. The fit function used is created of four Gaussians, one floats but is constrained to a window about the MIP peak. The other three have their μ's set at three points along E/p, 0.2, 0.5 and 0.90, these are also allowed to vary $\pm 25\%$. A set of these fits can be seen in Figure 5.12, once again all of the fit parameters are saved for the final fit to data.

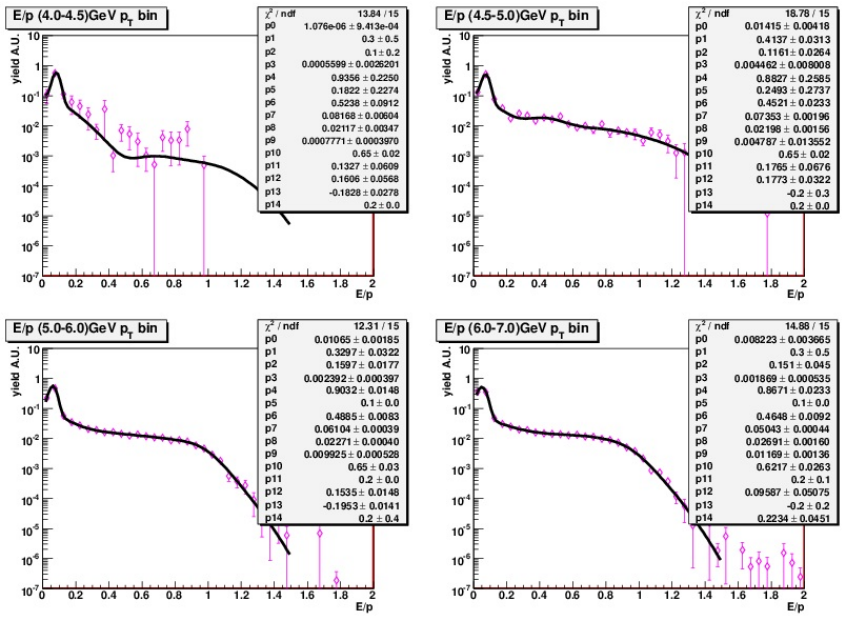

Figure 5.12: Fit to π E/p profiles

As with the conversions, since we extract no information using this fit other than the shape of the profile the six gaussian function presents no issues. All of the E/p profiles can be seen in Appendix B.4.

5.4.4 Ke3

$K^{\pm}$ and K_L^0 can decay in the region between the interaction point and the face of the drift chamber. The decays that can contaminate out measurement are called Ke3;

$$K^+ \rightarrow \pi^0 e^+ \nu$$

$$K^- \rightarrow \pi^0 e^- \bar{\nu}$$

$$K_L^0 \rightarrow \pi^{\pm} e^{\mp} \nu$$

The resulting decay electrons can pass all eID cuts with the notable exception in their behavior that the E/p will not be centered at one. The reconstructed p_T will be higher by a factor proportional to the fraction of the distance covered by the kaon before decaying. The reconstruction algorithm of the Drift Chamber assumes a $B \cdot dl$ starting at the interaction point, the tracks originating closer to the drift chamber will have a smaller sagitta and

hence be reconstructed momentum higher than the actual momentum.

These electrons will still deposit all of their energy into the Electromagnetic Calorimeter (EMC). E/p plots are made as a function of reconstructed p_T, so regardless of the parent momentum, any particular E/p distribution will have a sample of electrons of the same (mis)-reconstructed p_T with a range of E. As we go above the highest real p_T the spread in E (and E/p) narrows since now we will be looking at a sample of Ke3 electrons with only a small spread of actual p_T.

A Ke3 monte carlo was run to investigate the contribution of Ke3 to the background in the region of interest. The three kaon species were generated in equal proportion, $0 < \phi <= 2\pi$, $|\eta| < 0.5$, $|z| < 30cm$, the momentum given by an m_T scaled Hagedorn function and decay lengths dictated by the $c\tau$ of the particular Kaon. The decay products were than originated from these decay points and given a momentum vector dictated by the parent momentum vector, momentum sharing and boost.

This information is then propagated through PISA to produce simulated Data Storage Tapes (simDSTs), which can be treated as any data file. For each of our standard p_T bins an E/p profile is plotted, this is seen in Figure 5.13. All profiles are in Appendix B.5.

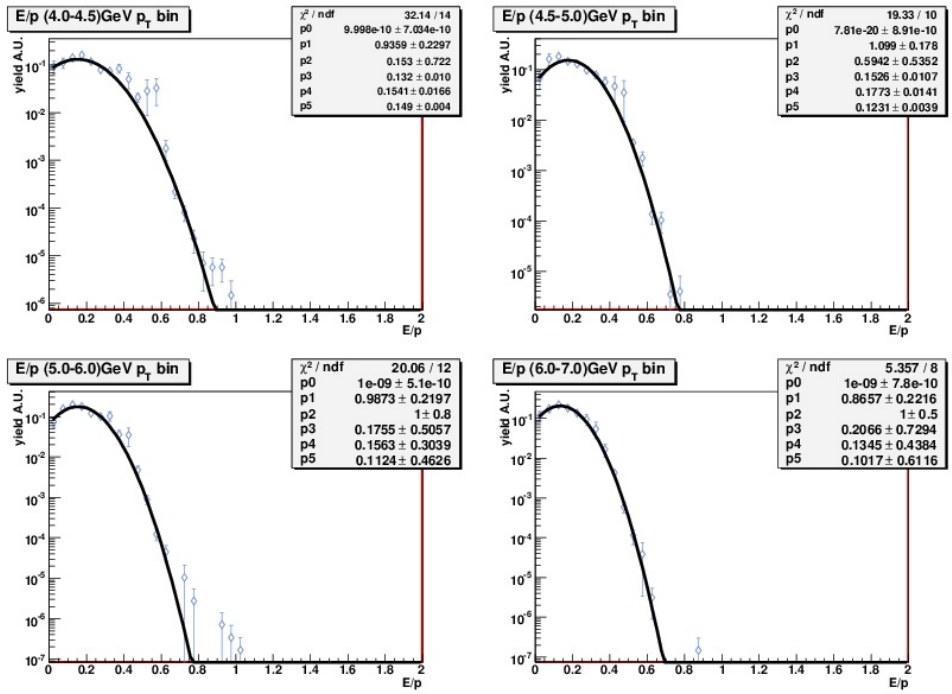

Figure 5.13: Ke3 E/p profiles

The figure demonstrates that as we cross the pion threshold the Ke3 contribution to the background is insignificant. In each of the profiles, just as with the electron profiles, a two gaussian fit is made, and, once again, the set of parameters for each bin is saved to be used in the overall fit function to the data.

5.4.5 Final Fit to Data

The final function is a sum of the three elements, the parameters determined in the previous fits are retained. The normalization constant of each fit is allowed to float however so that the final fit is essentially a weighted sum of the elements. The fit will test whether or not the function is constructed of the proper elements.

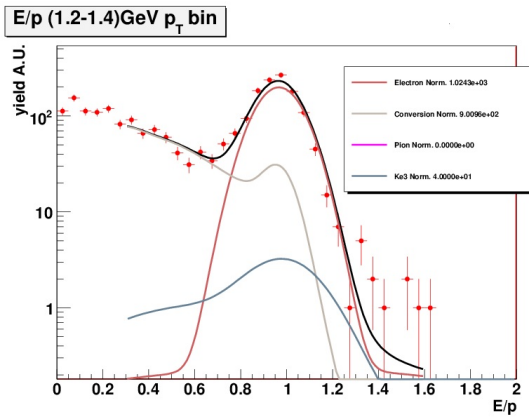
E/p (1.2-1.4)GeV p_T bin
yield A.U.
E/p
Electron Norm. 1.0243e+03
Conversion Norm. 9.0096e+02
Pion Norm. 0.0000e+00
Ke3 Norm. 4.0000e+01

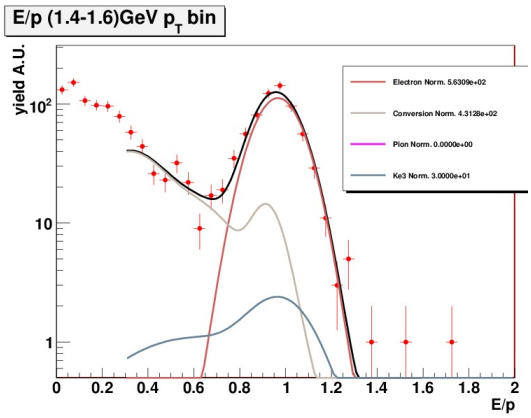
E/p (1.4-1.6)GeV p_T bin
yield A.U.
E/p
Electron Norm. 5.6309e+02
Conversion Norm. 4.3128e+02
Pion Norm. 0.0000e+00
Ke3 Norm. 3.0000e+01

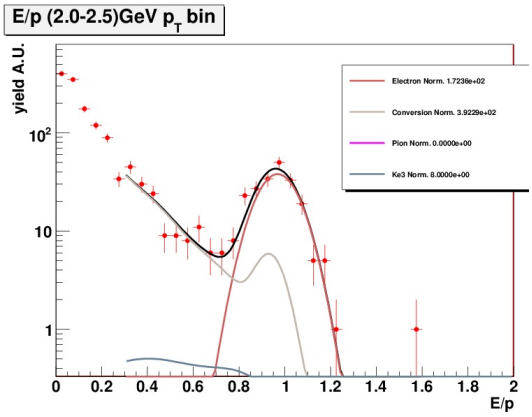
E/p (2.0-2.5)GeV p_T bin
yield A.U.
E/p
Electron Norm. 1.7236e+02
Conversion Norm. 3.9229e+02
Pion Norm. 0.0000e+00
Ke3 Norm. 8.0000e+00

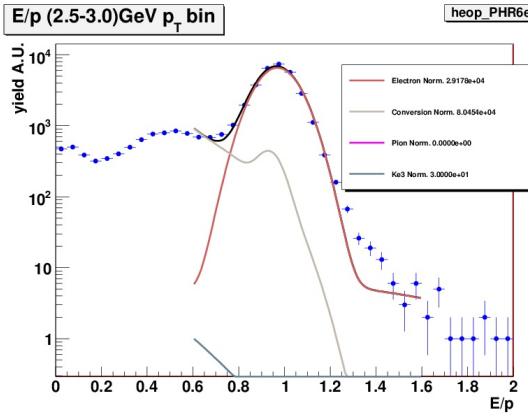
E/p (2.5-3.0)GeV p_T bin
heop_PHR6
yield A.U.
E/p
Electron Norm. 2.9179e+04
Conversion Norm. 8.0454e+04
Pion Norm. 0.0000e+00
Ke3 Norm. 3.0000e+01

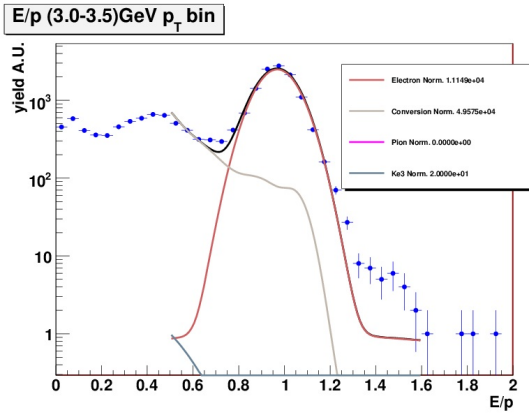
E/p (3.0-3.5)GeV p_T bin
yield A.U.
E/p
Electron Norm. 1.1149e+04
Conversion Norm. 4.9575e+04
Pion Norm. 0.0000e+00
Ke3 Norm. 2.0000e+01

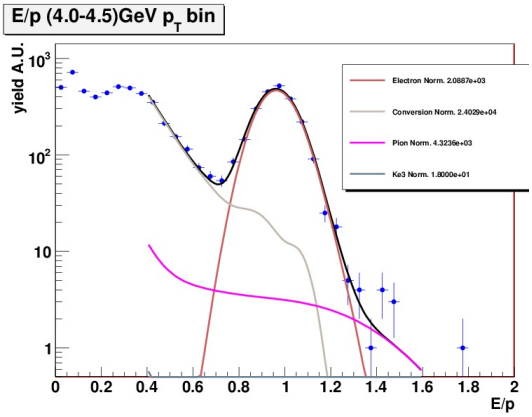
E/p (4.0-4.5)GeV p_T bin
yield A.U.
E/p
Electron Norm. 2.0887e+03
Conversion Norm. 2.4029e+04
Pion Norm. 4.3236e+03
Ke3 Norm. 1.8000e+01

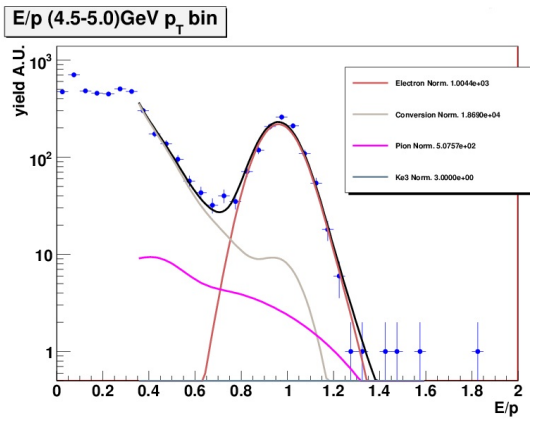
E/p (4.5-5.0)GeV p_T bin
yield A.U.
E/p
Electron Norm. 1.0044e+03
Conversion Norm. 1.8690e+04
Pion Norm. 5.0757e+02
Ke3 Norm. 3.0000e+00

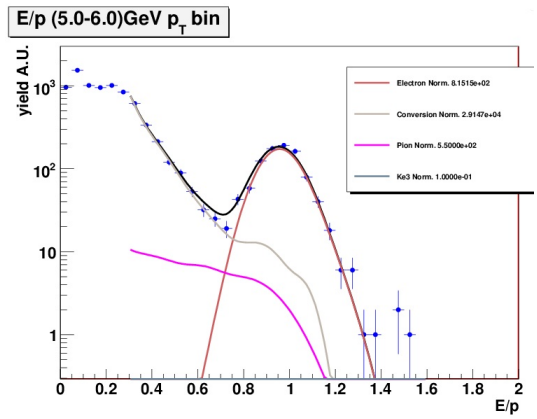
E/p (5.0-6.0)GeV p_T bin
yield A.U.
E/p
Electron Norm. 8.1515e+02
Conversion Norm. 2.9147e+04
Pion Norm. 5.5000e+02
Ke3 Norm. 1.0000e-01

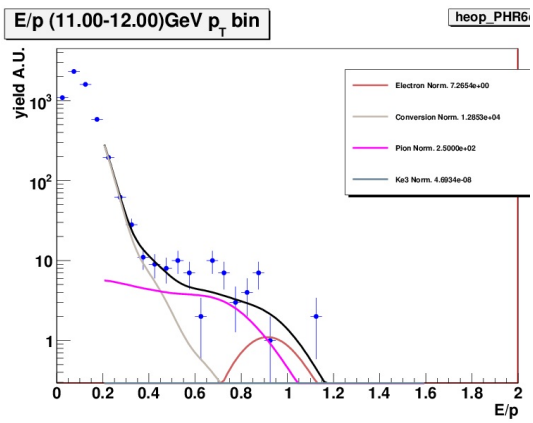
E/p (11.00-12.00)GeV p_T bin
heop_PHR6
yield A.U.
E/p
Electron Norm. 7.2654e+00
Conversion Norm. 1.2853e+04
Pion Norm. 2.5000e+02
Ke3 Norm. 4.6934e-08

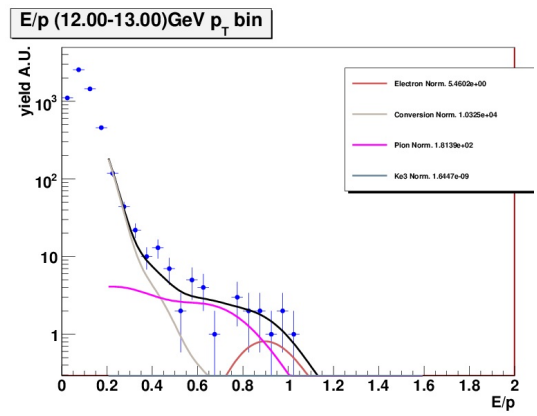
E/p (12.00-13.00)GeV p_T bin
yield A.U.
E/p
Electron Norm. 5.4602e+00
Conversion Norm. 1.0325e+04
Pion Norm. 1.8139e+02
Ke3 Norm. 1.6447e-09

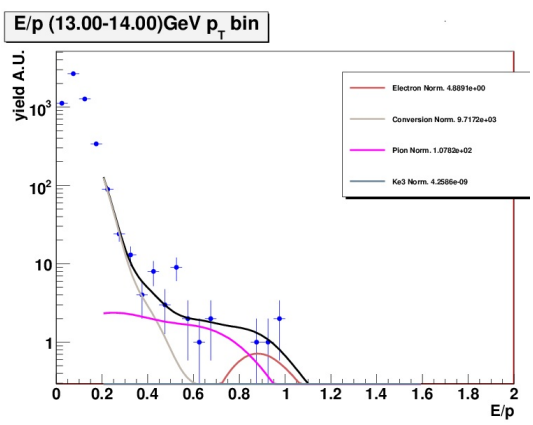
E/p (13.00-14.00)GeV p_T bin
yield A.U.
E/p
Electron Norm. 4.8891e+00
Conversion Norm. 9.7172e+03
Pion Norm. 1.0782e+02
Ke3 Norm. 4.2586e-09

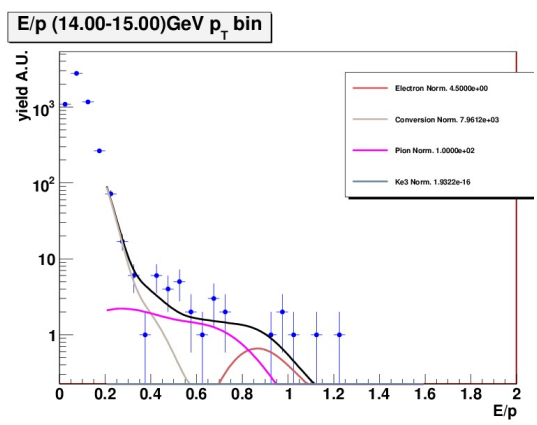
E/p (14.00-15.00)GeV p_T bin
yield A.U.
E/p
Electron Norm. 4.5000e+00
Conversion Norm. 7.9612e+03
Pion Norm. 1.0000e+02
Ke3 Norm. 1.9322e-16

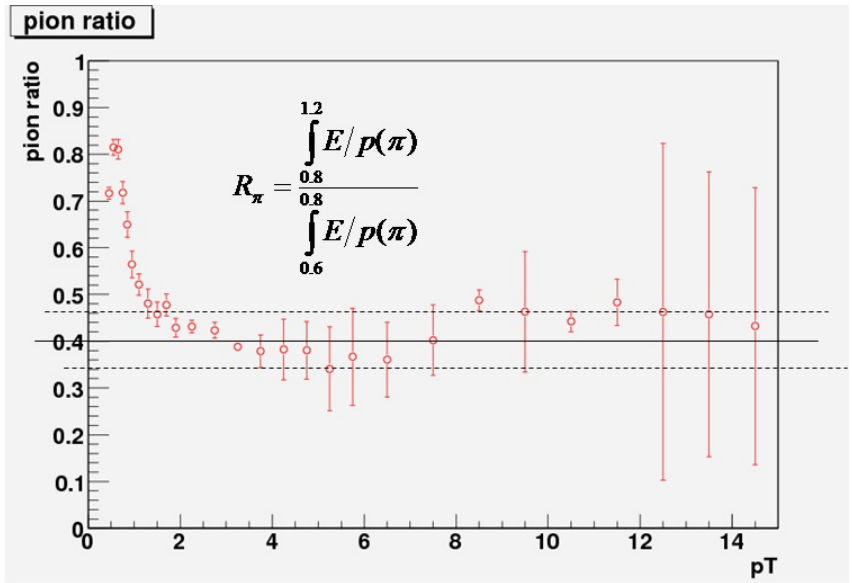

Figure 5.14: R_π determined from simulation with no eID cuts

All of the p_T bin plots can be seen in appendix B.6

5.5 Yield Fraction

Once it was established that a good understanding of the backgrounds was in hand a determination of R_π was made using E/p profiles from PISA, Fig. 5.14, the value of 0.4 was chosen. The background subtraction was to be implemented as a fractional yield of electrons in the E/p window of 0.8-1.2. The yield fraction was calculated for each p_T bin and applied to the inclusive invariant spectrum.

The yield fraction is defined as,

$$Y_f = \frac{\int_{0.8}^{1.2} \left[\frac{E}{p}\right]_{all} - R_\pi \int_{0.6}^{0.8} \left[\frac{E}{p}\right]_{all}}{\int_{0.8}^{1.2} \left[\frac{E}{p}\right]_{all}}. \tag{5.6}$$

Which is simply,

$$Y_f = \frac{N_e}{N_e + N_\pi} \tag{5.7a}$$

$$= \frac{N_e / N_e}{N_e / N_e + N_\pi / N_e}. \tag{5.7b}$$

We focus on the second term in the denominator of Eq. 5.7b,

$$\frac{N_\pi}{N_e} = \frac{\pi}{e} \frac{\int_{0.8}^{1.2} \left[\frac{E}{p}\right]_\pi}{\int_{0.0}^{2.0} \left[\frac{E}{p}\right]_\pi} \frac{f_\pi(n_1 \geq 5)}{f_e(n_1 \geq 5)}. \tag{5.8}$$

There are three terms in Eq. 5.8, the first is π/e, the ratio of π's to $e_\pm$ as presented to us by mother nature. This determined by fitting the most recent π data from PHENIX [30] with a Hagedorn function as in section 6.1.1. For electrons a FONLL function from PHENIX single electron paper [24] was fit with a free normalization constant, Fig 5.15. This is now only for the electrons from heavy flavor. However we can reverse engineer an inclusive function by using the ratio of non heavy flavor to heavy flavor electrons from Run 5[24]. First we recognize that the inclusive spectrum can be written as;

$$\frac{d^3\sigma}{dp^3}_{inclusive} = \frac{d^3\sigma}{dp^3}_{HF} * \frac{HF}{nonHF} + \frac{d^3\sigma}{dp^3}_{HF}, \tag{5.9a}$$

rearranging (5.9b)

$$= \frac{d^3\sigma}{dp^3}_{HF} * (1 + \frac{HF}{nonHF}). \tag{5.9c}$$

In Fig. 5.16 is a fit to the ratio $\frac{nonHF}{HF}$. This fit is inverted and, along with the fit of Fig 5.15, is plugged into Eq. 5.9 to get a final inclusive invariant cross section function, Fig.5.17 The two functions are then divided, in Fig 5.18 this is plotted as points in the 0.1GeV bins in which all initial p_T spectra are filled.

The second term of Eq. 5.8 is the fraction of π's in the window $0.8 \leq E/p < 1.2$, which is taken from simulation.

The third term of Eq. 5.8 is the fraction of electrons passing the n_1 cut

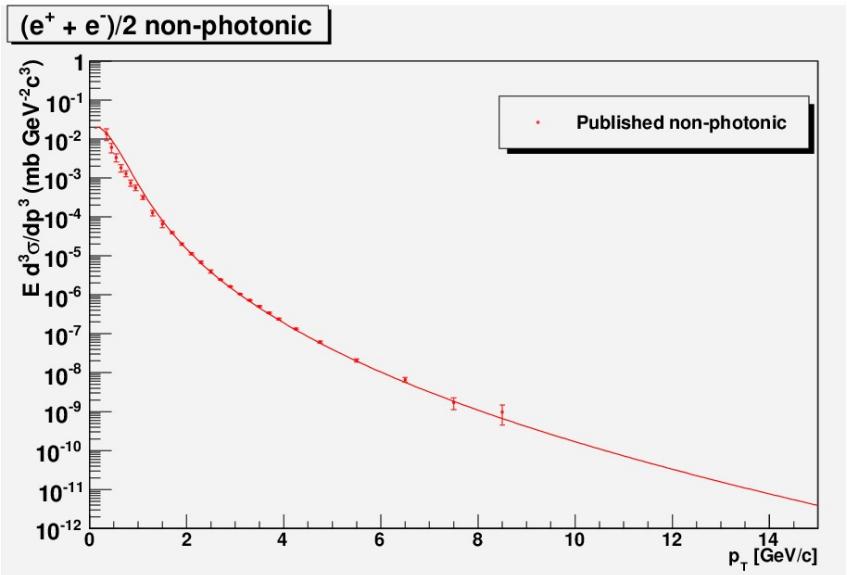

Figure 5.15: Fits $e^{+/-}$ published data.

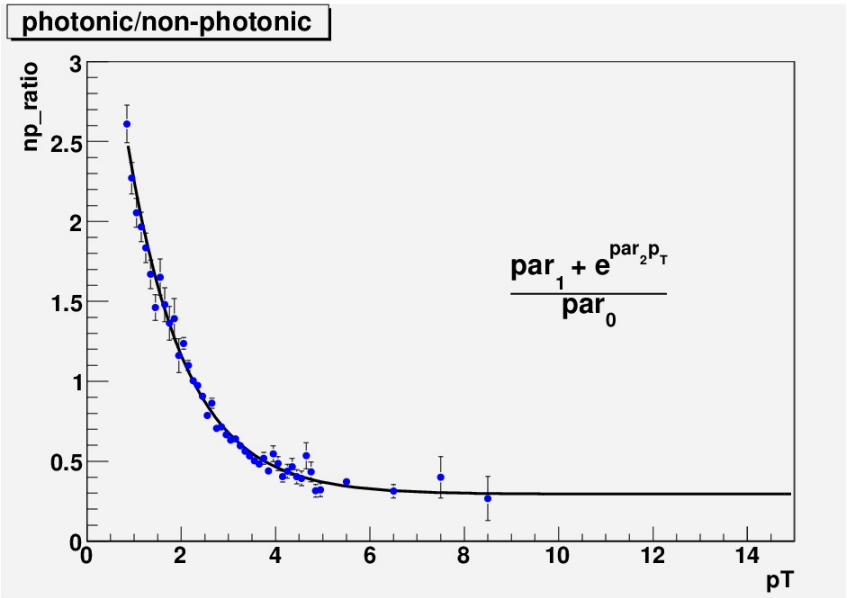

Figure 5.16: Fits published non heavy flavor to heavy flavor ratio.

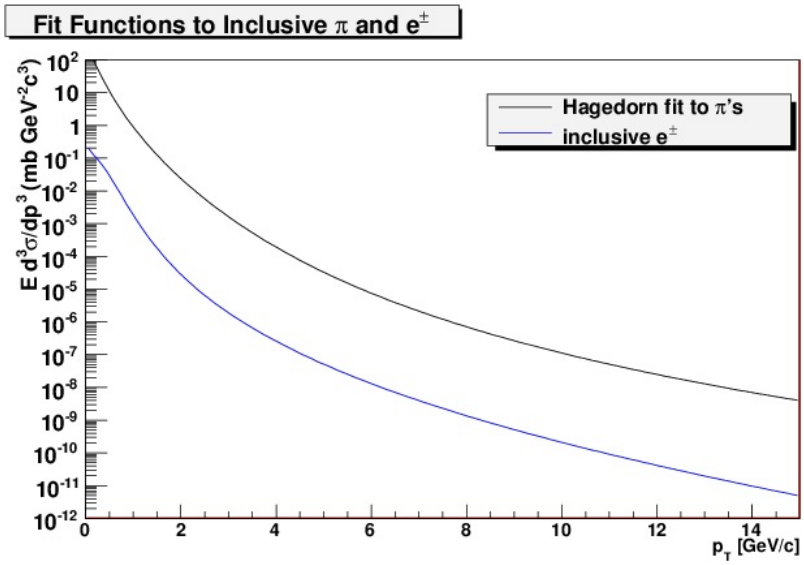

Figure 5.17: Fit functions for π's and inclusive $e^{\pm}$'s.

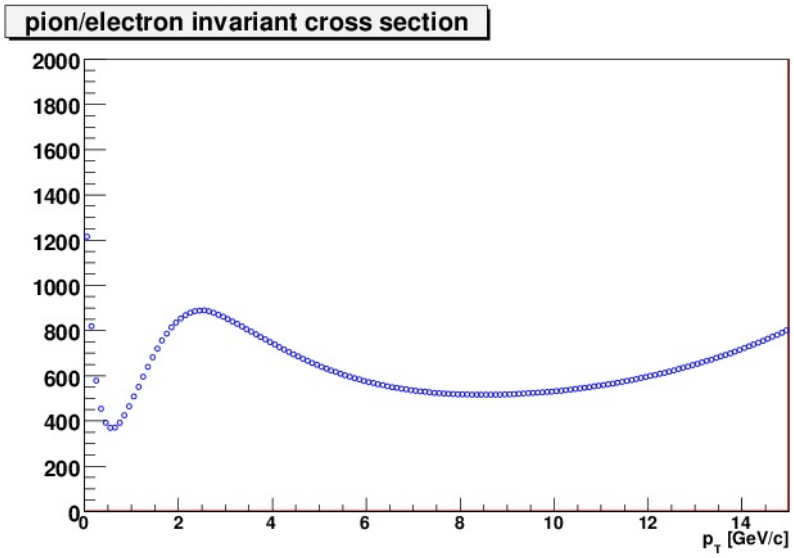

Figure 5.18: Division of fits, plotted in 0.01 GeV bins.

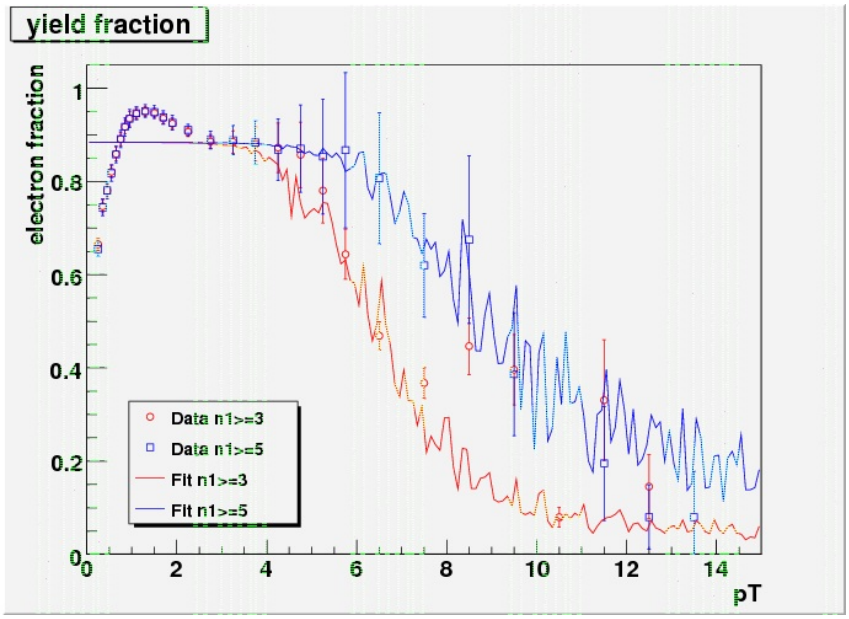

Figure 5.19: Final calculation of the yield fraction in simulation compared to data.

divided by the fraction of π's passing the same cut.

Once all of the factors were identified, the FastMC, along with the proper calibration of E and p, were used to produce the yield fraction plot again, Fig. 5.19, where we see a much better description of the data by the simulation. To use the FastMC output in PISA two sets of "turn on" factors for $n_1 = 3$ and 5. Each set of 200 values corresponded to 200 p_T bins of 0.10GeV width as this is the standard bin width of raw histograms used in this analysis. Each value is the fraction of π's that pass the $n_1 \geq 3(5)$ cut. These sets were used as a weight factor when filling histograms in PISA instead of the PISA RICH response.

5.6 Determination of R_π Using Reverse prob Cut

After having addressed the issues with PISA, a study of R_π was done in PISA and Run 5 CuCu 200GeV, using a reverse prob cut similar to other PHENIX work [31]. The CuCu was chosen because of expected higher pion production than in pp.

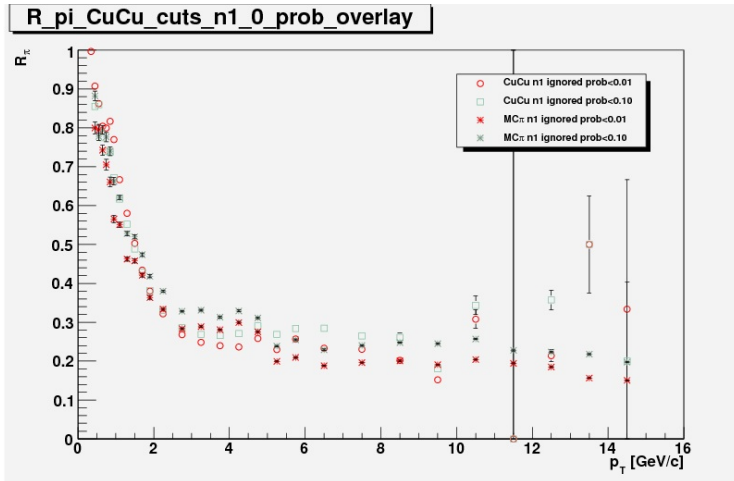

Figure 5.20: R_π from simulation and CuCu data calculated with RICH ignored and various prob cuts

An enhanced sample of pions was created by using two reverse prob cuts of $prob < 0.10$ and $prob < 0.01$ while ignoring the RICH. These cuts will exclude showers of a completely electromagnetic nature but should still retain π's that start showering hadronically but have one or more π^0's created in the shower. Such a hadronic shower will have the larger radius that will pass the prob cut but still deposit a larger fraction of the π's energy than a purely hadronic shower.

The quality cut (cf Sec. 3.3) was retained as it's best to work with high quality tracks. The track matching cut to the EMC was reduced to $\leq 1.5\sigma$ a further matching cut for the PC3 (directly in front of the EMC), constructed exactly as that of the EMC, was added and set to $\leq 1.5\sigma$. The purpose of these cuts was to eliminate electrons from $\pi^\pm$ decays. In the beginning of the study an attempt was made to create a sample of π's in data using a reverse n_1 cut and no prob cut, this was not successful but the tight matching were never removed.

One can see in Fig. 5.20 that R_π remains fairly constant over the p_T range $3 < p_T < 9$GeV in data and $3 < p_T < 15$GeV in MC and that MC and data track each other quite nicely. Even at low p_T where one assumes that the rise in R_π is due to ionization loss for π's rising rapidly.

The R_π that one extracts from this plot is somewhat lower than in Fig. 5.14 due to the reverse prob cut. Prob is a measure of the electromagnetic character of a shower. A reverse prob cut eliminates the electrons but it also tends

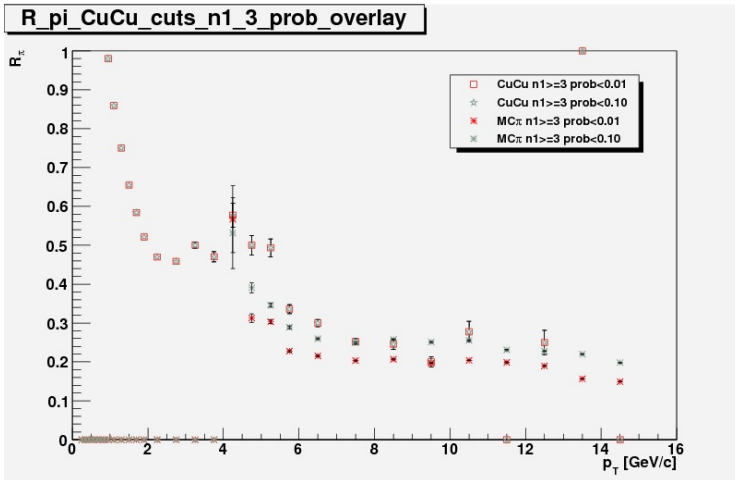

Figure 5.21: R_π from simulation and CuCu data calculated with RICH $n_1 \geq 3$ and various prob cuts

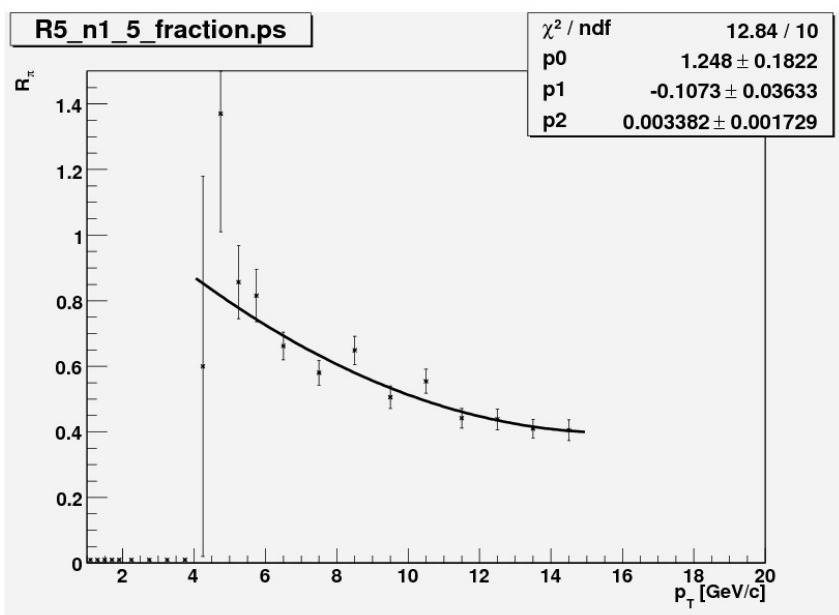

Figure 5.22: R_π from simulation with all eID cuts with a third degree polynomial fit

to eliminate the pions that shower completely electromagnetically and, coincidentally, populate the hi window preferentially, hence the lower R_π value in this plot.

Of equal importance is the observation that even when one cuts down on the number of π's showering electromagnetically, the remaining hadron energy loss mechanisms in the EMC are still variable enough, and that variability is still insensitive enough to p_T, to keep R_π constant.

An $n_1 \geq 3$ was added and the results are plotted in Fig. 5.21. The MC points are at zero until the RICH starts firing but the data still show counts. These are most likely not π's and not statistically significant compared to π's as they are not enough to cause the data and MC to diverge at low p_T on Fig. 5.20.

Once the Cherenkov threshold begins to be crossed we see a jump in R_π that then begins to decay. These π's have a reconstructed p_T that is LOWER than their real p_T, usually these are balanced by the π's of the opposite sense but they are being excluded for the moment as the the threshold is crossed. This happens because of the finite momentum resolution of the real DCH. The feature of note here is that the simulated DCH is behaving exactly the same way, demonstrating that our momentum recalibrator and the FastMC results are working.

Now that all of the pieces are finally assembled and tested, a final run of π's through PISA was made to determine R_π. In this case all of the eID cuts that are used in the analysis are used to "select" π's. The plot of the final R_π can be seen in Fig. 5.22, with a third degree polynomial fit. It is this fit that will be used to subtract he π contamination for the final spectrum.

5.7 Comparison Subtraction Techniques

We have now developed three methods to subtract the hadronic background of our measurement of electrons. In the yield fraction technique we calculated the fraction of electrons in the $0.8 \leq E/p < 1.2$ window. The overall fit function was successfully constructed of the elements that would comprise our raw measured signal, we used the fit to π's to subtract them from the raw yield. Then, finally, the ratio method using R_π which was finally chosen as the preferred subtraction technique.

Throughout the process, refinements were made to PISA such as the mo-

mentum recalibrator, the turn on behavior of π's in the RICH and weighting functions for the various species derived from up to date data, most particularly from PHENIX if possible.

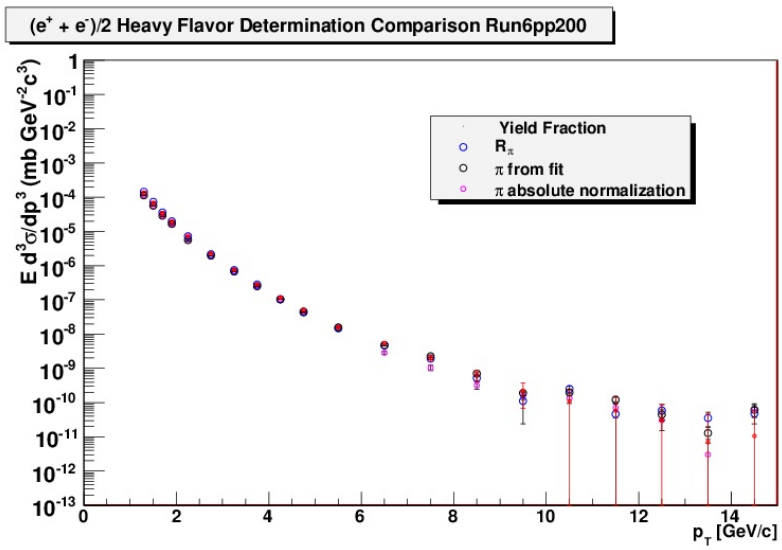

Figure 5.23: Four different methods of determining the heavy flavor cross section

Also included in the plot is a set of points labeled "π absolute normalization". In this curve the background π's were created in in simulation with a weighting function, the modified Hagedorn Eq. 6.1. This function is fit to π data in a range that encompasses the range of our measurement, Fig. 6.1, Sec. 6.1.1, so it is quite reliable. (In fact, all π simulations use this weighting function.) After being run through PISA the generated π's are treated just as any data instead of the floating normalization as in the background function creation. The resulting invariant cross section of simulated π's was then subtracted from the inclusive invariant cross section measurement as well as the cocktail to arrive at the curve in the plot.

We know from Fig. 5.18 that the ratio of pions to electrons in pp collisions at 200 GeV is $\approx 800 - 1000$ at high p_T. We calculated in simulation that the number of pions will be reduced by our eID cuts by a factor 0f 10^3. The black line in Fig. 5.24 was created by multiplying the curve of Fig 5.18 by the fraction of π's passing all eID cuts calculated in simulation.

We compare this to data in Fig. 5.24 in which the ratio of the π yield to electron yield for each of the four techniques is plotted. The curves start

from zero at the π threshold and plateau at high p_T. This is as expected as the number of Cherenkov γ's from π's also plateaus and the ratio of the invariant cross sections of π's to electrons, Fig. 5.18, is reasonably flat in this region. The plateau is at ≈ 1 and since this plot is the inverse of the signal to background ratio, this is also ≈ 1. This means that any systematic error on the background estimation is translated directly to the final result. Put another way, the larger is π/e the greater is the effect of any error in the determination of the background.

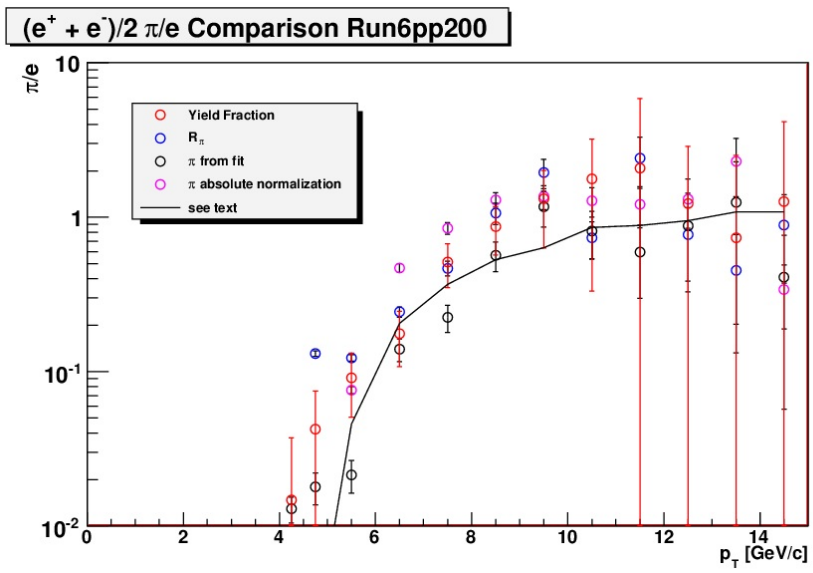

Figure 5.24: π/e ratio of the four different methods of determining the heavy flavor cross section

The final decision was to use the R_π subtraction technique as originally planned. It has the subjective advantage of being more intuitive. On the more objective level, using R_π avoids the subtlety of the proper time to apply the subtraction as it is a ratio. Also, the larger errors that would be the price of using a simple subtraction are "pushed" into the uncertainty of of the determination of R_π itself.

5.8 Systematic Error of R_π

To make a systematic error determination for R_π we plot $\frac{R_\pi^{data}}{R_\pi^{MC}}$ with the conditions that n_1 is ignored and the two reverse prob cuts, $prob < 0.10$ &

$prob < 0.01$. This is plotted in Fig. 5.25.

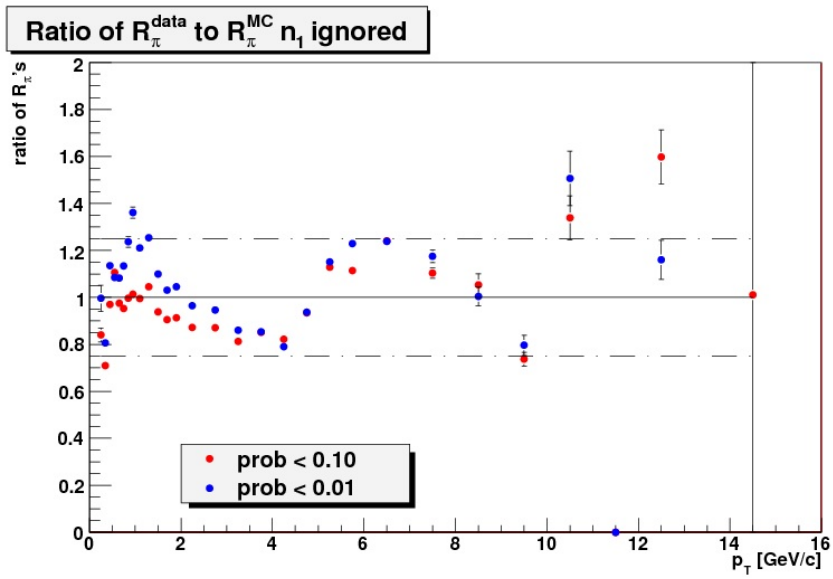

Figure 5.25: Ratio of R_π's, the solid line is at 1 and the dashed lines are at $\pm 25\%$

We will make the conservative estimate that since most all points up to 10 GeV fit within a band from 0.75-1.00 that the systematic error on R_π is 25%.

Chapter 6

Final Spectrum

6.1 Cocktail Calculation

The PHENIX detector is very good at identifying and measuring the properties of electrons such as energy and momentum. What PHENIX does not do well is identifying the sources of the electrons. The EXODUS[32, 33] event generator and decay machine was developed to subtract off the electrons from non heavy flavor decays from an inclusive spectrum of all electrons. The sum of all the undesired electrons is called, by PHENIX, the cocktail. The electron sources in the cocktail are of two types, photonic and non-photonic.

We will describe the inclusion of the following photonic sources;

- Dalitz decays of light neutral mesons: $\pi^0, \eta, \omega, \eta^{'}, \phi$.
- Conversions of γ's from decays of these mesons.
- Conversion of direct γ's, e.g. from quark-gluon Compton scattering.

The non-photonic sources are;

- Di-electron decays of light vector mesons: ρ, ω, ϕ.
- Di-electron decays of the vector mesons J/Ψ and Υ.
- Weak kaon decays, known as K_{e3} decays.
- Virtual direct γ's from the initial hard scattering processes.

decay	branching ratio
$\pi^0 \to \gamma e^+ e^-$	$1.198x10^{-2}$
$\eta \to \gamma e^+ e^-$	$0.5x10_{-2}$
$\eta^{'} \to \gamma e^+ e^-$	$5.6x10_{-4}$
$\rho \to e^+ e^-$	$4.44x10^{-5}$
$\omega \to e^+ e^-$	$7.15x10^{-5}$
$\omega \to \pi^0 e^+ e^-$	$5.9x10^{-4}$
$\phi \to e^+ e^-$	$3.09x10^{-4}$
$\phi \to \eta e^+ e^-$	$1.3x10^{-4}$
$J/\Psi \to e^+ e^-$	$5.94x10^{-2}$
$\Upsilon \to e^+ e^-$	$2.38x10^{-2}$
$K^{\pm} \to \pi^0 e^{\mp} \nu_e$	$5.08x10^{-2}$
$K^0_L \to \pi^{\pm} e^{\mp} \nu_e$	$40.55x10^{-2}$

Table 6.1: Decays channels in EXODUS

Particle properties, e.g. masses and branching ratios come from the PDG Handbook [28].

Each of the parent particles in Tab. 6.1 has a p_T distribution from which they are generated. These parent distributions are set by the user, the parameterizations will be detailed in Sec. 6.1.1. The normalization of particle yields is tied to the π^0 and is given by dN_{π^0}/dy a user input. The relative normalization of the other mesons the ratio $(dN_{meson}/dy)/(dN_{\pi^0}/dy)$ is required to be input by the user. The decay machine in EXODUS has generic algorithms for two- and three-body decays as well as Dalitz decays. The decay machine fills p_T spectra of the decay products. The Dalitz decay algorithm uses the electron pair mass distributions in [34], it also includes electromagnetic form factors from [35] and it takes into account the electrons are not emitted isotropically from the γ in its rest frame but follows a $(1 + \cos^2\theta)$ distribution.

The electron cocktail for pp collisions at $\sqrt{s} = 200$ GeV in this analysis is an update of the corresponding cocktails generated for Run-5 [24]. Here we will focus on documenting the updated cocktail input, the resulting cocktail, and the corresponding systematic error. We assume that all mesons have a constant rapidity density in one unit of rapidity centered about zero and a homogeneous distribution in azimuthal angle. Transverse momentum distributions are based on measurements in PHENIX where possible.

6.1.1 Cocktail Input

π's

The most important cocktail input is the invariant differential cross section of $\pi's$. This is obtained by a simultaneous fit to the charged pion spectra from [30] and the neutral pion spectrum from [36] with a modified Hagedorn parametrization;

$$E\frac{d^3\sigma}{dp^3} = A\left(\frac{e^{-(ap_T+bp_T^2)}p_T}{p_0}\right)^{-1}. \tag{6.1}$$

We can see this fit in Fig. 6.1 with the fit parameters. The χ^2/ndf of 0.519 indicates a good fit. Further evidence of this is seen in Fig. 6.2 where the data points are divided by the fit. This ratio was itself fit with a zeroth order polynomial with a result of one. The results of the Hagedorn fit are compiled in Table 6.1.1, we can then calculate the rapidity density, dN/dy, using the Hagedorn function. Since the Hagedorn is fit to an invariant cross section the result is an invariant cross section which can be written as,

$$E\frac{d^3\sigma}{dp^3} = \frac{1}{\pi}\frac{1}{2}\frac{1}{p_T}\sigma_{inel}\frac{dN}{dydp_T}. \tag{6.2}$$

We then solve for, (6.3)

$$\frac{dN}{dydp_T} = 2\pi p_T\frac{1}{\sigma_{inel}}E\frac{d^3\sigma}{dp^3}, \tag{6.4}$$

then integrate to get (6.5)

$$\frac{dN}{dy} = 2\pi\frac{1}{\sigma_{inel}}\int_0^\infty p_T E\frac{d^3\sigma}{dp^3} \tag{6.6}$$

parameter	pp 200 GeV
$\frac{dN}{dy}$	1.1346
$A[mb\ GeV^{-2}c^3]$	377 ± 60
$a\left[\left(\frac{GeV}{c}\right)^{-1}\right]$	0.356 ± 0.014
$b\left[\left(\frac{GeV}{c}\right)^{-2}\right]$	0.068 ± 0.019
$p\left[\frac{GeV}{c}\right]$	0.70 ± 0.02
n	8.25 ± 0.04

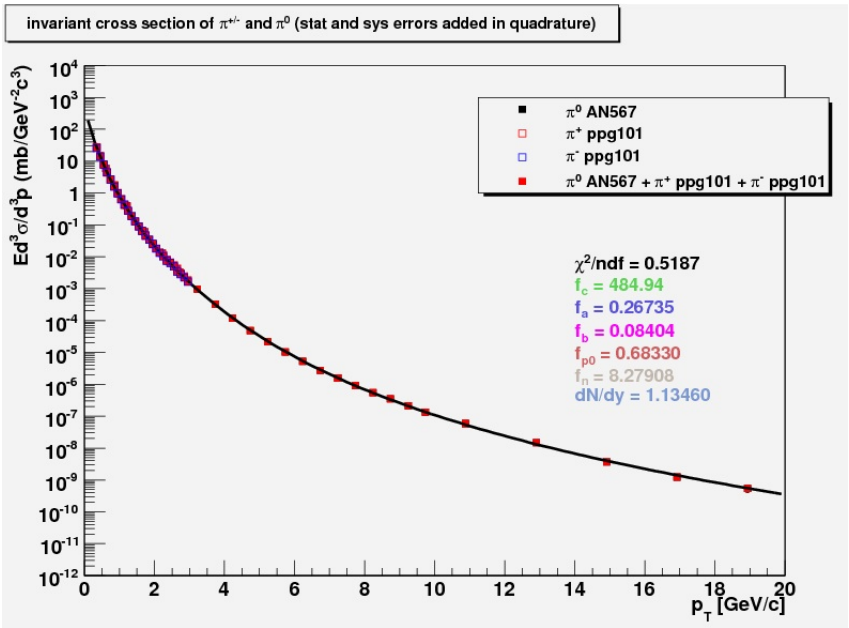

Figure 6.1: Hagedorn fit to combined neutral and charged π's

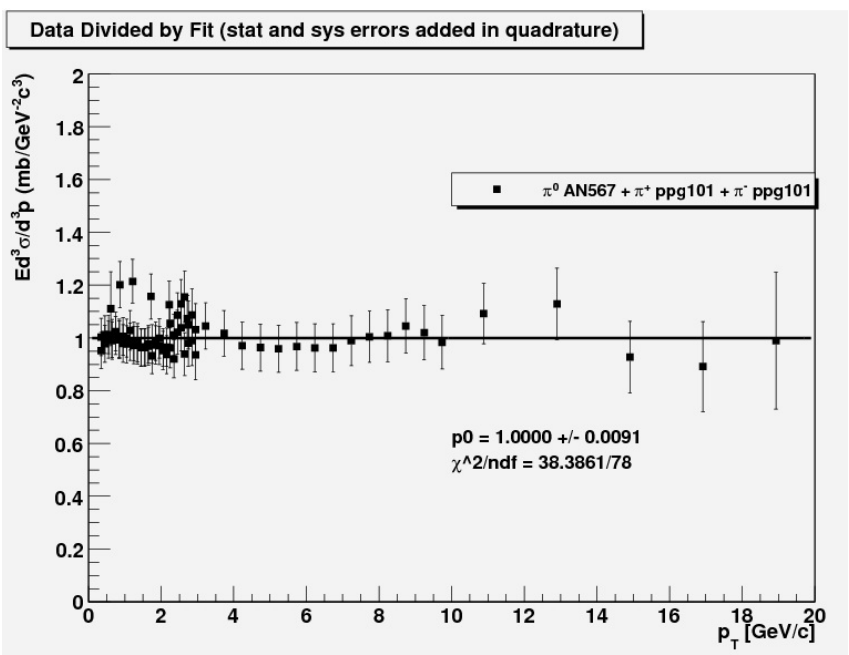

Figure 6.2: Measured combined neutral and charged π's spectrum divided by Hagedorn fit. cf. 6.1

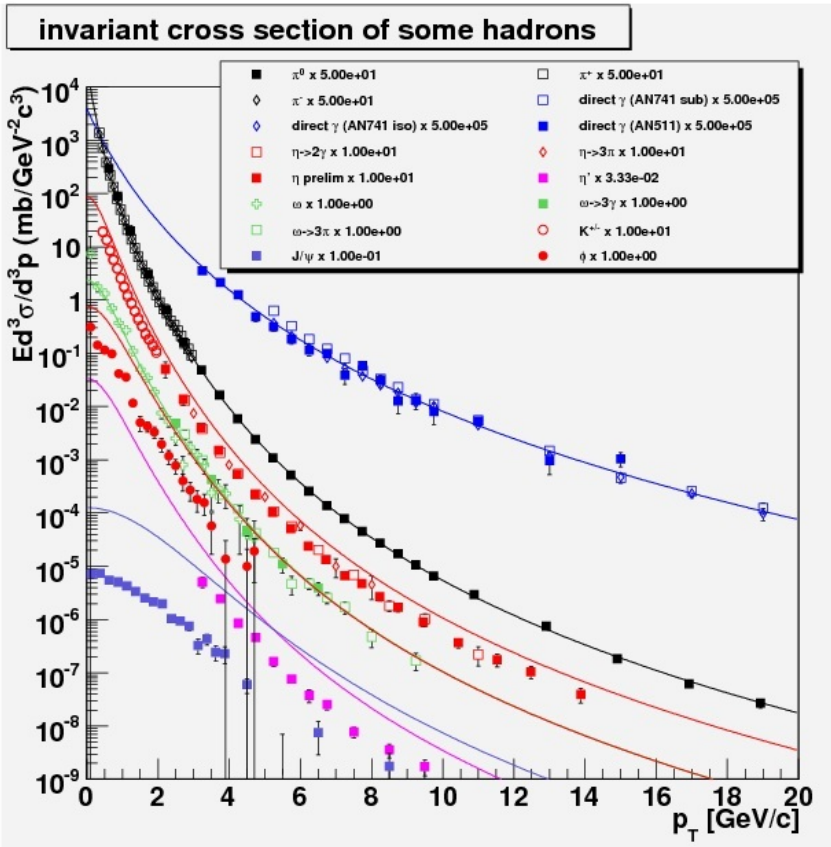

Figure 6.3: Hagedorn fit, with m_T scaling, to various meson species

Other Mesons

For all other mesons we replace p_T in Eq.6.1 with $\sqrt{m^2 - m_\pi^2 + (p_T/c)^2}$, this is called m_T scaling. The m_T scaled Hagedorn is then compared to the differential invariant cross section for each meson species with all parameters held constant, Fig. 6.3. The alignments are not quite right so each spectrum is divided the appropriately m_T scaled Hagedorn function, Fig. 6.4. A zeroth order polynomial is fit to each ratio, the result is then used as a normalization constant for the m_T scaled Hagedorn for each species and re plotted. We now see that the fits are quite good, Fig 6.5.

In order to extract the meson yield we integrate the fits over all p_T to obtain dN/dy using Eq. 6.6. The input to EXODUS is $(\frac{dN}{dy})_{meson}/(\frac{dN}{dy})_\pi$. Results,

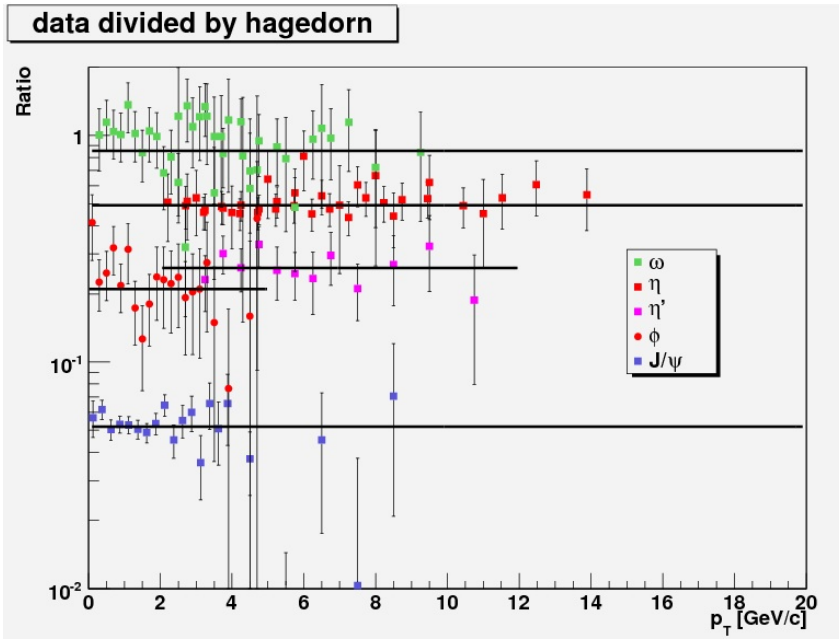

Figure 6.4: Cross sections divided by m_T scaled Hagedorn

	$\frac{dN}{dy}\mid_{y=0}$	relative error	meson/π	data used
p + p				
π	1.135	10%	1.0	PHENIX [30], [36]
η	9.26 x 10^{-2}	3.28%	8.16 x 10^{-2}	PHENIX [37]
ρ	8.95 x 10^{-2}	30%	8.81 x 10^{-2}	[38]
ω	6.97 x 10^{-2}	5.76%	6.14 x 10^{-2}	PHENIX [39] [40]
ϕ	7.99 x 10^{-3}	8.21%	7.04 x 10^{-3}	PHENIX [40]
η'	1.20 x 10^{-2}	7.63%	1.06 x 10^{-2}	PHENIX [41]
J/ψ	1.716x 10^{-5}	3.13%	1.51 x 10^{-5}	PHENIX [42]
Υ	1.1 x 10^{-7}	50%	1.10 x 10^{-7}	PHENIX [43] [44]
ψ'	2.5 x 10^{-6}	30%	2.46 x 10^{-6}	[45]
K	1.14 x 10^{-1}	50%	1.00 x 10^{-1}	PHENIX [46]

Table 6.2: meson rapidity densities used in our meson decay generator.

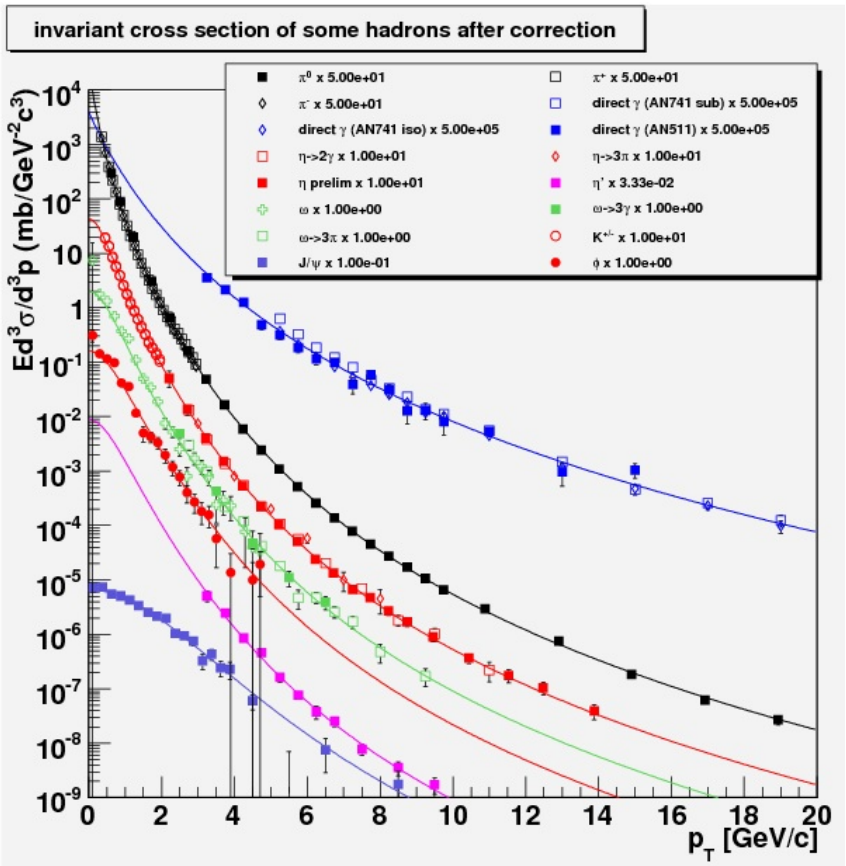

Figure 6.5: Corrected m_T scaled Hagedorn, compared to various meson species

uncertainties, and references to data are given in Table 6.2 The ψ' is determined by the ratio $\sigma_{\psi'}/\sigma_{J/\psi} = 0.14 \pm 0.03$ [45]. To include the Υ, the ratio of $d\sigma_{\Upsilon}/dy = 5.0 \pm 1.8nb$ [43] to $B.R.d\sigma_{J/\psi}/dy = 45.3 \pm 1.0(stat) \pm 5.4(sys) \pm 4.5(global)nb$ [44] with B.R.$(J/\psi \to e^+e^-) = 5.94\%$ [28]. For the ρ meson we assume $\sigma_\rho/\sigma_\omega = 1.15 \pm 0.15$, consistent with values found in jet fragmentation [38].

Electrons from Conversions

The contribution of photon conversions to the electrons in the cocktail depends on the configuration of the detector. These conversions are not explicitly implemented in EXODUS, the p_T spectra of conversion electrons are very similar to the spectra of electrons from Dalitz decays. A simulation of π^0's is used to determine the ratio of electrons from conversions of photons from $\pi^0 \to \gamma\gamma$ decays to electrons from $\pi^0 \to \gamma e^+e^-$ (Dalitz) decays with the detector in the Run 6 configuration. This was determined to be 0.429. The other meson Dalitz decays are scaled properly account for the fact that the branching ratio for the Dalitz decay relative to the two photon decay grows slightly with increasing parent meson mass.

Kaon Decays: K_{e3}

$K^\pm$ and K_L^0 can decay in the region between the interaction point and the face of the drift chamber. The decays that can contaminate out measurement are called Ke3;

$$K^+ \to \pi^0 e^+ \nu,$$
$$K^- \to \pi^0 e^- \bar{\nu},$$
$$K_L^0 \to \pi^\pm e^\mp \nu.$$

The contribution from K_{e3} decays is shown to be negligible in Sec: 5, consequently the only change made to the present cocktail was to update the meson/pion ratio for kaons.

Direct Radiation

Contributions to the cocktail from virtual direct photons and from the conversion of real direct photons are derived from the measured real direct

photon spectra as published in [3]. There are two contributions to the inclusive electron spectra from direct radiation of photons.

- Conversion of direct real photons, e.g. from quark-gluon Compton scattering.
- Direct virtual photons $\gamma^* \rightarrow e^+e^-$.

Once again the relationship between these two is about the same as for Dalitz decays of light mesons and the corresponding two photon decays. So we have a real or direct photon ($\pi^0 \rightarrow \gamma\gamma$) or a virtual photon ($\pi^0 \rightarrow \gamma e^+e^-$). Because of this an imaginary particle called a "direct pion" was implemented as a parent particle for these photons. The direct pion is defined as a neutral pion with an invariant p_T spectrum and normalization chosen such that the spectrum of decay photons from the two photon decay is matched to the spectrum of measured direct photons.

We start with an invariant p_T spectrum from the latest direct photon PHENIX data [3]. EXODUS was used to produce a ratio of pions divided by all photons from pions, Fig. 6.6. This ratio was used to scale up the data points to a direct pion spectrum.

The resulting direct pion spectrum is then fit with,

$$E\frac{d^3\sigma}{dp^3} = \frac{p_0}{\left(e^{-p_3 p_T - p_4 p_T^2} + \frac{p_T}{p_1}\right)^{p_2}}, \tag{6.7}$$

the EXODUS weighting function for direct pions, as seen in Fig. 6.7. The parameters of the fit are then put into EXODUS. By construction, the Dalitz electron spectrum of the direct pion would be identical to the spectrum of electrons from direct virtual photons if the ratio between Dalitz and conversion electrons would be the same for (true) pion and for direct radiation. This is not the case. The virtual photon mass, in principle, is not limited and, therefore, we have implemented a relative normalization between "Dalitz" and "conversion" contributions from direct radiation that increases with p_T of the parent virtual direct photon,

$$\text{Relative Norm.} = 0.255 \left(\frac{log\left(\frac{p_T^{pair}}{0.547}\right)}{log\left(\frac{0.547}{0.135}\right)} \right). \tag{6.8}$$

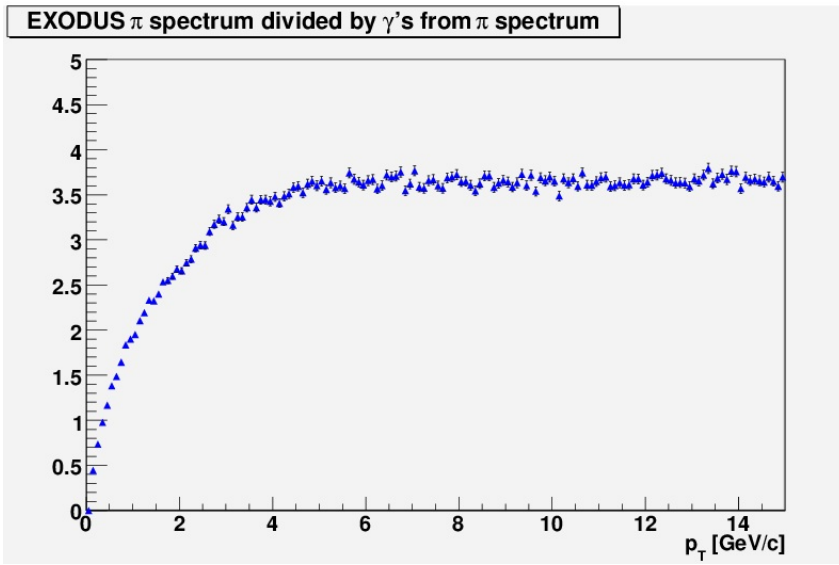

Figure 6.6: Ratio of π invariant spectrum to the invariant spectrum of all π decay γ's.

The normalization of the direct pion is accomplished by comparing the direct photon output of EXODUS to data, Fig. 6.7, the normalization constant given to EXODUS is adjusted until the direct photon output matches data. A ratio of the direct photon data to direct photons from EXODUS is plotted in Fig. 6.9, the zeroth order polynomial fit yields a value of one.

6.1.2 Systematic Error on Cocktail

To calculate the systematic error of the cocktail each input element is separately varied by its systematic error. Each element will cause a fractional change in the final cocktail spectrum. These fractional changes are added in quadrature to produce the total relative error of the cocktail.

The following systematic errors are assigned to the various inputs and the resulting in upper and lower systematic errors on the cocktail are shown in Fig. 6.11:

- Pion spectrum (black curves): obtained via full cocktail calculations using pion spectra moved up (down) by the systematic uncertainty of the pion spectrum as input.
- Meson to pion ratios: the sys. uncertainties are listed in Table6.2. Since

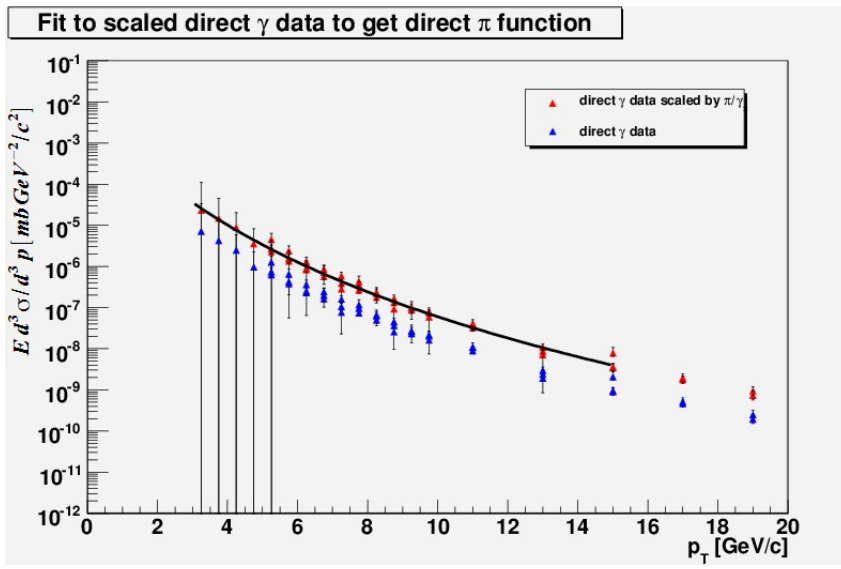

Figure 6.7: Direct photon data, blue(lower) triangles. The red(lower) triangles are this same data scaled by π/γ ratio to represent the direct pions. The black line is the fit whose parameters are entered into EXODUS.

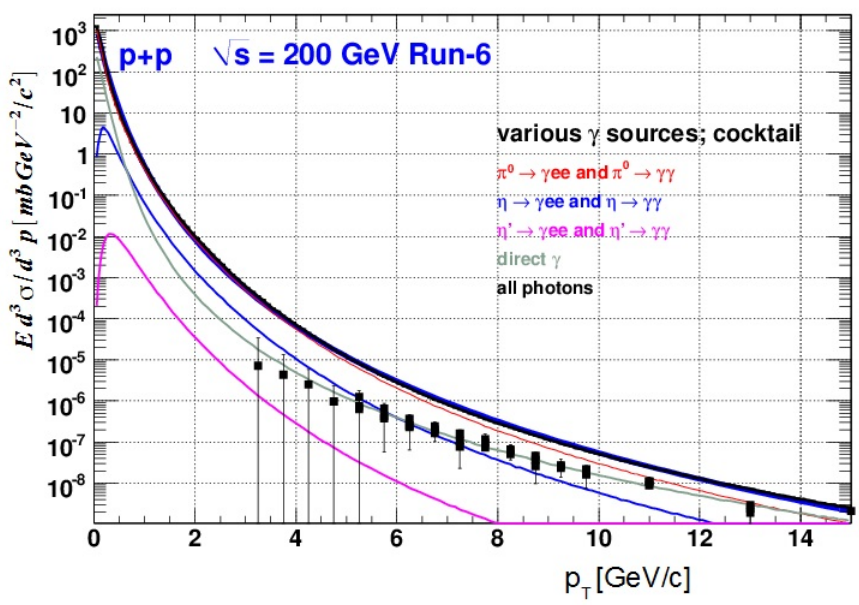

Figure 6.8: Direct γ data from [3] plotted with the various γ spectra from EXODUS.

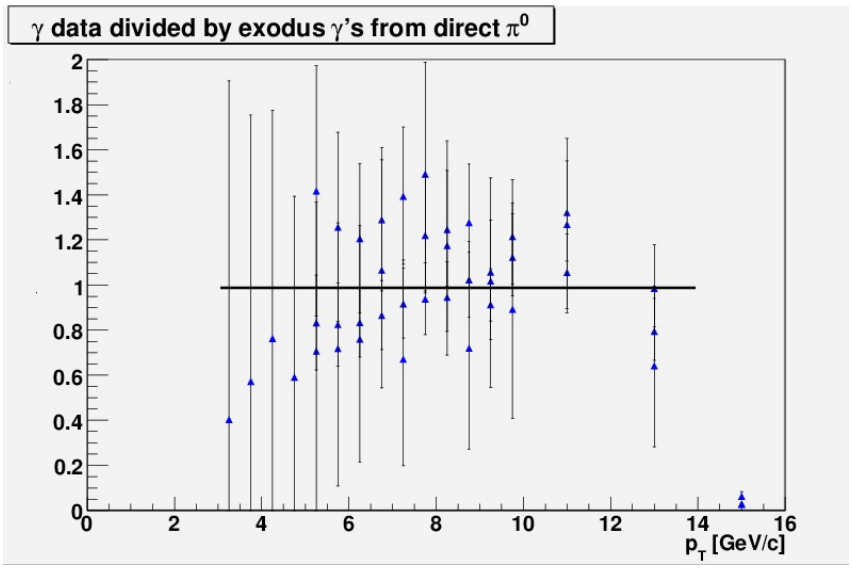

Figure 6.9: Ratio of direct γ data from [3] to direct γ from EXODUS.

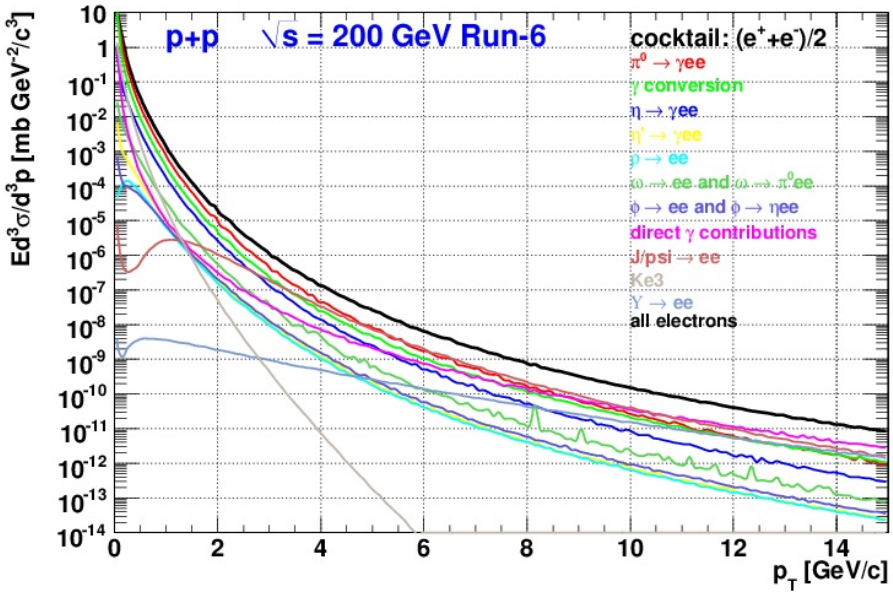

Figure 6.10: The final cocktail

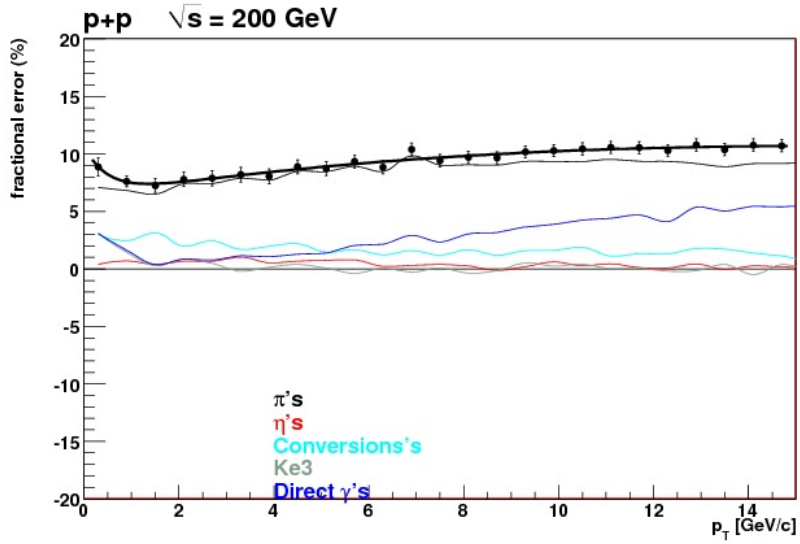

Figure 6.11: Individual contributions to the cocktail systematic error. The total error is depicted by the data points which are shown together with a fit

the contributions from all other mesons are much smaller than the contribution from η decay (red curve) the resulting systematic uncertainties are tiny ($< 1\%$) and, therefore, almost invisible as isolated curves in Fig. 6.11.

- Conversion material in the aperture (light blue curves in Fig. 6.11): 10 % systematic error (p_T independent).
- Ke3 decay (green curves in Fig. 6.11): 50 % systematic error (relevant only at low p_T).
- Direct radiation (blue curves in Fig. 6.11):obtained from the systematic error quoted for the direct photon measurement.

We show only the upper systematics as they are symmetric with the lower. The points in Fig. 6.11 are a quadratic sum of the five curves. The thick black line is a fit to the points using,

$$sys.error[\%] = p_0 * exp(p_1 * p_T) + p_2 + p_3 * p_T + p_4 * p_T^2 + p_5 * p_T^2. \quad (6.9)$$

Equation 6.9 with the parameters in Fig. 6.12 is then used to calculate the relative systematic error of the cocktail.

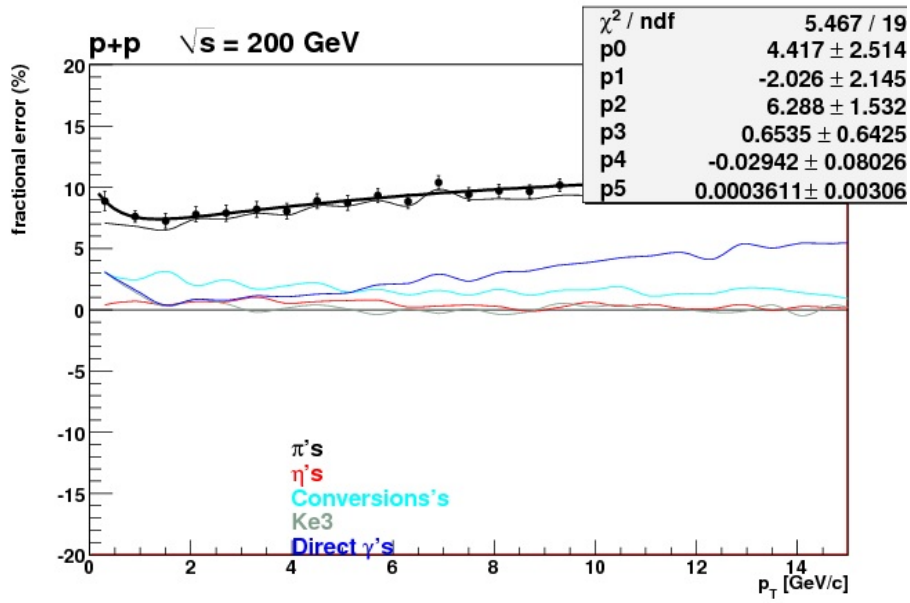

Figure 6.12: Same as Fig. 6.11, now showing fit parameters

6.2 Systematic Errors

The error bars so far have been strictly statistical. We now have to add the errors introduced by our technique and the detector, the systematic errors. The source of the systematic errors, their assigned values, and the explanations are as follows.

1. **Absolute normalization**
   - **BBC cross section** (9.6%) Sec. 4.2
   - **BBC bias** ϵ_{bias} (2.7%)
   - **Total normalization** (10.0%) This is the quadratic sum of the two items above.
2. **Common part of the analysis**
   - **Geometrical Acceptance** (9.86%) Sec. 4.3
   - **eID**
     - **E/p cut efficiency** (variable) Sec. 4.3.1
     - **RICH eID cut efficiency** ($0.26\% \bigoplus 0.40\% = 0.48\%$) Sec. 4.3.2

- **EMC matching efficiency** (0.53%)
- **prob cut efficiency** (0.51%)

3. R_{pi} **determination** (25%) Above π threshold in RICH. See 5.6
4. **Trigger Correction.** (3%) See Sec. 4.4.1
5. **Cocktail** (variable) See Sec. 6.1

The systematic errors given above are propagated to the Final Heavy flavor electron cross section and then added in quadrature. For example, the components of item 2, (the common part of analysis), added in quadrature and contributed to the inclusive electron differential cross section. In the cocktail analysis, the quadratic sum of the inclusive cross section and the cocktail error is the error of heavy flavor electron cross section.

6.3 Heavy Flavor Spectrum

In Sec. 4.6 we produced the final inclusive invariant cross section of electron *candidates* as there is still an obvious contamination at $p_T > 6.0$GeV. These need to be subtracted out and the means to to this were described in Chap. 5. Once again we will subtract the background using,

$$N_e = \int_{0.8}^{1.2} \left[\frac{E}{p}\right]_{all} - R_\pi \int_{0.6}^{0.8} \left[\frac{E}{p}\right]_{all}. \tag{6.10}$$

In addition, our goal is an invariant cross section spectrum for electrons from heavy flavor decays. The inclusive spectrum has electrons from a variety of sources that PHENIX (only at present!) does not have the ability to discriminate. These electrons are subtracted using the cocktail of electron sources as described in Sec. 6.1.

Throughout the analysis chain the data are kept in three dimensional arrays, the dimensions being p_T, E/p and n_1. In this way one can choose the n_1 cut at will and also plot either the E/p profiles per p_T bin or the p_T spectrum itself projecting out just the high E/p window. The other key advantage is that all three dimensions are scaled by the same factors, trigger efficiency (where applicable), BBC efficiency, acceptance correction etc. with this and the fact that R_π is dimensionless the subtraction of Eq. 6.10 can be performed when the data are in units of invariant cross section.

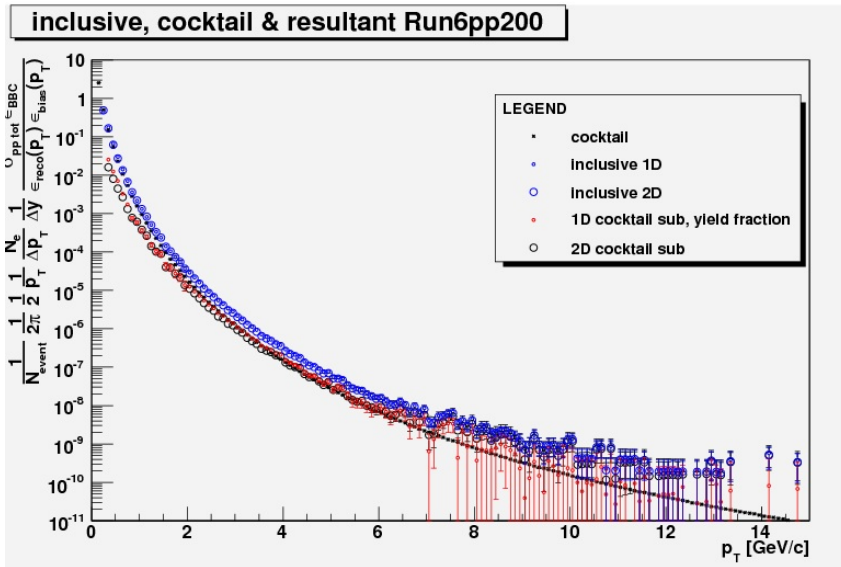

Figure 6.13: The inclusive spectrum with the cocktail and two different subtracted spectra (see text)

In Fig 6.13 we now see the inclusive spectrum plotted with the cocktail to get a sense of their relative magnitudes. In the legend are the terms "1D" and "2D", these are used to distinguish two methods to produce the spectra. In the 1D case the inclusive p_T spectrum is a one dimensional histogram that is filled in the analysis code using all eID cuts including E/p. In this case we constructed the yield fraction as a multiplicative factor to remove the hadronic background.

In the 2D case the final plot is made from the original three dimensional histogram as mentioned above. The n_1 axis is collapsed as a projection to a two dimensional histogram of p_T and E/p. One can then easily produce the yields in the Hi and Lo windows and use R_π. In this way all corrections are factorable and the R_π subtraction is applied as an arithmetic subtraction that can commute with the cocktail subtraction. In addition we eliminate the need to propagate the error of the yield fraction. We are left with the statistical error of the two windows and the systematic error of R_{pi}.

The reason to include the two methods in Fig 6.13 was to demonstrate the 2D method produced the 1D method up to this point. The red points are the cocktail subtracted 1D points, they also have had their hadronic background subtracted using the yield fraction multiplicative factor. The black circles are the 2D cocktail subtracted points there is no background subtraction as yet, the contrast of the red points and black circles shows the degree of contami-

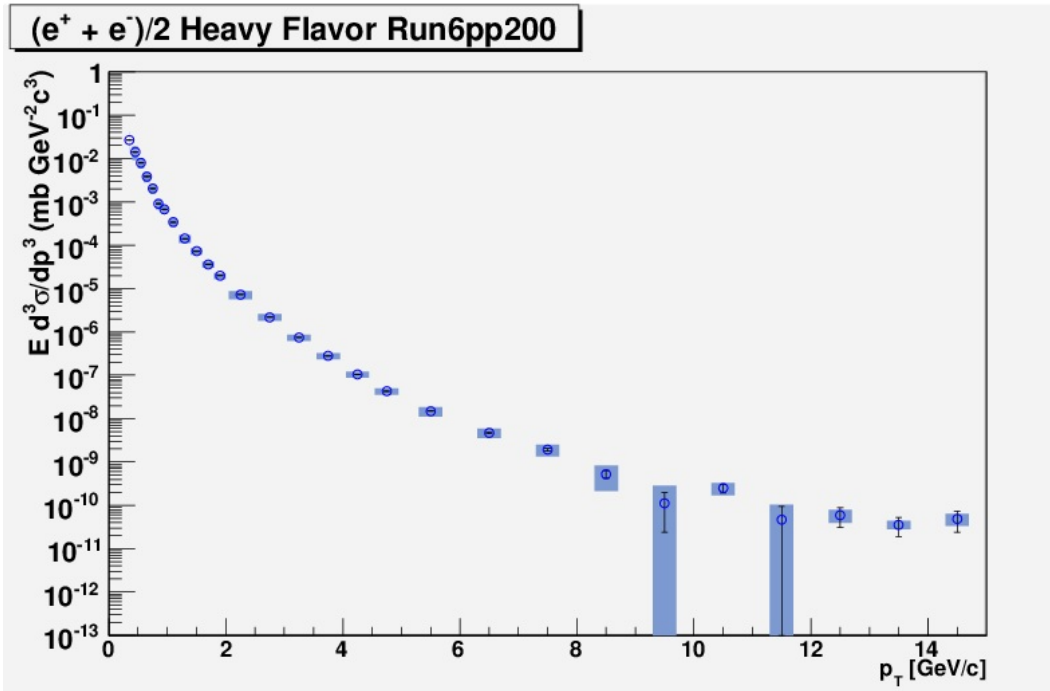

Figure 6.14: Heavy flavor invariant cross section for Run 6 with systematic errors

nation.

So at the end we have for the final systematic error calculation

$$Sys_{total}(\%) = Sys_{Cocktail} \bigoplus Sys_{Common}(10\%) \bigoplus Sys_{R_\pi}(25\%). \qquad (6.11)$$

The systematic error is added as colored boxes about each point in the spectrum, Fig. 6.14.

Chapter 7

Implications for Heavy Flavor Production

7.1 Comparison to previously published PHENIX data

The spectrum of Fig. 7.1 was plotted alongside previous PHENIX data[31], to check for consistency a ratio was made of the two spectra. Note that the published data ends at 8.5GeV and that our measurement extends to 14.5GeV. To make a comparison on a linear scale the two data sets of Fig. 7.1 are divided by a FONLL shape from [47] that is scaled to the published data.

In Fig.7.2 we see three panels. The top panel is the ratio of published data to the scaled FONLL shape, to see that it is scaled properly. The middle panel shows our data divided by the FONLL shape. The bottom panel is now our data divided by both the published data points and the FONLL shape. All statistical and systematic errors are included, no error is assigned to the fit of the top panel. We see that the ratio in the bottom panel is consistent with one within the errors.

7.2 Final Invariant Cross Section

In Fig.7.3 we see the final spectra with background and cocktail subtraction as well as all errors both statistical and systematic. The numbers corresponding to the points in the figure can be found in Table A.7.

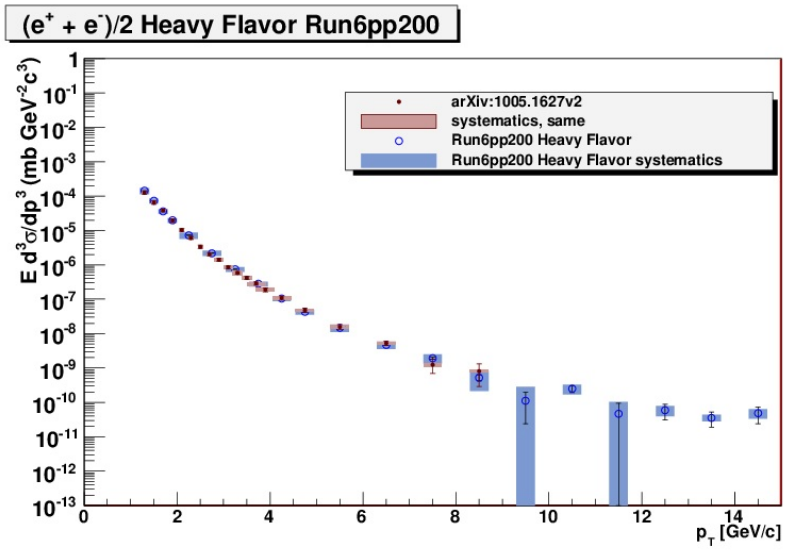

Figure 7.1: Heavy flavor invariant cross section for Run 6 and previous PHENIX data.

Also on the plot are theory predictions for charm and bottom cross section as well as the sum with upper and lower limits. As was done for Run 5[24] we use the FONLL predictions of the charm and bottom cross sections calculated by Cacciari, Nason and Vogt[47]. The bottom panel of Fig. 7.3 is a division of the data by the theoretical prediction including the upper and lower limits.

In Fig. 7.4 the published data has been added. The final element of Fig. 7.4 comes from a theoretical prediction of electrons from Drell-Yan mechanism, the annihilation of quark-antiquark pairs in the opposite colliding protons. The contribution to the total number of electrons is expected to rival the heavy flavor contribution at p_T's on the order of 15-20GeV. In the plot, a prediction of Armesto, Cacciari, Daineseand, Salgado and Wiedemann[48] is plotted with the other spectra and, as predicted, the Drell-Yan electrons do not represent a significant fraction of the measured electrons.

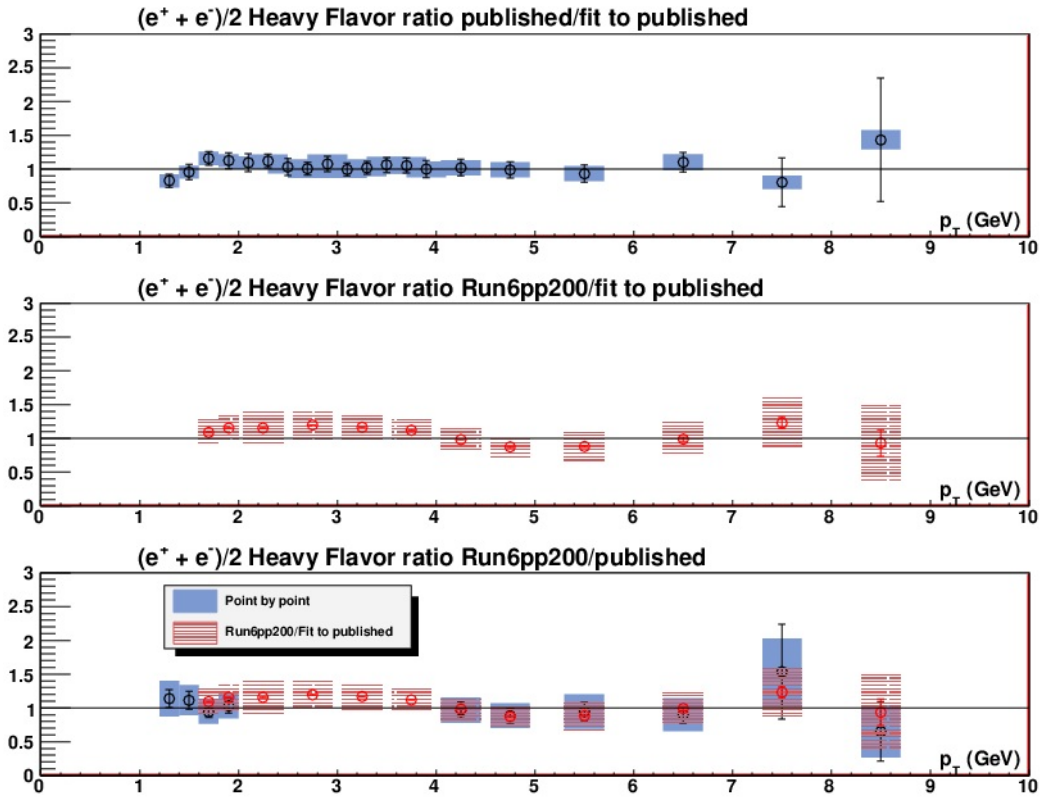

Figure 7.2: Ratios showing agreement of current measurement to ppg077

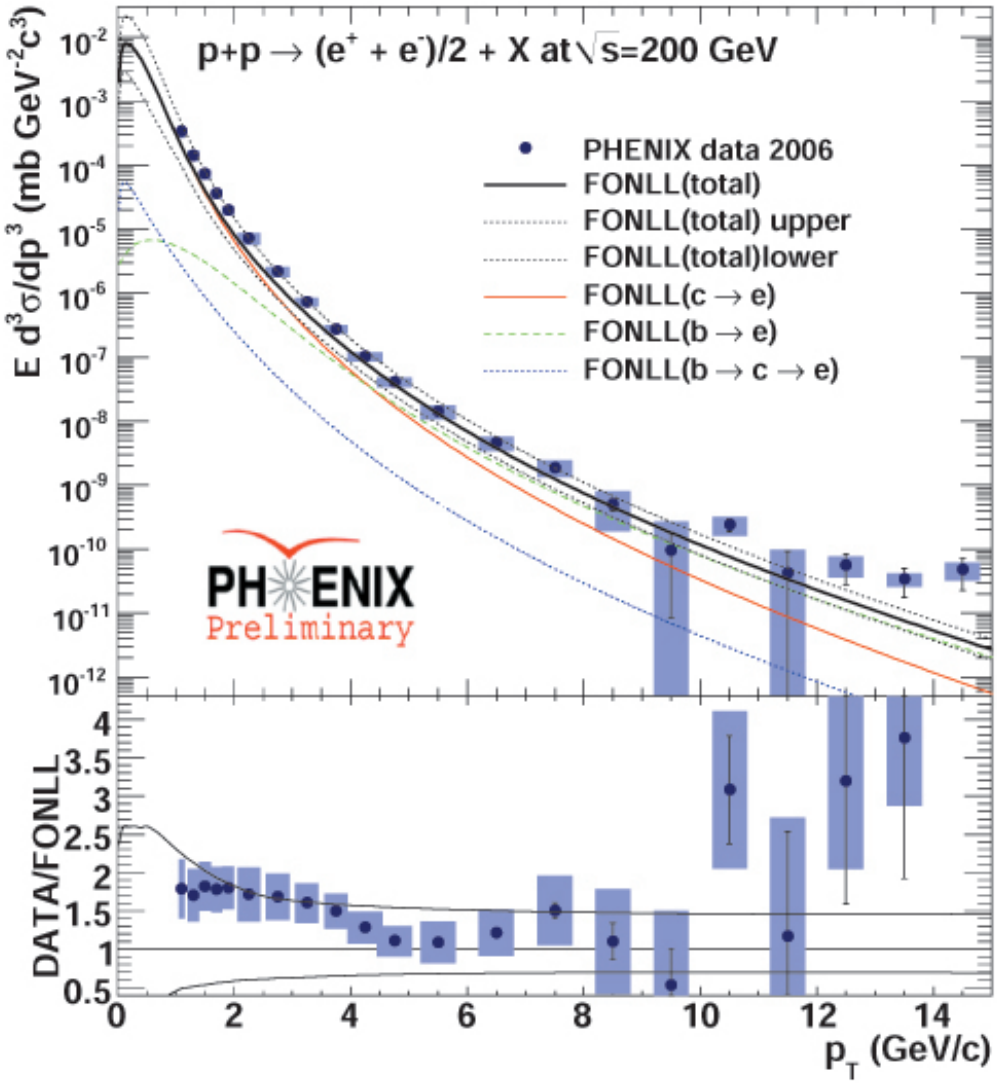

Figure 7.3: Final spectrum with theory curves and systematic errors Run 6

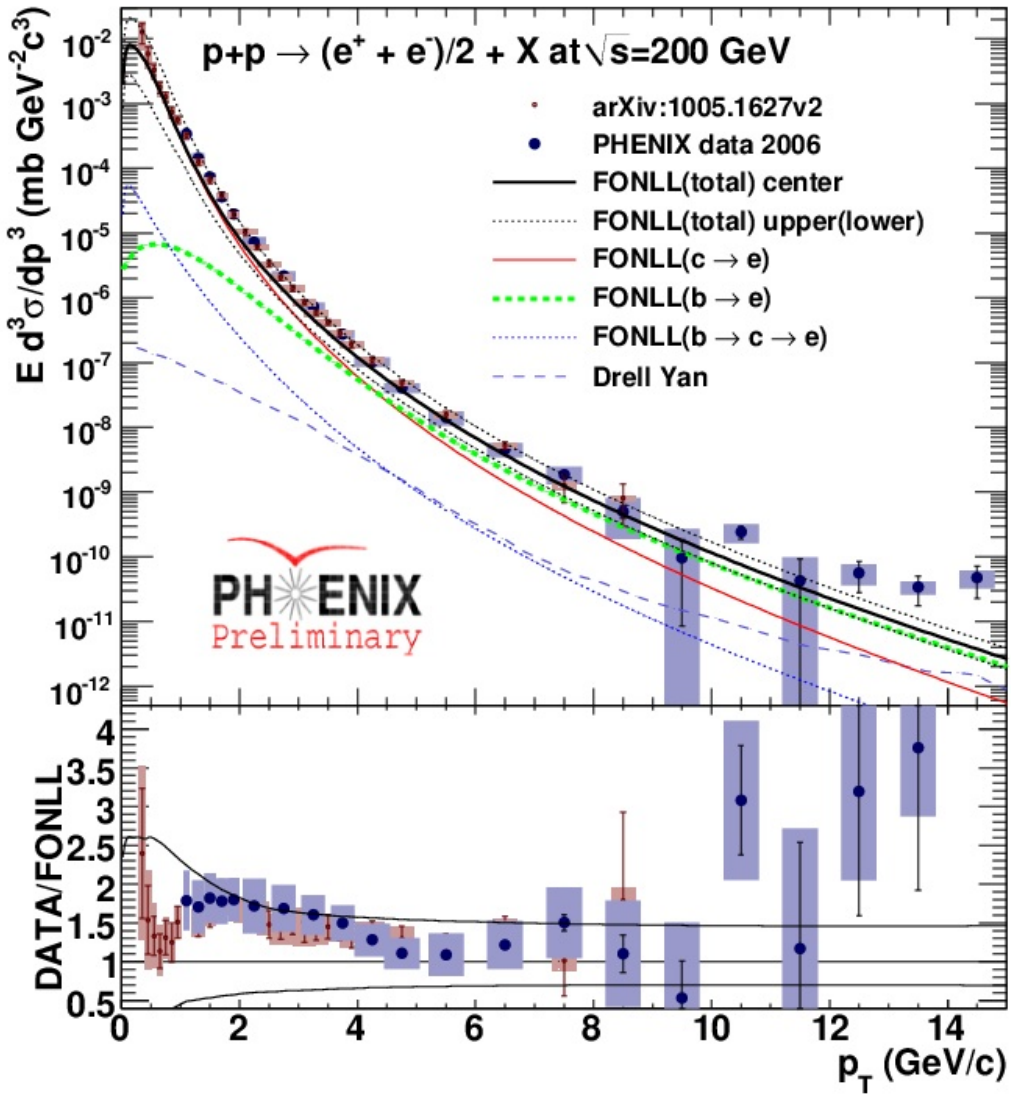

Figure 7.4: Final spectrum with Drell-Yan and published PHENIX data.

7.3 Heavy Flavor Cross Sections

In this section we compare our data with the First Order Next to Leading Logarithm (FONLL) calculations of [47, 49]. Their calculation of the charm and bottom cross sections for pp at $\sqrt{s} = 200GeV$ at mid-rapidity are,

$$\sigma_{c\bar{c}}^{FONLL} = 256^{+400}_{-146}\mu b, \tag{7.1}$$

and

$$\sigma_{b\bar{b}}^{FONLL} = 1.87^{+0.99}_{-0.67}\mu b. \tag{7.2}$$

In Figs. 7.5-7.7 we compare our data to the differential invariant cross section predictions for electrons from D and B mesons in pp at 200 GeV, the contribution of electrons from $B \to D \to e^{+/-}$ was combined with the the $B \to e^{+/-}$.

To estimate the cross sections for charm and bottom production we make the reasonable assumption that the shapes of the FONLL curves are correct. This then allows us to find scale factors C_D and C_B that fit the FONLL calculations to our data;

$$\frac{d\sigma_D^{measured}}{dy} = \frac{d\sigma_{FONLL_D}}{dy} * C_D \pm \sigma_{C_D}, \tag{7.3a}$$

so then,

$$\sigma_{c\bar{c}}^{measured} = \sigma_{c\bar{c}}^{FONLL} * C_D \pm \sigma_{C_D}. \tag{7.3b}$$

Similarly for B mesons,

$$\frac{d\sigma_B^{measured}}{dy} = \frac{d\sigma_{FONLL_B}}{dy} * C_B \pm \sigma_{C_B}, \tag{7.4a}$$

$$\Rightarrow \sigma_{b\bar{b}}^{measured} = \sigma_{b\bar{b}}^{FONLL} * C_B \pm \sigma_{C_B}. \tag{7.4b}$$

We made a series of fits in Figs. 7.5-7.7, the nature of which, explained in each caption, contemplate these three additional assumptions;

1. That $\sigma_{c\bar{c}}^{FONLL}/\sigma_{b\bar{b}}^{FONLL}$ is correct, so we fit with only one parameter, C_{DB}, Fig. 7.5 and the first line of Table 7.1.

$$\sigma_{c\bar{c}}^{measured} = \sigma_{c\bar{c}}^{FONLL} * 1.482 \pm 0.109 = 379.4 \pm 27.90\mu b$$
$$\sigma_{b\bar{b}}^{measured} = \sigma_{b\bar{b}}^{FONLL} * 1.482 \pm 0.109 = 2.77 \pm 0.20\mu b$$

   The χ^2/ndf is quite good.

2. That C_D and C_B have to be fine tuned separately, this is the fit of Fig 7.6 and the second line of Table 7.1.

$$\sigma_{c\bar{c}}^{measured} = \sigma_{c\bar{c}}^{FONLL} * 1.925 \pm 0.288 = 492.8 \pm 73.73\mu b$$

$$\sigma_{b\bar{b}}^{measured} = \sigma_{b\bar{b}}^{FONLL} * 0.885 \pm 0.374 = 1.65 \pm 0.70 \mu b$$

Electrons from bottom are expected to surpass those of charm at 4GeV[47], in Fig 7.6 the crossing point for electron yield from bottom to surpass charm is at $\approx 8GeV$, the bottom cross section is apparently lower than calculated by FONLL, while the charm cross section is significantly larger.

3. In preparation to calculating an upper limit for the bottom we fit only bottom points from 6 GeV to get C_B, Fig. 7.7 and the third line of Table 7.1.

$$\sigma_{b\bar{b}}^{measured} = \sigma_{b\bar{b}}^{FONLL} * 2.299 \pm 0.489 = 4.30 \pm 0.91 \mu b$$

The conclusion is that the single electron measurement at high p_T constrains the $c\bar{c}$ and $b\bar{b}$ cross sections but since the spectral shapes are similar the data does not allow a precise determination of $\sigma_{b\bar{b}}$.

We now have three bottom and two charm cross sections determined by our "scaling method", there is an additional systematic error that needs to be assigned to each cross section. This error arises from the two steps of converting the differential invariant cross section for electrons to that of D(B) mesons and then converting to charm(bottom) quarks in full phase space.

To understand these systematic errors we use the technique of [24], with a small modification, to calculate the total charm cross section, this we call our "integration method". There are four steps;

1. The integrated cross section $d\sigma^e/dy(p_T > p_{Tlow})$ is calculated from the differential invariant cross section, Fig. 7.4.

2. The cross section is extrapolated to $p_T = 0$ to get the integrated cross section $d\sigma^e/dy$ at mid rapidity for all p_T.

3. This is then converted into a charm cross section at mid rapidity $(d\sigma_{c\bar{c}}/dy|_{y=0})$ using a total electron branching ratio of charm $(BR(c \to e))$,

$$\frac{d\sigma_{c\bar{c}}}{dy} = \frac{1}{BR(c \to e)} \frac{1}{C_{e/D}} \frac{d\sigma^e}{dy}. \tag{7.5}$$

4. Lastly, the cross section is extrapolated to the entire rapidity range to obtain the total charm production cross section $\sigma_{c\bar{c}}$.

Since we make the assumption that the FONLL shapes are correct we can combine steps 1 and 2 and integrate the appropriate FONLL shape over the entire p_T spectrum and apply the correction factors from Table 7.1 to get $d\sigma^e/dy$. For the fit of Fig 7.5 this gives

$$\frac{d\sigma^{c\to e}}{dy} = 10.722 \pm 0.789 \pm 1.82\mu b. \tag{7.6}$$

All measurements quoted with two errors are of the format $value \pm stat \pm sys$. The systematic error is the average value of the systematic errors of the first nine points of the data, the points that will dominate the fit. Moving these points up and down by these correlated errors will move the value of the scaling factor from the fit no more than the 17% average value.

The next step is to apply Eq. 7.5 using $(BR(c \to e)) = 9.5 \pm 1.0\%$ and $C_{e/D} = 0.935$ [24],

$$\frac{d\sigma_{c\bar{c}}}{dy} = \frac{1}{0.095 \pm 0.01}\,\frac{1}{0.935}\,10.722 \pm 0.789 \pm 1.82\mu b = 120.7 \pm 8.9 \pm 24.0\mu b. \tag{7.7}$$

The systematic error from Eq. 7.6 is added in quadrature with the 1/9.5 relative error of $(BR(c \to e))$

Lastly a correction factor of 0.225 ± 0.034, which is for the extrapolation to the entire rapidity range from $d\sigma/dy$ to $\sigma_{c\bar{c}}$ plus an additional "rapidity spread factor" of 0.96 [24],

$$\sigma_{c\bar{c}} = \frac{1}{0.225 \pm 0.034}\,\frac{1}{0.96}\,120.7 \pm 8.9 \pm 24.0\mu b = 558 \pm 41.2 \pm 140\mu b. \tag{7.8}$$

The total systematic error is then 25% so we assign this as the systematic error on the calculation of the total cross sections using the scaling of the FONLL total cross sections.

In the case of the fit of the B FONLL shape to the data above 6 GeV we assign a 40% systematic error. This figure is what would be the total

systematic error on $\sigma_{b\bar{b}}$ if we could calculate it using the integration method as we do $\sigma_{c\bar{c}}$. In this situation the data points from 6 GeV and above have a systematic error of 36%, once this is propagated through all of the steps one arrives at the 40% figure.

We wish to quote an upper limit on $\sigma_{b\bar{b}}$ at the 90% level, the measured value with the statistical and systematic errors added in quadrature is

$$\sigma_{b\bar{b}}^{measured} = 4.30 \pm 1.95 \mu b.$$

Since the range of this measurement is all physical the upper limit with a 90% confidence level is simply defined as,

$$\sigma_{b\bar{b}}^{UL} = \sigma_{b\bar{b}}^{measured} + 1.66\sigma = 4.30 + 3.23 = 7.53 \mu b$$

	C_D	C_B	C_{DB}	χ^2	χ^2/ndf
Fig. 7.5	N/A	N/A	1.482 ± 0.109	10.654	0.592
Fig. 7.6	1.925 ± 0.288	0.885 ± 0.374	N/A	7.885	0.438
Fig. 7.7	0.000 fixed	2.299 ± 0.489	N/A	5.247	0.656

Table 7.1: Scale factors from fitting FONLL shapes to data.

	$\sigma_{c\bar{c}}$ integral method	$\sigma_{c\bar{c}}$ scaling method
Fig. 7.5	558.82 ± 41.10 ± 140.06	379.4 ± 27.9 ± 95.1
Fig. 7.6	725.87 ± 108.60 ± 181.92	492.8 ± 73.73 ± 123.5

Table 7.2: Total charm cross sections

	$\sigma_{b\bar{b}}$ scaling method
Fig. 7.5	2.77 ± 0.20 ± 0.69
Fig. 7.6	1.65 ± 0.70 ± 0.41
Fig. 7.7	4.30 ± 0.91 ± 1.72

Table 7.3: Total bottom cross sections

In Tables 7.2 & 7.3 are summarized all of the various total cross section measurements with all errors. These have been plotted, alongside other mea-

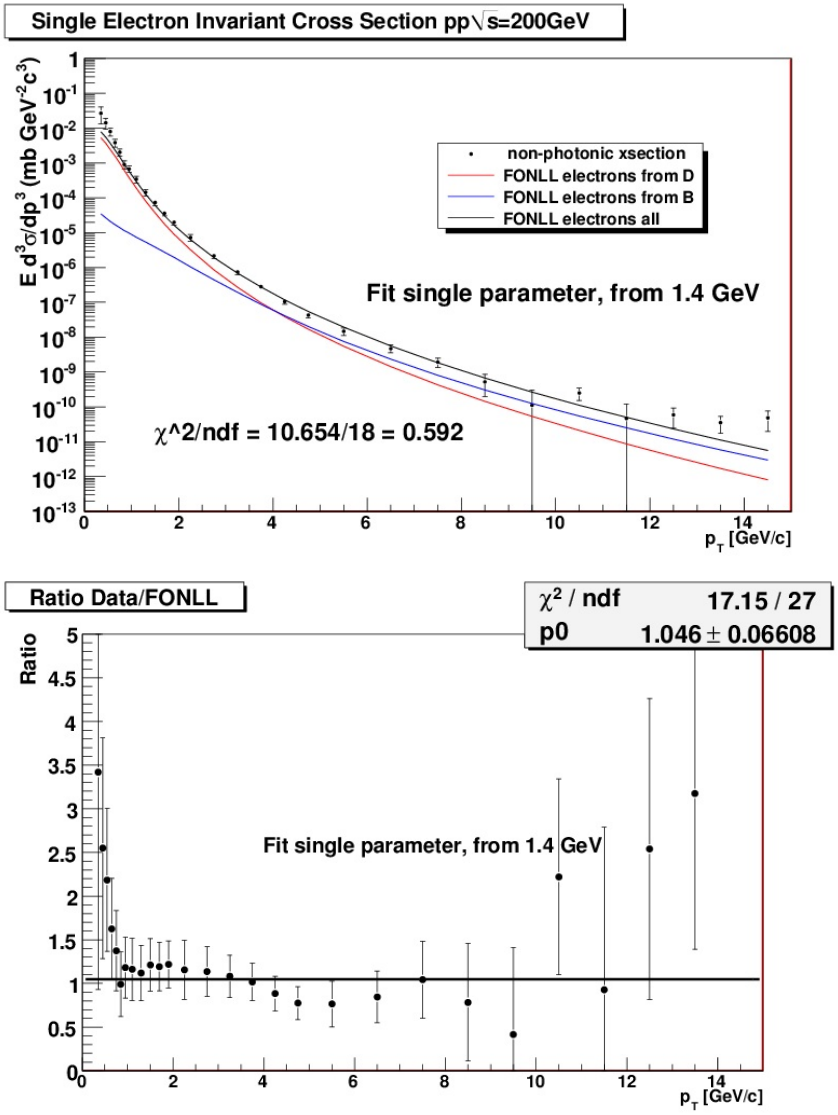

Figure 7.5: Fit to heavy flavor spectrum with a single parameter with the sum of the D & B curves from 1.4 GeV and above.

surements and the FONLL prediction, in Figs. 7.8 and 7.9. The error bars for the measurements are the statistical and systematic errors added in quadrature. As has been already mentioned, in the case of our scaling method of determining $\sigma_{b\bar{b}}$ using only the fit of the FONLL shape for electrons from B mesons, we have chosen to represent this measurement as an upper limit to $\sigma_{b\bar{b}}$. The bar at the right of the line is the upper limit of the quadratic sum of the statistical and systematic error, the point of the arrow the lower limit to allow the possibility of the actual value being lower still.

We see in the figures that our measurement is consistent, within errors, with the other measurements and the FONLL prediction. The error bars are somewhat correlated for all of the measurement as we all rely on theoretical and monte carlo (e.g. PYTHIA event generator) predictions of the terms in going from the differential cross section for electrons to a total cross section for heavy flavor production. What we have done is to reduce the error bars in two ways. We have reduced the systematic errors of the overall spectrum. The systematic error of the cocktail was reduced by the introduction of the latest hadron data.

Most importantly, our background subtraction technique allowed us to extend the differential spectrum for electrons well beyond previous measurements while keeping the systematic error comparable to the cocktail error at lower p_T. This then allowed a tighter constraint on the fit of the FONLL shapes further reducing the systematic error of the final result.

We made 4 determinations of $\sigma_{c\bar{c}}$ and 2 of $\sigma_{b\bar{b}}$ then compared them to published data and theory in Figs. 7.8 & 7.9. In the case of charm there were no surprises that we are consistent with the other measurements, the low end of the p_T spectrum dominates and our measurement was not meant to improve this. Being consistent with previous PHENIX data does mean though that our measurement is significantly larger than the theoretical FONLL prediction, essentially twice as large.

The STAR measurement of 2007 is inconsistent with all measurements and the theory prediction. This has since been corrected as the STAR collaboration made a careful study of the material in the STAR detector that had not been accounted for previously. It was discovered that the photonic electron background from conversions was much higher than previously estimated [50]. The second STAR measurement reflects this change.

The expectation was that our single electron measurement would improve the determination of the bottom cross section since significant portion of our measurement contains the p_T range that is expected to be dominated by elec-

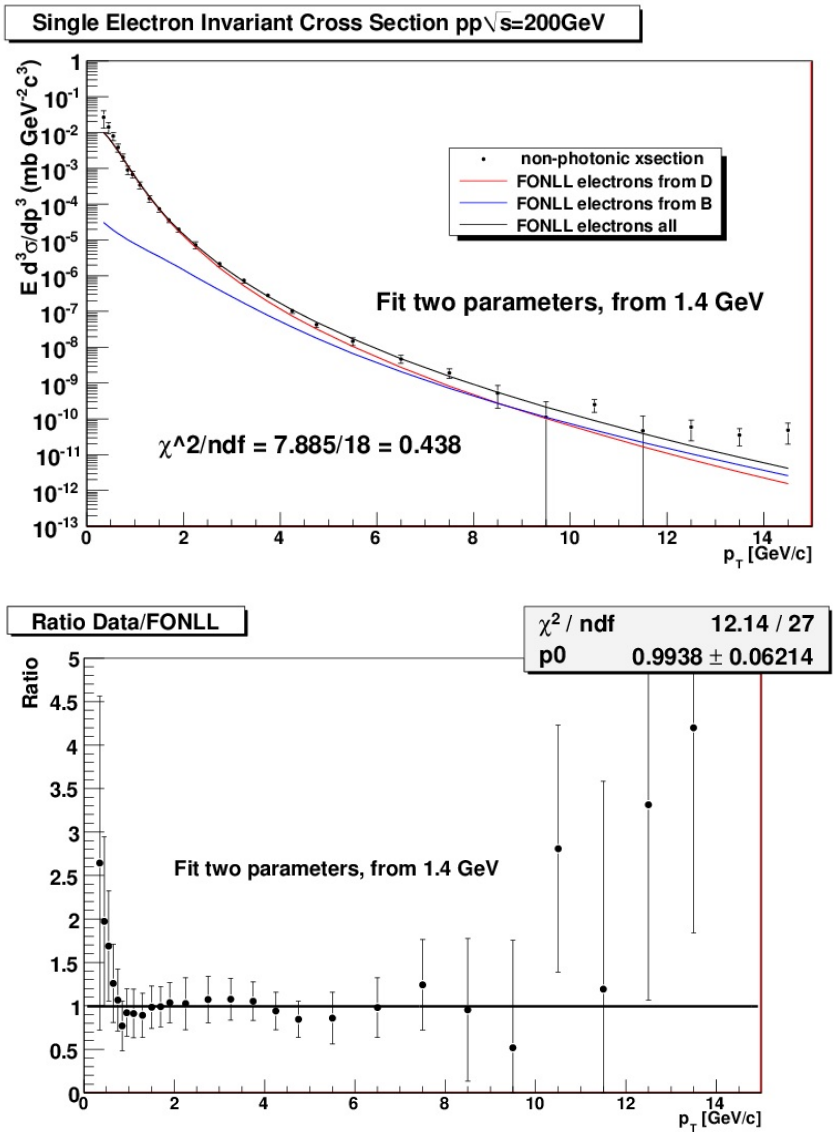

Figure 7.6: Fit to heavy flavor spectrum with both D and B from 1.4 GeV and above.

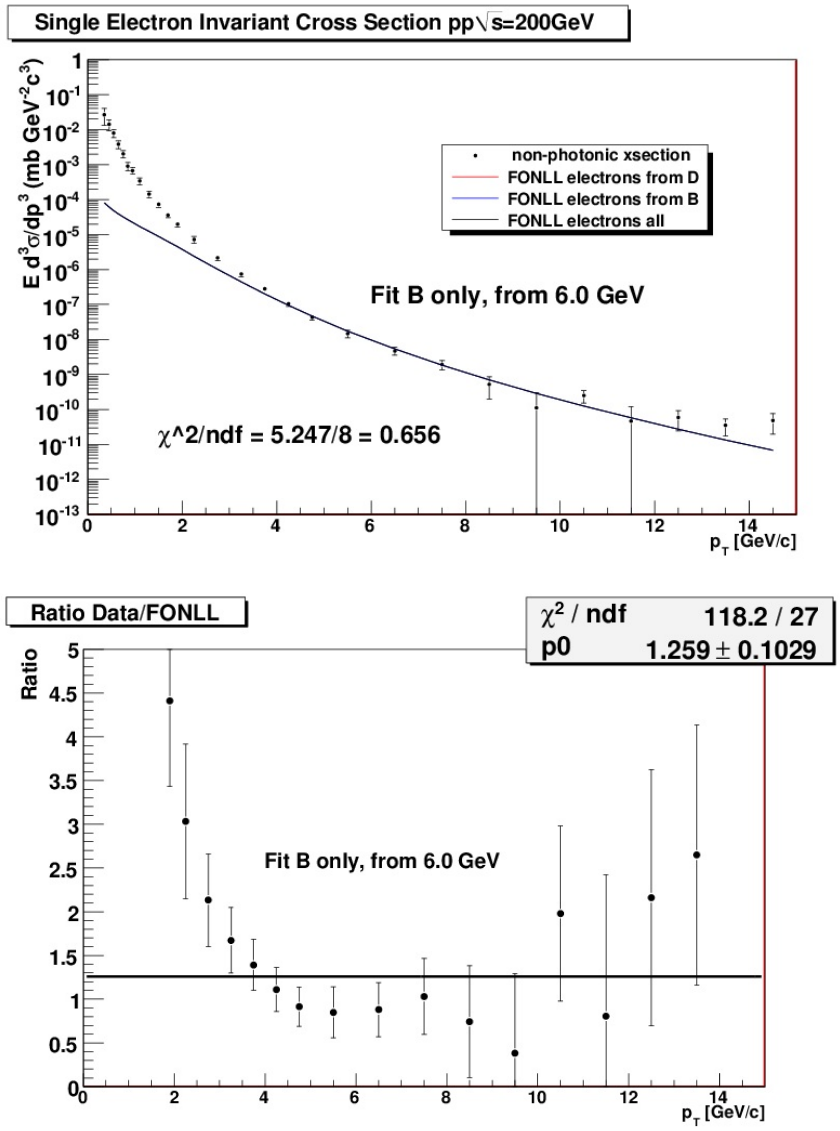

Figure 7.7: Fit to heavy flavor spectrum with B only from 6 GeV and above.

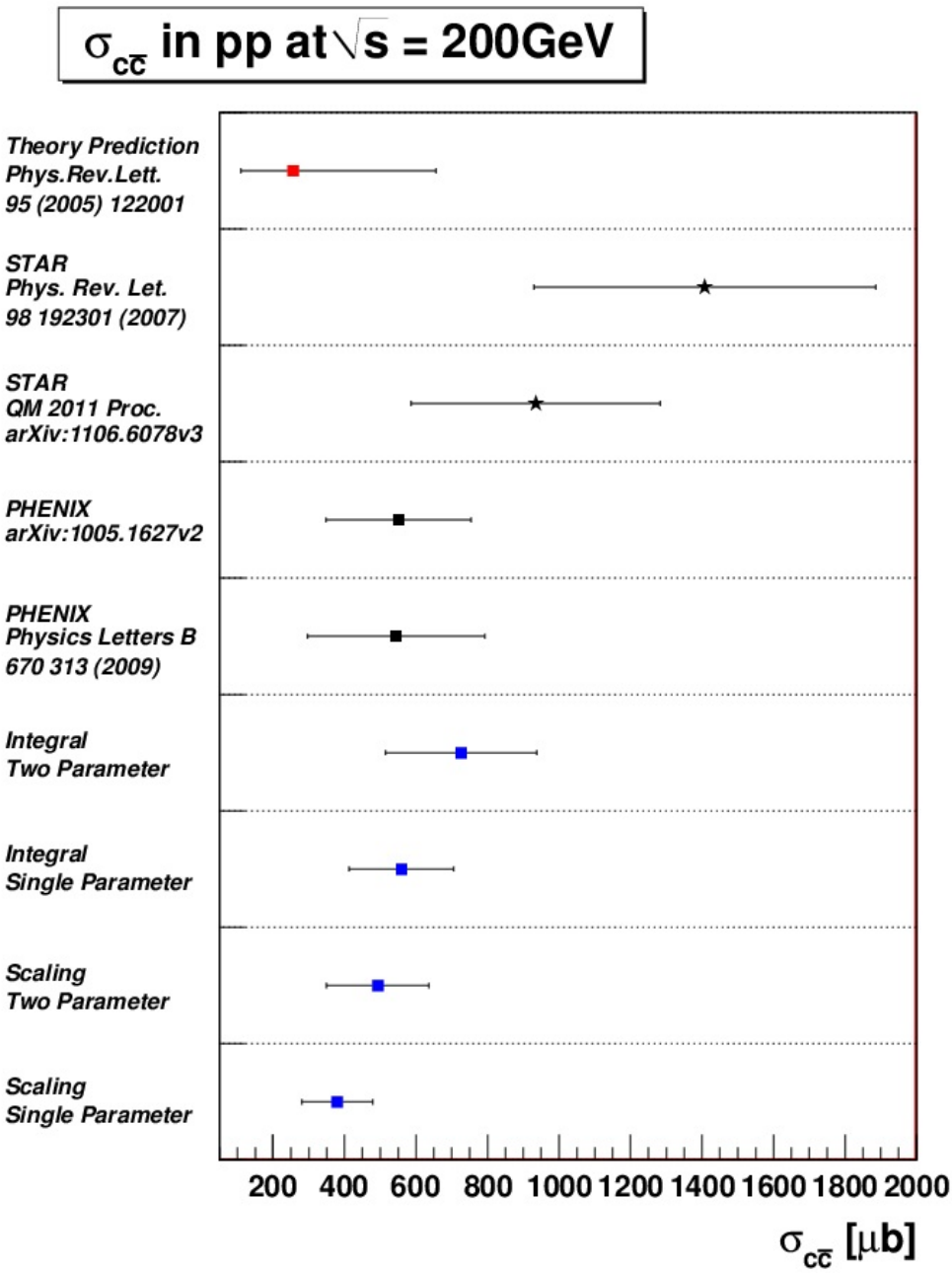

Figure 7.8: Our cross section calculations compared with other measurements and the FONLL prediction.

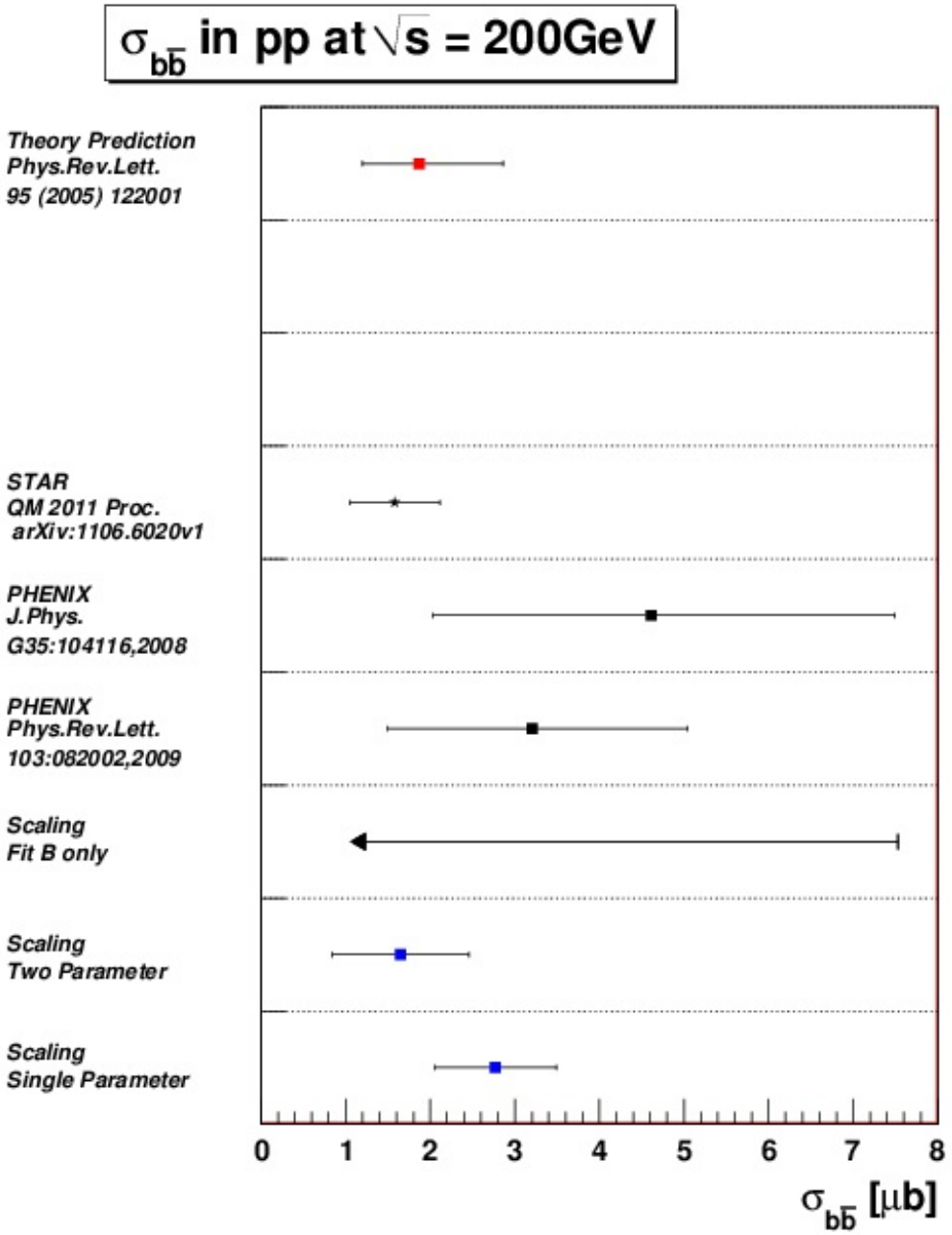

Figure 7.9: Our cross section calculations compared with other measurements and the FONLL prediction.

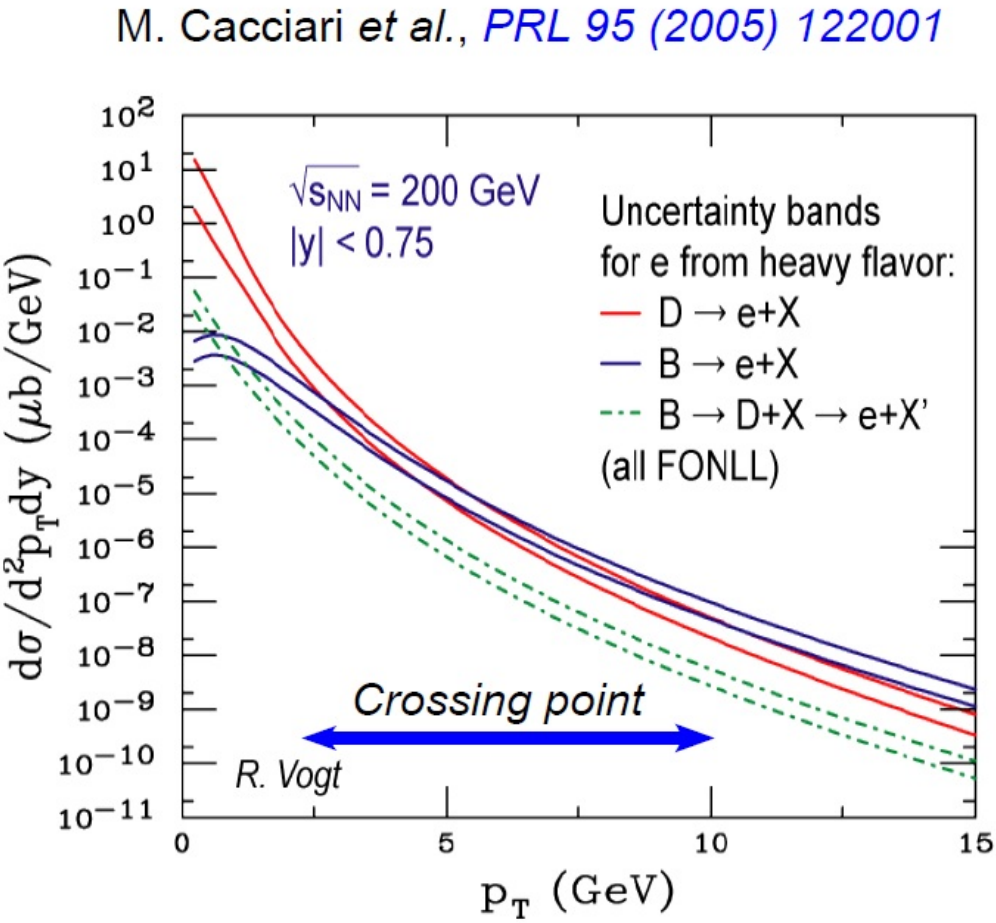

Figure 7.10: The variation of the crossing point of bottom quark dominance.

trons from bottom quarks. In Fig. 7.10 we see the variation of the crossing point to bottom dominance, the highest expected crossing point is at 10GeV so we would appear to have achieved the lever arm that we sought. However this figure also exposes the issue in the bottom calculation, the range of possible crossing points is large, from 2.5-10GeV, this is because the two spectral shapes are so similar.

This is why we proposed the three scenarios in which we varied the constraints on the bottom determination. To get an upper limit we fit the bottom FONLL shape alone to the points from 8GeV and above. In Fig. 7.9 we notice that our measurement of $\sigma_{b\bar{b}}$ consistent with theory and STAR, our measurement is at the lower range of previous PHENIX measurements.

In Figs. 7.11 & 7.12 we plot the various measurements of $\sigma_{c\bar{c}}$ and $\sigma_{b\bar{b}}$ as a function of center of mass energy for pp collisions. The 200 GeV points are our measurements, they are displaced somewhat along the X axis so as to be clearly visible. These 200 GeV points now give some restriction to the theoretical predictions, the range of the X axis is to the TeV range where the LHC experiments are working hard to add measurements

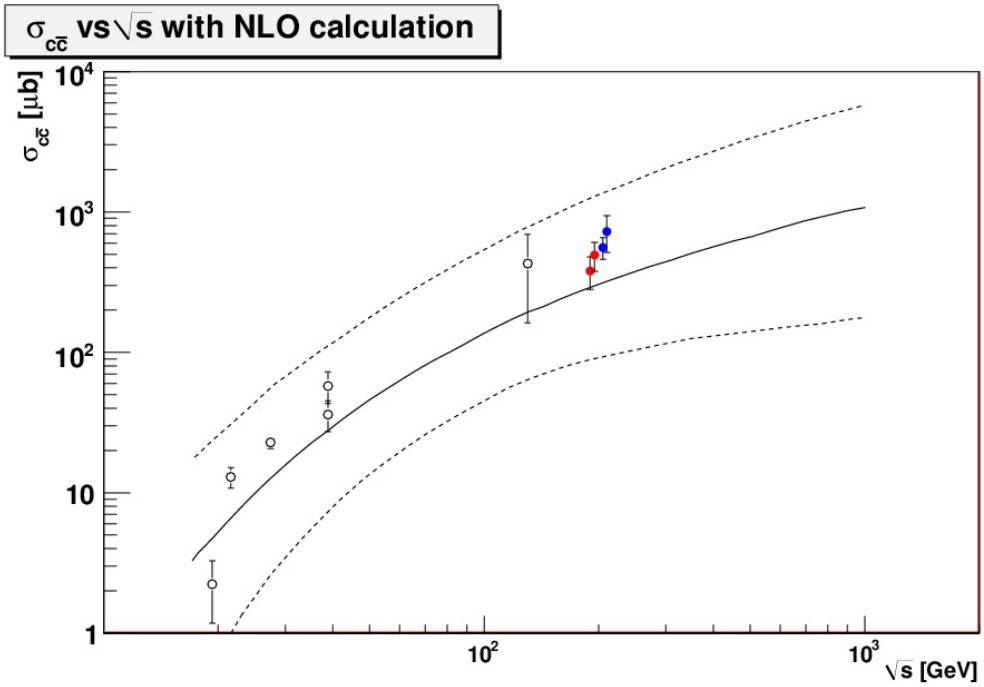

Figure 7.11: Our cross section calculations compared with other measurements and the FONLL prediction. The red and blue points are our measurements, Table 7.2. The red points are from the scaling method and the blue points are the integral method. All points are displaced slightly along the abscissa to make them visible, all measurements are at $\sqrt{s} = 200GeV$.

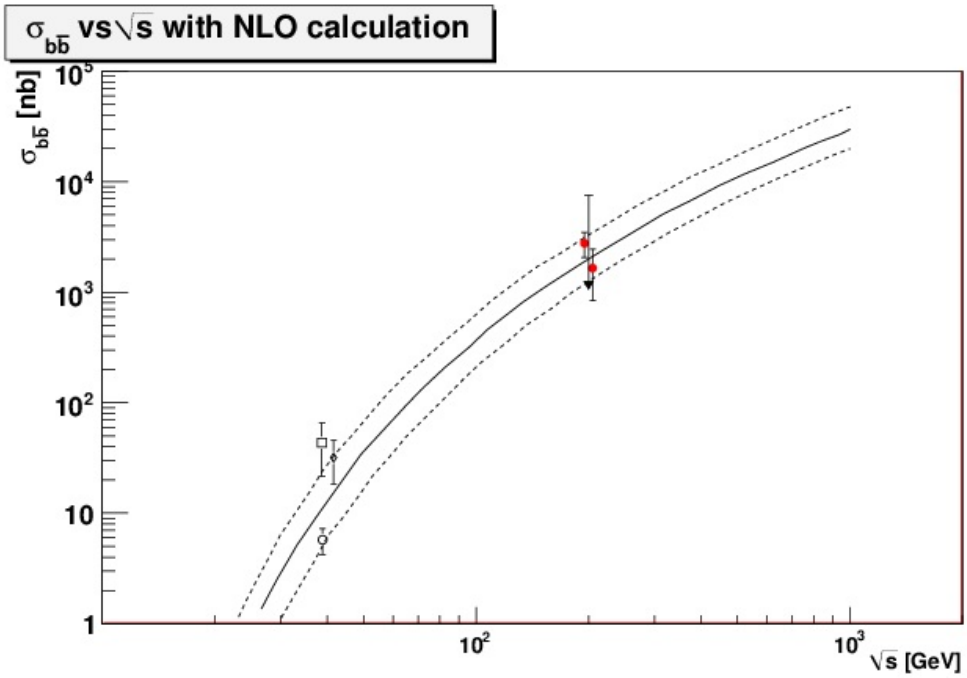

Figure 7.12: Our cross section calculations compared with other measurements and the FONLL prediction.The black arrow is the upper limit measurement and the red points are the other two measurements from Table 7.3. The red points are displaced slightly along the abscissa to make them visible, all measurements are at $\sqrt{s} = 200GeV$.

Chapter 8

Summary and Outlook

In this thesis we have presented a measurement of high p_T single electrons in pp collisions at center of mass energy of 200 GeV from heavy flavor quarks. We have significantly extended the spectrum over previously published data, from 8.5 GeV to 14.5 GeV. We did this by overcoming the issue of hadron contamination in the p_T's above 6GeV, it is at this value that the principal electron identification sub system of PHENIX, the RICH, can no longer reject hadrons.

This was done by exploiting the energy deposition characteristics of both hadrons, principally π's, and electrons in the electromagnetic calorimeters. The backgrounds inherent in this measurement at the PHENIX detector were modeled in detail to investigate the effect of each background (or lack thereof) on our measurement.

Our measurement of the heavy flavor single electron spectrum provides the pp reference that is used to compare the various collision environments as we explore the existence and properties of the Quark Gluon Plasma. However the calculation of the total cross section for charm and bottom production at this energy is also of critical importance. Heavy flavor production should provide a precise measurement of the parton distribution in the nucleon as well as nuclear shadowing effects [51]. The experiments at RHIC provide the first measurements of heavy flavor, charm and bottom, production cross section in pp collisions at 200 GeV. This allows to constrain theoretical predictions for this energy region which have significant uncertainties.[52]

We made four determinations of $\sigma_{c\bar{c}}$ and 2 of $\sigma_{b\bar{b}}$ and compared them to published data and theory. The expectation was that our single electron measurement would improve the determination of the bottom cross section since a

significant portion of our measurement contains the p_T range that is expected to be dominated by electrons from bottom quarks, however this turned out not to be conclusive as the two spectral shapes are so similar.

At the present time, PHENIX has no ability to distinguish electrons from charm and bottom, additional information is needed. In the future this will be provided by a new detector system. As a major upgrade to PHENIX a silicon vertex detector was installed in Run 10 (2010) and has begun to take data. The silicon vertex tracker will allow PHENIX to distinguish tracks from charm and bottom in AuAu collisions.[53] The inner two of four layers have four million channels and will have an occupancy rate of $< 2\%$ in a central AuAu collision. The spatial resolution of these inner layers is of the order of $50\mu m$ so the vertex detector will easily be able to separate B mesons ($c\tau = 464\mu m$) from D mesons ($c\tau = 125\mu m$).

Appendix A

Tables

R6 $n_1 \geq 5$ p_T range	MB raw $0.6 \leq E/p < 0.8$	MB raw $0.8 \leq E/p < 1.2$	ERT raw $0.6 \leq E/p < 0.8$	ERT raw $0.8 \leq E/p < 1.2$
1.2-1.4	191 ± 13.82	1130 ± 33.62	6418 ± 80.11	135996 ± 368.78
1.4-1.6	80 ± 8.94	593 ± 24.35	5885 ± 76.71	125186 ± 353.82
1.6-1.8	39 ± 6.25	322 ± 17.94	5287 ± 72.71	97236 ± 311.83
1.8-2.0	21 ± 4.58	188 ± 13.71	4464 ± 66.81	68542 ± 261.81
2.0-2.5	32 ± 5.66	196 ± 14.00	7254 ± 85.17	85127 ± 291.77
2.5-3.0	8 ± 2.83	71 ± 8.43	3166 ± 56.27	29818 ± 172.68
3.0-3.5	5 ± 2.24	22 ± 4.69	1341 ± 36.62	11300 ± 106.30
3.5-4.0	0 ± 0.00	7 ± 2.65	541 ± 23.26	4686 ± 68.45
4.0-4.5	1 ± 1.00	5 ± 2.24	276 ± 16.61	2159 ± 46.47
4.5-5.0	1 ± 1.00	2 ± 1.41	151 ± 12.29	1061 ± 32.57
5.0-6.0	0 ± 0.00	3 ± 1.73	123 ± 11.09	855 ± 29.24
6.0-7.0	0 ± 0.00	0 ± 0.00	93 ± 9.64	329 ± 18.14
7.0-8.0	0 ± 0.00	0 ± 0.00	83 ± 9.11	165 ± 12.85
8.0-9.0	0 ± 0.00	1 ± 1.00	72 ± 8.49	81 ± 9.00
9.0-10.0	0 ± 0.00	2 ± 1.41	52 ± 7.21	42 ± 6.48
10.0-11.0	0 ± 0.00	0 ± 0.00	24 ± 4.90	28 ± 5.29
11.0-12.0	0 ± 0.00	0 ± 0.00	23 ± 4.80	15 ± 3.87
12.0-13.0	0 ± 0.00	0 ± 0.00	8 ± 2.83	8 ± 2.83
13.0-14.0	0 ± 0.00	0 ± 0.00	3 ± 1.73	4 ± 2.00
14.0-15.0	0 ± 0.00	0 ± 0.00	7 ± 2.65	6 ± 2.45

Table A.1: raw numbers Run6 $n_1 \geq 5$

p_T range	Data Raw Counts	Yield Fraction	Yield Electrons	Cocktail Scaled	Heavy Flavor Raw Counts
1.2-1.4	1130.00 ± 33.62	0.999995 ± 0	1129.99 ± 33.62	811.57 ± 0.00	318.43 ± 9.47
1.4-1.6	593.00 ± 24.35	0.999992 ± 0	593.00 ± 24.35	405.76 ± 0.00	187.24 ± 7.69
1.6-1.8	322.00 ± 17.94	0.999976 ± 0	321.99 ± 17.94	212.62 ± 0.00	109.38 ± 6.10
1.8-2.0	188.00 ± 13.71	0.999933 ± 0	187.99 ± 13.71	117.57 ± 0.00	70.42 ± 5.14
2.0-2.5	196.00 ± 14.00	0.999842 ± 0	195.97 ± 14.00	124.84 ± 0.00	71.13 ± 5.08
2.5-3.0	29818.00 ± 172.68	0.999387 ± 0	29799.72 ± 172.57	16415.30 ± 0.00	13384.42 ± 77.51
3.0-3.5	11300.00 ± 106.30	0.99796 ± 0	11276.95 ± 106.08	5822.16 ± 0.00	5454.79 ± 51.31
3.5-4.0	4686.00 ± 68.45	0.995033 ± 0	4662.72 ± 68.11	2325.03 ± 0.00	2337.69 ± 34.15
4.0-4.5	2159.00 ± 46.47	0.985472 ± 0	2127.63 ± 45.79	1031.68 ± 0.00	1095.95 ± 23.59
4.5-5.0	1061.00 ± 32.57	0.959388 ± 0	1017.91 ± 31.25	495.56 ± 0.00	522.35 ± 16.04
5.0-6.0	855.00 ± 29.24	0.917993 ± 0	784.88 ± 26.84	401.56 ± 0.00	383.32 ± 13.11
6.0-7.0	329.00 ± 18.14	0.853633 ± 0	280.85 ± 15.48	130.11 ± 0.00	150.74 ± 8.31
7.0-8.0	165.00 ± 12.85	0.682127 ± 0	112.55 ± 8.76	50.10 ± 0.00	62.46 ± 4.86
8.0-9.0	81.00 ± 9.00	0.545 ± 0	44.15 ± 4.91	21.86 ± 0.00	22.28 ± 2.48
9.0-10.0	42.00 ± 6.48	0.456371 ± 0	19.17 ± 2.96	10.53 ± 0.00	8.63 ± 1.33
10.0-11.0	28.00 ± 5.29	0.407669 ± 0	11.41 ± 2.16	5.48 ± 0.00	5.93 ± 1.12
11.0-12.0	15.00 ± 3.87	0.368369 ± 0	5.53 ± 1.43	3.02 ± 0.00	2.51 ± 0.65
12.0-13.0	8.00 ± 2.83	0.357233 ± 0	2.86 ± 1.01	1.74 ± 0.00	1.12 ± 0.40
13.0-14.0	4.00 ± 2.00	0.305654 ± 0	1.22 ± 0.61	1.03 ± 0.00	0.19 ± 0.09
14.0-15.0	6.00 ± 2.45	0.227798 ± 0	1.37 ± 0.56	0.63 ± 0.00	0.73 ± 0.30

Table A.2: Heavy flavor raw yield, yield fraction.

p_T range	Data Raw Counts	Cocktail Scaled	$\pi's$ Scaled Fit	Heavy Flavor Raw Counts
1.2-1.4	1130 ± 33.62	811.57 ± 0	0.00 ± 0.00	318.44 ± 9.47
1.4-1.6	593 ± 24.35	405.76 ± 0	0.00 ± 0.00	187.25 ± 7.69
1.6-1.8	322 ± 17.94	212.62 ± 0	0.00 ± 0.00	109.39 ± 6.10
1.8-2.0	188 ± 13.71	117.57 ± 0	0.00 ± 0.00	70.43 ± 5.14
2.0-2.5	196 ± 14.00	124.84 ± 0	0.00 ± 0.00	71.16 ± 5.08
2.5-3.0	29818 ± 172.68	16415.30 ± 0	0.00 ± 0.00	13402.70 ± 77.62
3.0-3.5	11300 ± 106.30	5822.16 ± 0	0.00 ± 0.00	5477.84 ± 51.53
3.5-4.0	4686 ± 68.45	2325.03 ± 0	0.00 ± 0.00	2360.97 ± 34.49
4.0-4.5	2159 ± 46.47	1031.68 ± 0	27.57 ± 5.25	1099.75 ± 23.67
4.5-5.0	1061 ± 32.57	495.56 ± 0	18.72 ± 4.33	546.72 ± 16.78
5.0-6.0	855 ± 29.24	401.56 ± 0	17.96 ± 4.24	435.48 ± 14.89
6.0-7.0	329 ± 18.14	130.11 ± 0	40.36 ± 6.35	158.54 ± 8.74
7.0-8.0	165 ± 12.85	50.10 ± 0	30.22 ± 5.50	84.68 ± 6.59
8.0-9.0	81 ± 9.00	21.86 ± 0	29.36 ± 5.42	29.78 ± 3.31
9.0-10.0	42 ± 6.48	10.53 ± 0	22.66 ± 4.76	8.80 ± 1.36
10.0-11.0	28 ± 5.29	5.48 ± 0	12.56 ± 3.54	9.96 ± 1.88
11.0-12.0	15 ± 3.87	3.02 ± 0	5.59 ± 2.36	6.39 ± 1.65
12.0-13.0	8 ± 2.83	1.74 ± 0	3.75 ± 1.94	2.52 ± 0.89
13.0-14.0	4 ± 2.00	1.03 ± 0	2.22 ± 1.49	0.74 ± 0.37
14.0-15.0	6 ± 2.45	0.63 ± 0	1.74 ± 1.32	3.62 ± 1.48

Table A.3: Heavy flavor raw yield, $\pi's$ from fit.

p_T range	Data Raw Counts	Cocktail Scaled	$\pi's$ Abs Norm	Heavy Flavor Raw Counts
1.2-1.4	1130 ± 33.62	811.57 ± 0	0.00 ± 0.00	318.44 ± 9.47
1.4-1.6	593 ± 24.35	405.76 ± 0	0.00 ± 0.00	187.25 ± 7.69
1.6-1.8	322 ± 17.94	212.62 ± 0	0.00 ± 0.00	109.39 ± 6.10
1.8-2.0	188 ± 13.71	117.57 ± 0	0.00 ± 0.00	70.43 ± 5.14
2.0-2.5	196 ± 14.00	124.84 ± 0	0.00 ± 0.00	71.16 ± 5.08
2.5-3.0	29818 ± 172.68	16415.30 ± 0	0.00 ± 0.00	13402.70 ± 77.62
3.0-3.5	11300 ± 106.30	5822.16 ± 0	0.00 ± 0.00	5477.84 ± 51.53
3.5-4.0	4686 ± 68.45	2325.03 ± 0	0.00 ± 0.00	2360.97 ± 34.49
4.0-4.5	2159 ± 46.47	1031.68 ± 0	0.06 ± 0.04	1127.26 ± 24.26
4.5-5.0	1061 ± 32.57	495.56 ± 0	6.33 ± 0.82	559.11 ± 17.16
5.0-6.0	855 ± 29.24	401.56 ± 0	60.35 ± 2.37	393.09 ± 13.44
6.0-7.0	329 ± 18.14	130.11 ± 0	105.18 ± 3.39	93.71 ± 5.17
7.0-8.0	165 ± 12.85	50.10 ± 0	75.82 ± 2.50	39.08 ± 3.04
8.0-9.0	81 ± 9.00	21.86 ± 0	45.65 ± 1.52	13.49 ± 1.50
9.0-10.0	42 ± 6.48	10.53 ± 0	24.23 ± 0.81	7.23 ± 1.12
10.0-11.0	28 ± 5.29	5.48 ± 0	15.71 ± 0.51	6.81 ± 1.29
11.0-12.0	15 ± 3.87	3.02 ± 0	8.22 ± 0.28	3.76 ± 0.97
12.0-13.0	8 ± 2.83	1.74 ± 0	4.54 ± 0.16	1.73 ± 0.61
13.0-14.0	4 ± 2.00	1.03 ± 0	2.79 ± 0.09	0.18 ± 0.09
14.0-15.0	6 ± 2.45	0.63 ± 0	1.52 ± 0.06	3.84 ± 1.57

Table A.4: Heavy flavor raw yield, $\pi's$ from absolute normalization.

p_T range	Data Raw Counts	Cocktail Absolute Norm	π's $R_\pi * \text{lo_window}$	Heavy Flavor Raw Counts
1.2-1.4	1130 ± 33.62	811.57 ± 0	0.00 ± 0.00	318.44 ± 17.84
1.4-1.6	593 ± 24.35	405.76 ± 0	0.00 ± 0.00	187.25 ± 13.68
1.6-1.8	322 ± 17.94	212.62 ± 0	0.00 ± 0.00	109.39 ± 10.46
1.8-2.0	188 ± 13.71	117.57 ± 0	0.00 ± 0.00	70.43 ± 8.39
2.0-2.5	196 ± 14.00	124.84 ± 0	0.00 ± 0.00	71.16 ± 8.44
2.5-3.0	29818 ± 172.68	16415.30 ± 0	0.00 ± 0.00	13402.70 ± 115.77
3.0-3.5	11300 ± 106.30	5822.16 ± 0	0.00 ± 0.00	5477.84 ± 74.01
3.5-4.0	4686 ± 68.45	2325.03 ± 0	0.00 ± 0.00	2360.97 ± 48.59
4.0-4.5	2159 ± 46.47	1031.68 ± 0	0.00 ± 0.00	1127.32 ± 33.58
4.5-5.0	1061 ± 32.57	495.56 ± 0	123.01 ± 3.78	442.43 ± 21.03
5.0-6.0	855 ± 29.24	401.56 ± 0	93.50 ± 3.20	359.94 ± 18.97
6.0-7.0	329 ± 18.14	130.11 ± 0	64.49 ± 3.56	134.40 ± 11.59
7.0-8.0	165 ± 12.85	50.10 ± 0	52.58 ± 4.09	62.33 ± 7.89
8.0-9.0	81 ± 9.00	21.86 ± 0	41.78 ± 4.64	17.36 ± 4.17
9.0-10.0	42 ± 6.48	10.53 ± 0	27.76 ± 4.28	3.70 ± 1.92
10.0-11.0	28 ± 5.29	5.48 ± 0	11.86 ± 2.24	10.66 ± 3.26
11.0-12.0	15 ± 3.87	3.02 ± 0	10.61 ± 2.74	1.37 ± 1.17
12.0-13.0	8 ± 2.83	1.74 ± 0	3.48 ± 1.23	2.78 ± 1.67
13.0-14.0	4 ± 2.00	1.03 ± 0	1.25 ± 0.62	1.72 ± 1.31
14.0-15.0	6 ± 2.45	0.63 ± 0	2.82 ± 1.15	2.54 ± 1.59

Table A.5: Raw Non-Photonic $\pi's$ subtracted using R_π Run6 $n_1 \geq 5$

p_T range	Data Raw Counts	Cocktail Absolute Norm	Data lo window	γ conversions lo window	π's $R_\pi *$ lo_window	Heavy Flavor Raw Counts
1.2-1.4	1130 ± 33.62	811.57 ± 0	191 ± 13.82	117.88 ± 10.8571	0.00 ± 0.00	318.44 ± 9.47
1.4-1.6	593 ± 24.35	405.76 ± 0	80 ± 8.94	48.99 ± 6.99919	0.00 ± 0.00	187.25 ± 7.69
1.6-1.8	322 ± 17.94	212.62 ± 0	39 ± 6.25	31.12 ± 5.57838	0.00 ± 0.00	109.39 ± 6.10
1.8-2.0	188 ± 13.71	117.57 ± 0	21 ± 4.58	17.90 ± 4.23036	0.00 ± 0.00	70.43 ± 5.14
2.0-2.5	196 ± 14.00	124.84 ± 0	32 ± 5.66	18.87 ± 4.34356	0.00 ± 0.00	71.16 ± 5.08
2.5-3.0	29818 ± 172.68	16415.30 ± 0	3166 ± 56.27	2312.34 ± 48.0868	0.00 ± 0.00	13402.70 ± 77.62
3.0-3.5	11300 ± 106.30	5822.16 ± 0	1341 ± 36.62	830.04 ± 28.8104	0.00 ± 0.00	5477.84 ± 51.53
3.5-4.0	4686 ± 68.45	2325.03 ± 0	541 ± 23.26	322.59 ± 17.9607	0.00 ± 0.00	2360.97 ± 34.49
4.0-4.5	2159 ± 46.47	1031.68 ± 0	276 ± 16.61	183.36 ± 13.541	0.00 ± 0.00	1127.32 ± 24.26
4.5-5.0	1061 ± 32.57	495.56 ± 0	151 ± 12.29	84.83 ± 9.2101	53.91 ± 1.65	511.53 ± 15.70
5.0-6.0	855 ± 29.24	401.56 ± 0	123 ± 11.09	85.96 ± 9.2712	28.16 ± 0.96	425.28 ± 14.54
6.0-7.0	329 ± 18.14	130.11 ± 0	93 ± 9.64	25.19 ± 5.01865	47.02 ± 2.59	151.87 ± 8.37
7.0-8.0	165 ± 12.85	50.10 ± 0	83 ± 9.11	14.58 ± 3.81866	43.34 ± 3.37	71.56 ± 5.57
8.0-9.0	81 ± 9.00	21.86 ± 0	72 ± 8.49	8.32 ± 2.885	36.95 ± 4.11	22.19 ± 2.47
9.0-10.0	42 ± 6.48	10.53 ± 0	52 ± 7.21	4.36 ± 2.08846	25.43 ± 3.92	6.03 ± 0.93
10.0-11.0	28 ± 5.29	5.48 ± 0	24 ± 4.90	2.52 ± 1.58692	10.62 ± 2.01	11.90 ± 2.25
11.0-12.0	15 ± 3.87	3.02 ± 0	23 ± 4.80	1.44 ± 1.19932	9.95 ± 2.57	2.04 ± 0.53
12.0-13.0	8 ± 2.83	1.74 ± 0	8 ± 2.83	0.82 ± 0.907563	3.12 ± 1.10	3.14 ± 1.11
13.0-14.0	4 ± 2.00	1.03 ± 0	3 ± 1.73	0.67 ± 0.820471	0.97 ± 0.48	2.00 ± 1.00
14.0-15.0	6 ± 2.45	0.63 ± 0	7 ± 2.65	0.38 ± 0.613641	2.67 ± 1.09	2.70 ± 1.10

Table A.6: Raw Non-Photonic $\pi's$ subtracted using R_π Run6 $n_1 \geq 5$

p_T range (GeV)	Inv. Cross Sect.	stat. error	sys. error
1.2-1.4	1.429E-04	1.535E-06	2.872E-05
1.4-1.6	7.271E-05	6.759E-07	1.276E-05
1.6-1.8	3.623E-05	3.170E-07	6.003E-06
1.8-2.0	1.988E-05	1.619E-07	3.117E-06
2.0-2.5	7.256E-06	3.641E-08	1.493E-06
2.5-3.0	2.183E-06	8.935E-09	3.843E-07
3.0-3.5	7.459E-07	2.593E-09	1.185E-07
3.5-4.0	2.798E-07	8.602E-10	4.163E-08
4.0-4.5	1.051E-07	5.044E-10	1.690E-08
4.5-5.0	4.273E-08	4.765E-10	7.428E-09
5.0-6.0	1.486E-08	1.856E-10	3.620E-09
6.0-7.0	4.741E-09	1.478E-10	1.169E-09
7.0-8.0	1.925E-09	1.290E-10	5.656E-10
8.0-9.0	5.278E-10	1.103E-10	3.111E-10
9.0-10.0	1.112E-10	8.742E-11	1.771E-10
10.0-11.00	2.504E-10	5.526E-11	8.052E-11
11.00-12.00	4.666E-11	4.958E-11	5.596E-11
12.00-13.00	5.933E-11	2.829E-11	2.022E-11
13.00-14.00	3.575E-11	1.659E-11	8.014E-12
14.00-15.00	4.864E-11	2.463E-11	1.507E-11

Table A.7: Differential invariant cross section of electrons ($(N_{e^+} + N_{e^-})/2$) from heavy-flavor decays for 200 GeV $p + p$ collisions at mid-rapidity. The cross section and corresponding errors are in units of millibarns. This table is in reference to Fig. 7.3

p_T range (GeV)	Inv. Cross Sect.	sys. error cocktail	sys. error R_{pi}	sys. error "combined"
1.2-1.4	1.429E-04	2.491E-05	0.000E+00	1.429E-05
1.4-1.6	7.271E-05	1.049E-05	0.000E+00	7.271E-06
1.6-1.8	3.623E-05	4.786E-06	0.000E+00	3.623E-06
1.8-2.0	1.988E-05	2.401E-06	0.000E+00	1.988E-06
2.0-2.5	7.256E-06	1.305E-06	0.000E+00	7.256E-07
2.5-3.0	2.183E-06	3.163E-07	0.000E+00	2.183E-07
3.0-3.5	7.459E-07	9.202E-08	0.000E+00	7.459E-08
3.5-4.0	2.798E-07	3.082E-08	0.000E+00	2.798E-08
4.0-4.5	1.051E-07	1.141E-08	6.718E-09	1.051E-08
4.5-5.0	4.273E-08	4.696E-09	3.856E-09	4.273E-09
5.0-6.0	1.486E-08	2.512E-09	2.142E-09	1.486E-09
6.0-7.0	4.741E-09	6.631E-10	8.382E-10	4.741E-10
7.0-8.0	1.925E-09	2.203E-10	4.840E-10	1.925E-10
8.0-9.0	5.278E-10	7.155E-11	2.982E-10	5.278E-11
9.0-10.0	1.112E-10	2.665E-11	1.747E-10	1.112E-11
10.0-11.00	2.504E-10	1.790E-11	7.441E-11	2.504E-11
11.00-12.00	4.666E-11	6.963E-12	5.533E-11	4.666E-12
12.00-13.00	5.933E-11	4.421E-12	1.881E-11	5.933E-12
13.00-14.00	3.575E-11	2.502E-12	6.722E-12	3.575E-12
14.00-15.00	4.864E-11	1.851E-12	1.414E-11	4.864E-12

Table A.8: Individual Systematic Errors

Appendix B

Supplementary Figures

B.1 eID Selection Cut Profiles

B.1.1 EMC Matching

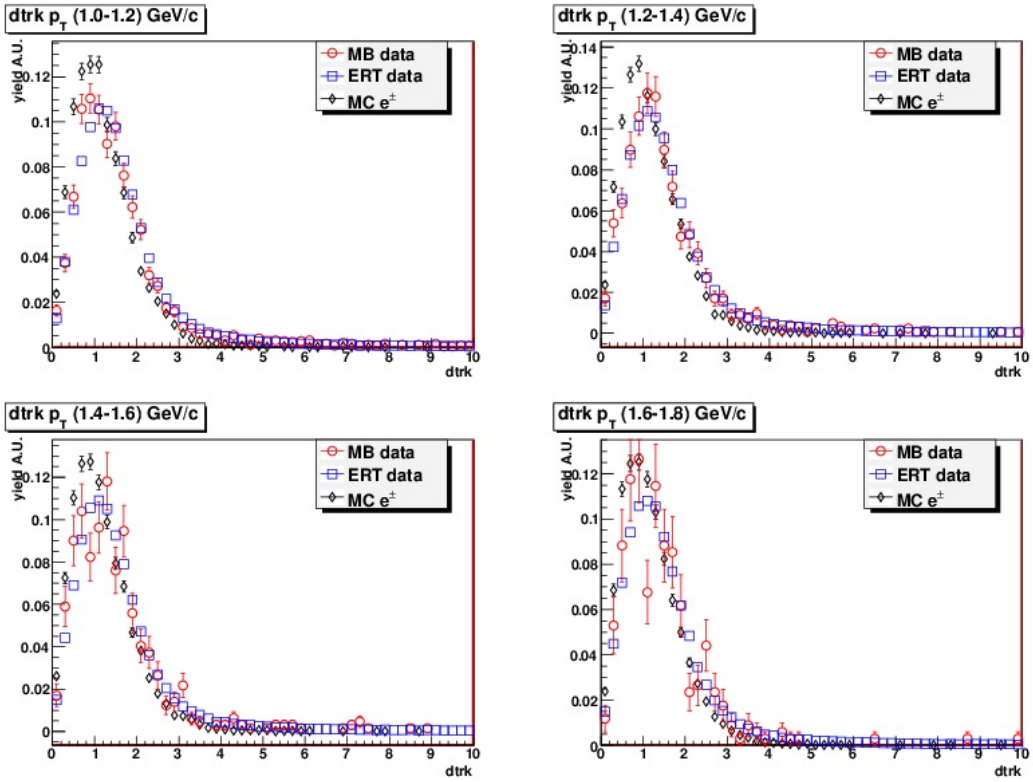

Figure B.1: EMC matching cut profiles.

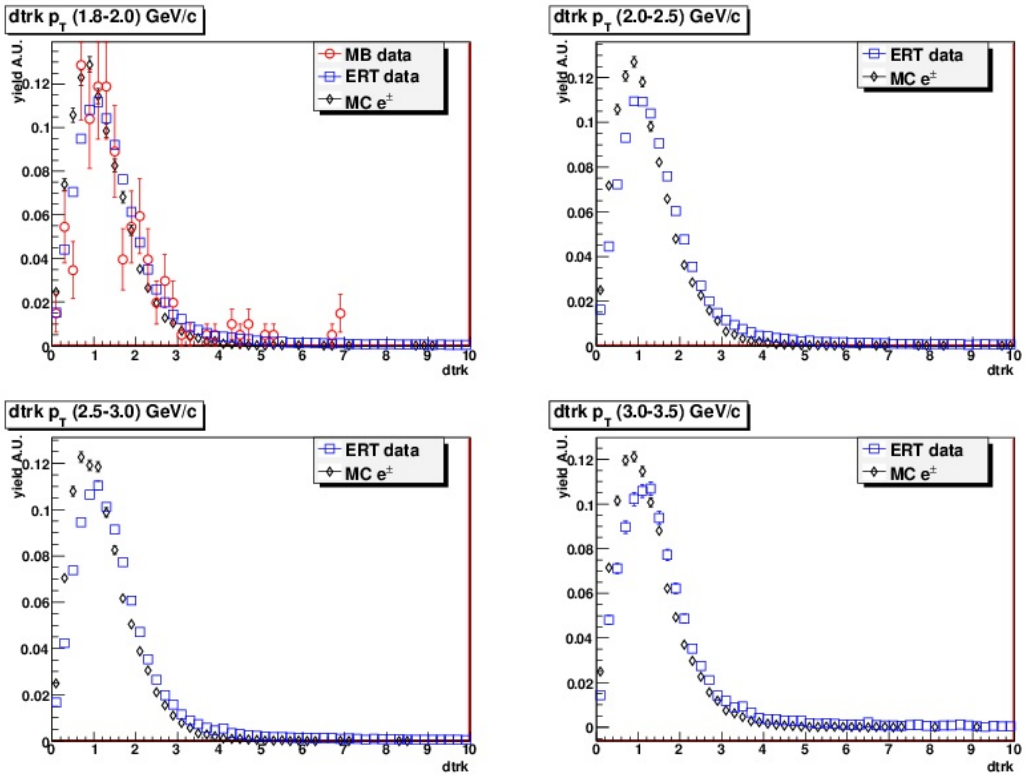

Figure B.2: EMC matching cut profiles.

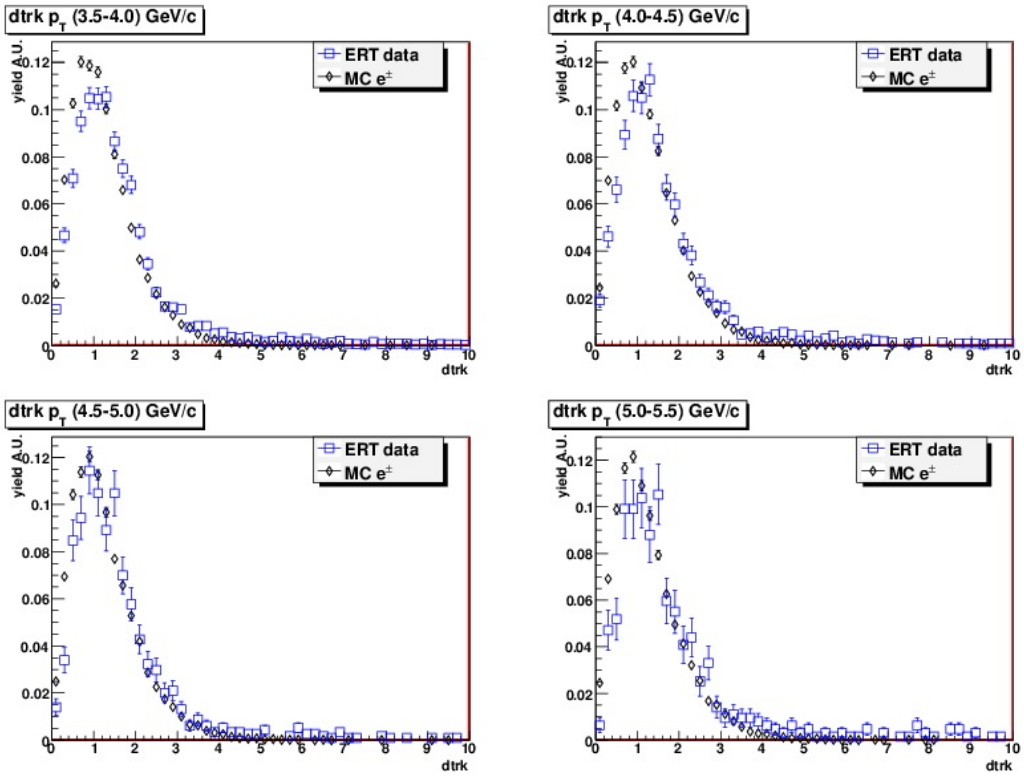

Figure B.3: EMC matching cut profiles.

B.1.2 Shower Shape

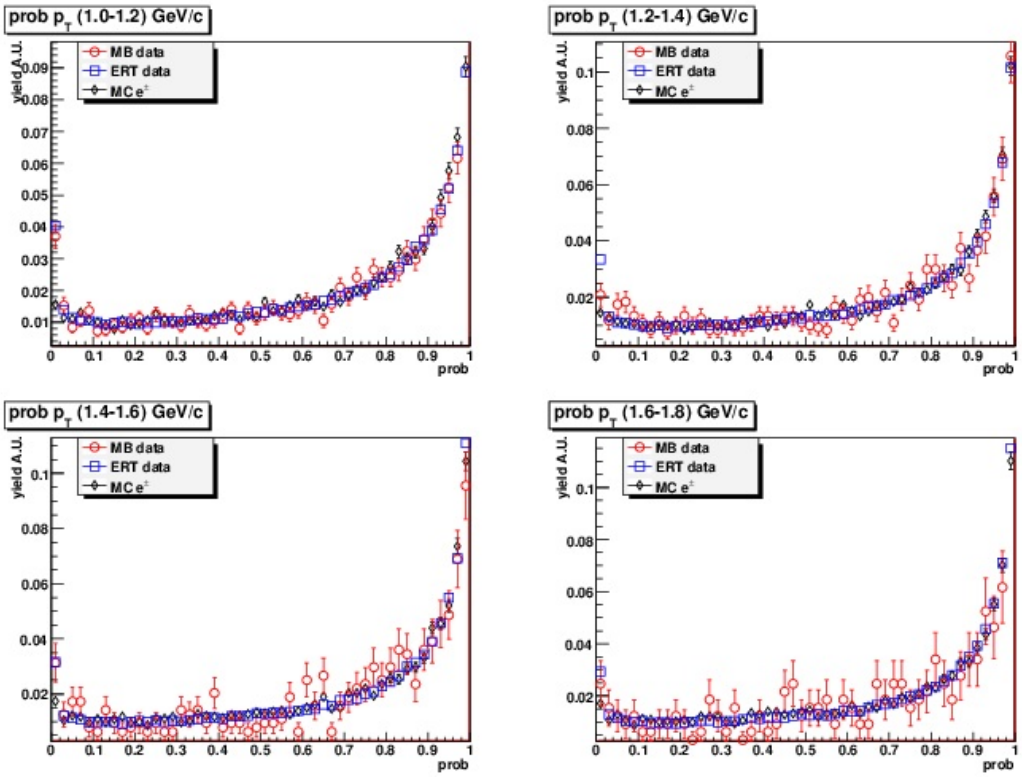

Figure B.4: Shower shape cut profiles.

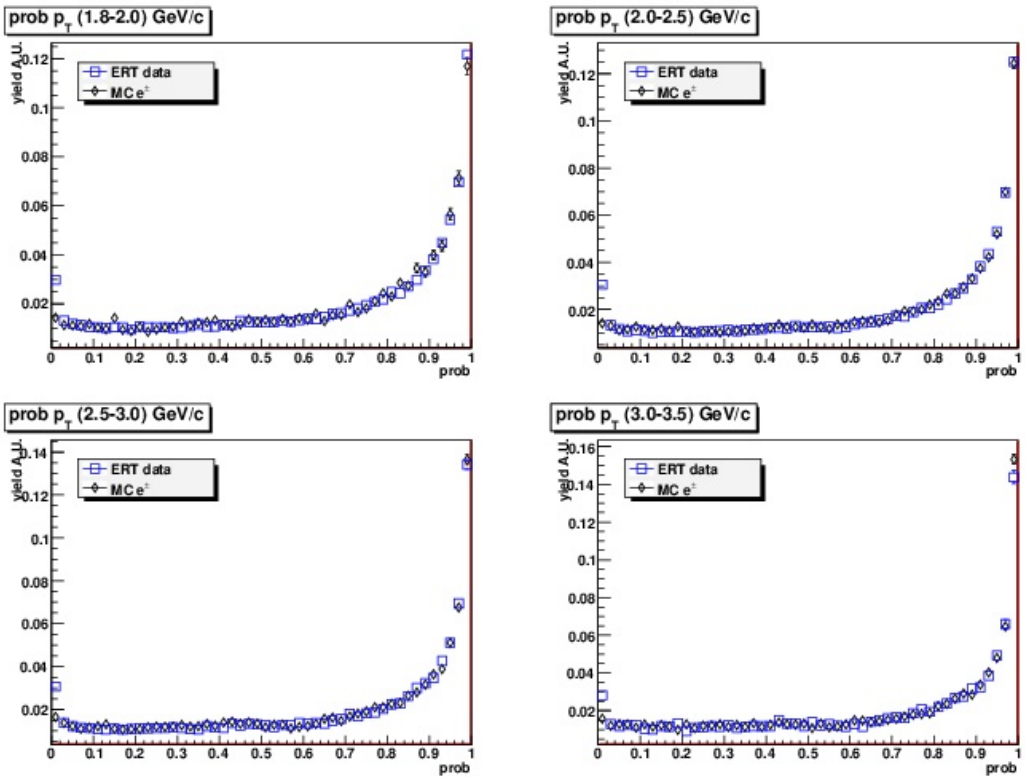

Figure B.5: Shower shape cut profiles.

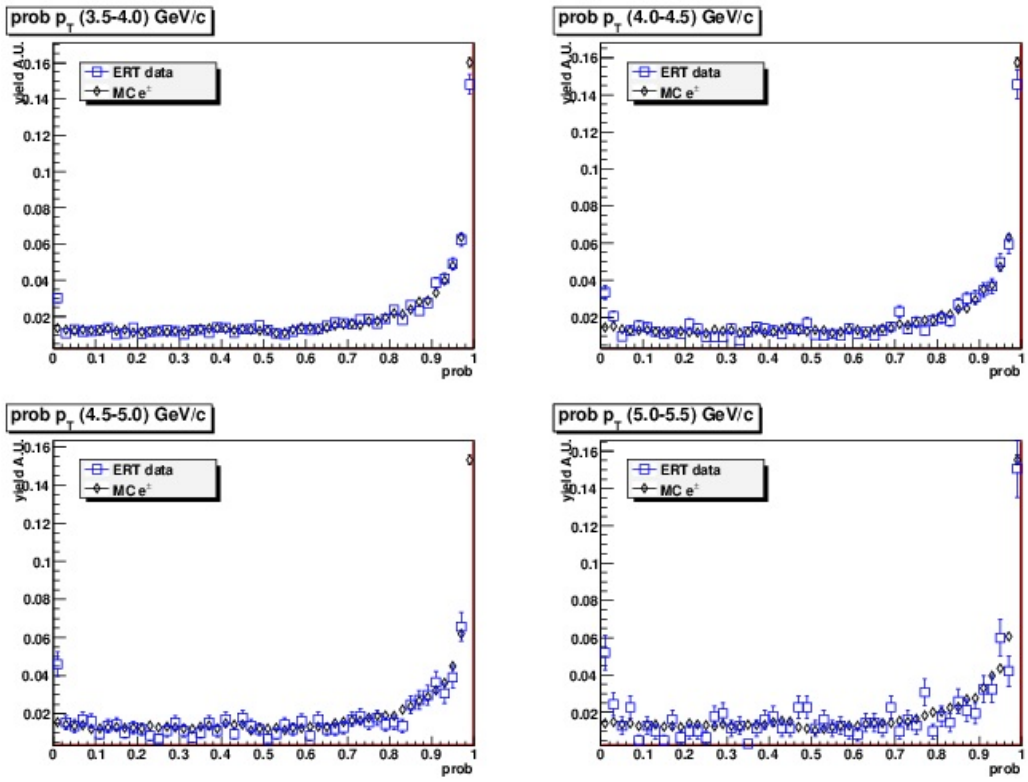

Figure B.6: Shower shape cut profiles.

B.1.3 RICH Variable

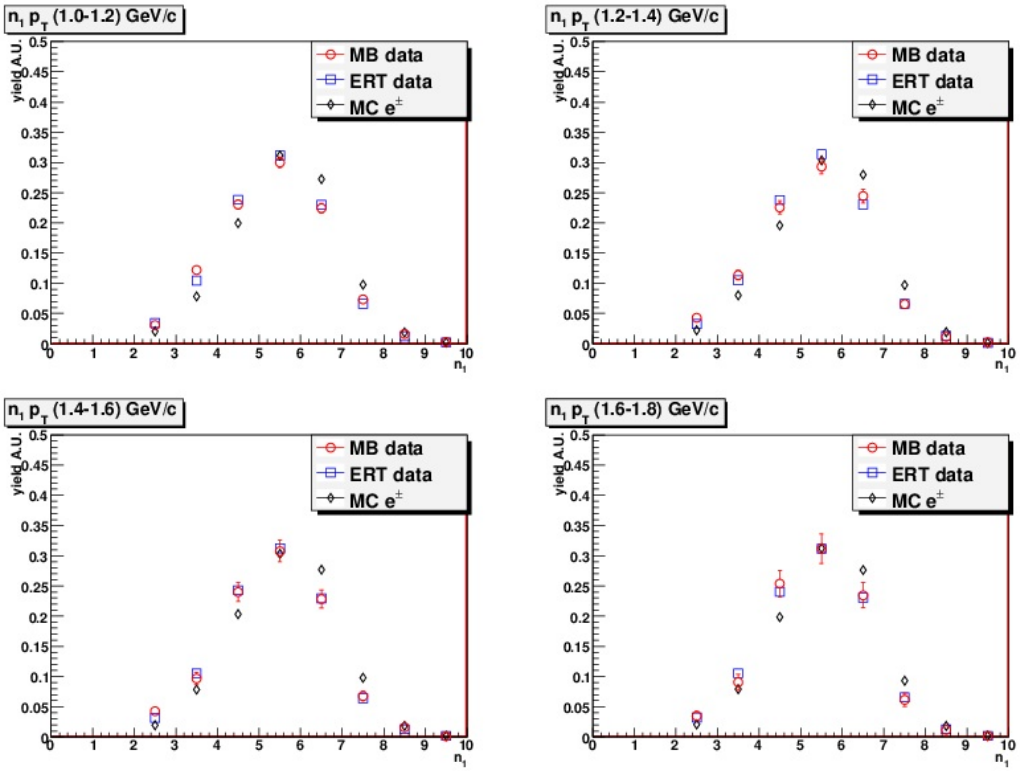

Figure B.7: RICH cut profiles.

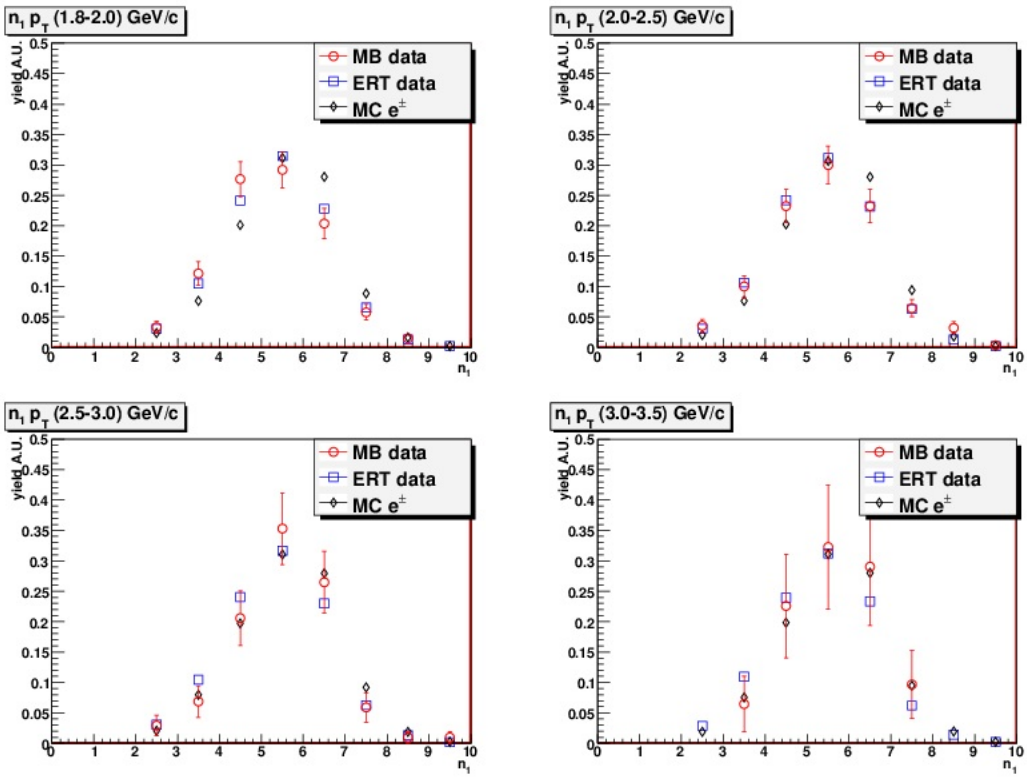

Figure B.8: RICH cut profiles.

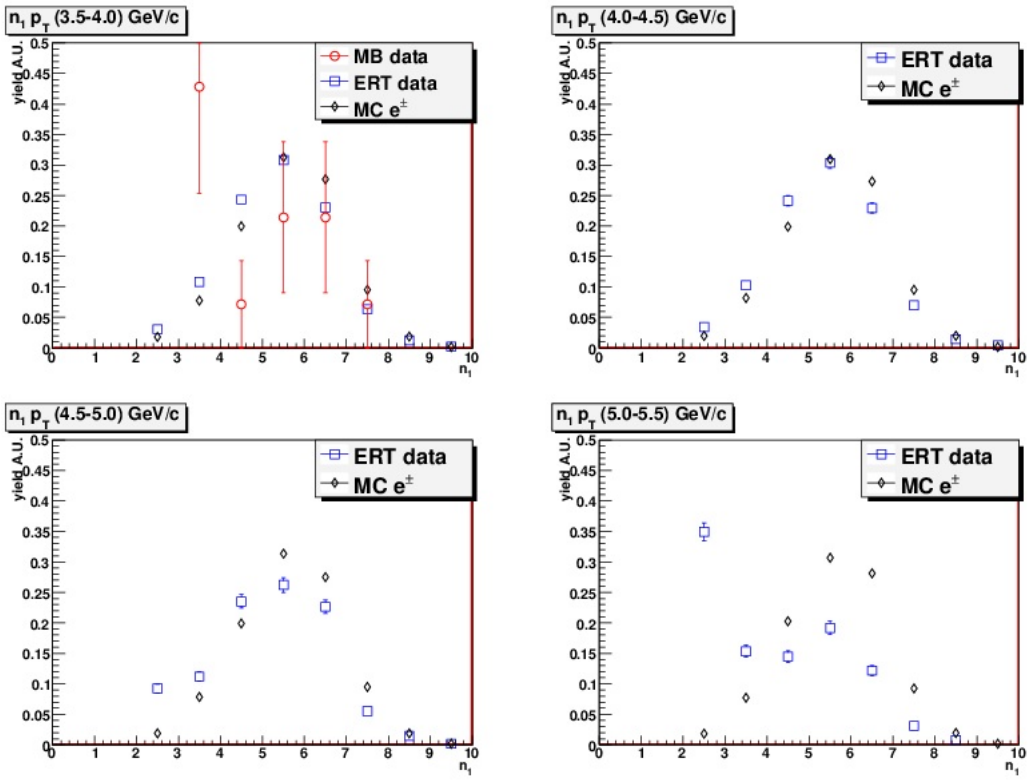

Figure B.9: RICH cut profiles.

B.2 Fits to electron E/p profiles

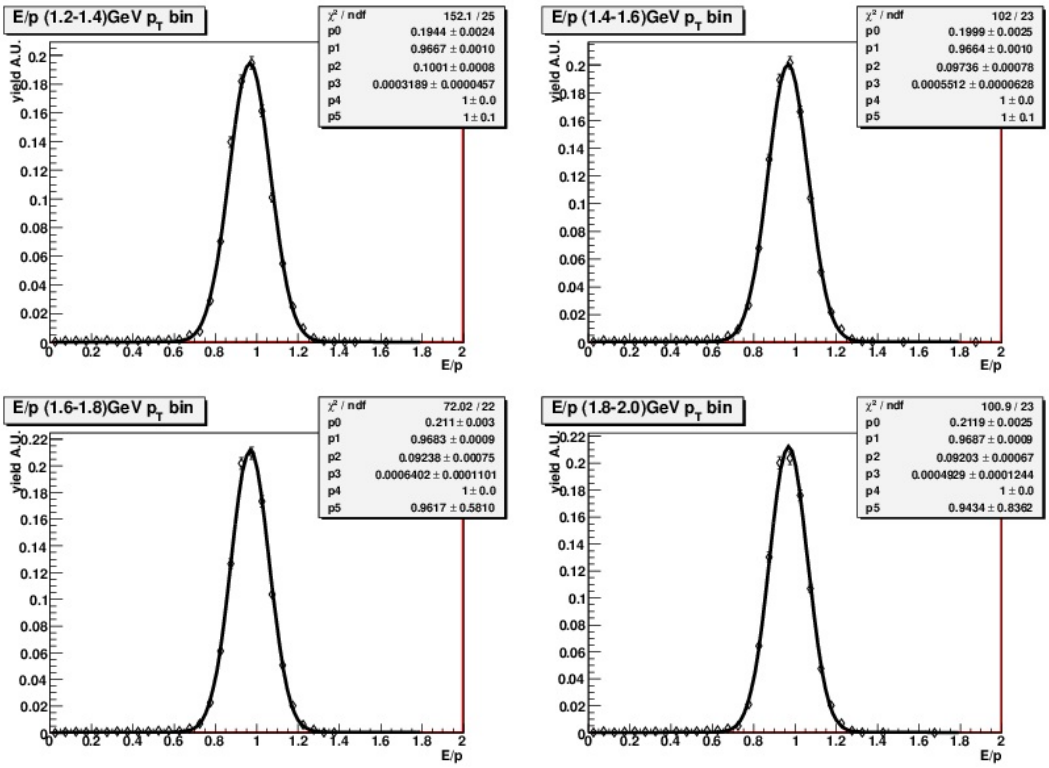

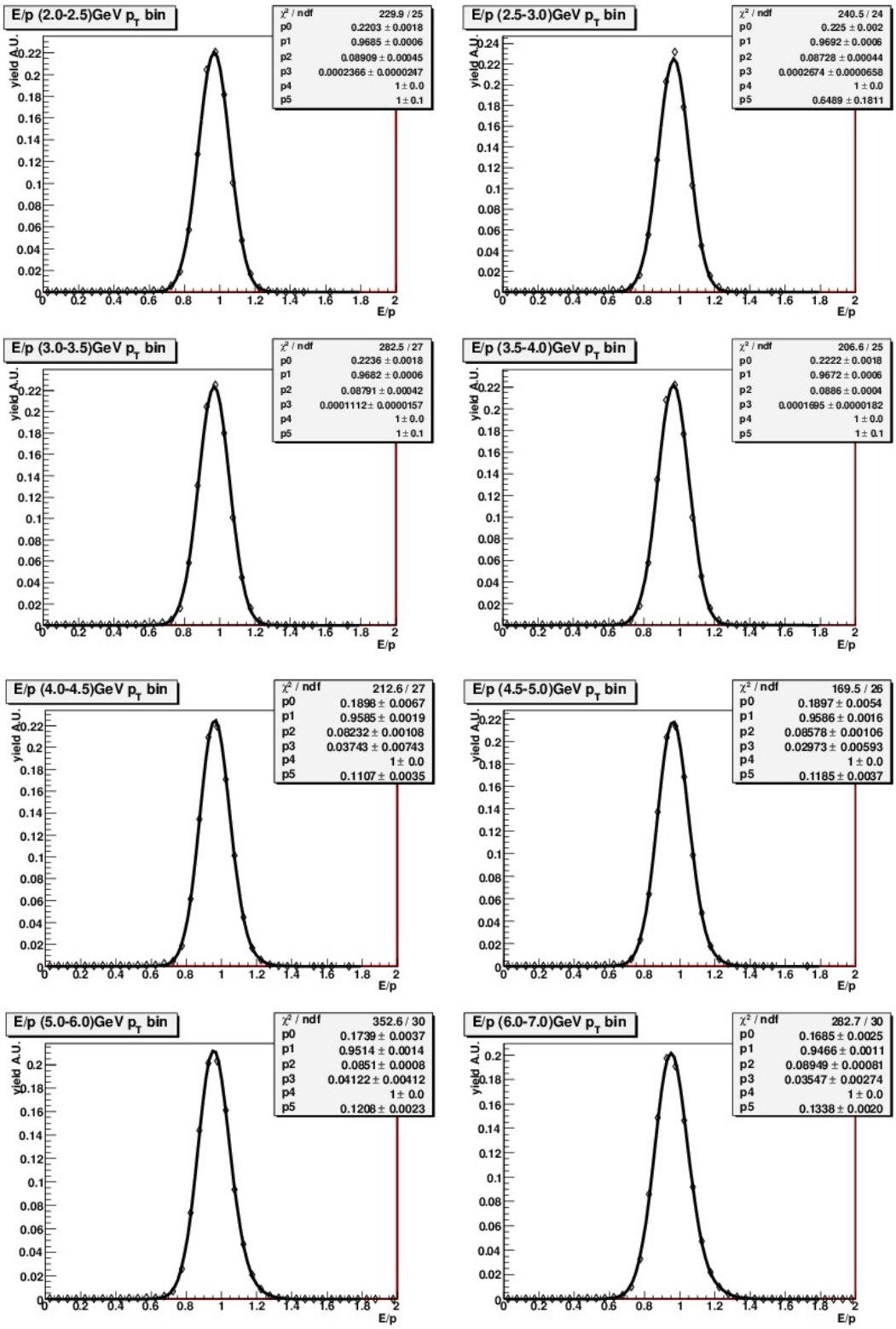
E/p (2.0-2.5)GeV p_T bin
χ^2 / ndf 229.9 / 25
p0 0.2203 ± 0.0018
p1 0.9685 ± 0.0006
p2 0.08909 ± 0.00045
p3 0.0002366 ± 0.0000247
p4 1 ± 0.0
p5 1 ± 0.1
E/p (2.5-3.0)GeV p_T bin
χ^2 / ndf 240.5 / 24
p0 0.225 ± 0.002
p1 0.9692 ± 0.0006
p2 0.08728 ± 0.00044
p3 0.0002674 ± 0.0000658
p4 1 ± 0.0
p5 0.6489 ± 0.1811
E/p (3.0-3.5)GeV p_T bin
χ^2 / ndf 282.5 / 27
p0 0.2236 ± 0.0018
p1 0.9682 ± 0.0006
p2 0.08791 ± 0.00042
p3 0.0001112 ± 0.0000157
p4 1 ± 0.0
p5 1 ± 0.1
E/p (3.5-4.0)GeV p_T bin
χ^2 / ndf 206.6 / 25
p0 0.2222 ± 0.0018
p1 0.9672 ± 0.0006
p2 0.0886 ± 0.0004
p3 0.0001695 ± 0.0000182
p4 1 ± 0.0
p5 1 ± 0.1
E/p (4.0-4.5)GeV p_T bin
χ^2 / ndf 212.6 / 27
p0 0.1898 ± 0.0067
p1 0.9585 ± 0.0019
p2 0.08232 ± 0.00108
p3 0.03743 ± 0.00743
p4 1 ± 0.0
p5 0.1107 ± 0.0035
E/p (4.5-5.0)GeV p_T bin
χ^2 / ndf 169.5 / 26
p0 0.1897 ± 0.0054
p1 0.9586 ± 0.0016
p2 0.08578 ± 0.00106
p3 0.02973 ± 0.00593
p4 1 ± 0.0
p5 0.1185 ± 0.0037
E/p (5.0-6.0)GeV p_T bin
χ^2 / ndf 352.6 / 30
p0 0.1739 ± 0.0037
p1 0.9514 ± 0.0014
p2 0.0851 ± 0.0008
p3 0.04122 ± 0.00412
p4 1 ± 0.0
p5 0.1208 ± 0.0023
E/p (6.0-7.0)GeV p_T bin
χ^2 / ndf 282.7 / 30
p0 0.1685 ± 0.0025
p1 0.9466 ± 0.0011
p2 0.08949 ± 0.00081
p3 0.03547 ± 0.00274
p4 1 ± 0.0
p5 0.1338 ± 0.0020
yield A.U.
E/p

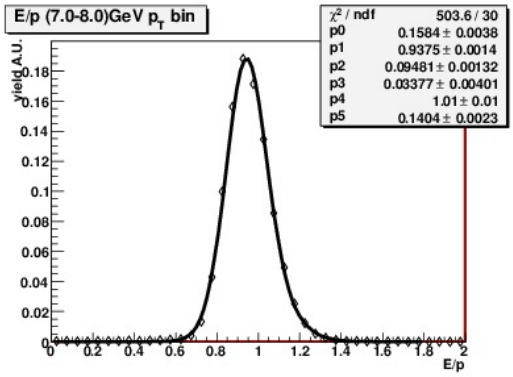
E/p (7.0-8.0)GeV p_T bin
χ^2 / ndf 503.6 / 30
p0 0.1584 ± 0.0038
p1 0.9375 ± 0.0014
p2 0.09481 ± 0.00132
p3 0.03377 ± 0.00401
p4 1.01 ± 0.01
p5 0.1404 ± 0.0023
yield A.U.
E/p

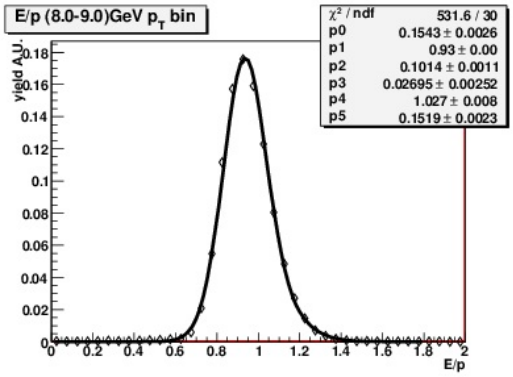
E/p (8.0-9.0)GeV p_T bin
χ^2 / ndf 531.6 / 30
p0 0.1543 ± 0.0026
p1 0.93 ± 0.00
p2 0.1014 ± 0.0011
p3 0.02695 ± 0.00252
p4 1.027 ± 0.008
p5 0.1519 ± 0.0023
yield A.U.
E/p

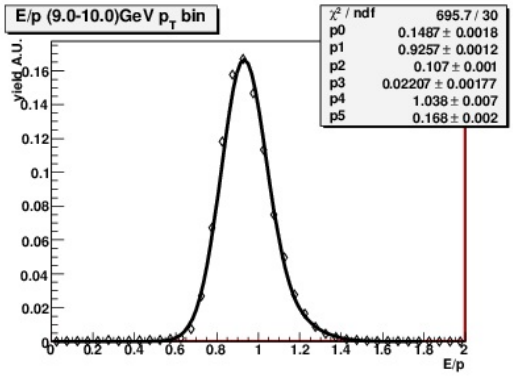
E/p (9.0-10.0)GeV p_T bin
χ^2 / ndf 695.7 / 30
p0 0.1487 ± 0.0018
p1 0.9257 ± 0.0012
p2 0.107 ± 0.001
p3 0.02207 ± 0.00177
p4 1.038 ± 0.007
p5 0.168 ± 0.002
yield A.U.
E/p

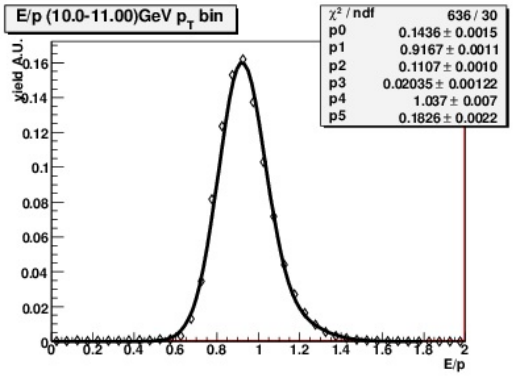
E/p (10.0-11.00)GeV p_T bin
χ^2 / ndf 636 / 30
p0 0.1436 ± 0.0015
p1 0.9167 ± 0.0011
p2 0.1107 ± 0.0010
p3 0.02035 ± 0.00122
p4 1.037 ± 0.007
p5 0.1826 ± 0.0022
yield A.U.
E/p

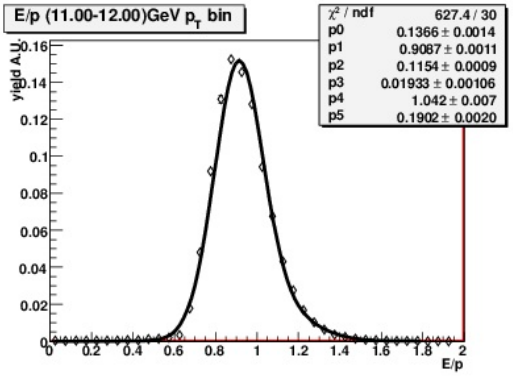
E/p (11.00-12.00)GeV p_T bin
χ^2 / ndf 627.4 / 30
p0 0.1366 ± 0.0014
p1 0.9087 ± 0.0011
p2 0.1154 ± 0.0009
p3 0.01933 ± 0.00106
p4 1.042 ± 0.007
p5 0.1902 ± 0.0020
yield A.U.
E/p

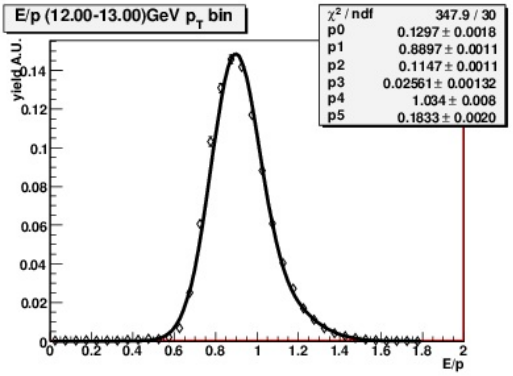
E/p (12.00-13.00)GeV p_T bin
χ^2 / ndf 347.9 / 30
p0 0.1297 ± 0.0018
p1 0.8897 ± 0.0011
p2 0.1147 ± 0.0011
p3 0.02561 ± 0.00132
p4 1.034 ± 0.008
p5 0.1833 ± 0.0020
yield A.U.
E/p

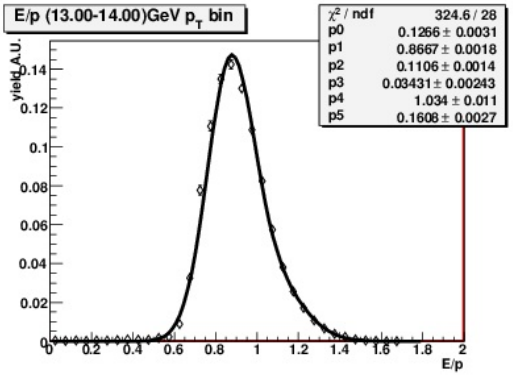
E/p (13.00-14.00)GeV p_T bin
χ^2 / ndf 324.6 / 28
p0 0.1266 ± 0.0031
p1 0.8667 ± 0.0018
p2 0.1106 ± 0.0014
p3 0.03431 ± 0.00243
p4 1.034 ± 0.011
p5 0.1608 ± 0.0027
yield A.U.
E/p

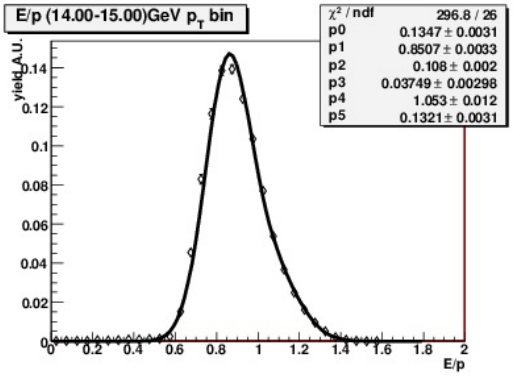
E/p (14.00-15.00)GeV p_T bin
χ^2 / ndf 296.8 / 26
p0 0.1347 ± 0.0031
p1 0.8507 ± 0.0033
p2 0.108 ± 0.002
p3 0.03749 ± 0.00298
p4 1.053 ± 0.012
p5 0.1321 ± 0.0031
yield A.U.
E/p

B.3 Fits to γ conversion electron E/p profiles

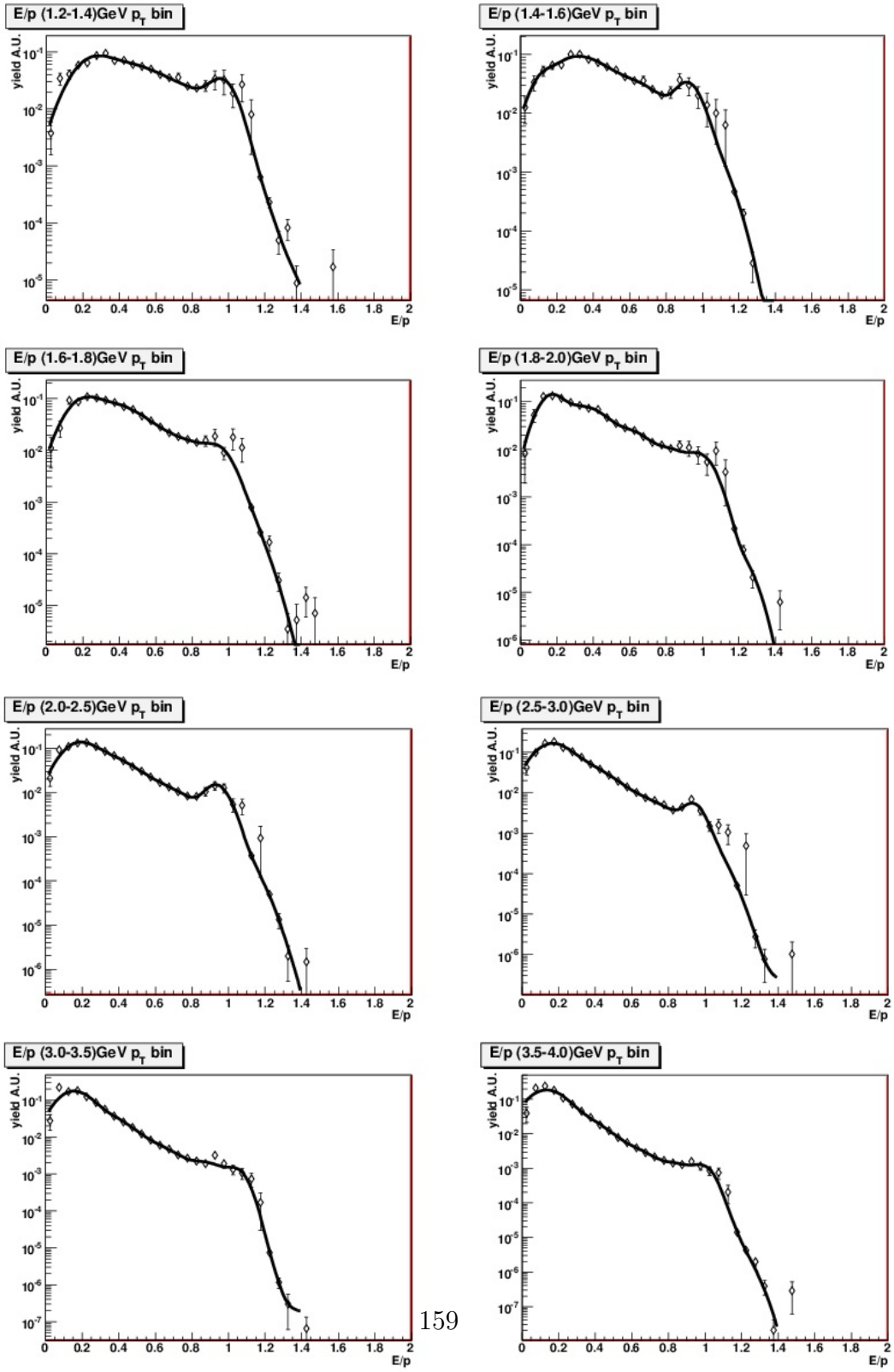

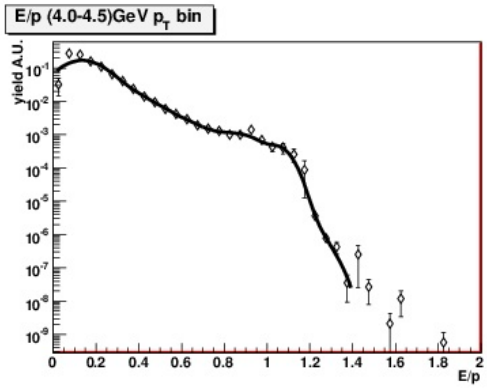
E/p (4.0-4.5)GeV p_T bin
yield A.U.
E/p

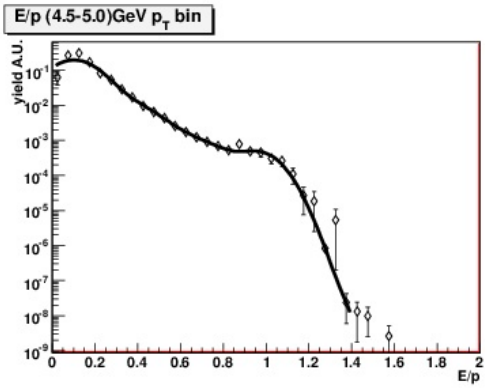
E/p (4.5-5.0)GeV p_T bin
yield A.U.
E/p

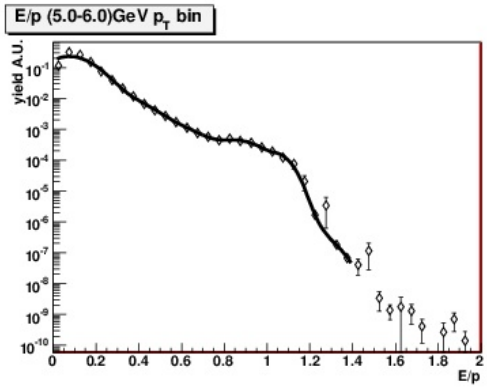
E/p (5.0-6.0)GeV p_T bin
yield A.U.
E/p

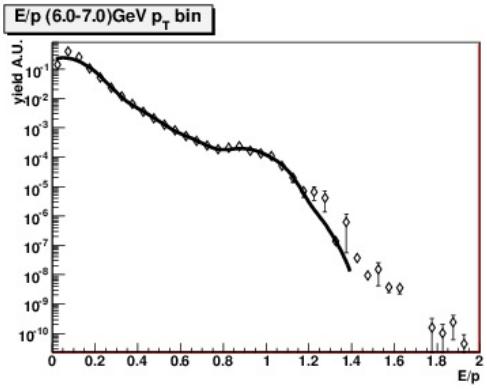
E/p (6.0-7.0)GeV p_T bin
yield A.U.
E/p

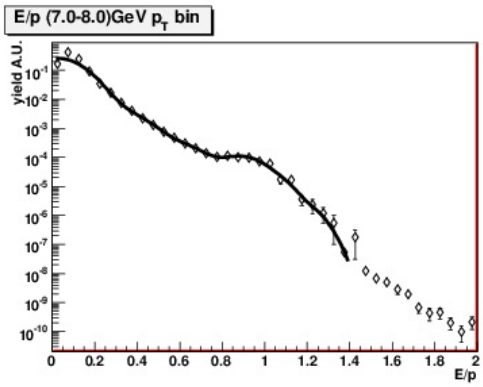
E/p (7.0-8.0)GeV p_T bin
yield A.U.
E/p

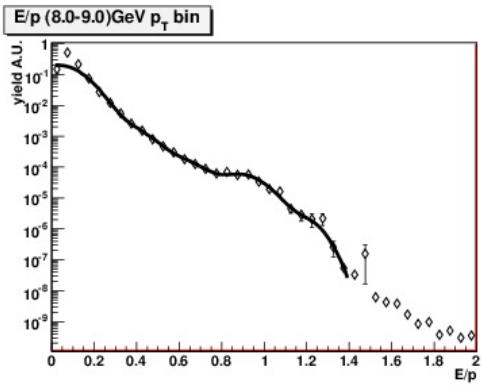
E/p (8.0-9.0)GeV p_T bin
yield A.U.
E/p

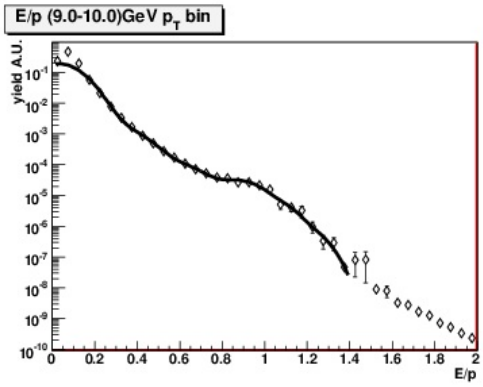
E/p (9.0-10.0)GeV p_T bin
yield A.U.
E/p

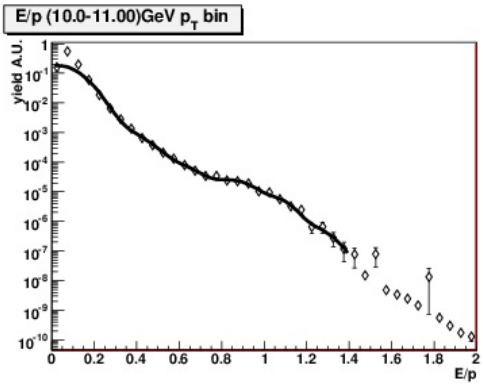
E/p (10.0-11.00)GeV p_T bin
yield A.U.
E/p

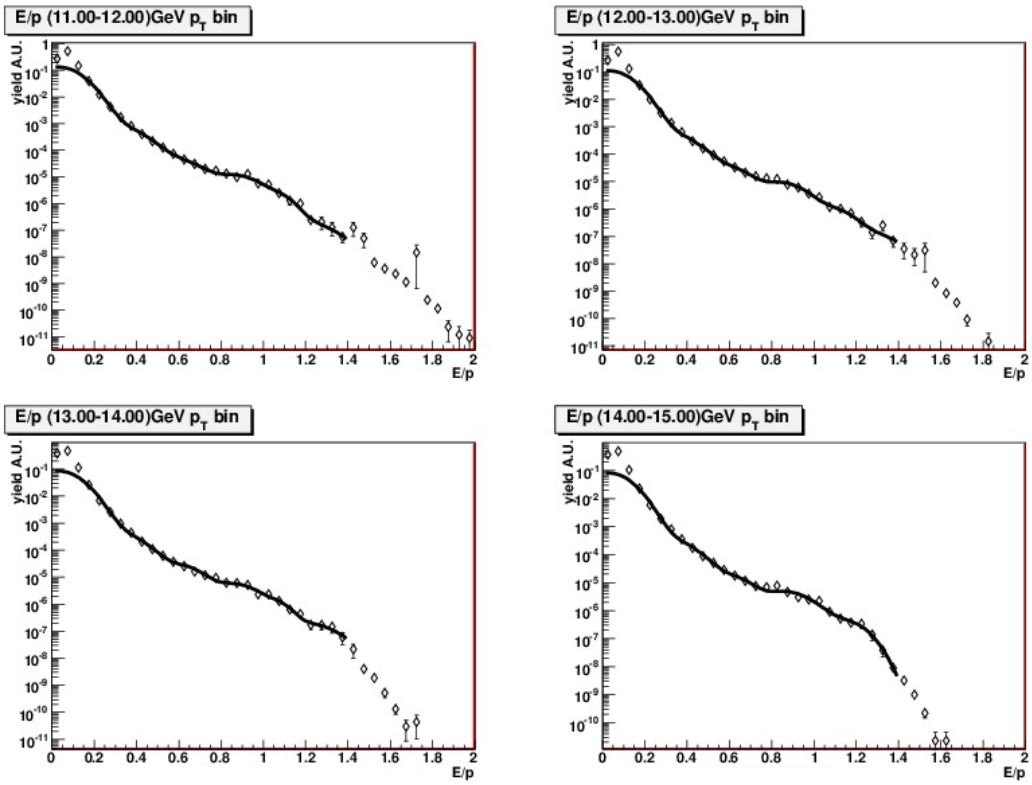
E/p (11.00-12.00)GeV p_T bin
E/p (12.00-13.00)GeV p_T bin
E/p (13.00-14.00)GeV p_T bin
E/p (14.00-15.00)GeV p_T bin
yield A.U.
E/p

B.4 Fits to π E/p profiles

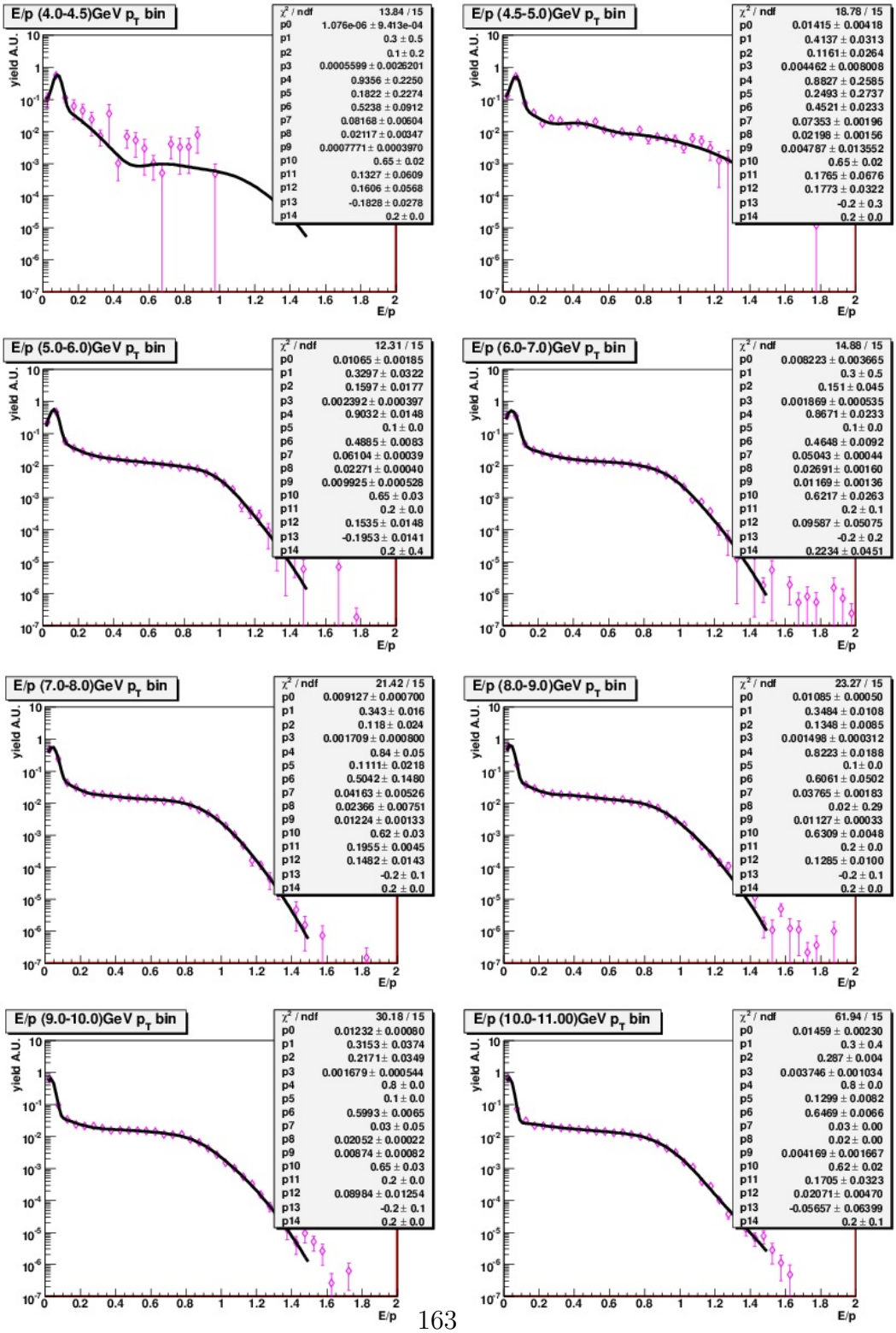

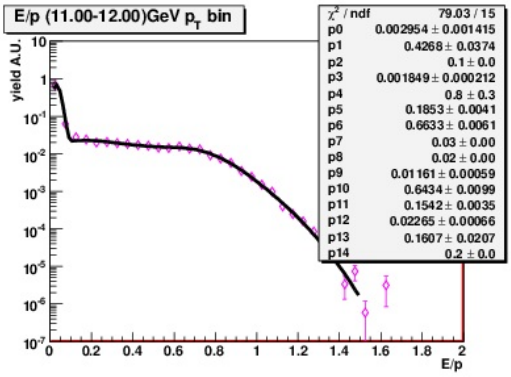
E/p (11.00-12.00)GeV p_T bin
χ^2 / ndf 79.03 / 15
p0 0.002954 ± 0.001415
p1 0.4268 ± 0.0374
p2 0.1 ± 0.0
p3 0.001849 ± 0.000212
p4 0.8 ± 0.3
p5 0.1853 ± 0.0041
p6 0.6633 ± 0.0061
p7 0.03 ± 0.00
p8 0.02 ± 0.00
p9 0.01161 ± 0.00059
p10 0.6434 ± 0.0099
p11 0.1542 ± 0.0035
p12 0.02265 ± 0.00066
p13 0.1607 ± 0.0207
p14 0.2 ± 0.0
yield A.U.
E/p

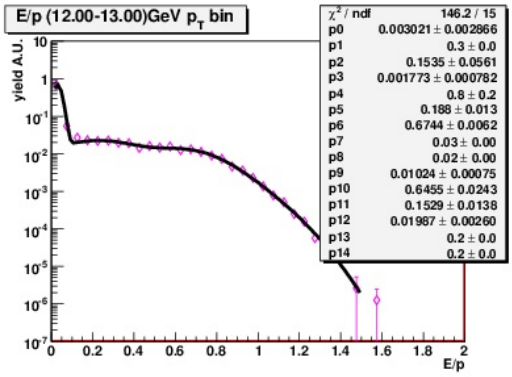
E/p (12.00-13.00)GeV p_T bin
χ^2 / ndf 146.2 / 15
p0 0.003021 ± 0.002866
p1 0.3 ± 0.0
p2 0.1535 ± 0.0561
p3 0.001773 ± 0.000782
p4 0.8 ± 0.2
p5 0.188 ± 0.013
p6 0.6744 ± 0.0062
p7 0.03 ± 0.00
p8 0.02 ± 0.00
p9 0.01024 ± 0.00075
p10 0.6455 ± 0.0243
p11 0.1529 ± 0.0138
p12 0.01987 ± 0.00260
p13 0.2 ± 0.0
p14 0.2 ± 0.0
yield A.U.
E/p

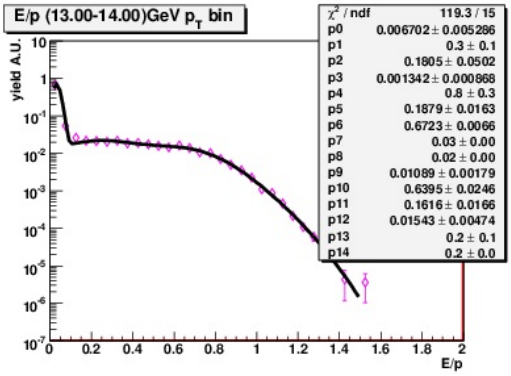
E/p (13.00-14.00)GeV p_T bin
χ^2 / ndf 119.3 / 15
p0 0.006702 ± 0.005286
p1 0.3 ± 0.1
p2 0.1805 ± 0.0502
p3 0.001342 ± 0.000868
p4 0.8 ± 0.3
p5 0.1879 ± 0.0163
p6 0.6723 ± 0.0066
p7 0.03 ± 0.00
p8 0.02 ± 0.00
p9 0.01089 ± 0.00179
p10 0.6395 ± 0.0246
p11 0.1616 ± 0.0166
p12 0.01543 ± 0.00474
p13 0.2 ± 0.1
p14 0.2 ± 0.0
yield A.U.
E/p

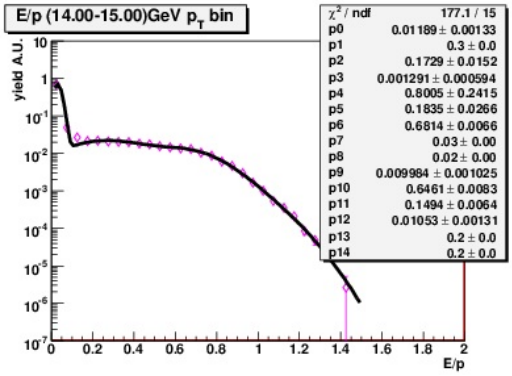
E/p (14.00-15.00)GeV p_T bin
χ^2 / ndf 177.1 / 15
p0 0.01189 ± 0.00133
p1 0.3 ± 0.0
p2 0.1729 ± 0.0152
p3 0.001291 ± 0.000594
p4 0.8005 ± 0.2415
p5 0.1835 ± 0.0266
p6 0.6814 ± 0.0066
p7 0.03 ± 0.00
p8 0.02 ± 0.00
p9 0.009984 ± 0.001025
p10 0.6461 ± 0.0083
p11 0.1494 ± 0.0064
p12 0.01053 ± 0.00131
p13 0.2 ± 0.0
p14 0.2 ± 0.0
yield A.U.
E/p

B.5 Fits to Ke3 E/p profiles

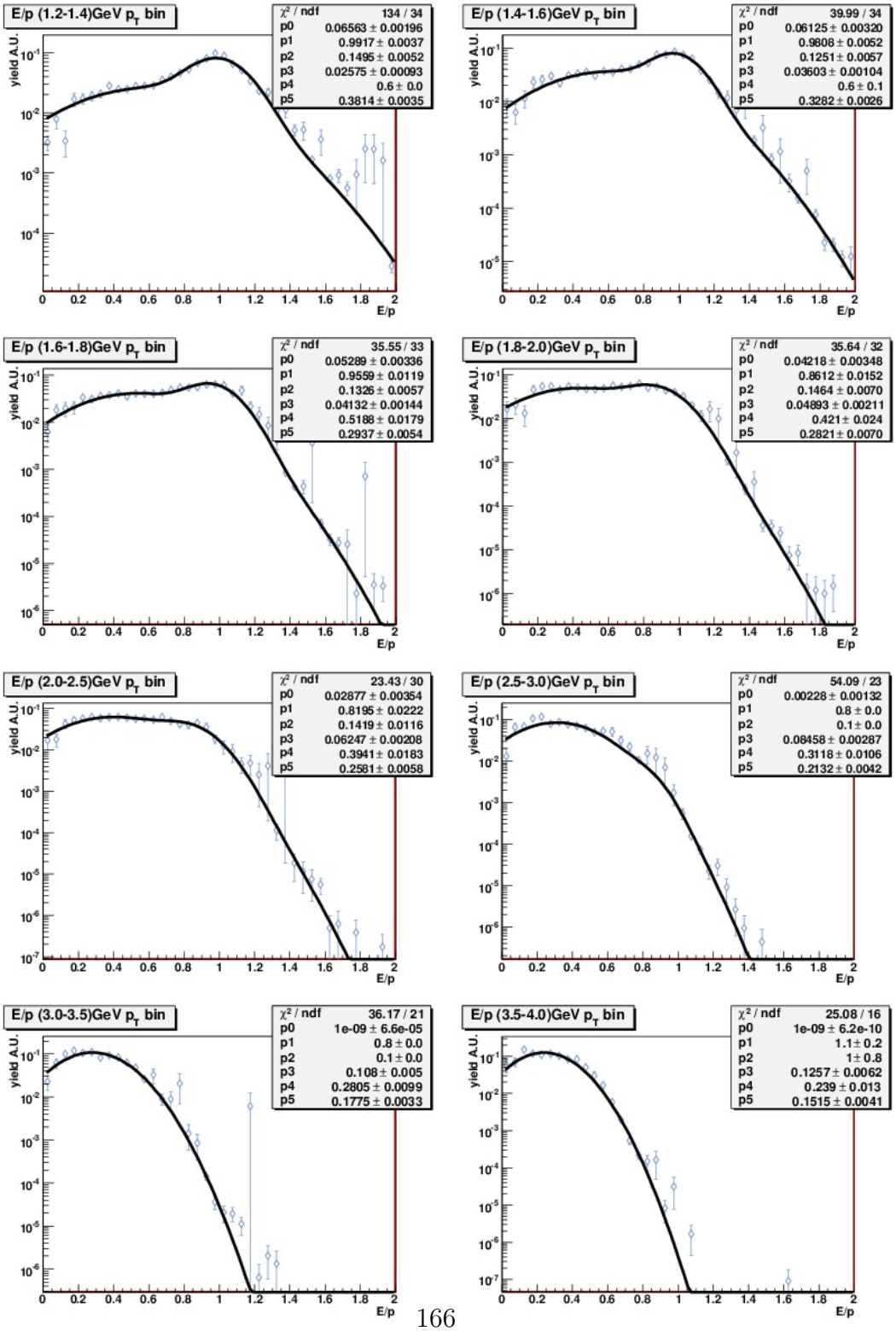

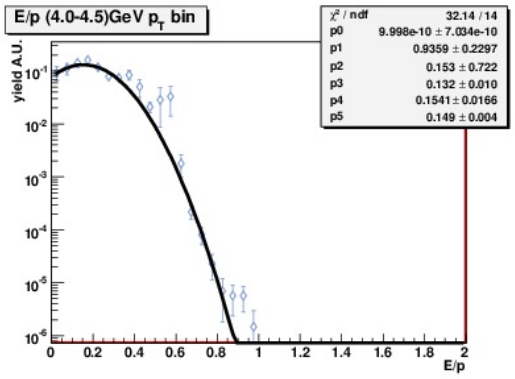
E/p (4.0-4.5)GeV p_T bin
χ^2 / ndf 32.14 / 14
p0 9.998e-10 ± 7.034e-10
p1 0.9359 ± 0.2297
p2 0.153 ± 0.722
p3 0.132 ± 0.010
p4 0.1541 ± 0.0166
p5 0.149 ± 0.004
yield A.U.
E/p

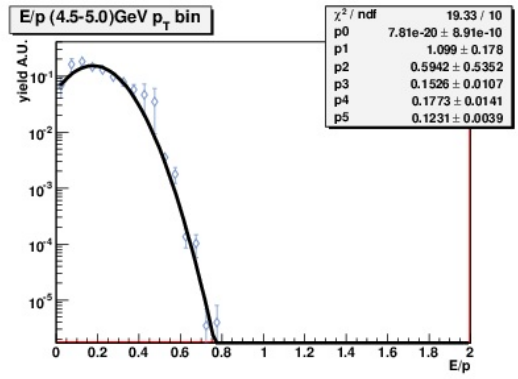
E/p (4.5-5.0)GeV p_T bin
χ^2 / ndf 19.33 / 10
p0 7.81e-20 ± 8.91e-10
p1 1.099 ± 0.178
p2 0.5942 ± 0.5352
p3 0.1526 ± 0.0107
p4 0.1773 ± 0.0141
p5 0.1231 ± 0.0039
yield A.U.
E/p

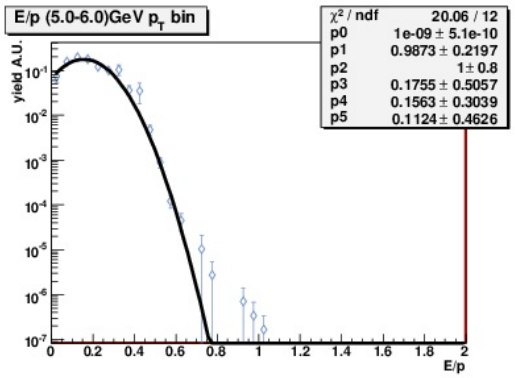
E/p (5.0-6.0)GeV p_T bin
χ^2 / ndf 20.06 / 12
p0 1e-09 ± 5.1e-10
p1 0.9873 ± 0.2197
p2 1 ± 0.8
p3 0.1755 ± 0.5057
p4 0.1563 ± 0.3039
p5 0.1124 ± 0.4626
yield A.U.
E/p

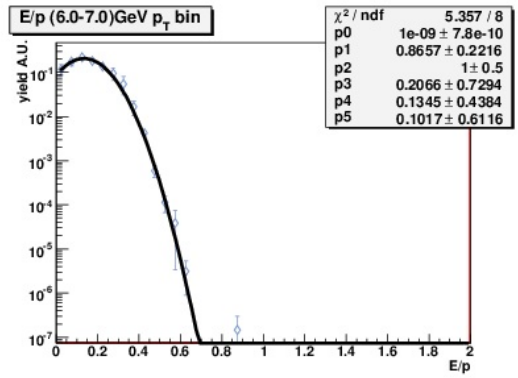
E/p (6.0-7.0)GeV p_T bin
χ^2 / ndf 5.357 / 8
p0 1e-09 ± 7.8e-10
p1 0.8657 ± 0.2216
p2 1 ± 0.5
p3 0.2066 ± 0.7294
p4 0.1345 ± 0.4384
p5 0.1017 ± 0.6116
yield A.U.
E/p

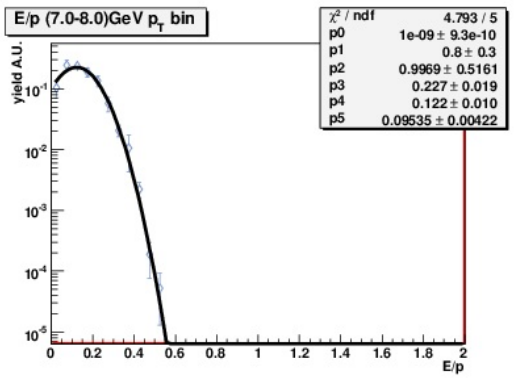
E/p (7.0-8.0)GeV p_T bin
χ^2 / ndf 4.793 / 5
p0 1e-09 ± 9.3e-10
p1 0.8 ± 0.3
p2 0.9969 ± 0.5161
p3 0.227 ± 0.019
p4 0.122 ± 0.010
p5 0.09535 ± 0.00422
yield A.U.
E/p

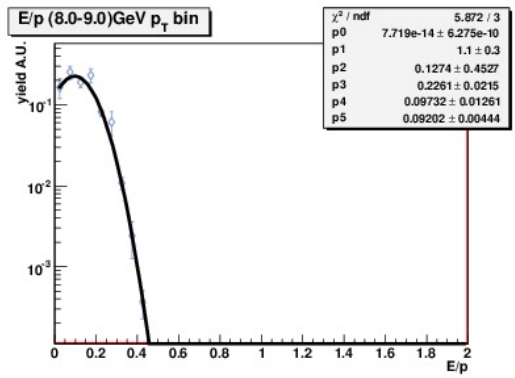
E/p (8.0-9.0)GeV p_T bin
χ^2 / ndf 5.872 / 3
p0 7.719e-14 ± 6.275e-10
p1 1.1 ± 0.3
p2 0.1274 ± 0.4527
p3 0.2261 ± 0.0215
p4 0.09732 ± 0.01261
p5 0.09202 ± 0.00444
yield A.U.
E/p

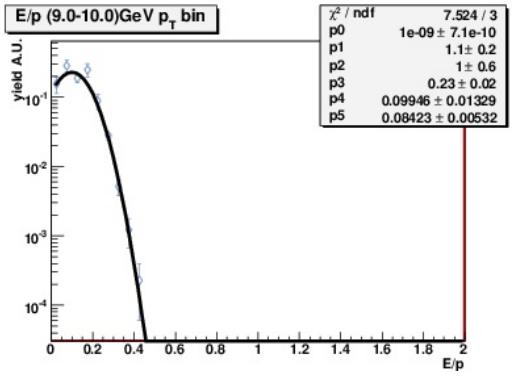
E/p (9.0-10.0)GeV p_T bin
χ^2 / ndf 7.524 / 3
p0 1e-09 ± 7.1e-10
p1 1.1 ± 0.2
p2 1 ± 0.6
p3 0.23 ± 0.02
p4 0.09946 ± 0.01329
p5 0.08423 ± 0.00532
yield A.U.
E/p

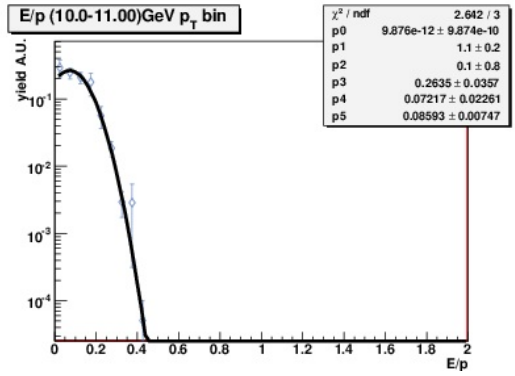
E/p (10.0-11.00)GeV p_T bin
χ^2 / ndf 2.642 / 3
p0 9.876e-12 ± 9.874e-10
p1 1.1 ± 0.2
p2 0.1 ± 0.8
p3 0.2635 ± 0.0357
p4 0.07217 ± 0.02261
p5 0.08593 ± 0.00747
yield A.U.
E/p

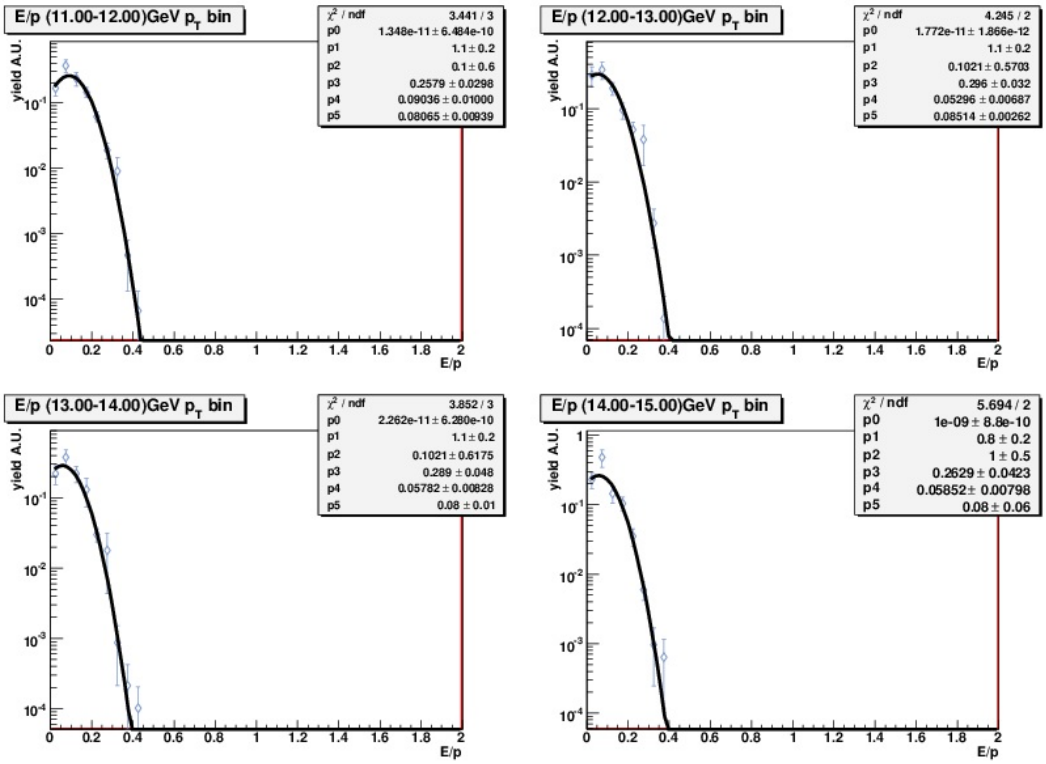
E/p (11.00-12.00)GeV p_T bin
χ^2 / ndf 3.441 / 3
p0 1.348e-11 ± 6.484e-10
p1 1.1 ± 0.2
p2 0.1 ± 0.6
p3 0.2579 ± 0.0298
p4 0.09036 ± 0.01000
p5 0.08065 ± 0.00939
E/p (12.00-13.00)GeV p_T bin
χ^2 / ndf 4.245 / 2
p0 1.772e-11 ± 1.866e-12
p1 1.1 ± 0.2
p2 0.1021 ± 0.5703
p3 0.296 ± 0.032
p4 0.05296 ± 0.00687
p5 0.08514 ± 0.00262
E/p (13.00-14.00)GeV p_T bin
χ^2 / ndf 3.852 / 3
p0 2.262e-11 ± 6.280e-10
p1 1.1 ± 0.2
p2 0.1021 ± 0.6175
p3 0.289 ± 0.048
p4 0.05782 ± 0.00828
p5 0.08 ± 0.01
E/p (14.00-15.00)GeV p_T bin
χ^2 / ndf 5.694 / 2
p0 1e-09 ± 8.8e-10
p1 0.8 ± 0.2
p2 1 ± 0.5
p3 0.2629 ± 0.0423
p4 0.05852 ± 0.00798
p5 0.08 ± 0.06
yield A.U.
E/p

B.6 Fits to data E/p profiles

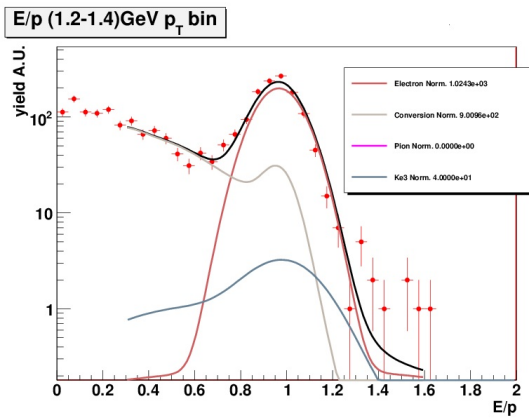

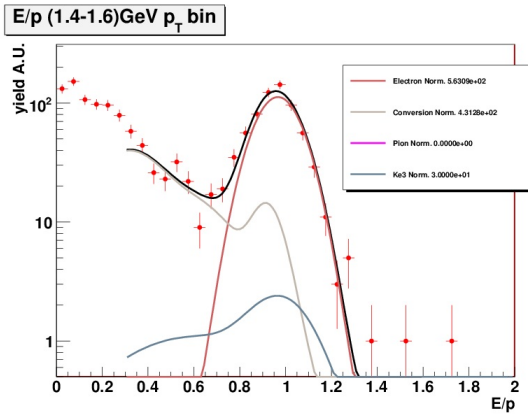

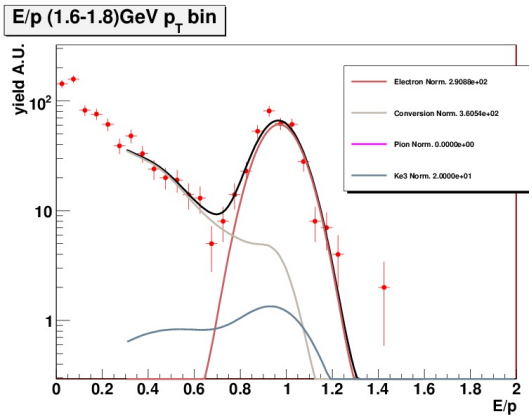

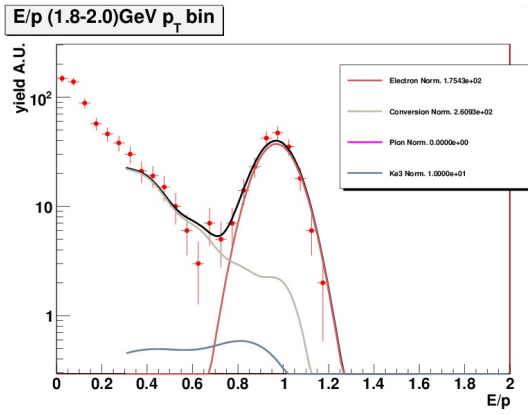

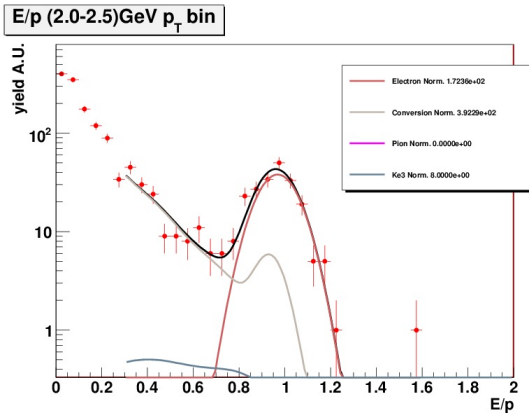

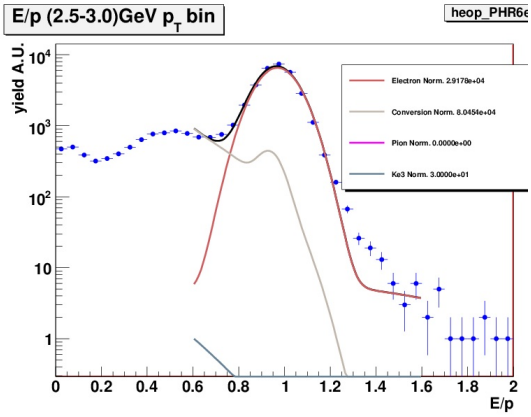

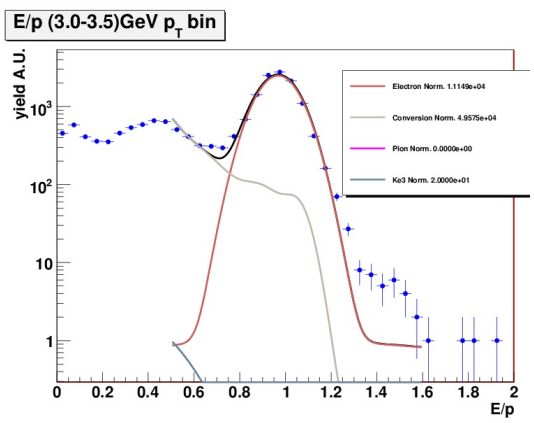
E/p (3.0-3.5)GeV p_T bin
yield A.U.
E/p
Electron Norm. 1.1149e+04
Conversion Norm. 4.9575e+04
Pion Norm. 0.0000e+00
Ke3 Norm. 2.0000e+01

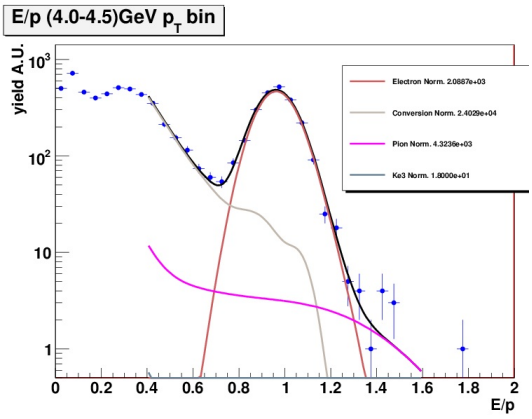
E/p (4.0-4.5)GeV p_T bin
yield A.U.
E/p
Electron Norm. 2.0887e+03
Conversion Norm. 2.4029e+04
Pion Norm. 4.3236e+03
Ke3 Norm. 1.8000e+01

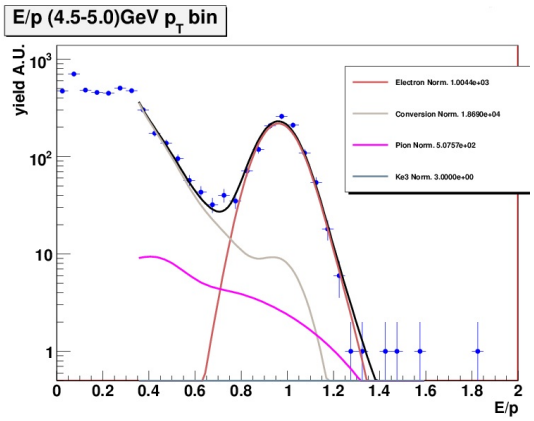
E/p (4.5-5.0)GeV p_T bin
yield A.U.
E/p
Electron Norm. 1.0044e+03
Conversion Norm. 1.8690e+04
Pion Norm. 5.0757e+02
Ke3 Norm. 3.0000e+00

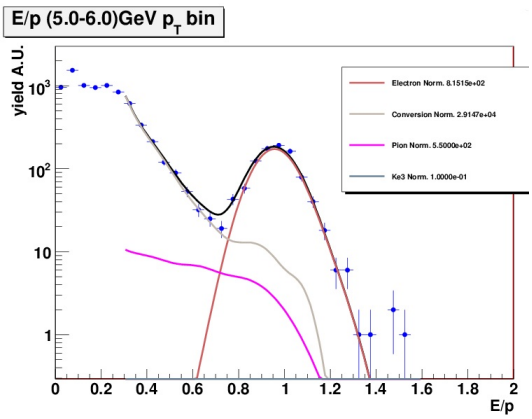
E/p (5.0-6.0)GeV p_T bin
yield A.U.
E/p
Electron Norm. 8.1515e+02
Conversion Norm. 2.9147e+04
Pion Norm. 5.5000e+02
Ke3 Norm. 1.0000e-01

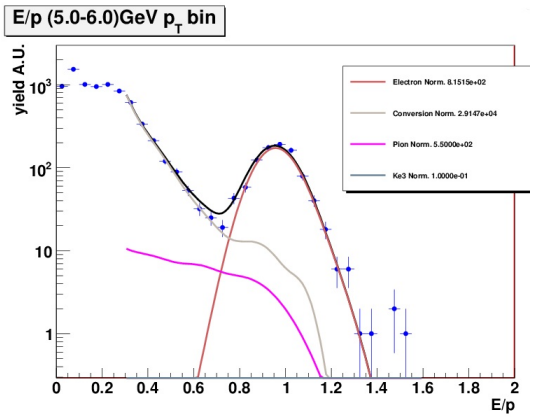
E/p (5.0-6.0)GeV p_T bin
yield A.U.
E/p
Electron Norm. 8.1515e+02
Conversion Norm. 2.9147e+04
Pion Norm. 5.5000e+02
Ke3 Norm. 1.0000e-01

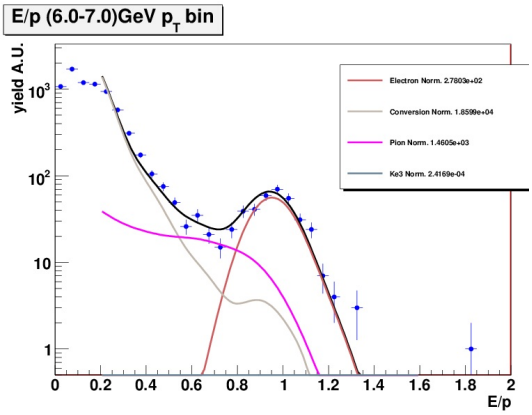
E/p (6.0-7.0)GeV p_T bin
yield A.U.
E/p
Electron Norm. 2.7803e+02
Conversion Norm. 1.8599e+04
Pion Norm. 1.4605e+03
Ke3 Norm. 2.4169e-04

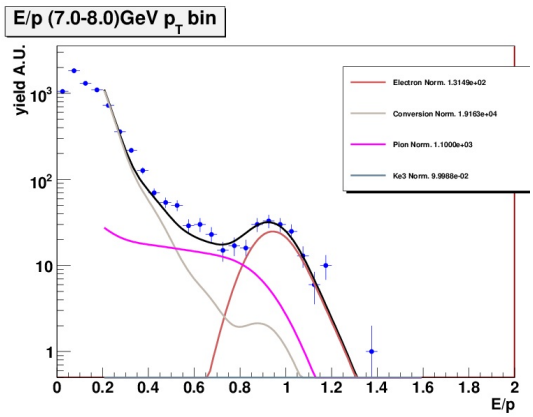
E/p (7.0-8.0)GeV p_T bin
yield A.U.
E/p
Electron Norm. 1.3149e+02
Conversion Norm. 1.9163e+04
Pion Norm. 1.1000e+03
Ke3 Norm. 9.9988e-02

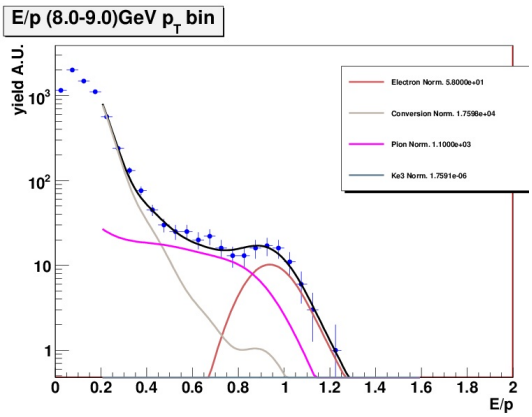
E/p (8.0-9.0)GeV p_T bin
yield A.U.
E/p
Electron Norm. 5.8000e+01
Conversion Norm. 1.7598e+04
Pion Norm. 1.1000e+03
Ke3 Norm. 1.7591e-06

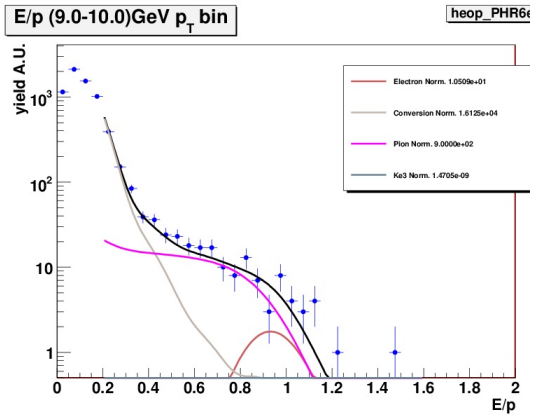
E/p (9.0-10.0)GeV p_T bin
heop_PHR6
yield A.U.
E/p
Electron Norm. 1.0509e+01
Conversion Norm. 1.6125e+04
Pion Norm. 9.0000e+02
Ke3 Norm. 1.4705e-09

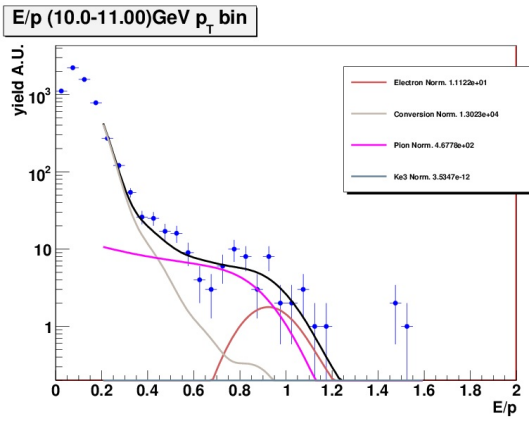
E/p (10.0-11.00)GeV p_T bin
yield A.U.
E/p
Electron Norm. 1.1122e+01
Conversion Norm. 1.3023e+04
Pion Norm. 4.6778e+02
Ke3 Norm. 3.5347e-12

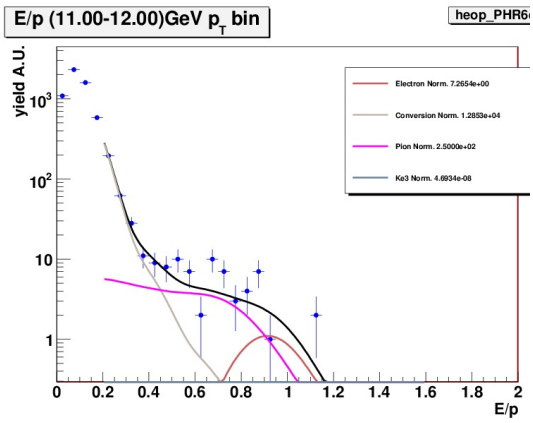
E/p (11.00-12.00)GeV p_T bin
heop_PHR6
yield A.U.
E/p
Electron Norm. 7.2654e+00
Conversion Norm. 1.2853e+04
Pion Norm. 2.5000e+02
Ke3 Norm. 4.6934e-08

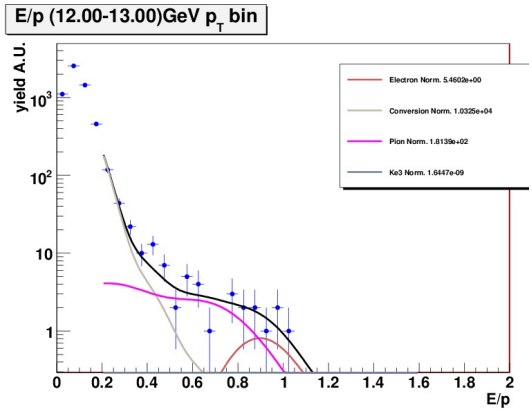
E/p (12.00-13.00)GeV p_T bin
yield A.U.
E/p
Electron Norm. 5.4602e+00
Conversion Norm. 1.0325e+04
Pion Norm. 1.8139e+02
Ke3 Norm. 1.6447e-09

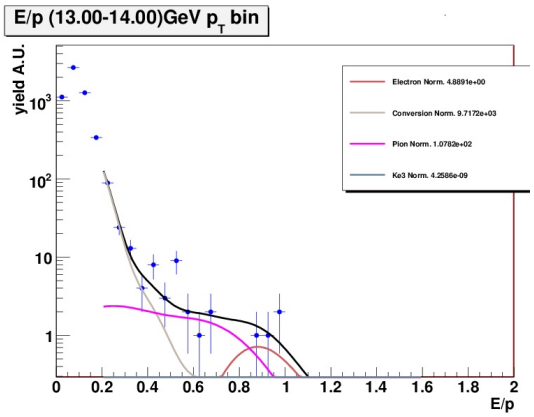
E/p (13.00-14.00)GeV p_T bin
yield A.U.
Electron Norm. 4.8891e+00
Conversion Norm. 9.7172e+03
Pion Norm. 1.0782e+02
Ke3 Norm. 4.2586e-09
E/p

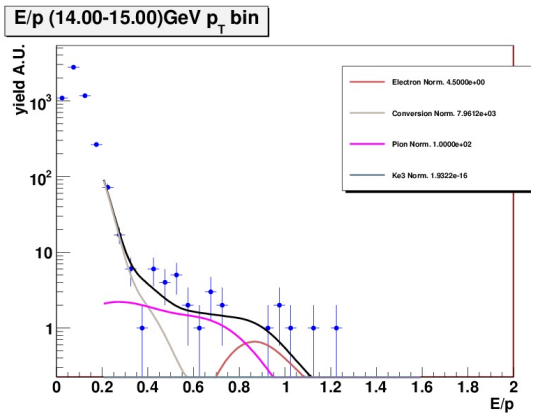
E/p (14.00-15.00)GeV p_T bin
yield A.U.
Electron Norm. 4.5000e+00
Conversion Norm. 7.9612e+03
Pion Norm. 1.0000e+02
Ke3 Norm. 1.9322e-16
E/p

Bibliography

[1] Wikipedia Contributors. Hough transform. *Wikipedia, The Free Encyclopedia*, https://secure.wikimedia.org/wikipedia/en/wiki/Hough_transform, 3 April 2011 at 19:53 UTC (cited April 2011).

[2] J. Kamin A. Drees, T. Hemmick. *PHENIX internal analysis note 858*.

[3] R. Bennett and K. Okada. *PHENIX internal analysis note 741*.

[4] I. Arsene et al. *Nucl. Phys.*, A757:1, 2005.

[5] K. Adcox et al. *Nucl. Phys.*, A757:184, 2005.

[6] B.B. Back et al. *Nucl. Phys.*, A757:28, 2005.

[7] J. Adams et al. *Nucl. Phys.*, A757:102, 2005.

[8] M. Creutz. *Quarks, Gluons and Lattices*. Cambridge University Press, 1985.

[9] R. Vogt. *Ultrarelativistic Heavy-Ion Collisions*. Elsevier Science, 2007.

[10] G. Sterman et al. Handbook of perturbative qcd. *Rev. Mod. Phys.*, 67: 157–248, 1995.

[11] M. Harrison, T. Ludlam, and S. Ozaki. The relativistic heavy ion collider project: RHIC and its detectors. *Nuclear Inst. and Methods in Physics Research A*, 499(2-3):235–880, March 2003.

[12] D. Bettoni et al. *Nuclear Instruments and Methods A*, A236:264, 1985.

[13] D. Bettoni et al. *Nuclear Instruments and Methods A*, A252:272, 1986.

[14] Stephen C. Johnson, John W. No, Federica Ceretto, Axel Drees, Thomas K. Hemmick, Barbara Jacak, and For The Phenix Collaboration. Three-dimensional track finding in the phenix drift chamber by a combinatorial hough transform method, 1998.

[15] Stephen C. Johnson, John W. No, Federica Ceretto, Axel Drees, Thomas K. Hemmick, Barbara Jacak, and For The Phenix Collaboration. Three-dimensional track finding in the phenix drift chamber by a combinatorial hough transform method, 1998.

[16] various. Homepage for spec (the standard performance evaluation corporation). http://www.spec.org, .

[17] K. Adcox et al. *Nucl. Instr. Meth.*, A497:263–293, 2003.

[18] Y. Akiba et al. *Nucl. Instr. Meth.*, A433:143–148, 1999.

[19] Wikipedia Contributors. Hough transform. *Wikipedia, The Free Encyclopedia*, https://secure.wikimedia.org/wikipedia/en/wiki/Hough_transform, 3 April 2011 at 19:53 UTC (cited April 2011).

[20] Phenix conceptional design report.

[21] various. Phenix emcal subsystem. http://www.phenix.bnl.gov/phenix/WWW/emcal/emcal.html, .

[22] various. *Experimental Techniques in High-Energy Nuclear and Particle Physics*. World Scientific Pub Co Inc, 1992.

[23] various. *Instrumentation in high energy physics*, volume 9 of *Advanced series on directions in high energy physics*. Singapore River Edge, N.J. World Scientific, 1992.

[24] Y. Akiba et al. *PHENIX internal analysis note 065*, .

[25] S. Belikov et al. *PHENIX internal analysis note 184*, .

[26] S. S. Adler et al. *Phys. Rev. Lett.*, 91:241803, 2003.

[27] Alexander Bazilevsky. *PHENIX Analysis Note AN567, and private communication.*

[28] C. Amsler et al. *Physics Letters*, B667:1, 2008.

[29] M. J. Tannenbaum. Smearing and binning of falling spectra. *PHENIX Analysis Note 62*, 2001.

[30] Tatsuya Chujo et al. *PHENIX internal analysis note 567*, .

[31] Y. Akiba et al. *PHENIX internal analysis note 077*, .

[32] R. Averbeck. *PHENIX internal analysis note 349*.

[33] R. Averbeck, A. Dres, Y. Akiba, and T. Hachiya. *PHENIX internal analysis note 089*.

[34] G.J. Gournaris and J.J. Sakurai. *Phys.Rev.Lett.*, 21:244, 1968.

[35] N. Kroll and W. Wada. *Phys.Rev.*, 98:1355, 1955.

[36] K. Boyle et al. *PHENIX Paper Preparation Group report 101*, .

[37] Frank Ellinghaus. *PHENIX preliminary data, private communication*.

[38] W.M. Yao et al. *Journal of Physics*, G33:1, 2006.

[39] Sasha Milov Victor Riabov, Yuri Riabov. *PHENIX internal analysis note 523*.

[40] A. Toia T. Dahms, A. Drees. *PHENIX internal analysis note 614*.

[41] Dmitry Ivanishchev et. al. *PHENIX internal analysis note 873*, .

[42] Abby Bickley et. al. *PHENIX Paper Preparation Group 069*, .

[43] C.L. Silva, M. Rosati, and V. Hanger. *PHENIX internal analysis note 802*.

[44] Marisilvia Donadelli, Marzia Rosati, and Cesar Luiz da Silva. *PHENIX internal analysis note 722*.

[45] R. Gavai et al. *Int. J. Mod. Phys*, A10:3043, 1995.

[46] Tatsuya Chujo, Masahiro Konno, Michael Tannenbaum, and Shengli Huang. *PHENIX Paper Preparation Group 101*.

[47] Matteo Cacciari, Paolo Nason, and Ramona Vogt. *Phys.Rev.Lett.*, 95: 122001, 2005.

[48] N. Armesto, M. Cacciari, A. Daineseand C.A. Salgado, and U.A. Wiedemann. *Phys. Lett.*, B637:362–366, 2006.

[49] R. Vogt. *Eur.Phys.J.ST*, 155:213–222, 2008.

[50] H. Agakishiev (et al.). *Phys.Rev. D*, 83:052006, 2011.

[51] Z. Lin and M. Gyulassy. *Phys.Rev.Lett.*, 77:1222, 1996.

[52] R. Vogt, editor. *Systematics of Heavy Quark Production at RHIC*, 2002. 18th Winter Workshop on Nuclear Dynamics.

[53] M.Baker et. al. For The Phenix Collaboration. Proposal for a silicon vertex tracker (vtx) for the phenix experiment, 2007.